Nanostructured Titania Coatings for Drug-Eluting Medical Implants

THÈSE N^O 4478 (2009)

PAR

Karin DITTMAR

EPFL

ÉCOLE POLYTECHNIQUE
FÉDÉRALE DE LAUSANNE

Suisse
2009

ABSTRACT

Medical implants delivering drugs are used to ensure efficient medication at body sites, at which the conventional administration of drugs is insufficient. The application of drug-delivery coatings is a beneficial concept for implants exposed to mechanical loads, such as orthopedic implants or cardiovascular stents. Many of the commercially available coated stent-implants are designed to release a drug locally and at a predefined rate out of a polymer matrix in order to prevent the re-blocking of the artery. The polymer matrices of such so-called drug-eluting stents (DES) can either be bio-degradable or inert. In spite of their successful drug-release capability, they often fail with regard to biocompatibility and long-term chemical and mechanical stability. The aim of the project is to create a novel, nanostructured, ceramic drug-delivering coating for stents, which exhibits an improved performance as compared to the one of conventional DES-implants. The present work addresses the processing and characterization of a nanoporous coating, its drug-loading and release behavior as well as its cytocompatibility.

A nanostructured titania (TiO_2) coating was deposited on either 316L stainless steel or silicon wafer supports by a multi-step dip coating process involving TiO_2-nanoparticle and polymer template suspensions. A subsequent sintering step burned the polymer template particles to create drug reservoirs in the thin coating, which has a thickness of 1.2 μm. These drug reservoirs have a diameter of 1 μm and are surrounded by a porous ceramic structure. This surrounding ceramic structure exhibits a mean pore width of 76 nm and has an open porosity of 50 % as was determined by small angle neutron scattering and mercury intrusion porosimetry. The presence of the drug reservoirs further increases the porosity and hence the drug-load capability of the coating. In addition, the coating was characterized with regard to the specific surface area by the Brunauer-Emmett-Teller (BET)-method, the crystal phases of TiO_2 by X-ray diffraction (XRD) and the elemental composition by X-ray photoelectron spectroscopy (XPS).

From cardiovascular DESs, therapeutical agents, which either reduce the activation of the immune system or inhibit cell growth, are released into the coronary artery tissue to prevent the local re-blocking of the artery. In the present study, the cell growth inhibiting drug paclitaxel (PTX) was successfully loaded into the highly porous titania coatings by a low-pressure, solvent evaporation technique. The pharmaceutical was accumulated in the drug reservoirs, in the pores of the surrounding ceramic structure and on top of the coating. The total quantity of loaded drug could be varied by changing the coating's structure or the

parameters of the drug-loading process. The maximum quantity of PTX incorporated into the coatings was comparable with the amount of PTX in the commercially available Taxus^{TM} DES of 1 μg/mm^2. The *in vitro* release tests of PTX from the coatings into ultra pure water revealed a slow, continuous liberation of the therapeutical agent. After one month of testing, only 11 % of initially incorporated drug were released. The obtained release profile is similar to the one of a PTX-eluting stent. Further release tests of PTX from the titania coatings into bovine plasma were performed and the findings compared to a release profile of the Taxus^{TM} stent.

In vitro cytotoxicity tests were accomplished, in which isolated, primary, bovine endothelial cells were brought in direct contact to the non-PTX-loaded titania coatings. First results indicate that the nanostructured TiO$_2$-coatings on wafer and 316L stainless steel supports are cytocompatible.

A technology platform has been established, which comprises the characterization of the titania coatings, the loading and quantification of PTX as well as the cytotoxicity evaluation. Factors affecting each of these issues were identified. The findings of the present study will contribute to optimize the nanostructured, ceramic drug-eluting coating for its implementation in DESs and to adapt it to various biomedical applications.

Keywords: nanostructured coating, drug-eluting stent, cytotoxicity

ZUSAMMENFASSUNG

Wirkstofffreisetzende Implantate werden angewandt, um die Medikation an den Körperstellen sicherzustellen, in denen die Dosis des herkömmlich verabreichten Medikamentes nicht ausreicht. Die Anwendung wirkstofffreisetzender Beschichtungen ist vorteilhaft für Implantate, die mechanischen Beanspruchungen unterliegen. Solche sind zum Beispiel orthopädische Implantate oder kardiovaskuläre Gefässprothesen, so genannte „Stents". Viele der kommerziell erhältlichen, beschichteten Stents sind so konstruiert, dass sie kontrolliert einen Wirkstoff aus einer Polymerbeschichtung freisetzen. Diese Wirkstoffe verhindern eine Wiederverschliessung der Arterie nach der Implantation. Die Polymermatrizes der wirkstofffreisetzenden Stents (WFS) können bio-degradabel oder inert sein. Trotz ihrer erfolgreichen Anwendung als Wirkstofffreisetzungssysteme versagen sie häufig wegen ungenügender Biokompatibilität, sowie ihrer chemischen und mechanischen Langzeitstabilität. Ziel war es, eine neue nanostrukturierte, wirkstofffreisetzende Keramikbeschichtung für Stents zu entwickeln, die eine bessere Leistungsfähigkeit als herkömmliche WFS aufweist. Die vorliegende Arbeit befasst sich vornehmlich mit der Herstellung und Charakterisierung einer nanoporösen Keramikbeschichtung, deren Beladung mit einem Wirkstoff und dessen Freisetzung, sowie ihrer Zytokompatibilität.

Eine nanostrukturierte Titanoxidschicht (TiO_2) wurde durch eine mehrstufige Tauchbeschichtung auf rostfreiem Stahl der Spezifikation 316L oder Siliziumwafer aufgebracht. Dabei wurden Suspensionen aus TiO_2-Nanopartikeln und strukturgebenden Polymerpartikeln verwendet. Im darauf folgenden Sinterschritt wurden die strukturgebenden Polymerpartikel ausgebrannt, um Wirkstoffreservoirs in der 1.2 µm dicken Schicht zu bilden. Diese Wirkstoffreservoirs haben einen Durchmesser von 1 µm und werden von einer porösen Keramikstruktur umgeben. Die umgebende Keramikstruktur hat eine offene Porosität von 50 % und einen mittleren Porendurchmesser von 76 nm, der mit Kleinwinkelneutronenstreuungs- und Quecksilberporosimetrie bestimmt wurde. Die Präsenz der Wirkstoffreservoirs erhöht die Porosität und somit die Beladungskapazität der Beschichtung mit dem Wirkstoff. Weitere Eigenschaften der Beschichtung wurden bestimmt, wie zum Beispiel die spezifische Oberfläche mit der Brunauer-Emmett-Teller (BET)-Methode, die kristallinen Phasen des TiO_2 mit Röntgenbeugung und die chemische Zusammensetzung mit Photoelektronenspektroskopie.

Von kardiovaskulären WFS werden Medikamente in das Gewebe der Koronararterie freigesetzt, um eine lokale Wiederverschliessung der Arterie zu verhindern. Ihre

Wirkungsweise besteht darin, entweder die Aktivierung des Immunsystems zu verringern oder das Zellwachstum zu hemmen. In der vorliegenden Studie wurde die poröse Titanoxidschicht erfolgreich mit dem zellwachstumshemmenden Wirkstoff Paclitaxel (PTX) durch eine Lösungsmittel-Verdunstungs-Methode beladen. PTX war in den Wirkstoffreservoirs, in den Poren der umgebenden Keramikstruktur und auf der Oberfläche der Beschichtung angereichert. Die Wirkstoffquantität in der Keramikschicht konnte durch die Struktur der Beschichtung und durch die Methode der Wirkstoffbeladung variiert werden. Die maximale Beladung von PTX in der Schicht ist vergleichbar mit dem Anteil PTX in dem kommerziell erhältlichen Taxus^{TM} WFS von 1 µg/mm^2. Die Versuche zur Wirkstofffreisetzung von PTX aus der Beschichtung in Reinstwasser zeigten eine langsame, kontinuierliche Liberation des Medikamentes. Nach einem Monat waren nur 11 % des anfänglich eingebrachten Wirkstoffs abgegeben. Das gemessene Freisetzungsprofil war dem eines PTX-beladenen Stents ähnlich. Weitere Wirkstofffreisetzungsversuche von PTX aus der porösen Schicht in Rindsplasma wurden durchgeführt und die Ergebnisse mit dem Freisetzungsprofil des Taxus^{TM} WFSs verglichen.
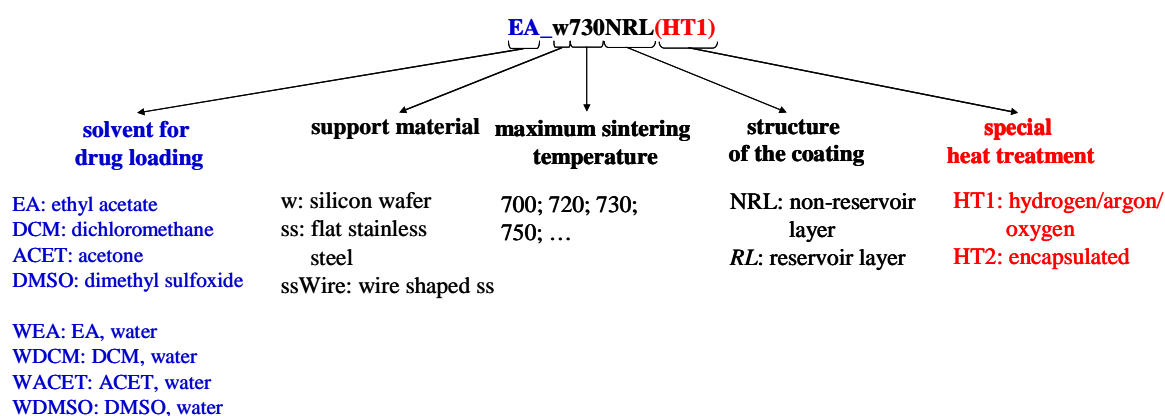
Getestet wurde ausserdem die *in vitro* Zytotoxizität der Beschichtung. Dabei wurden isolierte, primäre Rinderendothelialzellen in direkten Kontakt mit nicht-PTX-beladenen Titanoxidbeschichtungen gebracht. Erste Ergebnisse wiesen darauf hin, dass die nanostrukturierten Schichten auf dem Siliziumwafer und den Stahlsubstraten zytokompatibel sind.

Es konnte eine Technologieplattform entwickelt werden, die die Charakterisierung der Titanoxidschichten, die Wirkstoffbeladung, Freisetzung und auch die Überprüfung der Zytotoxizität umfasst. Faktoren, die diese Sachverhalte beeinflussen, konnten identifiziert werden. Die Ergebnisse der vorliegenden Arbeit werden in Zukunft dazu beitragen, die nanostrukturierte, wirkstofffreisetzende Keramikbeschichtung für die Anwendung in einem WFS zu optimieren und an weitere biomedizinische Anwendungen anzupassen.

Schlagwörter: nanostrukturierte Beschichtung, wirkstofffreisetzender Stent, Zytotoxizität

LABELING OF SAMPLES

The samples used in the present study hold the following systematic labeling. The modification of the solvent used in the drug-loading procedure (highlighted in blue) is only added to the sample label in Chapter 5: "Drug-Loading of The Thin Titania Films and Drug-Release". Special heat treatments (labeled in red), which are deviating from the conventional one, are only applied in the names of the samples in Chapter 6: "Preliminary *In Vitro* Cytotoxicity Tests".

EA_w730NRL(HT1)

solvent for drug loading	support material	maximum sintering temperature	structure of the coating	special heat treatment
EA: ethyl acetate DCM: dichloromethane ACET: acetone DMSO: dimethyl sulfoxide WEA: EA, water WDCM: DCM, water WACET: ACET, water WDMSO: DMSO, water	w: silicon wafer ss: flat stainless steel ssWire: wire shaped ss	700; 720; 730; 750; …	NRL: non-reservoir layer *RL*: reservoir layer	HT1: hydrogen/argon/oxygen HT2: encapsulated

ACKNOWLEDGEMENTS

First of all, I would like to express my sincerest gratitude to Prof. Heinrich Hofmann for his constant support, supervision and trust during my Ph.D. thesis. I want to thank him for the great working conditions and working atmosphere, from which we all benefit at LTP.

I also would like to thank Dr. Laurent-Dominique Piveteau from Debiotech SA for his many good advices, supervision and reviewing of this work. A special thank goes also to Dr. Heike Hall-Bozic and Dr. Katharina Maniura for having spent their precious time on the evaluation of this work.

A special thank goes furthermore to the following people:

- Arnaud Tourvieille de Labrouhe for his constant support in many topics related to this work.

- Dr. Marco Cantoni and Dr. Graham Knott from EPFL for their help in electron microscopy.

- Dr. Joachim Kohlbrecher from Paul Scherrer Institute (PSI) in Villigen, Switzerland, for small angle neutron scattering porosimetry, Dr. Alexis Bourgeois from SOPRA SA for ellipsometric porosimetry and Dr. Gwenn LeSaout (EPFL) for help in mercury intrusion porosimetry measurements.

- Dr. Ulrich Aschauer for molecular dynamics simulations.

- Nicolas Xanthopoulos for the support in X-ray photoelectron spectroscopy.

- Prof. Jacques Lemaître for his support in the statistical design of experiments.

- Claudia Strehler, Leire Mendia, Laetitia Galea, Sébastien Silvant, Samuel Schenk, Adriano Waszyk and Nawal Jorio, whom I had the pleasure to guide through their semester and master projects.

- Michaël François for the help with *in vitro* cell testing.

▪ The members of the atelier.

And of course I want to thank all my colleagues and friends from LTP, especially Nok with who I shared the office, for the many inspiring moments we experienced together at work and beyond.

Finally, I would like to address special thanks to my parents Rudi and Marlene, my sisters Susanne and Anne, as well as to Christoph and all my friends for their constant support during all these years.

TABLE OF CONTENTS

CHAPTER I

1 INTRODUCTION

1.1   Coronary artery disease and the application of stents

Coronary Artery Disease (CAD) is the most common type of heart disease and the leading cause of death in the developed countries. Today CAD affects more than 10 million people in the US every year [1, 2]. It originates from unhealthy lifestyles, like living on a noxious diet, getting insufficient exercise or being exposed to stress situations. This can abet atherosclerosis, which is the formation of plaque at the inner walls of the arteries, like illustrated in Figure 1-1 (a) [2, 3].

(a)	(b)	(c)
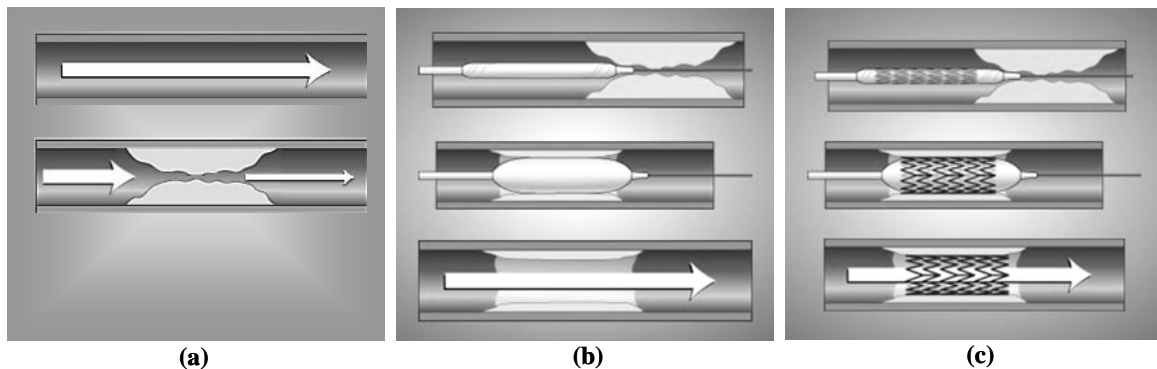
Figure 1-1 (a) Atherosclerosis, (b) balloon angioplasty (PTCA), where a catheter with a small balloon is inserted into the blocked section of the artery and inflated, in order to compress the plaque and to open the artery, (c) stenting, in which a stent is inserted into the coronary artery by PTCA [4].

The coronary arteries, which supply oxygen-rich blood to the heart muscle, become hardened and narrowed. Hence the blood flow to the heart is reduced and less oxygen delivered to the heart muscle. This can generate angina, heart attack and in the worst case death. Angina is chest pain or discomfort, which arises when insufficient blood is delivered to the heart muscle [5]. A heart attack evolves, when a blood clot formed at the site of atherosclerosis blocks the blood flow to a section of the heart's muscle. This can cause its permanent damage or die off [6]. Persisting CAD with time can weaken the heart muscle and contribute to heart failure and arrhythmias. In heart failure, the heart is not able to pump blood to the rest of the body effectively. Arrhythmias are changes in the normal rhythm of the heartbeats. Treatment options include medication, coronary artery bypass surgery or catheter-based procedures.

Several types of catheter-based technologies are available. During Percutaneous Transluminal Coronary Angioplasty (PTCA), the physician passes a special balloon catheter into the narrowed segment of the artery. The balloon is then expanded, which opens the artery and compresses the blockage against the artery's wall, Figure 1-1 (b), [7]. This technique has become one of the most well-studied and most frequently performed procedures in modern medicine. In 2006, 1.3 million patients were treated with percutaneous coronary interventions in the US [8]. But about 30-40 % of patients, who undergo balloon angioplasty, may experience restenosis (re-narrowing) of the diseased artery segment within 6 months of the procedure [9, 10]. Restenosis is a complex inflammatory healing response after injury of the blood vessel [11]. Other incidents recorded after PTCA are acute recoil of the artery and abrupt vessel closure [12].

Hence researchers developed coronary stent-implants, which were launched on the market in 1987. Coronary stents are small, metal mesh-like tubes, like depicted in Figure 1-2, with typical sizes ranging from 8 to 38 mm in length and 2.5 to 4 mm outer diameter [12, 13].

Figure 1-2 Bare metal coronary artery stent [14].

They are inserted into the narrowed segment of the artery via PTCA. The procedure is also known as stenting. Therefore the implants are cramped on the balloon of the catheter during placing them at the site of atherosclerosis in the artery, Figure 1-1 (c). Afterwards the balloon is inflated with pressures of 12-18 atm [15]. The stent expands to increase its diameter of a factor of 2 or 3, which can cause deformations on some parts of the stent up to 10 % [12, 16, 17]. The implant is thus embedded into the vessel-wall and keeps the previously narrowed section of it open. The balloon is deflated and removed along with the catheter. The stent is left behind to serve as a metal support for the artery and to main the blood flow to the heart.

While stents virtually eliminated many of the complications of abrupt artery closure, problems like acute thrombosis and restenosis persisted, Figure 1-3. Thrombosis is the formation of a thrombus, composed of platelets and fibrin, which originates in the stents or around them [18]. This body response appears typically in a time up to 14, maximal 30 d after intervention. Restenosis includes inflammation responses of the body, such as neointimal hyperplasia and extracellular matrix production, Figure 1-3, and results in a blockage of the stented artery section. Neointimal hyperplasia is the overproliferation of the smooth muscle cells (SMCs), which are present in the middle layer of the artery (Figure 1-4). They are surrounded by a layer of endothelial cells (ECs) facing the lumen of the artery and by connective tissue in the external layer of the vessel. Although restenosis rates were lower when implanting bare metal stents (BMS) compared to performing only PTCA, 20-30 % of patients still experienced an in-stent restenosis [1, 10, 12]. Repeated interventions to re-open the obstructed artery were hence necessary.
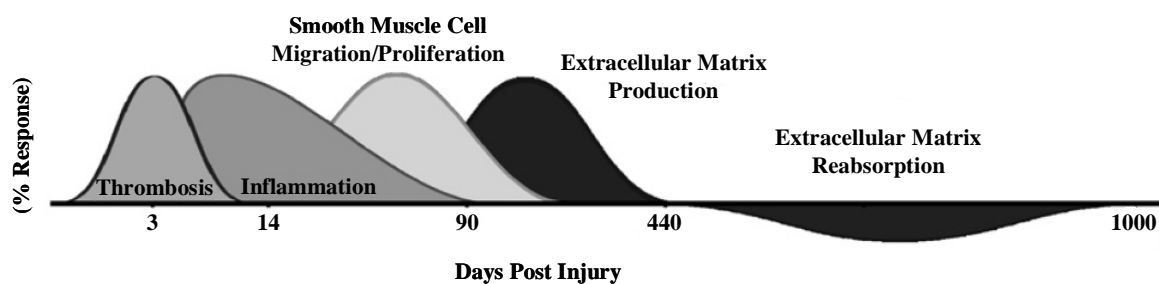
Figure 1-3 Blood vessel healing response to the implantation of bare metal stents [12].

Today the solution has moved away from purely mechanical devices. Several drugs, which were known to interrupt the biological processes that cause restenosis, have been tested. Stents coated with these drugs imbedded in a thin, permanent polymer for time-release, the so-called drug-eluting stents (DES), are on the market.
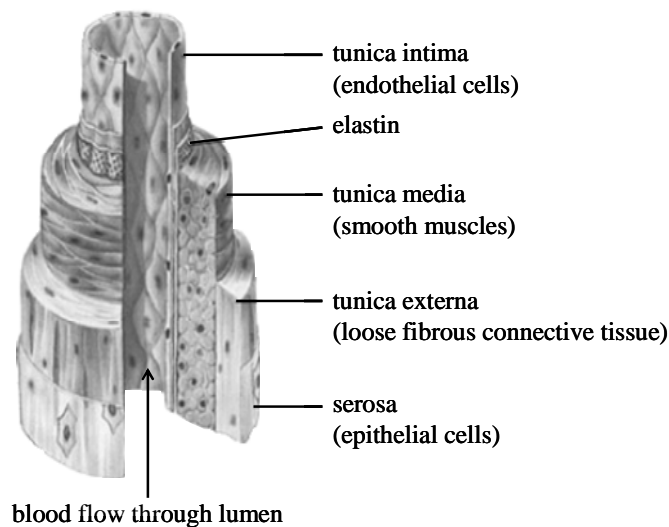
Figure 1-4 Structure of an artery, modified from [19].

The DES market is the largest market in revenues for a single type of medical device. In 2006, the US-market for coronary stents was estimated to be 5 billion US$, whereas 90 % were attributed to DES [20]. Commercially available DESs comprise a metal support, typically made of 316L stainless steel or CoCr alloys, on which a durable polymer coating is fabricated. The drug is dispersed in it. After implantation, the pharmacological agent is dissolved and released by diffusion through the polymer. The implantation of DESs reduced the restenosis rates to below 10 % and limited the incidents for acute (0-24 h) and subacute (24 h-30 d) thrombosis. The events of very late stent thrombosis, defined as occurring more than 1 year after implantation, recorded in the last two years in various studies were higher for DESs compared to BMSs [7, 18, 21, 22]. The incorporated drugs delay healing and hence decelerate re-endothelialization, resulting in the lack of neointimal strut coverage by endothelial cells. The commercially available DESs were coated with a permanent polymer, which persisted after drug elution. The presence of such a polymer resulted in hypersensitivity reactions in some cases [12]. The polymer detachment during expansion of the stent and the release of polymer debris created additionally adverse reactions [7]. Another problem facing the polymer approach is related to their fabrication. The need to dissolve the drugs and polymers in a common solvent for coating the stents can restrict the number of drugs available for the polymer-based drug-delivery. Because some solvents can alter the performance of the drugs. These certainties give motivation to work on new concepts for DESs. In this project the application of a well structured, titanium oxide (TiO_2) coating for stents will be explored.

1.2   Objectives of the study

Despite the successful application of drug-eluting stents (DESs) to prevent restenosis, the commercially available ones exhibit deficits in terms of their mechanical, chemical stability and their performance in the body. This project focuses on creating a nanostructured, drug-eluting, thin ceramic coating for stents. The work was conducted in the frame of a CTI-project and in collaboration with Debiotech SA, who owns patents to this technology [23, 24, 25].

The structured ceramic films, made of a biocompatible material like titania (TiO_2), are to be prepared on metal substrates typically used in stents. These are for instance 316L stainless steel (SS) or cobalt chromium alloys (CoCr). Ceramic coatings made of TiO_2 are commonly used in biomedicine to prevent the corrosion of the underlying metal or to trigger certain cell responses [13, 26, 27, 28]. In the present study it should furthermore serve as a drug carrier. Because TiO_2 is inert to many solvents, any solvent can be used for the drug-loading of the coating. For the formation of drug-eluting polymer coatings on the contrary, one has to be selective. One possible design of the ceramic coating is illustrated in Figure 1-5. It comprises a monolayer of large pores with diameters of 500-1000 nm, called reservoirs, embedded in a ceramic layer with smaller pores. The reservoirs increase the overall pore volume of the coating and serve as storage rooms for the drug. The surrounding porous ceramic structure, and especially the nanoporous layer on top, will be used to control the drug-release from the reservoirs by diffusion, Figure 1-6. Other designs of the coating might use a nanoporous layer with different properties to the ones of the surrounding porous ceramic structure. The special nanoporous layer can then modify the drug-release or mediate a certain cell response when it is implanted. In the following, a layer containing drug reservoirs will be abbreviated by "*RL*", a coating without reservoirs will be named "NRL".
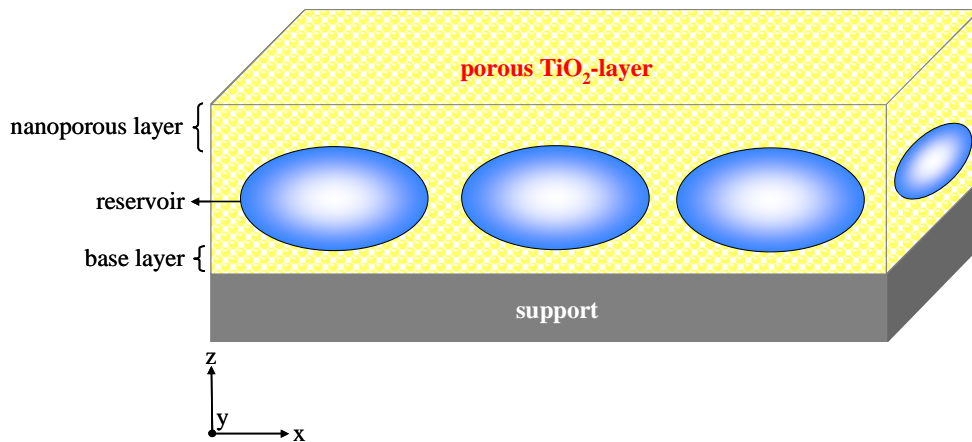
Figure 1-5 Scheme of the reservoir layer of the nanostructured, drug-delivering ceramic coating for medical implants.
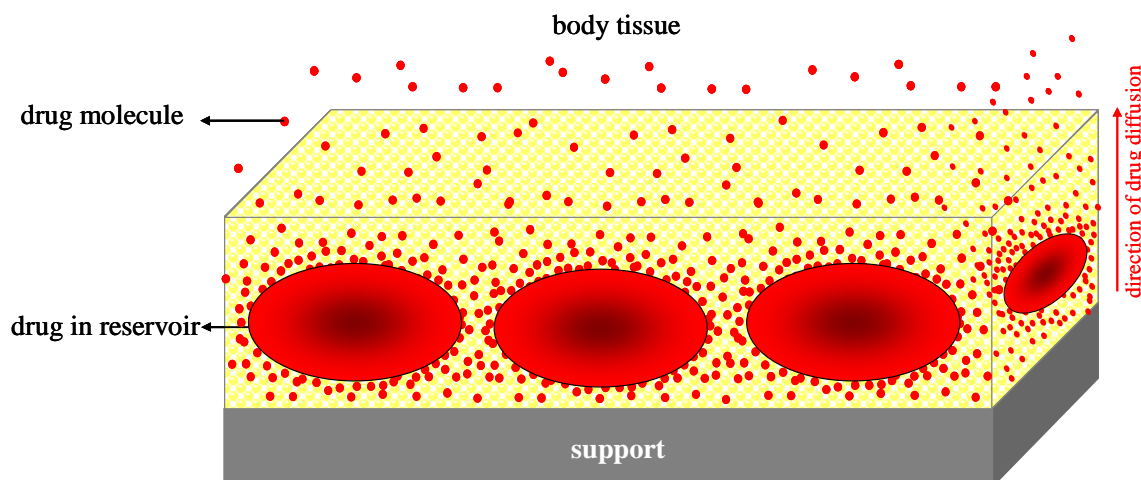
Figure 1-6 Scheme of a reservoir layer of the nanostructured, drug-delivering ceramic coating. The drug reservoirs are filled with the pharmaceutical agent and the drug molecules are released through the surrounding porous bulk structure into the body tissue.

Various parameters have to be taken into account when designing such nanostructured, ceramic coatings with respect to the final applications: the type of substrate, the structure of the coating, the chosen pharmaceutical, the desired drug-release for an efficient medication and more generally the materials involved in the processing. The nanostructured ceramic coating in a DES has to meet the following requirements:

- Mechanical stability during implantation and after stenting. A coronary stent has to withstand a certain deformation during implantation and the dynamic strain in the artery due to the permanent blood flow [13]. The metal support should prevent the recoil of the artery. The coating should exhibit no delamination from the support and no crack formation.

- A high porosity, achieved by the incorporation of the drug reservoirs, needs to ensure storage room for a sufficient quantity of the pharmaceutical agent.

- The pore density, pore size and their arrangement in the nanoporous layer should control the drug-release. The release mechanisms need to be understood to adapt the coating, to make it effective against restenosis and neointimal hyperplasia.

- The coating should possess a high biocompatibility. Biocompatibility is the ability of a material to perform with an appropriate host response in a specific application (Williams 1987) [13]. This term combines several aspects. An appropriate host response for instance includes the normal, uncomplicated healing. Applying to the stent, it should particularly trigger a fast re-endothelialization and hence prevent thrombus formation, besides being active against restenosis.

- ▪ Methods to prepare the drug-eluting coating should be adjustable, to apply it to various medical implants.

1.3   Thesis structure

The proof to apply the nanostructured ceramic coatings on stent-implants is complex and only some aspects will be covered in the present work. Emphases are given on first introducing the reader to the state of the art of the stent technology. The production and characterization of the nanostructured coatings made of titania will be pointed out further. In the last two chapters the drug-load and release capabilities of the coating will be evaluated, and its performance in an *in vitro* biological environment will be exploited in preliminary tests.

1.4   References

[1]   W.L. Hunter, "Drug-eluting stents: Beyond the hyperbole", *Advanced Drug Delivery Reviews*, Vol. 58, 2006, pp. 347-349.

[2]   V. N. Singh, P. Deedwania, "Coronary Artery Atherosclerosis", available at: http://emedicine.medscape.com/article/153647*,* April 2009.

[3]   U.S. Department of Health and Human Services, National Institutes of Health, "What is Coronary Artery Disease?", *Diseases and Conditions Index*, available at: http://www.nhlbi.nih.gov/health/dci/Diseases/Cad/CAD_WhatIs.html, April 2009.

[4]   "Heart Attack Basics", available at: http://www.heartsurgeons.com/ed2.html, April 2009.

[5]   U.S. Department of Health and Human Services, National Institutes of Health, "What is Angina?", *Diseases and Conditions Index*, available at: http://www.nhlbi.nih.gov/health/dci/Diseases/Angina/Angina_WhatIs.html, April 2009.

[6]   U.S. Department of Health and Human Services, National Institutes of Health, "What is a Heart Attack", *Diseases and Conditions Index*, available at: http://www.nhlbi.nih.gov/health/dci/Diseases/HeartAttack/HeartAttack_WhatIs.html, April 2009.

[7]   C. Lally, D.J. Kelly, P.J. Prendergast, "Stents", *Wiley Encyclopedia of Biomedical Engineering*, John Wiley & Sons, 2006.

[8]   "Angioplasty and cardiac Revascularization Statistics", available at: http://www.americanheart.org/presenter/jhtml?identifier=4439, April 2009.

[9]   W. H. Maisel, W. K. Laskey, "Drug Eluting Stents", *Circulation*, Vol. 115, 2007, pp. e426-e427.

[10]   G. Mani, M.D. Feldman, D. Patel, C.M. Agrawal*,* "Coronary stents: A materials perspective", *Biomaterials*, Vol. 28, 2007, pp. 1689-1710.

[11]   C. Indolfi, A. Mongiardo, A. Curcio, D. Torella, "Molecular Mechanisms of In-Stent Restenosis and Approach to Therapy with Eluting Stents", *Trends in Cardiovascular Medicine*, Vol. 13, 2003, pp. 142-148.

[12]   N. Kukreja, Y. Onuma, J. Daemen, P.W. Serruys, "The future of drug-eluting stents", *Pharmacological Research*, Vol. 57, 2008, pp. 171-180.

[13]   B.D. Ratner, A.S. Hoffman, F.J. Schoen, J.E. Lemons, "Biomaterials Science: An

Introduction to Materials in Medicine", *Elsevier Academic Press*, 2004.

[14] S. Sternberg, "The heart of a stent debate", *USA Today*, 2006, available at: http://www.usatoday.com/news/health/2006-12-05-stent-warning_x.htm, April 2009.

[15] H. M. Burt, W.L. Hunter, "Drug-eluting stents: A multidisciplinary success story", *Advanced Drug Delivery Reviews*, Vol. 58, 2006, pp. 350-357.

[16] P.W. Serruys, G. Sianos, A. Abizaid, J. Aoki, P. den Heijer, H. Bonnier, "The Effect of variable dose and release kinetics on neointimal hyperplasia using a novel paclitaxel-eluting stent platform: the paclitaxel in-stent controlled elution study (PISCES)", *Journal of the American College of Cardiology*, Vol. 46, 2005, pp. 253–60.

[17] F. Migliavacca, L. Petrini, V. Montanari, I. Quagliana, F. Auricchio, G. Dubini, "A predictive study of the mechanical behavior of coronary stents by computer modeling", *Medical Engineering and Physics*, Vol. 27, 2005, pp. 13-18.

[18] G. Lemesle, C. Dehaye, L. Bonello, A. de Labriolle, R. Waksman, A. Pichard, "Stent thrombosis in 2008: Definition, predictors, prognosis and treatment", *Archives of Cardiovascular Disease*, Vol. 101, 2008, pp. 769-777.

[19] S. I. Fox, "Human Physiology", *William C. Brown Publishers*, 1992.

[20] S. Venkatraman, F. Boey, "Release profiles in drug-eluting stents: Issues and uncertainties", *Journal of Controlled Release*, Vol. 120, 2007, pp. 149-160.

[21] T. C. Woods, A.R. Marks, "Drug-Eluting Stents", *Annual Review of Medicine*, Vol. 55, 2004, pp. 169-178.

[22] P. Lanzer, K. Sternberg, K-P. Schmitz, F. Kolodgie, G. Nakazawa, R. Virmani, "Drug-Eluting Coronary Stent Very Late Thrombosis Revisited", *Herz*, Vol. 33, 2008, pp. 334-342.

[23] H. Hofmann, F. Neftel, L.-D. Piveteau, "Reinforced porous coating", *Patent WO2007031972 (A1)*, 2007.

[24] H. Hofmann, F. Neftel. L.-D. Piveteau, "Porous Coating Loaded with a liquid or a solid substance", *Patent WO2007031968 (A2)*, 2007.

[25] L.-D. Piveteau, H. Hofmann, F. Neftel, "Anisotropic nanoporous coating", *Patent WO2007148240 (A2)*, 2007.

[26] J.S. Reed, "Principles of Ceramics Processing", *John Wiley and Sons*, 1995.

[27] G. Mendonça, D.B. Mendonça, F.J. Aragao, L.F. Cooper, "Advancing dental implant surface technology - From micron- to nanotopography", *Biomaterials*, Vol. 29, 2008, pp. 3822-3835.

[28] I.A. Karoussos, H. Wieneke, T. Sawitowski, S. Wnendt, A. Fischer, O. Dirsch, U. Dahmen, R. Erbel, "Inorganic Materials as drug delivery systems in coronary artery stenting", *Materialwissenschaft und Werkstofftechnik*, Vol. 33, 2002, pp. 738-746.

CHAPTER II

2 STATE OF THE ART

This chapter summarizes the state of the art of drug-eluting stents (DESs), including support materials, coatings and pharmaceutical agents. The methods to fabricate highly porous, structured ceramic coatings will be envisaged.

2.1 Drug-eluting stents

2.1.1 Commercially available systems

The first DES commercialized was the Cypher™ by Cordis Corp., whose approval by the US Food and Drug Administration (FDA) was obtained in 2003 [1]. The Cypher™ stent contains a stainless steel (SS) support, on which a thin durable polymer coating made of polyethylene-co-vinyl acetate and poly-n-butyl methacrylate is attached. The pharmaceutical agent sirolimus, also known as rapamycin, is embedded in it in a concentration of 140 $\mu g/cm^2$ [2, 3, 4]. Sirolimus is an immunosuppressive agent, which prevents restenosis by inhibiting vascular smooth muscle cell (SMC) migration, proliferation and growth [3, 4, 5]. It binds to an intracellular receptor protein and ultimatively induces cell arrest. Two formulations of these polymer coatings are available, generating either a fast or a slow release of the drug. In the fast release modification, the coating comprises a bi-layered structure: a parylene coating on top of the steel, which is covered by a drug-containing polymer. For the slow release formulation, three layers are applied: parylene, drug-

containing polymer and a pure polymer outermost, which limits the drug diffusion. While the fast release is characterized by a total drug-liberation in 15 d, the slow release lasts continuously up to 90 d [4].

Barely one year after the Cypher[TM] stent was launched on the market, the Taxus[TM] stent by Boston Scientific Corp. was FDA-approved [1]. It is made of a 316L SS platform, on which a thin, permanent polystyrene-b-isobutylene-b-styrene (SIBS) coating is present. It contains paclitaxel (PTX) in a concentration of 1 $\mu g/mm^2$. PTX was licensed by the FDA in 1992 as an antineoplastic agent to treat metastatic ovarian cancer. It is an anti-proliferative therapeutical agent promoting the microtubule assembly in cells by facilitating the polymerization of tubulin to stable microtubules. This stabilization can interrupt many cellular processes. For instance it inhibits the cell division by keeping the mitotic spindle. It stops the migration, activation and maintenance of the cytoskeletal support, as well as the intracellular and transmembrane protein transport. Referring to restenosis, it affects the development of neointimal hyperplasia by disrupting SMC migration and proliferation [6]. Because the drug is dispersed homogeneously in the polymer matrix, modulating the drug concentrations in the polymer can create three different release profiles: the fast, moderate and slow release. For the fast and moderate formulations, an initial burst-liberation of PTX up to 48 h is recorded. 55 % and 8 % of totally incorporated PTX is then released under *in vitro* conditions, respectively. The slow release modification is characterized by a continuous release up to two weeks. 90 % of PTX remains then still trapped in the polymer [3, 4]. The slow release configuration is applied in the commercialized Taxus[TM] stent.

Beneficial clinical outcomes of the implantation of DESs compared to BMSs were observed. The restenosis rates for DESs dropped significantly below 10 % [3, 7, 8, 9]. Events of acute (0-24 h) and subacute (24 h-30 d) thrombosis decreased. But a higher incidence of very late stent thrombosis, which occurs more than 1 year after implantation, for DESs compared to BMSs was recorded lately in different studies [10, 11]. Sirolimus and PTX delay healing and hence can hinder a complete re-endothelialization of the implant. The presence of the permanent polymer coating may contribute to stent thrombosis as a result of hypersensitivity reactions in some cases [3]. The removal of some parts of the coating during stenting can influence local drug concentrations in the artery-tissue [2, 12]. Intensive research to overcome these problems has directed the development of the second generation of DESs, which are now available on the European and US markets: the XienceV[TM] by Abbott Vascular Inc., the Promus[TM] by Boston Scientific Corp. and the Endeavor[TM] stent by Medtronic Vascular [1], Table 2-1.

Table 2-1 Drug-eluting stents in clinical use or under investigation. Copied from [3] and updated.

drug	stent support	coating	stent name	company	approval status
Sirolimus	SS	DP	Cypher select	Cordis	FDA/CE
	SS	BP	Supralimus	Sahajanand	CE
	SS	BP	CURA	Orbus Neich	
	SS	BP	Exel	JW Medical	
	SS	None	Yukon	Translumina	CE
	CoCr	BP	Supralimus-Core	Sahajanand	
Everolimus	CoCr	DP	Xience V	Abbott	FDA/CE
	CoCr	DP	Promus*	Boston Scientific	FDA/CE
	PLLA	BP	Absorb	Abbott	Trial
Zotarolimus	CoCr	DP	Endeavour	Medtronic	FDA/CE
	CoCr	DP	Endeavour resolute	Medtronic	Trial
Biolimus A9	SS	BP	Biomatrix	Biosensors	CE
	SS	BP	Nobori	Terumo	CE
	CoCr	BP	Xtent	Xtent	Trial
Tacrolimus	SS	None	Janus	Sorin	CE
	CoCr	BP	Maharoba	Kaneka	Trial
Pimecrolimus	CoCr	BP	Corio	Conor	
	CoCr	BP	Prolimus	Biotronik	Trial
	Magnesium	BP	Dreams	Biotronik	Trial
Paclitaxel	SS	DP	Taxus Liberte	Boston Scientific	FDA/CE
	SS	BP	Infinnium	Sahajanand	CE
	CoCr	BP	CoStar	Conor	CE
	SS	None	Axxion	Biosensors	CE
	Tyrosine polycarbonate	BP	REVA	REVA	Trial
Anti-CD34	SS	DP	Genous	Orbus Neich	CE

SS: stainless steel, CoCr: cobalt chromium, DP: durable polymer, BP: biodegradable polymer, PLLA: poly-L-lactic acid, CE: Conformité Européenne, FDA: Food and Drug Administration, *: PROMUS^{TM} Stent is a private-labeled XIENCE V™ everolimus-eluting coronary stent system manufactured by Abbott and distributed by Boston Scientific. XIENCE is a trademark of Abbott Laboratories group of companies [13].

Promus^{TM} is a copy of XienceV^{TM} licensed from Abbott and sold by Boston Scientific. They all contain CoCr support materials and the drug is present in durable polymer coatings. The XienceV^{TM} contains 100 µg/cm^2 everolimus in a poly(vinylidene) fluoride-co-hexafluoropropylene polymer matrix [14]. Everolimus is an analogue of rapamycin with the same mode of action as an antiproliferative agent [15]. The Endeavor^{TM} stent elutes zotarolimus from a phosphorylcholine polymer coating. Phosphorylcholine is a synthetic mimic of the outer wall of red blood cells and as such considered to be bioinert [2]. Zotarolimus is again a sirolimus analogue and effective against cell proliferation. The Endeavor^{TM} stent releases 70 % of the pharmaceutical within 30 d *in vitro*, and acts in the inflammatory response after stenting, like is depicted in Figure 1-3 [3].

First studies have shown a tendency that they are more effective against very late stent thrombosis than the first generation of DESs. But further evidence has to be adduced [13]. The companies, which sell the stents introduced so far, hold at the moment most of the US-stent market [16]. An overview of more licensed DESs, as well as stent systems in an advanced stage of development, were summarized by Kukreja *et al.* in 2008 and are displayed in Table 2-1 [3].

2.1.2 Support materials

Different types of support materials for stents are of current interest. They can be *non-degradable* or *degradable*. Their properties affect the mechanical stabilities and designs of stents, as is pointed out in Figure 2-1. The arrangement of the struts and the strut's geometries greatly vary in the displayed models.
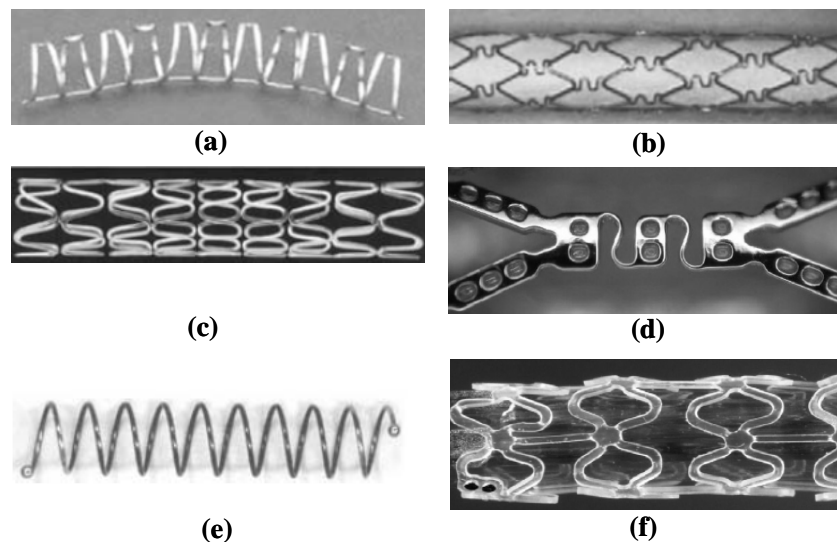
Figure 2-1 Examples of different stents used in humans: (a) balloon expandable 316L coil stent (Gianturco Roubin II[TM] by Cook Inc.), welded to an axial spine [2]; (b) balloon expanding 316L laser-cut steel tube stent (BxVelocity[TM]) [2]; (c) balloon expanding stainless steel stent, laser-cut and segments welded together (S7[TM], Medtronic) [2]; (d) CoStar[TM] Stent from Conor Medsystems showing ductile regions and passive elements in which drug reservoirs are fabricated [3]; (e) self expanding nitinol coil stent Cordiocoil[TM] (Medtronic) [2]; (f) totally biodegradable everolimus-eluting poly-l-lactic acid stent from Abbott Laboratories [3].

Non-degradable SS or CoCr are the supports of many different balloon expandable stent systems. SS is radiopaque with an adequate radial strength for stents and it is employed in many BMSs and in DESs. Besides using compact SS, a stent made of microporous SS was developed by Translumina [3, 17], which can serve as a matrix for drugs. It offers the potential to customize drug doses and drug-combinations, and it is therapeutically active with rapamycin. The tendency however is towards the use of CoCr. This alloy has a higher

radial strength and improved radiopacity than SS and allows for smaller stent struts. They can improve the biocompatibility of stents. The concept of the CoStar^{TM} DES from Conor Medsystems in Figure 2-1 (d), is based on CoCr. It has a special design, which promotes that sections of the stent experience higher deformations during stent deployment, whereas others stay passive elements. The passive sections are provided with drug reservoirs [3]. Other stents are based on the shape memory alloy nitinol (nickel-titanium, NiTi) and are self expandable, like the Cordiocoil^{TM} from Medtronic depicted in Figure 2-1 (e). A less frequently applied support for stents is tantalum. Besides its excellent corrosion resistance and biocompatibility, it is more brittle than SS. Hence these stents have a higher possibility for breaking during stenting. The pressure applied during the balloon deployment in PTCA needs to be accordingly lower and this often results in stent recoil. Stent recoil is the contraction of the stent's diameter from short after deployment to the end of the procedure. Commercially available tantalum stents are the Strecker^{TM} stent from Medi-Tech and the Tantalum Crossflex^{TM} from Cordis [2].

Fully *degradable stents* composed of poly-L-lactic acid (PLLA), such as the Absorb^{TM} stent from Abbot including Everolimus (Figure 2-1 (f)), showed promising results in clinical studies. Their safety has already been accomplished [3] and their mechanical properties seem to be favorable. The acute recoil after stenting was similar to the one of a CoCr based stent. The PLLA-stent is radiolucent and contains two platinum markers at each end to allow its identification by angiography. Angiography is a X-ray based technique to visualize the inside of blood vessels [3]. PLLA is fully metabolized into water and carbon dioxide after a certain time in the body. Hence PLLA stents are no permanent implants like the stents based on SS on CoCr. Another fully degradable stent made of tyrosine-derived polycarbonate, the REVA^{TM} stent, is currently under clinical evaluation [3]. Apart from the polymer based fully degradable stents, magnesium is in the focus of interest by Biotronik, Switzerland. It consists of a bioabsorbable magnesium (Mg) alloy, which corrodes in physiological environment into soluble Mg hydroxide, Mg chloride and hydrogen gas [5]. First clinical results regarding re-endothelialization and neointimal hyperplasia were contradictory when implanted in children. Reasons might be associated to the degradation products, whose formation is not well controllable. A drug-eluting version is under exploration [5, 18, 19]. A biodegradable stent composed of iron (Fe) was also tested. Its biodegradation involves the oxidation of Fe into ferrous ions, which dissolve in the biological media. It has been shown that the ferrous ions reduced the proliferation of SMCs in *in vitro* conditions. The presence of the ferrous ions thus might inhibit neointimal hyperplasia and might reduce thrombogenicity when implanted. Further testing is still required [5, 20].

2.1.3 Coatings

To improve the performance of stents, the mechanically stable supports are often coated. The coatings for coronary stents can be categorized into *passive* and *active* ones. Passive coatings do not change or contain drugs and focus on triggering a certain cell response. Active coatings change after implantation and/or elute pharmaceuticals.

A gold *passive coating* was produced on SS stent supports to increase the strut's visibility when having thin struts and to enhance their biocompatibility. The performance of the coating however depended strongly on its fabrication and the presence of impurities. In human tests the coating did not deliver satisfying results: a higher tendency for restenosis and an increased neointimal proliferation [5]. Another stent concept consists of an iridium oxide coating on a metal support. Iridium oxide is a biocompatible inert ceramic. The rationale behind applying this material is the following. Hydrogen peroxide is formed at a metal surface when it is corroding. This can cause inflammatory reactions in the artery. A metal coated with iridium oxide should promote the immediate conversion of hydrogen peroxide into water and oxygen, hence reducing inflammatory reactions and promoting re-endothelialization. Iridium oxide, on top of a gold coating on a stainless steel stent, was produced by Inflow Dynamics in the Lunar^{TM} stent. It was demonstrated that it triggered the fast re-endothelialization in humans because of its capability to prevent the production of free oxygen radicals, which can affect the adhesion and proliferation of endothelial cells. Restenosis rates of 13.8 % were recorded. The surface of SS produced little hydrogen peroxide and hence more investigations have to be made for evaluating the influence of this chemical reaction on restenosis [5, 21, 22, 23]. An amorphous hydrogenated semiconducting silicon-carbide (SiC) layer on top of a SS supporting stent showed promising results in *in vitro* tests: a reduction in platelet deposition with possibly reducing thrombosis and restenosis. However, clinical outcomes of the SiC-coated stents produced by Biotronik up to 6 month showed contradictory results in two studies. They were not significantly superior to BMSs [24, 25, 26, 27]. Despite that diamond-like carbon coatings on stents have shown improved biocompatibility [28, 29], the clinical tests have revealed incoherent results. In one study a significant reduction in stent thrombosis and restenosis was reported, while others recorded the coating to be inactive and not influencing the inflammatory response [30, 31]. Other researchers applied a titanium-nitric oxide coating to stainless steel stents. A decreased platelet adhesion and less neointimal hyperplasia compared to BMS was observed [3, 32].

As *active stent coatings* durable polymers were applied in the first and second generation of DESs. The focus has now been given to degradable polymers. PLLA coatings, containing drugs, are applied on SS supports in combination with different drugs. Examples are the Excel^{TM} stent from JW Medical and the CE-approved Supralimus-Core^{TM} from

Sahajanand Medical Technologies, both eluting sirolimus. A poly-lactic-glycolic acid (PLGA) coating, which contains PTX, is used in the CoStar^{TM} stent by Conor Medsystems, cf. Table 2-1. DES-concepts, which include inert inorganic coating materials for drug-release, have also become attractive [33]. A passive nanoporous hydroxyapatite coating under investigation by MIV Therapeutics Inc. showed good biocompatibility in animal studies, when compared to the performance of BMS. No significant difference in neointima formation was found after four weeks of implantation in rabbits. Next steps include the impregnation of the layer with anti-restenoic drugs and their evaluation [34, 35]. A SS stent coated with nanoporous aluminum oxide, in which tacrolimus was incorporated, exhibited disappointing results in terms of biocompatibility. The surface modification by the ceramic coating did not significantly affect the reduction of the neointima in a rabbit model. The release of tacrolimus resulted in a reduced neointima thickness. However, it was reported that this coating may liberate ceramic particle debris, which affect the antiproliferative effect of the drug and increase the neointima thickness [5, 36, 37].

2.1.4   *Pharmaceutical agents*

Besides the successful application of PTX and sirolimus in the first generation of DESs to reduce restenosis, attention has been given on employing various drug analogues in the new stent systems. Sirolimus analogues like everolimus, zotarolimus and biolimus A9, are now applied in different coatings, Table 2-1. They have the same mode of action like sirolimus, being immunosuppressive, but they might differ in their aqueous solubilities. Biolimus A9 was combined in a PLLA coating on a SS support creating the Biomatrix^{TM} stent (Biosensors International). After approximately 70 % of the drug were eluted over 30 d, a sustained release of the residual drug was governed by the polymer degradation over several months. The stent is effective and approved for the commercialization in Europe [38, 39, 40]. Another immunosuppressive drug employed is Tacrolimus. A CoCr stent coated with PLGA incorporating this drug is under exploration by Kaneka [3]. In other concepts, CoCr and Mg stents are coated with biodegradable polymers, in which pimecrolimus is dispersed. Pimecrolimus is a tacrolimus analogue and causes fewer side effects. An alternative approach focuses more on healing than on SMC-growth inhibition. In the Genous^{TM} stent from Orbus Neich, the SS support is coated with antibodies, which attract circulating endothelial progenitor cells. This encourages rapid endothelialization and lowers hence the risk of thrombosis [41, 42].

2.1.5   *Future of drug-eluting stents*

From the above discussed development trends of DESs, design criteria for an ideal

stent can be derived. The stent should provide a scaffold to prevent the recoil of the artery. Furthermore it needs to be deliverable and visible with appropriate radiopacity to enable its positioning. A stent should exhibit good fatigue properties during stenting as well as afterwards, when it is exposed to the cyclic stresses caused by the blood flow. A fast and total re-endothelialization is recommended, which helps to prevent stent thrombosis and limits neointimal hyperplasia [3, 43]. The drug-delivery should help to prevent restenosis and should not limit a fast re-endothelialization of the implant.

The commercially available DESs Cypher[TM] and Taxus[TM] have shown that inflammatory responses can evolve due to the presence of the durable polymer [4]. The drugs can cause a delayed healing of the blood vessel. Various kinds of combinations of materials are under investigation to produce the ideal DES. Many of them were listed above. Porous TiO_2-films have recently also gathered interest for the application in stents.

2.2   Titania for the application in stents

TiO_2 is a well studied mineral and has found its application in diverse areas. As powder it is used as a white pigment in paints, coatings, plastics, papers and cosmetics. On account of its ability to be transparent for visible, but absorbing UV-light, it is an essential component in sunscreens [44, 45]. In the field of photocatalysis TiO_2 is employed for the purification of wastewater, in the killing of bacteria and it might be effective against the growth of tumor cells [44, 46, 47]. The combination of the photocatalysis reaction and photoinduced superhydrophobicity has led to the development of titania coatings and cements with self-cleaning properties. Additional applications are as anti-reflective coatings by reason of its high refractive index or as oxygen gas sensors on the basis of its semiconducting features [44, 46]. TiO_2 as a semiconductor is moreover used in photovoltaics, in particular in solar cells for the direct production of energy or for splitting water to yield hydrogen. Furthermore it is implemented in biomedicine.

Titanium metal and its alloys have been employed in orthopedic and dental medical applications, because of their superior biocompatibility. They exhibit a stable, native oxide layer providing excellent corrosion resistance and contributing to osseointegration in bone implants [48, 49, 50, 51, 52, 53, 54]. However, titanium is not commonly used for making stents, because it has a lower tensile strength than CoCr [5, 55]. Hence there is a higher probability of tensile failure of the titanium stents when expanded to stresses beyond their yield stress. This condition can potentially occur during stenting [5]. However a titanium-nitride oxide coating was applied on a 316L SS support. It was found that it reduced platelet

and fibrinogen adhesion, resulting in a reduced neointimal hyperplasia. This coating technique is implemented in the Titan[TM] stent from Hexacath in France [56, 57]. Reported by Liu *et al*. in 2003, nitinol stents, which were coated with an anatase TiO_2 thin film by sol gel techniques, were effective in improving the corrosion resistance of the underlying NiTi-alloy. It exhibited an improved hemocompatibility compared to the bare NiTi [51]. Plant and coworkers used NiTi-alloys and performed an oxidizing heat treatment at 600 °C to thicken the TiO_2-layer on top of the alloy. This resulted in a reduction of the concentration of nickel ions on top of the surface. The lower nickel ion concentration influenced the cell attachment to the surface. A significant reduction in the oxidative stress on human umbilical vein ECs was registered compared to the one caused by the native NiTi [58]. A very recently published work from Peng *et al*. focused on the reaction of ECs and SMCs on porous nanotubular titanium oxide surfaces [59]. Highly ordered, vertically oriented, crystalline TiO_2-nanotube arrays with a diameter of 30 nm were prepared by anodic oxidation and were subjected to *in vitro* tests. The ECs proliferation was significantly enhanced compared to the one on flat TiO_2-surfaces. Cells had a more elongated morphology than on the flats and were assumed to have higher migration speeds. This would be beneficial for a fast re-endothelialization of the stent [59]. In contrast, the proliferation of the SMCs grown on the tubular surface decreased. Cell morphologies were more rounded shaped, cells were clustered and they seemed to minimize their contact with the nanotube surface in comparison to the flat controls. This effect might contribute to prevent neointimal hyperplasia on a stent [59]. No information was given on the mechanical stability of the coatings.

The loading of a nanoporous TiO_2-film, characterized by randomly arranged pores of a mean width of 5.5 nm, with the drug dexamethasone for the application in stents was reported by A.A. Ayon *et al.* [60]. Drug-loading was performed by immersion of the specimens into the drug/solvent solution, whereas the pores were filled by capillary permeation. The solvent was subsequently evaporated, leaving the solid drug in the pores. The method was optimized to obtain a drug-load comparable to the therapeutic dose. However, no photos of the drug's position in the coating, ensuring that the drug was present in the pores and not concentrated on the surface of the coating, were shown in their publication. Neither was information given about the drug-release kinetics or the mechanical stability of the coating.

2.3   Porous structuring of ceramic films

The nanostructured drug-eluting TiO_2-coating to be investigated in the present study, needs to be manufactured on complex stent geometries. The reservoirs arranged in a

monolayer are to be created by template particles [61, 62]. Various techniques have been employed up to date to achieve structured porous surfaces using colloidal particles and a detailed summary of these can be found in the thesis of F. Juillerat [63]. Only a few techniques will be mentioned at this point.

In the *one-step deposition techniques* the coating that needs to be structured and the template particles are deposited simultaneously on a substrate. As example, polystyrene (PS) sphere particles were mixed with silica sols and dip coated on a flat glass substrate by J.N. Wang and co-workers. Subsequent heating at 500 °C to burn the PS-templates created a ceramic layer with randomly distributed 500 nm holes in a surrounding finer porous structure. These coatings were superhydrophobic and can be used as self cleaning coatings [64, 65]. The size, shape and concentration of the templates in the sol direct the structure of the coatings. Hierarchically structured materials containing mesopores (diameters between 2 to 50 nm) and macropores (diameters > 50 nm) due to a combination of different sized, shaped templates in the sol, were also fabricated. These types of coatings found various applications, such as in heterogeneous catalysis or in separation processes involving large macromolecules [64, 66, 67, 68, 69].

Colloidal lithography is another technique that applies colloidal particles, deposited on a substrate, as a sacrificial mask for the subsequent deposition of the coating's material. Particles can be deposited either in ordered arrays, like depicted in Figure 2-2 (a) [70, 71,], or randomly [63, 72]. The big pores of the coating represented in Figure 2-2 (b), which were created by the removal of the mask particles, could represent the drug reservoirs in the nanostructured titania coating to be prepared.

In *soft lithography* particles act as a stamp to be imprinted into a soft substrate, mainly polymeric. Choi *et al*. have used silica 320 nm ordered arrays stamped on polyurethane films to form hole arrays [63, 73].

In the case of *laser techniques*, laser irradiation of PS and silica particles, spin-coated onto an aluminum thin film, have been shown to possibly lead to the formation of random hole arrays [74].

Another method employed to structure surfaces is *anodic oxidation*, which not necessarily requires the presence of colloidal particles. Porous alumina coatings with straight cylindrical pores were prepared for bone implants [59, 75]. Peng *et al*. produced in that way TiO_2-nanotube arrays with controlled straight pores of a certain diameter on titanium foils. Their potential to be used in stent-implants is currently under investigation [59].
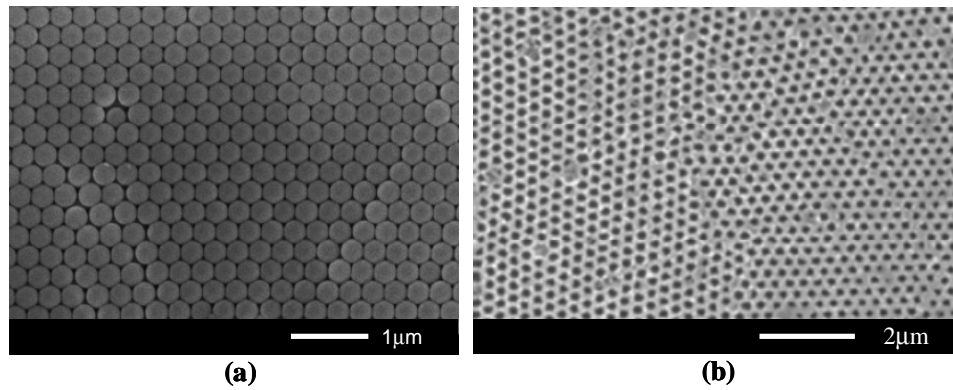
Figure 2-2 SEM-micrographs of (a) polystyrene colloidal crystal template after dip drawing process and (b) TiO$_2$-film structure after burn of the polymer templates [69].

In the techniques applying sacrificial particles, different methods are applied to remove them depending on their nature. These may either be based on chemical, thermal, irradiation or mechanical treatments [63]. The focus in the present study was put on using colloidal lithography for the production of the coatings, because preliminary work was already deduced by F. Juillerat [63].

2.4   References

[1]   "Approved coronary stents", *Center for Devices and Radiological Health, US Food and Drug Administration*, available at: http://www.accessdata.fda.gov/scripts/cdrh/devicesatfda/index.cfm?start_search=11&Search_Term=coronary%20stent&Approval_Date_From=&Approval_Date_To=04/29/2009&sort=approvaldatedesc&PAGENUM=10, April 2009.

[2]   C. Lally, D.J. Kelly, P.J. Prendergast, "Stents", *Wiley Encyclopedia of Biomedical Engineering*, John Wiley & Sons, 2006.

[3]   N. Kukreja, Y. Onuma, J. Daemen, P.W. Serruys, "The future of drug-eluting stents", *Pharmacological Research*, Vol. 57, 2008, pp. 171-180.

[4]   S. Venkatraman, F. Boey, "Release profiles in drug-eluting stents: Issues and uncertainties", *Journal of Controlled Release*, Vol. 120, 2007, pp. 149-160.

[5]   G. Mani, M.D. Feldman, D. Patel, C.M. Agrawal, "Coronary stents: A materials perspective", *Biomaterials*, Vol. 28, 2007, pp. 1689-1710.

[6]   K.R. Kamath, J.J. Barry, K.M. Miller, "The Taxus(TM) drug-eluting stent: A new paradigm in controlled drug delivery", *Advanced Drug Delivery Reviews*, Vol. 58, 2006, pp. 412-436.

[7]   T. C. Woods, A.R. Marks, "Drug-Eluting Stents", Annual Review of Medicine, Vol. 55, 2004, pp. 169-178.

[8]   "FDA News: FDA Appoves Drug-Eluting Stent for Clogged Heart Arteries", available at: http://www.fda.gov/bbs/topics/NEWS/2003/NEW00896.html, October 2008.

[9]   W.L. Hunter, "Drug-eluting stents: Beyond the hyperbole", *Advanced Drug Delivery Reviews*, Vol. 58, 2006, pp. 347-349.

[10]   G. Lemesle, C. Dehaye, L. Bonello, A. de Labriolle, R. Waksman, A. Pichard, "Stent thrombosis in 2008: Definition, predictors, prognosis and treatment", *Archives of Cardiovascular Disease*, Vol. 101, 2008, pp. 769-777.

[11]   P. Lanzer, K. Sternberg, K-P. Schmitz, F. Kolodgie, G. Nakazawa, R. Virmani, "Drug-Eluting Coronary Stent Very Late Thrombosis Revisited", *Herz*, Vol. 33, 2008, pp. 334-342.

[12]   C.W. Hwang, D. Wu, E.R. Edelman, "Physiolocical transport forces govern drug distribution for stent-based delivery", *Circulation*, Vol. 104, 2001, pp. 600-605.

[13]   "PROMUS® Everolimus-Eluting Coronary Stent System", available at:

http://www.stent.com/DisplayPage.bsci/id/4/1a1/m/IC/heart-stent-products/promus/promus-stent.html/page.bsc, April 2009.

[14] N. Ding, S.D. Pacetti, F.-W. Tang, M. Gada, W. Roorda, "Xience V^{TM} Stent Design and Rationale", *Journal of Interventional Cardiology*, Vol. 22, Supplement 1, 2009, pp. S18-S27.

[15] B.L. van der Hoeven, N.M.M. Pires, H.M. Warda, P.V. Oemrawsingh, B.J.M. van Vlijmen, P.H.A. Quax, M.J. Schalij, E.E. van der Wall, J.W. Jukema, "Drug-eluting stents: results, promises and problems," *International Journal of Cardiology*, Vol. 99, 2005, pp. 9-17.

[16] A. Nussbaum, "Boston Scientific Stents Less Effective Than Rivals (Update2)", available at: http://www.bloomberg.com/apps/news?pid=20601103&sid=aeQLKjs2QyUw&refer=us#, April 2009.

[17] R. Wessely, J. Hausleiter, C. Michaelis, B. Jaschke, M. Vogeser, S. Milz, "Inhibition of neointima formation by a novel drug-eluting stent system that allows for dose-adjustable, multiple, and on-site stent coating", *Artheriosclerosis, Thrombosis, and Vascular Biology*, Vol. 25, 2005, pp. 748–753.

[18] H. Eggebrecht, J. Rodermann, P. Hunold, A. Schmermund, D. Bose, M. Haude, R. Erbel, "Novel Magnetic Resonance-Compatible Coronary Stent: The Absorbable Magnesium-Alloy Stent," *Circulation*, Vol. 112, 2005, pp. e303-304.

[19] R. Erbel, C. Di Mario, J. Bartunek, J. Bonnier, B. de Bruyne, F.R. Eberli, "Temporary scaffolding of coronary arteries with bioabsorbable magnesium stents: a prospective, non-randomised multicentre trial", *The Lancet*, Vol. 369, 2007, pp. 1869–1875.

[20] P.P. Mueller, T. May, A. Perz, H. Hauser, M. Peuster, "Control of smooth muscle cell proliferation by ferrous iron", *Biomaterials*, Vol. 27, 2006, pp. 2193-2200.

[21] C. Di Mario, E. Grube, Y. Nisanci, N. Reifart, A. Colombo, J. Rodermann, R. Muller, S. Umman, F. Liistro, M. Montorfano, "MOONLIGHT: a controlled registry of an iridium oxide-coated stent with angiographic follow-up", *International Journal of Cardiology*, Vol. 95, pp. 329-331.

[22] C. Seliger, K. Schwennicke, C. Schaffar, "Influence of a rough, ceramic-like stent surface made of iridium oxide on neointimal structure and thickening", *European Heart Journal*, Vol. 21 (Suppl), 2000, pp. 286.

[23] F.A. Sgura, C. Di Mario, F. Liistro, M. Montorfano, A. Colombo, E. Grube, "The lunar stent characteristics and clinical results", *Herz*, Vol. 27, 2002, pp. 514-517.

[24] S.H. Monnink, A.J. van Boven, H.O. Peels, I. Tigchelaar, P.J. de Kam, H.J. Crijns, W. van Oeveren, "Silicon-carbide coated coronary stents have low platelet and leukocyte adhesion during platelet activation", *Journal of Investigative Medicine: The Official Publication of the American Federation for Clinical Research*, Vol. 47, 1999, pp. 304-310.

[25] L.F. Tanajura, A.A. Abizaid, F. Feres, I. Pinto, L. Mattos, R. Staico, "Randomized intravascular ultrasound comparison between patients that underwent amorphous hydrogenated silicon-carbide coated stent deployment versus uncoated stent", *Journal of the American College of Cardiology*, 2003, 41A-58A.

[26] M. Unverdorben, K. Sattler, R. Degenhardt, R. Fries, B. Abt, E. Wagner, H. Koehler, M. Scholz, H. Ibrahim, K. Tews, B. Hennen, G. Daemgen, H.K. Berthold, C. Vallbracht, "Comparison of a silicon carbide coated stent versus a noncoated stent in humans: the Tenax- versus Nir-Stent Study (TENISS)", *Journal of Interventional Cardiology*, Vol. 16, 2003, pp. 325-333.

[27] C. Bickel, H.J. Rupprecht, H. Darius, C. Binz, B. Hauröder, F. Krummenauer, J. Meyer, "Substantial reduction of platelet adhesion by heparin-coated stents", *Journal of Interventional Cardiology*, Vol. 14, 2001, pp. 407-413.

[28] K. Gutensohn, C. Beythien, J. Bau, T. Fenner, P. Grewe, R. Koester, K. Padmanaban, P. Kuehnl, "*In vitro* analyses of diamond-like carbon coated stents. Reduction of metal ion release, platelet activation, and thrombogenicity", *Thrombosis Research*, Vol. 99, 2000, pp. 577-585.

[29] S. Linder, W. Pinkowski, M. Aepfelbacher, "Adhesion, cytoskeletal architecture and activation status of primary human macrophages on a diamond-like carbon coated surface", *Biomaterials*, Vol. 23, 2002, pp. 767-773.

[30] A. Colombo, F. Airoldi, "Passive coating: the dream does not come true", Journal of Invasive Cardiology, Vol. 15, 2003, pp. 566–567.

[31] M.E. Korkmaz, E. Tayfun, H. Müderrisoglu, A. Yildirir, B. Ozin, M. Uluçam, M. Turan, "Carbon coating of stents has no effect on inflammatory response to primary stent deployment", Angiology, Vol. 53, 2002, pp. 563-568.

[32] S. Windecker, R. Simon, M. Lins, V. Klauss, F. R. Eberli, M. Roffi, "Randomized comparison of a titanium-nitride-oxide-coated stent with a stainless steel stent for coronary revascularization: the TiNOX trial", *Circulation*, Vol. 111, 2005; pp. 2617–2622.

[33] R. Wessely, J. Hausleiter, C. Michaelis, B. Jaschke, M. Vogeser, S. Milz, B. Behnisch, T. Schratzenstaller, M. Renke-Gluszko, M. Stöver, E. Wintermantel, A. Kastrati, A.

Schömig, "Inhibition of neointima formation by a novel drug-eluting stent system that allows for dose-adjustable, multiple, and on-site stent coating", *Arteriosclerosis, Thrombosis, and Vascular Biology*, Vol. 25, 2005, pp. 748-753.

[34] A. Rajtar, G. Kaluza, Q. Yang, D. Hakimi, D. Liu, M. Tsui, M. Lien, D. Smith, Jr. F.J. Clubb, T. Troczynski, "Hydroxyapatite-coated cardiovascular stents", *EuroIntervention*, Vol. 2, 2006, pp. 113–115.

[35] M. Tsui , "Calcium Phosphate coated stents comprising cobalt chromium alloy", Patent WO2009046532 (A1), 2009.

[36] H. Wieneke, O. Dirsch, T. Sawitowski, Y.L. Gu, H. Brauer, U. Dahmen, A. Fischer, S. Wnendt, R. Erbel, "Synergistic effects of a novel nanoporous stent coating and tacrolimus on intima proliferation in rabbits," *Catheterization and Cardiovascular Interventions: Official Journal of the Society for Cardiac Angiography & Interventions*, Vol. 60, 2003, pp. 399-407.

[37] M. Kollum, A. Farb, R. Schreiber, K. Terfera, A. Arab, A. Geist, "Particle debris from a nanoporous stent coating obscures potential antiproliferative effects of tacrolimus-eluting stents in a porcine model of restenosis", *Catheterization and Cardiovascular Interventions: Official Journal of the Society for Cardiac Angiography & Interventions*, Vol. 64, 2005, pp. 85–90.

[38] E. Grube, K.-E. Hauptmann, L. Buellesfeld, V. Lim, A. Abizaid, "Six-month results of a randomized study to evaluate safety and efficacy of a biolimus A9 eluting stent with a biodegradable polymer coating", *EuroIntervention*, Vol. 1, 2005, pp. 53–57.

[39] B. Chevalier, P.W. Serruys, S. Silber, E. Garcia, H. Suryapranata, K. Hauptmann, "Randomised comparison of NoboriTM, biolimus A9-eluting coronary stent with a Taxus®, paclitaxel-eluting coronary stent in patients with stenosis in native coronary arteries: the Nobori 1 trial", *EuroIntervention*, Vol. 2, 2007, pp. 426–434.

[40] R.A. Costa, A.J. Lansky, A. Abizaid, R. Mueller, Y. Tsuchiya, K. Mori, "Angiographic results of the first human experience with the biolimus A9 drug-eluting stent for de novo coronary lesions", *American Journal of Cardiology*, Vol. 98, 2006, pp. 443–446.

[41] H.J. Duckers, T. Soullie, P. Den Heijer, B. Rensing, R. De Winter, M. Rau, "Accelerated vascular repair following percutaneous coronary intervention by capture of endothelial progenitor cells promotes regression of neointimal growth at long term follow-up: final results of the Healing II trial using an endothelial progenitor cell capturing stent (Genous R stent)[TM]", *EuroIntervention*, Vol. 3, 2007, pp. 350–358.

[42] H.J. Duckers, S. Silber, R. De Winter, P. Den Heijer, B. Rensing, M. Rau, "Circulating

endothelial progenitor cells predict angiographic and intravascular ultrasound outcome following percutaneous coronary interventions in the HEALING-II trial: evaluation of an endothelial progenitor cell capturing stent", *EuroIntervention*, Vol. 3, 2007, pp. 67–75.

[43] J. Ako, H.N. Bonneau, Y. Honda, P.J. Fitzgerald, "Design Criteria for the Ideal Drug-Eluting Stent", *The American Journal of Cardiology*, Vol. 100 (8B), 2007, pp. 3M-9M.

[44] X. Chen, S. Mao, "Titanium Dioxide Nanomaterials: Synthesis, Properties, Modifications, and Applications," *Chemical Reviews*, Vol. 107, 2007, pp. 2891-2959.

[45] R. Zallen, M. Moret, "The optical absorption edge of brookite TiO_2", *Solid State Communications*, Vol. 137, 2006, pp. 154-157.

[46] U. Diebold, "The surface science of titanium dioxide", *Surface Science Reports*, Vol. 48, 2003, pp. 53-229.

[47] P. Evans, D. Sheel, "Photoactive and antibacterial TiO_2 thin films on stainless steel", *Surface and Coatings Technology*, Vol. 201, 2007, pp. 9319-9324.

[48] M.C. Advincula, F.G. Rahemtulla, R. C. Advincula, E.T. Ada, J.E. Lemons, S.L. Bellis, "Osteoblast adhesion and matrix mineralization on sol-gel derived titanium dioxide", *Biomaterials*, Vol. 27, 2006, pp. 2201-2212.

[49] N. Huang, P. Yang, Y.X. Leng, J.Y. Chen, H. Sun, J. Wang, G.J. Wang, P.D. Ding, T.F. Xi, Y. Leng, "Hemocompatibility of titanium oxide films", *Biomaterials*, Vol. 24, 2003, pp. 2177-2187.

[50] C. Lin, S. Yen, "Biomimetic growth of apatite on electrolytic TiO_2 coatings in simulated body fluid", *Materials Science and Engineering: C*, Vol. 26, 2006, pp. 54-64.

[51] J. Liu, D. Yang, F. Shi, Y. Cai, "Sol-gel deposited TiO_2 film on NiTi surgical alloy for biocompatibility improvement", *Thin Solid Films*, Vol. 429, 2003, pp. 225-230.

[52] B.D. Ratner, A.S. Hoffman, F.J. Schoen, J.E. Lemons, "Biomaterials Science: An Introduction to Materials in Medicine", *Elsevier Academic Press*, 2004.

[53] G. Mendonça, D.B. Mendonça, F.J. Aragao, L.F. Cooper, "Advancing dental implant surface technology - From micron- to nanotopography", *Biomaterials*, Vol. 29, 2008, pp. 3822-3835.

[54] E. Wintermantel, S.-W. Ha, "Medizintechnik mit biokompatiblen Werkstoffen und Verfahren", Springer, 2002.

[55] J.R. Davis, "Handbook of materials for Medical Devices", *ASM International*, 2003.

[56] M. Mosseri, I. Tamari, M. Plich, Y. Hasin, M. Brizines, A. Frimerman, "Short- and long-term outcomes of the titanium-NO stent registry", Cardiovascular Revascularization Medicine, Vol. 6, 2005, pp. 2–6.

[57] S. Windecker, R. Simon, M. Lins, V. Klauss, F.R. Eberli, M. Roffi, G. Pedrazzini, T. Moccetti, P. Wenaweser, M. Togni, D. Tuller, R. Zbinden, C. Seiler, J. Mehilli, A. Kastrati, B. Meier, O.M. Hess, "Randomized Comparison of a Titanium-Nitride-Oxide-Coated Stent With a Stainless Steel Stent for Coronary Revascularization. The TiNOX Trial", *Circulation*, 2005, pp. CIRCULATIONAHA.104.486647.

[58] S.D. Plant, D.M. Grant, L. Leach, "Behaviour of human endothelial cells on surface modified NiTi alloy", *Biomaterials*, Vol. 26, 2005, pp. 5359-5367.

[59] L. Peng, M.L. Eltgroth, T.J. LaTempa, C.A. Grimes, und T.A. Desai, "The effect of TiO_2 nanotubes on endothelial function and smooth muscle proliferation", *Biomaterials*, Vol. 30, 2009, pp. 1268-1272.

[60] A. A. Ayon, M. Cantu, K. Chava, C. M. Agrawal, M.D. Feldman, D. Johnson, D. Patel, D. Marton, "Drug loading of nanoporous TiO_2 films", *Biomedical Materials*, Vol. 1, 2006, pp. L11-L15.

[61] H. Hofmann, F. Neftel, L.-D. Piveteau, "Reinforced porous coating", *Patent WO2007031972 (A1)*, 2007.

[62] L.-D. Piveteau, H. Hofmann, F. Neftel, "Anisotropic nanoporous coating", *Patent WO2007148240 (A2)*, 2007.

[63] F. Juillerat, "Self-assembled nanostructures prepared by colloidal chemistry", Thesis, Ecole Polytechnique Fédérale de Lausanne, 2005.

[64] R.-A. Doong, S.-M. Chang, Y.-C. Hung, I.-L. Kao, "Preparation of highly ordered titanium dioxide porous films: Characterization and photocatalytic activity", *Separation and Purification Technology*, Vol. 58, 2007, pp. 192-199.

[65] Q.F. Xu, J.N. Wang, I.H. Smith, K.D. Sanderson, "Superhydropobic and transparent coatigs based on removable polymeric spheres", *Journal of Materials Chemistry*, Vol. 19, 2009, pp. 655-660.

[66] D. Grosso, G.J. De A. A. Soler-Illia, E.L. Crepaldi, B. Charleux, C. Sanchez, "Nanocrystalline Transition-Metal Oxide Spheres with Controlled Multi-Scale Porosity", *Advanced Functional Materials*, Vol. 13, 2003, pp. 37-42.

[67] Z.Y. Yuan, T.Z. Ren, B.L. Su, "Hierarchially Mesostructured Titania Materials with an Unusual Interior Macroporous Structure", *Advanced Materials*, Vol. 15, 2003, pp. 1462-1465.

[68] D. Kuang, T. Brezesinski, B. Smarsly, "Hierarchial Porous Silica Materials with Trimodal Pore System Using Surfactant Templates", *Journal of the American Chemical Society*, Vol. 126, 2004, pp. 10534-10535.

[69] Y.Fu, Z. Jin, W. Xue, Z. Ge, "Ordered Macro-Mesoporous nc-TiO$_2$ Films by Sol-Gel Method Using Polystyrene Array and Triblock Copolymer Bitemplate", *Journal of the American Ceramic Society*, Vol. 91, 2008, pp. 2676-2682.

[70] H. Ko, H. Lee, J. Moon, "Fabrication of colloidal self-assembled monolayer (SAM) using monodisperse silica and its use as a lithographic mask", *Thin Solid Films*, Vol. 447-448, 2004, pp. 638-644.

[71] P. Jiang, M. J. McFarland, "Wafer-scale periodic nanohole arrays templated from two-dimensional nonclose-packed colloidal crystals", *Journal of the American Chemical Society*, Vol. 127, 2004, pp. 3710-3711.

[72] F. A. Denis, P. Hanarp, D. S. Sutherland, Y. F. Dufrêne, "Nanoscale chemical patterns fabricated by using colloidal lithography and self-assembled monolayers", *Langmuir*, Vol. 20, 2004, pp. 9335-9339.

[73] D.-G. Choi, S. G. Jang, H. K. Yu, S.-M. Yang, "Two-dimensional polymer nanopattern by using particle-assisetd soft lithography", Chemistry of Materials, Vol. 16, 2004, pp. 3410-3413.

[74] S. M. Huang, M. H. Hong, B. S. Lukyanchuk, Y. W. Zheng, W. D. Song, Y. F. Lu, T. C. Chong, "Pulsed laser-assisted surface structuring with optical near-field ehanced effects", *Journal of Applied Physics*, Vol. 92, 2002, pp. 2495-2500.

[75] E. P. Briggs, A.R. Walpole, P. R. Wilshaw, M. Karlsson, E. Palsgard, "Formation of highly adherent nano-porous alumina on Ti-based substrates: a novel bone implant coating", *Journal of Materials Science, Materials in Medicine*, Vol. 15, pp. 1021-2029.

CHAPTER III

3 AIMS OF THE THESIS

The feasibility to use the nanostructured TiO_2-coatings, which are introduced in Chapter 1.2, as drug-eluting films on stents will be evaluated. Complex testing is required to judge if the coatings have the potential to be applied on a stent. In the frame of this thesis, the following topics will be in the focus of interest:

- The characterization of the structural and chemical features of two modifications of the titania layers (with and without reservoirs), when produced on 316L stainless steel (SS) and on silicon wafer model supports.

- Finding and controlling the procedures to load the therapeutical agent paclitaxel (PTX) into the porous films. They will be optimized to yield a drug concentration of $1\ \mu g/mm^2$ in the coating, which corresponds to the dose used in the commercially available Taxus^{TM} stent. PTX will be used as a model drug, because it is approved by the US Food and Drug Administration (FDA) for its application in drug-eluting stents (DESs) and it is a non-patented drug freely available.

- Performing *in vitro* PTX-release tests in water and bovine plasma. The release kinetics will be deduced and compared with literature findings. The transport governing factors during the drug-liberation from the coating will be identified. This will help to possibly change the coating's properties to adapt it to various desired release profiles.

- Preliminary *in vitro* cytotoxicity tests of the coatings when exposed to a direct

contact with primary bovine endothelial cells will be performed. They serve as first biocompatibility evaluations of the coatings.

More detailed information regarding the production of the thin TiO_2-films on simple and complex steel geometries, as well as its mechanical behavior during expansion can be found in the doctoral thesis of A. Tourvieille de Labrouhe*. He studied the formation of cracks and their propagation in the nanostructured titania coatings, which were exposed to deformations greater than 40 %. His findings were acquired in parallel to the ones in the present study. Both studies are complementary to each other and were deduced within the framework of the project Nanostent, supported by the Innovation Promotion Agency (CTI), Switzerland and the industrial partner Debiotech SA, Switzerland. The developed technology platforms will provide Debiotech SA a powerful tool to adapt the coatings to various applications.

---

*A. Tourvieille de Labrouhe, " Nanostructured ceramic coatings for deformable medical implants such as stents", Thesis, Ecole Polytechnique Fédérale de Lausanne, 2009

CHAPTER IV

4 CHARACTERIZATION OF THE STRUCTURED TITANIA FILMS

4.1 Background and Introduction

Ceramic coatings have proven to be beneficial to increase the performance of the underlying bulk material. As insulators, ceramic coatings are applied in electronic devices, like in wire and heater elements, or in microelectronic circuits. They can protect their support material in high temperature environments or from wear and deformation due to the good hardness. Permanent ceramic films and coatings can be used to protect materials from reaction and corrosion in harsh environments [1, 2]. Various ceramic coatings are applied in medical implants, which are exposed to the biological environment [3, 4, 5, 6, 7], like was mentioned previously in Chapter 2.1.3 and Chapter 2.2.

Some common methods to create thin ceramic films are physical vapor deposition (PVD), chemical vapor deposition (CVD), thermal spray processing, solution and sol gel techniques. Methods like CVD and PVD allow the production of dense films as well as porous films when templates are involved. However in some cases, the coverage of complex geometries is difficult [1, 2]. In the present study, highly porous films with well ordered reservoirs are to be fabricated. The reservoirs are to be created by colloidal lithography, cf. Chapter 2.3. The method of choice to create the nanostructured titania coatings was dip coating, which allows an easy coverage of the complex shaped stent. The coating's thickness, obtained by dip coating a support into a colloidal particles suspension, is

controlled by the concentration of the colloidal particles and binders, the particle size and of the surface tension of the support [2]. The viscosity of the suspension and the withdrawal speed also have an influence. An equation derived by Landau and Levich relates these parameters [8]. The thickness of the deposited film by dip coating, H, can be calculated as

$$H = 0.94 \cdot \frac{(\eta \cdot v)^{\frac{2}{3}}}{\gamma_{LV}^{\frac{1}{6}} \cdot (\rho \cdot g)^{\frac{1}{2}}}$$ (4-1),

with η: dynamic viscosity of the suspension, v: withdrawal speed, γ_{LV} liquid/vapor surface tension, ρ the density of the suspension and g the acceleration due to gravity. By simply varying one of the parameters, e.g. the withdrawal velocity, different coating thicknesses can be achieved. The main advantages of dip coating are that complex geometries can be coated in a controlled, fast and inexpensive way. The combination of colloidal lithography and dip coating is already established for coatings with structured porosities, like was demonstrated in Chapter 2.3. This made dip coating an attractive technique to be used in this study to form the porous TiO_2-coatings on stent implants.

It was important to characterize the structural features of the produced coatings in regard to their application in a drug-eluting stent (DES). In the following, a short summary of the main definitions and classifications of porous structures is given, which will be used further. Regarding the pore sizes, the International Union of Pure and Applied Chemistry (IUPAC) has defined a *micropore* as a pore with an internal width of less than 2 nm, a *mesopore* with an internal width between 2 and 50 nm and a *macropore* as a pore with a width greater than 50 nm. The term *nanopore* does not yet have a precise definition, but is commonly used to describe pore widths in the range of 0.1 to 100 nm [9]. Possible shapes of pores in a porous solid are pointed out in Figure 4-1. Pores completely isolated from the surrounding are named *closed pores*, such as in (a). They influence the bulk properties like strength, but would not contribute to the drug-load and release. The others are termed *open pores* (b, c, d, e and f), which would be responsible for the drug transport. Some may be open at one end (b), they are called *blind pores*. Others might be open at two ends (e), named *through pores*. Pores can also be classified according to their shape: they may be *cylindrical* (c), (f) or *inkbottle shaped* (b), *funnel* (d) or *slit-shaped* [10].

An important parameter affecting the diffusion of molecules through a porous solid is the *tortuosity* of the pores. It is defined as the ratio of the effective diffusion length in a pore to the distance between its ends [9]. The *porosity* of a porous bulk is the ratio of the pore volume to the overall volume occupied by the solid [9].
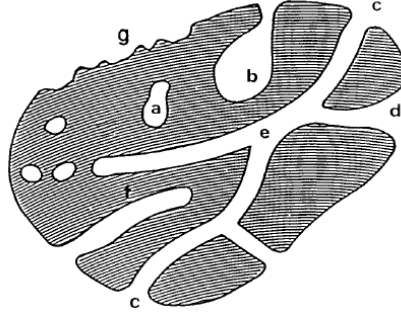
Figure 4-1 A schematic cross section of a porous solid representing all possible types of pores. (a): closed pore, (b to f): open pores, whereas (b), (f) in particular are blind pores, and (c), (e) through pores [10].

Another important characteristic of a porous solid is its *specific surface area*, S_{BET}. It represents the ratio of the total surface area available, including the one of the open pores and the one of the lateral area of the specimen, to the sample mass. The *mean equivalent spherical grain diameter* from the specific surface area, d_{BET}, can be calculated as

$$d_{BET} = \frac{6}{\rho_{theo} \cdot S_{BET}}$$ (4-2),

with ρ_{theo}: *theoretical density* of the porous structure excluding all pores. Another density describing porous structures is the skeletal density ρ_s, which represents the density of the material including all closed pores and inaccessible voids. The Archimedes density, ρ_{Arch}, denotes the density of the whole porous structure including all pores and voids.

In this chapter, the production of the thin titania coatings in the non-reservoir (NRL) and reservoir layer (*RL*) modifications by dip coating will be presented. Anatase initial nanoparticles, with a diameter smaller than 50 nm, were chosen rather than micrometer sized particles, because:

- Nanopores and high porosities can be created in the coating. This is necessary to incorporate the drug and to release it in a controlled way.

- The total contact area between the nanoparticles and the support is higher and thus might contribute to a better adhesion of the coating on the steel support.

- The higher specific surface area of the nanoparticles allows a densification at lower sintering temperatures.

- Anatase is the stable crystalline morphology of TiO_2 for particles with a diameter smaller than 100 nm [11].

4.2 Materials and methods for the production of the thin films and the bulks

The fabrication of the thin titania films on 316L stainless steel (SS) or silicon wafer supports will be explained. Because their structural characterization was difficult, like will be pointed out in Chapter 4.5.1, equivalent bulk titania bodies with a cylindrical shape were prepared.

4.2.1 Suspensions

The porous films and bulks were created with initial anatase TiO_2-nanoparticles, which were purchased from TechPowder SA, Switzerland. This powder had the specifications like shown in Table 4-1, with an average particle diameter from the specific surface area, d_{BET}, of 21.5 nm and an agglomerate factor of 2.9. To form a stable colloidal suspension to be used for the sample preparation, the initial powder was dispersed in water with binder to obtain suspension "*TP1*". It was composed of 6.8 %wt TiO_2, 3.8 %wt poly vinyl alcohol (PVA, Mowiol 3-96 from Clariant, Germany) and water. The pH was adjusted to 10.5 with technical ammonia. A suspension without binder and a solid content of 13 %wt, "*TP2*", was used to prepare samples for dilatometry. The higher solid content formed bigger bulk bodies necessary for this analysis. Before the suspensions were applied, they were sonicated with ultrasound (DG-100-36, Telesonic Ultrasonics) for 10 min to disrupt agglomerates. To manufacture reservoir containing layers (*RL*s), a water based *template suspension* containing 5 %wt spherical polymer templates (Latex Microsphere Suspension, Duke Scientific Corporation), with a mean diameter of 1 µm, was employed.

Table 4-1 Specifications of the initial titania powder used to produce the nanostructured films and bulks.

characteristics of the titania powder	
crystal phase	anatase
specific surface area, S_{BET} (m^2/g)	75.4
average particle diameter, d_{BET} (nm)	21.5
median particle diameter, d_{v50} (nm)	62.0*
agglomerate factor	2.9
density (g/cm^3)	3.7

* see for Figure A-1 in Appendix

4.2.2 Supports for the thin films

The thin TiO_2-films were prepared on two different support materials: *316L stainless steel (SS)* and *silicon wafers*.

The 316L stainless steel supports (Metallica SA, Switzerland) had a rectangular shape with a length of 50 mm, a width of 10 mm and a thickness of 1.25 mm. The SS exhibited the following composition: carbon (C) < 0.03 %wt, chromium (Cr) = 16-18 %wt, nickel (Ni) = 10-14 %wt, molybdenum (Mo) = 2-3 %wt, manganese (Mn) < 2 %wt, silicium (Si) < 1 %wt, phosphor (P) < 0.045 %wt, sulfur (S) < 0.03 %wt [12]. Prior to the application of the ceramic film, the metal specimens were electrochemically polished. This process served for a reduction in roughness of the surface and for a brightening and passivation of the stainless steel [13]. The electrolyte, composed of 15 %vol deionized water (Christ ministil P-12, 0.5 µS/cm), 35 %vol phosphoric acid (85 %wt, Acros organics) and 50 %vol glycerol (95 %wt Glycerol synthetic, Acros organics), was heated up to 90 °C in a glass beaker. The metal workpiece was used as an anode (+), the cathode (-) corresponded to a metal mesh surrounding the interior of the beaker. Both electrodes were covered by the electrolyte and attached to the laboratory power supply (EA-PS 2016-100). If a current density of 0.75 A/cm^2 between the anode and the cathode was applied, metal ions from the surface of the specimens were removed. The electrolyte acted as a conductor and allowed the metal ions to be drawn to the cathode, where the reduction reaction was taking place and hydrogen gas formed. After polishing for 5 min, a mean roughness, R_a, of 100 nm was measured by laser profilometry (UBM-microfocus) [14].

Silicon wafers with a 100 nm SiO_2 layer (Silicon-Wafer, P/Bor <100>, double sided polished and 100 nm SiO_2, Si-Mat Silicon Materials) were used as model supports for the titania coatings. They were easier to handle in respect of cutting or porosimetry analyses than the SS.

Before the coatings were applied to any type of support, they passed through a 3-step cleaning procedure to remove grease and dust. Specimens were firstly immersed in a water/soap solution and put into an ultrasonic bath for 5 min. After the same procedure was performed secondly in acetone and thirdly in ethanol, the specimens were dried under air flow and then dip coated.

4.2.3 *Films by dip coating*

The thin films were prepared by a multi-step dip coating technique. Depending on the desired microstructure-non-reservoir layer (NRL) or reservoir layer (*RL*)-the process parameters were adjusted according to Table 4-2. By dipping the supports multiple times into the TiO_2-suspension (Precision dip coating system PL 3201, Speedline Technologies) and pulling them out with a defined withdrawal speed, a NRL was obtained. The same thicknesses of the NRLs were deduced by two methods. One method was to withdraw the

specimens with two times 90 mm/min and one time with 250 mm/min from the suspension TP1. In the second method, the specimens were withdrawn consecutively 4 times with 1000 mm/min. Between each dip, the deposited film was dried for 20 min at 37 °C and 10 % relative humidity in a climatic test cabinet (RUMED®).

To create *RL*s, a support was dipped one time into the TP1 suspension and withdrawn with 90 mm/min. Subsequently after drying, it was dipped into the template suspension and pulled out with a speed of 90 mm/min. The specimens were then once again dipped into the TiO$_2$-suspension and withdrawn with a speed of 90 mm/min, before in the last step being pulled out of the titania suspension with 250 mm/min, Table 4-2.

Table 4-2 Parameters of the dip coating to produce titania non-reservoir layers (NRL) and reservoir layers (*RL*) on either stainless steel (SS) or wafer (w) supports.

sample	*support*	*structure*	*number of dips / withdrawal speed (mm/min)*	
			TiO$_2$-suspension	*template-suspension*
ss730NRL	steel	NRL	2/90; 1/250	-
ss730*RL*	steel	*RL*	2/90; 1/250	1/90
w800NRL	wafer	NRL	2/90; 1/250 *or* 4/1000	-
w800*RL*	wafer	*RL*	2/90; 1/250	1/90
f800NRL	wafer	NRL	4/1000	-
w730NRL	wafer	NRL	2/90; 1/250 *or* 4/1000	-
w730*RL*	wafer	*RL*	2/90; 1/250	1/90

The strong adhesion of the thin films on the supports, as well as the small amount of porous material available, made it difficult to perform standardized analyses for the pore size characterization with the films (cf. Chapter 4.5.1). An alternative way had to be found to get access to the structural parameters. Therefore bulk titania samples in the NRL-modification were prepared.

4.2.4   Bulks by slip casting

Bulk samples were prepared by slip casting. The TiO$_2$-suspension was degassed at 200 mbar for 10 min (Epovac Stuers) to eliminate air, which might have caused a false, lower density of the green bodies compared to the one in the films. A cellulose nitrate filter (Whatman) with a cutoff diameter of 0.2 µm was placed onto a highly porous gypsum plate, which served to take up the liquid coming from the suspension. On top of the filter a rubber mould of a height of 20 mm with cylindrical holes exhibiting a diameter of 15 mm was mounted. The TiO$_2$-suspension was carefully introduced into the cylindrical voids of the mould with a pipette. The set-up was covered by a glass plate to avoid contamination and left for drying at room atmosphere for 7 d. The generated green bodies had a shape of a

pellet with a diameter of 10 mm and a height of 2 mm.

4.2.5   Sintering of the films and the bulks

The heat treatments of the films and bulks were carried out in a tubular furnace (Model 54434, Lindberg) under continuous gas flow with 0.342 l/min. The sintering cycle consisted of 3 main stages, like illustrated in Figure 4-2. With a rate of 4.5 °C/min, samples were heated in air up to 450 °C. This temperature was maintained for 60 min to remove the organic binder by thermolysis. To densify the TiO_2-nanoparticles, a second heating step up to a maximum sintering temperature, T_{max}, in an atmosphere of air and argon (Ar)* followed. Ar as an inert gas was employed to protect the steel from oxidation at elevated temperatures. The dwell time at T_{max} was 80 min before the samples were cooled to room atmosphere.
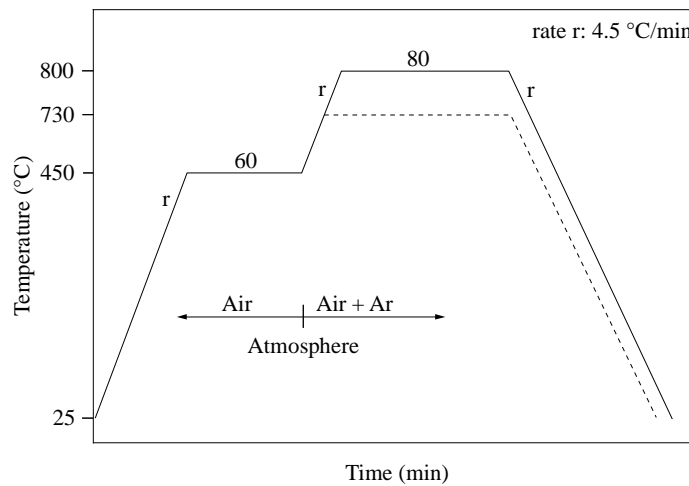
Figure 4-2 Sintering cycles of the films and bulks with representative maximum sintering temperatures, T_{max}, of 730 and 800 °C. r denotes the heating rate, Ar: argon.

The sintering parameters applied on the various film samples are summarized in Table 4-3. Sample names contain the information of the applied support material (ss or w), the maximum sintering temperature and their modification (NRL or *RL*). Except of f800NRL, all films were sintered while being attached to the support. The coatings of the samples f800NRL, hence the letter "f", were removed from the silicon supports before the heat treatment. They were produced to determine the influence of the support material on the coating's structure. The maximum sintering temperatures of the various cylindrical bulks are depicted in Table 4-4. The names of the bulks contain "b" for the bulk-modification and the value of the maximum sintering temperature.

* The exact concentrations of argon and air were not determined. But it was observed that the TiO_2 in the films was not reduced, which was expected by applying argon gas. Reasons were that argon was not purified before its application and that the oven showed a leakage. The oxygen partial pressure in the oven during sintering was not measured.

Table 4-3 Conditions used for the sintering of the TiO_2-films produced by dip coating. T_{max} represents the maximum sintering temperature.

sample	ss730NRL	ss730RL	w800NRL	w800RL	f800NRL	w730NRL	w730RL
T_{max} (°C)	730	730	800	800	800	730	730
substrate (yes/no)	yes	yes	yes	yes	no	yes	yes

Table 4-4 Conditions used for the sintering of the TiO_2-bulks produced by slip casting. T_{max} represents the maximum sintering temperature.

sample	b700	b720	b740	b750	b770	b800	b820
T_{max} (°C)	700	720	740	750	770	800	820

4.3 Methods for the characterization of the porous structures

4.3.1 Microscopy

The quality of the deposited TiO_2-films at different steps of the dip coating were examined by an optical microscope (Olympus B071 equipped with an Altra 20 Soft Imaging System; Software analySIS getIT, Olympus Soft Imaging Solutions GmbH). In addition, the density and dispersion of the deposited template microbeads was observed by optical microscopy.

Micrographs of the top views of the coatings and the bulks were taken by a scanning electron microscope (SEM, XLS 30, Philips). Photos of the cross sections of the films on wafers, which could easily be prepared by cutting with a diamond knife, were taken by a high resolution scanning electron microscope (XL-30SFEG, Philips). Focused ion beam (FIB) cutting in combination with scanning electron micrography was used to obtain images for the grain size analysis of NRLs. Manipulation of the machine and image processing was performed by M. Cantoni, Center for Electron Microscopy (CIME), EPF Lausanne. The titania coated specimens were therefore mounted on the stage of a FEI Nova 600 Nanolab FIB. On a selected area, platinum was deposited to provide a smooth, conducting surface. Cross sections were prepared every 10 nm using the FIB at 30 kV and a beam current of 300 nA. Backscattered electron scanning images were recorded at accelerating voltages of 4 kV. The set of 2-dimensional images were processed using the software ImageJ.

4.3.2 X-ray diffraction

Determinations of the crystal phases of TiO_2, during and after the sintering, were performed with three different X-ray diffraction (XRD) methods. The applied technique depended on the existing shape of the ceramic as a powder, as a thin film on wafer or stainless

steel, or as a bulk.

The powder in its initial state, the films w800NRL, f800NRL, w730NRL, w730*RL* and the bulks were characterized by *powder XRD* (X' Pert Pro, PANalytical), with a Cu-K$_\alpha$-radiation, an operation voltage of 40 kV, a current of 50 mA and a step size of 0.017 °2Theta. The films were detached from the supports prior to analysis. *Thin film XRD* was performed by A. Neels at the Centre Suisse d'Electronique et de Microtechnique, CSEM, in Neuchâtel, Switzerland. Data were acquired on a Panalytical MRD PRO instrument with a copper filament at a gazing incident angle of 1° (ω) in the range of 10 to 100 °2Theta. This technique was employed to measure the phases of the coatings on SS supports, ss730NRL and ss730*RL*. *In situ XRD* (X'Pert Pro instrument, PANalytical) during sintering was performed using a CuK$_\alpha$-radiation, an operation voltage of 40 kV, a current of 40 mA and a step size of 0.008 °2Theta. The aim was to observe the phase transition of TiO$_2$ while heating. Hence the conventional heat treatment was modified to collect a statistical sufficient amount of intensity counts. X-ray spectra were recorded each before and after a heating step, during which the temperature was kept constant for each additional 30 min. The T$_{max}$ chosen was 800 °C and helium was selected instead of argon, because this gas had lower background absorption. Only bulk samples and no films were applied in this experiment. The quantitative phase analyses of anatase and rutile of all measurements were evaluated using the Rietveld refinement method and the software X'Pert High Score Plus (PANalytical) [15].

4.3.3 Densities

The *theoretical densities* of the films and bulks were deduced from the XRD measurements. The *skeletal densities*, which include closed pores and inaccessible voids, were determined by helium-pycnometry (AccuPyc 1330, Micrometics). The *bulk densities* of the porous bulk samples were determined by the Archimedes method. The corresponding mean values were acquired from three replicas.

4.3.4 Specific surface area

The specific surface area, S$_{BET}$, was measured by nitrogen adsorption on a Micrometics Gemini 2376 using the Brunauer-Emmett-Teller (BET) method. Each type of specimen was measured in triplicates.

4.3.5 Grain size analysis

Common methods, which are usually employed to determine the grain size, were

inappropriate for the TiO_2-coatings. The epoxy resin, typically infiltrated into the porous structure for stabilization, failed to penetrate throughout coating. Subsequent grinding caused the breakout of small particles from the coating. One way out was to make perfectly polished cross sections of the thin films by FIB and recording SEM-images, cf. Chapter 4.3.1. For representative statistical results, a minimum of 400 TiO_2-grains was counted in the images, using the linear intercept method of the program LINCE (Lince Linear Intercept, Version 2.4.2., Technical University Darmstadt, Materialwissenschaften, Nichtmetallisch-Anorganische Werkstoffe).

4.3.6　Porosimetry

Various methods, which are based on different physical models, were applied to determine the porosity of the titania nanostructures. The porosity and pore size distribution (PSD) of the films, which were not removed from the support prior to the analysis, were measured by the three following techniques:

- *Ellipsometric porosimetry (EP),*

- *Small angle neutron scattering (SANS),*

- *Stereology.*

Two methods were employed to determine the porosity and PSD of the films, which were detached from the wafer support before analysis, and of the bulks:

- *Mercury intrusion porosimetry (MIP),*

- *Nitrogen sorption porosimetry (NSP).*

A summary of the analyses performed on the specimens is presented in Table 4-5.

Table 4-5 Summary of the methods used for pore size determinations of particular samples.

method	*sample*
ellipsometric porosimetry (EP)	ss730NRL, w730NRL
small angle neutron scattering porosimetry (SANS)	w730NRL, w730*RL*
stereology	w730NRL
mercury intrusion porosimetry (MIP)	w730NRL, w800NRL, f800NRL, b740
nitrogen sorption porosimetry (NSP)	b740

In the following section methods used, when the films were not detached from the supports, are pointed out. More detailed information will be given for EP, because it might become in the future a powerful technique for the structural characterization of highly

porous, thin films. Also some principles of SANS will be explained, because it is not a commonly used method to determine PSDs and porosities. The other techniques will not be elucidated in detail, because they are standardized.

4.3.6.1 *Ellipsometric porosimetry*

The basic principle of EP is to measure the change in the optical properties of the porous film, while performing an adsorption/desorption experiment to obtain an adsorption isotherm, Figure 4-3 [16]. Ellipsometric parameters, which characterize the change in polarization of an incoming light beam upon reflection on the film, are recorded. This behavior is determined by the coating's properties, such as thickness, refractive index or dielectric constant. The emitted radiation E, with a defined wavelength λ, can be decomposed into a linearly polarized component, E_p, which is oscillating parallel to the plane of incidence. The second component, E_s, is perpendicular to the plane of incidence and parallel to the sample surface. The polarized light falls onto the specimen. After the specular reflection at the sample, the radiation passes a second polarizer and goes into the detector. The amplitudes of the s- and p- components of the waves, after reflection and normalized to their initial values, are measured and result in the amplitude ratio upon reflection, tan(ψ). Also the phase shift, Δ, of the waves is evaluated [17].
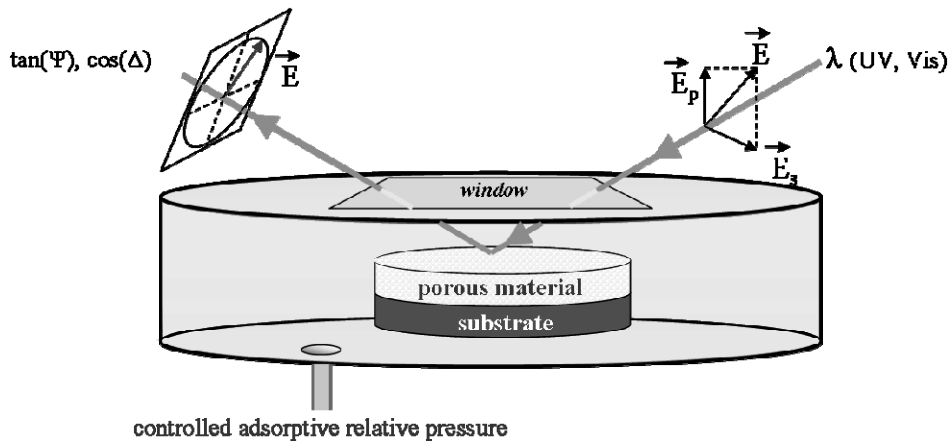
Figure 4-3 Schematic of the ellipsometric porosimetry. The sample is placed in a vacuum chamber, in which the relative pressure of the adsorptive can be controlled. The incoming beam with a specific wavelength λ enters the chamber through the optical window. The optical properties, tan(ψ) and cos (Δ), of the porous material on the substrate are monitored by ellipsometry during the whole adsorption/desorption process [18].

It is obvious that these parameters alter when a solvent adsorbs in the porous film. Models are applied to calculate the adsorption isotherms from the change in these optical properties. First the alteration of adsorptive volume is determined from the shift in refractive index over the relative pressure with the so called Lorentz-Lorentz equation [16, 18]. The

dependence of the adsorptive volume on the relative pressure is the adsorption isotherm used to calculate the PSD. Based on the Kelvin equation for cylindrical pores [9],

$$-\ln(p_e / p^0) = \frac{2 \cdot \gamma_{lv} \cdot V_m \cdot \cos(\theta_c)}{R \cdot T \cdot r_k}$$

(4-3),

with p_e: equilibrium vapor pressure, p^0: saturation vapor pressure, γ_{lv}: liquid/vapor surface tension of the adsorbed liquid, V_m: molar volume of the condensate, θ_c: the wetting angle of the adsorptive, R: ideal gas constant of 8.3145 J/(mol·K), T: temperature, r_k: the radius of the meniscus of the adsorptive or Kelvin radius. From that equation the pore size distribution can be deduced [16, 18]. Besides the characterization of the PSD in micro- and mesoporous coatings [16], EP can deliver additional data about the film thicknesses, refractive indices, extinction coefficients and Young moduli.

The EP-measurements and evaluations of the titania films applied in the present study were performed by A. Bourgeois at the company SOPRA SA. A wavelength of the incoming beam of 633 nm and an incident angle of 60 ° were applied. First the refractive index and the thickness of the coatings were determined by conventional ellipsometric measurements under nitrogen flow. The open porosity was ascertained by varying the relative pressure of the adsorbent toluene and recording the change in refractive index. Furthermore the volume adsorbed isotherms were recorded, from which the PSDs using a cylindrical pore model were deduced.

4.3.6.2 *Small angle neutron scattering*

Radiation scattering from solids can be used to determine porosities and PSDs. The scattering arises from variations in the scattering length densities of different materials and occurs over distances exceeding the interatomic spacing. Neutron scattering can give structural information on length scales of 1 to 100 nm. This technique is established in the characterization of hard matter and soft matter [19, 20, 21]. For instance, the pores in metals or the conformation of polymers in solution can be examined. In a SANS experiment, a beam of collimated neutrons is directed at the sample. Fractions of the incident beam are either transmitted, absorbed or scattered by the sample (Figure 4-4). A detector of the dimensions dx and dy is positioned at a certain distance from the sample and at a scattering angle θ_{SANS}. It records the flux of the scattered radiation into a solid angle element [22].

(a)

(b)
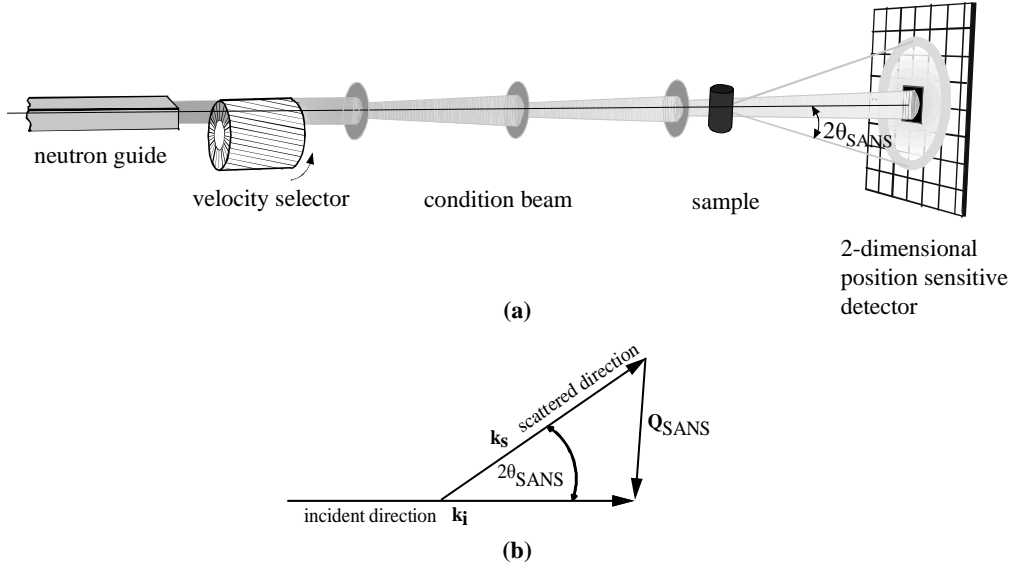
Figure 4-4 (a) Illustrates a schemata of a small angle neutron scattering (SANS) experiment. (b) displays the scattering vector: the incoming wave with the wave vector **k$_i$** gets scattered at an object as **ks**. **Q$_{SANS}$** is the resulting scattering vector [23].

The value measured during small angle scattering is the scattering intensity, I(Q$_{SANS}$), as a function of the modulus of the scattering vector Q$_{SANS}$, like depicted in Figure 4-5 (a). I(Q$_{SANS}$) is described as [9]

$$I(Q_{SANS}) = n_p \cdot V_p^{\ 2} \cdot (\rho_p - \rho_s) \cdot P(Q_{SANS}) \cdot S(Q_{SANS}) \tag{4-4},$$

with Q$_{SANS}$ the modulus of the scattering vector:

$$Q_{SANS} = |\mathbf{Q}_{SANS}| = \frac{4 \cdot \pi \cdot \sin(\theta_{SANS})}{\lambda} \tag{4-5}.$$

The variables in Equation (4-4) are n$_p$: the pore number density, V$_p$: pore volume, ρ_p, ρ_s: scattering length densities of the pores and the solid. P(Q$_{SANS}$) represents the shape factor, which depends on the size and shape of the pores. It describes the decay of scattering intensity at low Q$_{SANS}$, a domain of the scattering curve also known as the Guinier region. S(Q$_{SANS}$) is the interparticle structure factor, describing the effect of interference of the scattering waves from individual pores.
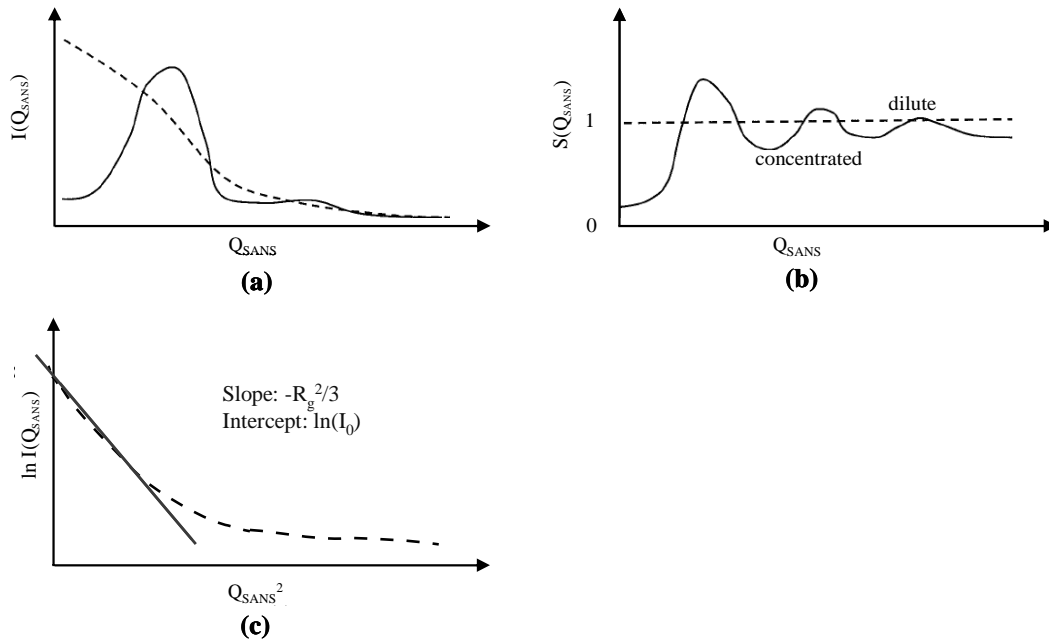
Figure 4-5 (a) Represents the interparticle structure factor $S(Q_{SANS})$ of diluted (dashed line) and concentrated particles of a small angle neutron scattering (SANS) experiment [24]. (b) illustrates the scattering curves for diluted (dashed line) and concentrated particles [24]. The Guinier approximation to determine the pore size by SANS is shown in (c).

For spherical and dilute pores, that means the pores scatter independently, $S(Q_{SANS})$ equals 1, like is illustrated in Figure 4-5 (b). $P(Q_{SANS})$ simplifies for low Q_{SANS}, and Equation (4-4) can be re-written as

$$I(Q_{SANS}) = I_0 \cdot \exp\left(-\frac{Q_{SANS}^2 \cdot R_g^2}{3}\right) \tag{4-6},$$

with I_0: initial beam intensity and R_g: mean radius of gyration of the pores [9]. The mean radius of gyration is related to the pore radius, r_p, by

$$r_p = \sqrt{\frac{5 \cdot R_g}{3}} \tag{4-7}.$$

Equation (4-6) is an example of Guinier's law, which is valid for $Q_{SANS} \cdot R_g < 1$. To obtain the desired PSD from the scattering data, the Guinier plot as depicted in Figure 4-5 (c) is drawn. A linear approximation for small Q_{SANS}^2 delivers the slope of $-R_g^2/3$ and the intercept $\ln(I_0)$. The pore radius r_p can then be derived with Equation (4-7) [9].

The evaluation of PSDs of thin, porous films by SANS was first recorded by Wu and co-workers [20]. They used a stack of 6 silica films, each with a thickness of 1 µm, to

increase the scattering intensity as compared to one single film. The wafer supports did not significantly contribute to the signal. A similar method was applied in the present study. SANS measurements were performed by J. Kohlbrecher at the Paul Scherrer Institute (PSI), Villigen, Switzerland using the SANSII beamline. Three different types of samples were analyzed. Silicon wafers without coating and heat treated at a maximum sintering temperature of T_{max} of 730 °C served as a reference. The titania coatings on wafers in the modification of a NRL (w730NRL) and *RL* (w730*RL)* were furthermore applied (Table 4-5). Prior to analysis, the samples were cut with a diamond knife to each having a surface area of 1 cm^2. Ten samples of one kind were then stacked and placed into the sample holder. The neutron beam was directed normal to the surface of the stack in such a way that the illuminated area occupied a diameter of 8 mm. The applied wavelengths, which directed the length scales to be analyzed in the films, were 0.4549; 0.6369 and 1.9593 nm. They ensured the measurement of pore widths between 0-100 nm. The obtained scattering data were mathematically fitted to the Guinier approximation. The PSD was therefore deduced from a model, assuming dilute, spherical pores.

4.3.6.3   Stereology

Stereology is based on the observation of cross sections of the solid, recorded by optical or electron microscopy, and deducing the porosities [9, 10]. The cross sections of the NRL- coatings obtained by FIB milling were subjected to the porosity evaluation with the program LINCE, as was explained in Chapter 4.3.1 and Chapter 4.3.5. Instead of measuring the grain sizes, the amount of pores were evaluated from the linear intercepts with the so-called foreign phase, representing the voids.

4.3.6.4   Mercury intrusion porosimetry

The porosity of different film and bulk samples was measured by mercury intrusion porosimetry (MIP) with the low pressure unit Pascal 140 and the high pressure unit Pascal 440 series (Thermo Electron Corporation). To fill the samples into the glass capillary for the analyses, it was necessary to crush them to form fragments in the size of approximately 1 mm^2. The PSDs were deduced from the data by applying a cylindrical pore model. Samples were analyzed each in triplicates.

4.3.6.5   Nitrogen sorption porosimetry

Only b745 bulk samples were analyzed by nitrogen sorption porosimetry (NSP) with an ASAP 2010 from Micrometrics. Prior to analysis, the samples were crushed to form small

debris, which were filled into the analysis capillary. Subsequent drying for 1 h at 200 °C was followed by a second drying step for 16 h at 200 °C under vacuum. Data analysis was done using the Barret, Joyner and Halenda (BJH) model and taking into account multilayer adsorption in cylindrical pores.

4.3.7 Dilatometry

The dilatometer (802S, Bähr Thermoanalyse GmbH; Eidgenössische Technische Hochschule Zürich, Switzerland) used for the study of the sintering behavior of the TiO_2-nanoparticles was equipped with a quartz displacement bar and a sapphire reference. During the experiment, bulk samples were heated with a rate of 1 °C/min in argon atmosphere up to 1000 °C. The relative length change as a function of time and temperature was recorded.

4.4 Methods for the surface characterization of the thin films

4.4.1 X-ray photoelectron spectroscopy

The chemical composition of the TiO_2-films on wafer supports (w730NRL, w730*RL*) and on stainless steel supports (ss730NRL, ss730*RL*) was determined by X-ray photoelectron spectroscopy (XPS). Measurements were performed on an AXIS ULTRA instrument (Kratos) in ultra high vacuum with a monochromatic Al $K_{\alpha mono}$ radiation at 15.0 kV and 150 W. The survey scans were done in an energy range of 0-1100 eV with a pass energy of 80 eV and an acquisition time of 120 s. The binding energy was referenced to the C 1s photoelectron peak at 285.0 eV. Curve fitting and quantification were carried out using the processing software CasaXPS, V2.3.14 (Neal Fairley). The elements in the spectra were referenced on spectra found in literature [25] and in the XPS database of the National Institute of Standards and Technology (NIST) [26].

4.4.2 Contact angle measurements

The contact angles of the TiO_2-suspension with the wafer and the polished 316L stainless steel supports were determined by the sessile drop method on an OCA 35, Data Physics Instrument. Therefore 2 µl of suspension were pipetted manually on the surface of the sample. After 20 s a photo was taken and the contact angle automatically evaluated by the software SCA20. The same method was applied to measure the contact angles of the titania coatings w730NRL, w730*RL*, ss730NRL and ss730*RL* with water.

4.4.3   Roughness determinations

The mean roughnesses, R_a, of the samples w730NRL, w730*RL*, ss730NRL and ss730*RL* were measured by mechanical profilometry (Alpha Step 200, TENCOR INSTRUMENTS). For comparison, the topography of the specimen w730*NRL* was additionally measured by atomic force microscopy (AFM) on a CPII instrument (Veeco).

4.5   Results

4.5.1   Structure of the films on stainless steel supports

The SEM-micrographs of the top views of both, a titania non-reservoir layer (NRL) and a reservoir layer (*RL*), are shown in Figure 4-6. The sample ss730NRL, sintered at a maximum sintering temperature of 730 °C, exhibited slightly connected titania particles with some small agglomerates (sa) in the size of 300 nm (Figure 4-6 (b)). The TiO$_2$-grains had a mean grain diameter of approximately 100 nm. A high porosity, represented by the dark grey, interconnected voids, was observed. Big, white spots in Figure 4-6 (a) represent agglomerates of the nanoparticles in a size of 1 μm (ba). They were present as agglomerates in the titania suspension and were deposited during dip coating.
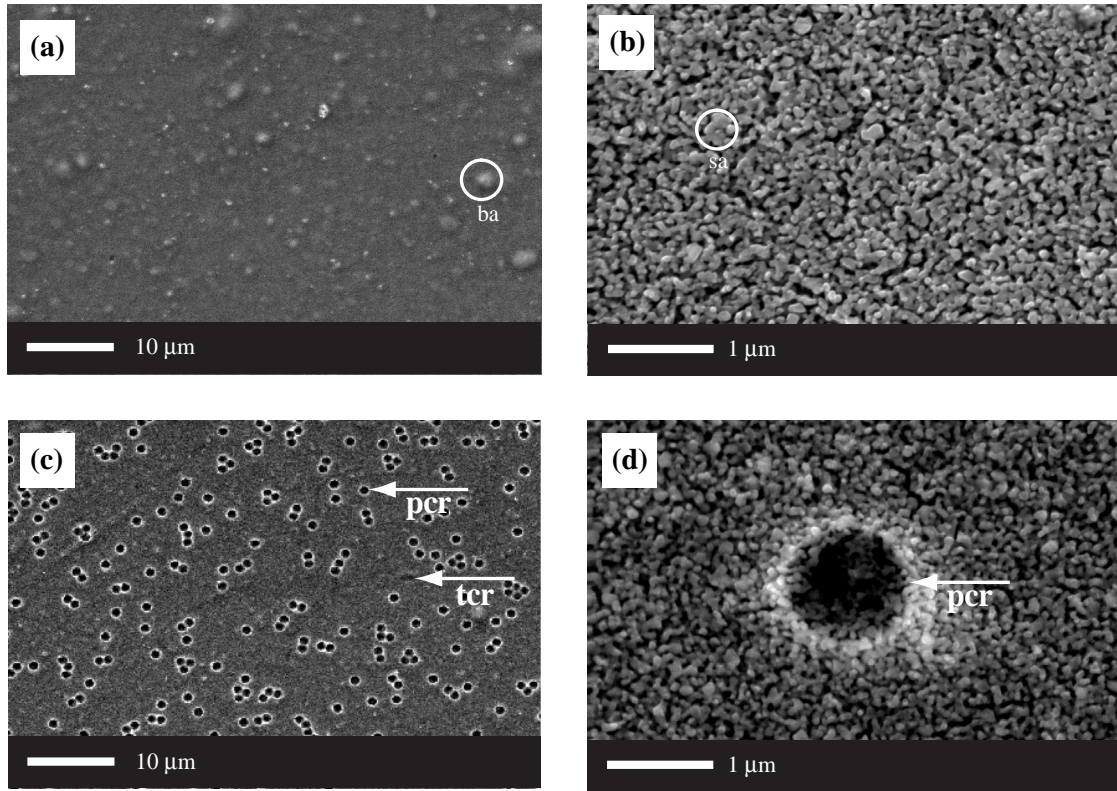
Figure 4-6 SEM-micrographs of the top views of (a), (b) the titania layer in the NRL-modification on a stainless steel support (ba: big agglomerate; sa: small agglomerate). (c) and (d) display the titania reservoir layer on a stainless steel support with partially closed reservoirs (pcr) and totally closed reservoirs (tcr).

The microstructures of ss730*RL* depicted in Figure 4-6 (c) and (d) show partially closed (pcr) and totally closed reservoirs (tcr), which exhibit a diameter of 1 µm. They were created by the burn of the spherical template particles and are surrounded by a porous structure, which is equal to the structure of a NRL. Whereas most of the reservoirs were well dispersed in the films, a few islands of arranged particles were present. They evolved from the agglomerate formation of the polymer beads during their deposition by dip coating. This could be could be visualized by optical microscopy, Figure 4-7. The density of microbeads was counted to be ~150000 beads/mm^2 geometric surface area.
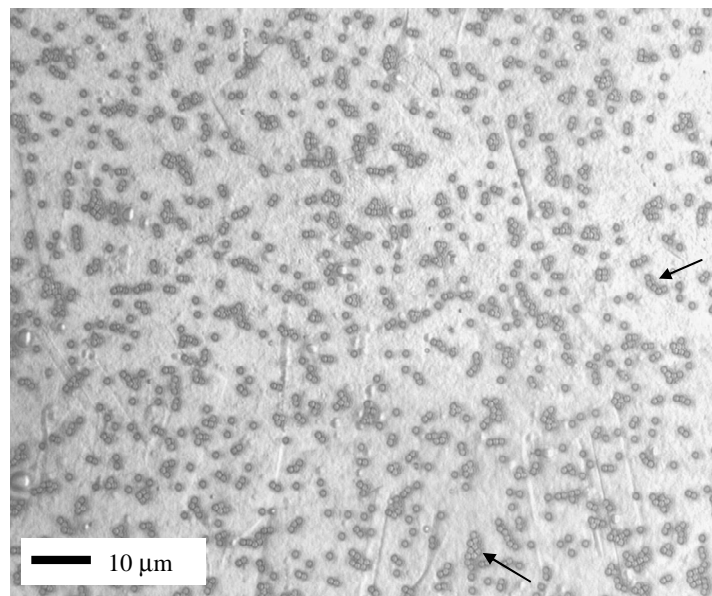
Figure 4-7 Optical micrograph of deposited microbeads-templates on a non-sintered reservoir layer. The black arrows indicate agglomerated microbeads.

Further analyses of the films on the steel supports turned out to be difficult. It was impossible to obtain cross sections of the specimens, revealing information about the 3D shape of the macropores, the TiO$_2$-grain sizes and the overall film thickness. But some parameters could be deduced by ellipsometry. The measured ellipsometric parameters, tan(ψ) and cos(Δ), were fit by a regression model to calculate the thickness of the films: 561.2 ± 5.5 nm, Figure A-2 in Appendix. However, the quality of the obtained mathematical fit was bad and was caused by the interference with signals from the rough, underlying SS support [18].

The anatase phase content of the thin films on stainless steel did not depend on their morphology NRL or *RL*. Thin film XRD revealed an anatase phase content of 73.93 ± 13.22 %wt and 77.87 ± 23.05 %wt of the coatings of the samples ss730NRL and ss730*RL*, respectively. The residual crystal phase was rutile, the high temperature stable form of TiO$_2$, Figure 4-8.
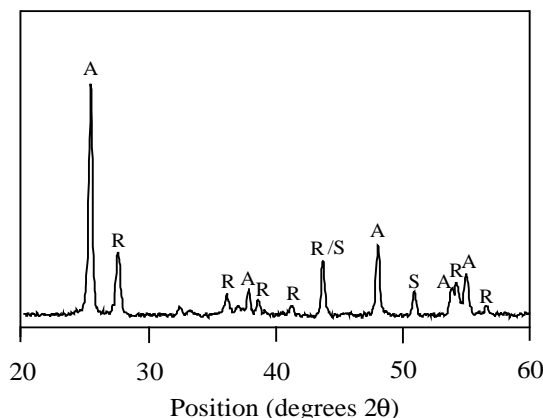
Figure 4-8 XRD-spectrum of a non-reservoir titania coating on a stainless steel support. A: anatase, R: rutile, S: background from the steel support.

One could deduce the theoretical densities of the films from the phase distributions: 3.97 ± 0.05 g/cm^3 for ss730NRL and 3.95 ± 0.09 g/cm^3 for ss730*RL*. It was not possible to determine the skeletal and Archimedes densities, as well as the BET-surface areas. The films could not be scratched off the supporting steel, which would have been necessary to perform the analyses. They adhered too strongly on the support. On one hand, a good adhesion of the coatings is beneficial for the application in stents. This issue is discussed in the thesis of A. Tourvieille de Labrouhe [27]. On the other hand, this made it difficult to acquire basic and important information about the coating's structure. The porosity could not be determined by mercury intrusion porosimetry (MIP) and nitrogen sorption porosimetry (NSP). Small angle neutron scattering (SANS), where the coating could have stayed on the support during analysis, was not performed of the titania films on steel. A high scattering from the steel itself would have overlapped the signal from the porous coating, making an evaluation of the PSD impossible [23].

Ellipsometric porosimetry (EP) revealed no exact answer of the porosity of ss730NRL. That the porosity was greater than 5.8 % was obtained from an incomplete adsorption isotherm using toluene, Figure 4-9. At a high relative pressure, no plateau of the refractive index and thus of the adsorbed volume was attained in the isotherm. Hence it was not possible to evaluate the PSD from the data. The SS supports were in the following replaced by silicon wafers to being able to exploit the film structures.

4.5.2   Structure of the films on silicon wafer supports

The micrographs of the top views of the TiO$_2$-films in a NRL- and *RL*-modification, which were produced on wafers and sintered with a maximum sintering temperature of 730 °C, are displayed in Figure 4-10. They look alike the ones of the coatings on the steel

supports. The NRL of the sample w730NRL in Figure 4-10 (a) and (b) exhibited a high concentration of interconnected, randomly oriented pores between the TiO_2-particles. The reservoir containing coating in Figure 4-10 (c) and (d), is characterized by randomly dispersed, partially closed (pcr) and totally closed reservoirs (tcr). They are embedded in a porous structure, which is equivalent to the one of the NRLs, having a high porosity.

(a)

(b)
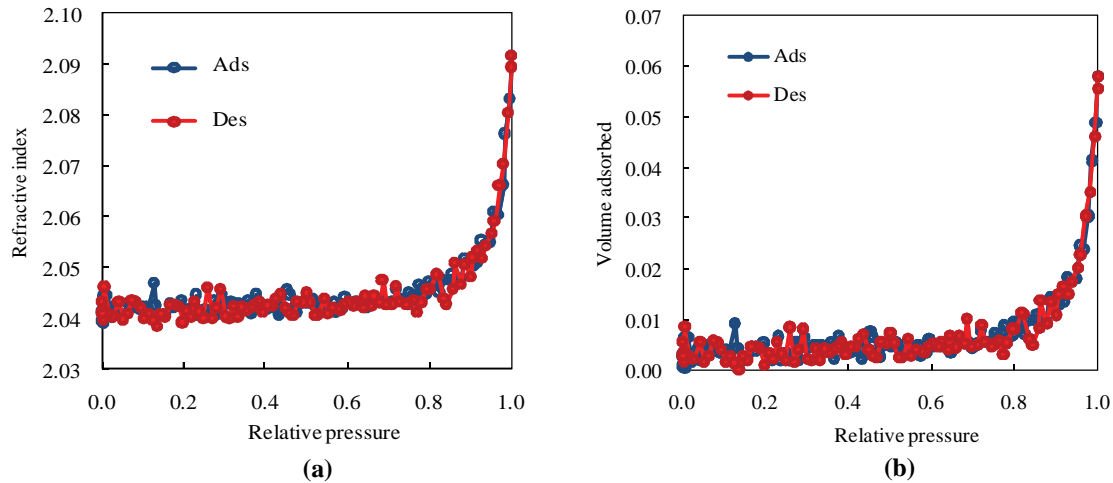
Figure 4-9 Isotherms as obtained from ellipsometric porosimetry. (a) refractive index isotherm and (b) volume adsorbed isotherm of a NRL on stainless steel ("Ads": adsorption; "Des": desorption) [18].
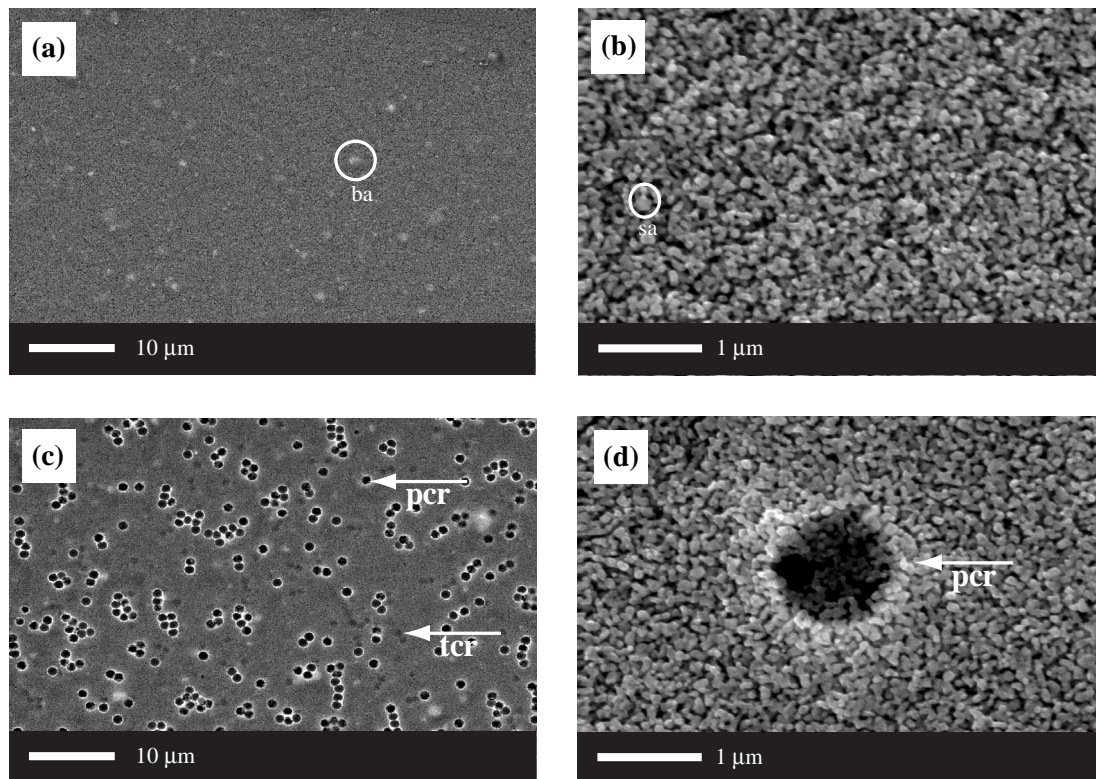
Figure 4-10 SEM-micrographs of the top views of (a), (b) the titania layer in the NRL-modification on a wafer support (ba: big agglomerate; sa: small agglomerate). (c) and (d) display the titania reservoir layer on a wafer support with partially closed reservoirs (pcr) and totally closed reservoirs (tcr).

The cross sections of the two thin TiO_2-films in the NRL- and *RL*-modifications are depicted in Figure 4-11. Both films exhibited the same thickness of 1.1 µm. This was in accordance with the thickness of w730NRL determined by ellipsometry: 1.25 µm. The recorded ellipsometric parameters, $\tan(\psi)$ and $\cos(\Delta)$, could be well fitted to a regression model to obtain the thickness of the coating (Figure A-3 in Appendix). No significant interferences of the signals from the support's roughness were observed.
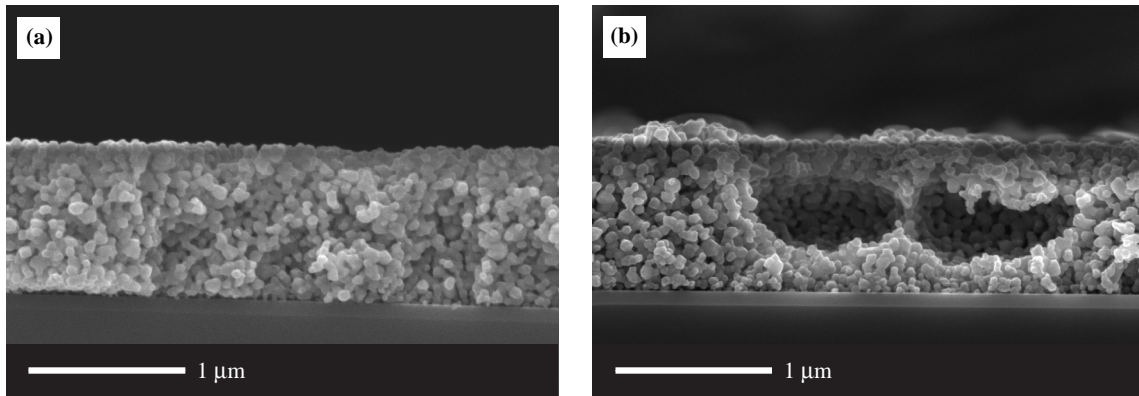
Figure 4-11 SEM-micrographs of the cross sections of the thin TiO_2-films created on wafer supports. (a) non-reservoir layer and (b) reservoir layer with totally closed drug reservoirs.

The ellipsoidal voids of w730*RL* in Figure 4-11 (b) were entirely surrounded by the porous NRL-structure. They exhibited the greatest elongation of 1 µm in the directions parallel to the support. They were half that size, 0.5 µm, in the thickness direction of the film. The distribution of the TiO_2-grain size was deduced from FIB-cross sections, Figure 4-12 (a). The median grain diameter of the number distribution, d_{N50}, was 75 ± 8 nm, the most frequent diameter, d_{mode}, 65 ± 10 nm and the mean diameter, d_{mean}, 87 ± 11 nm, Figure 4-12 (b). This result was in good agreement with the mean diameter calculated from specific surface area with Equation (4-2), d_{BET}, of 91.35 ± 5.52 nm, Table 4-6.
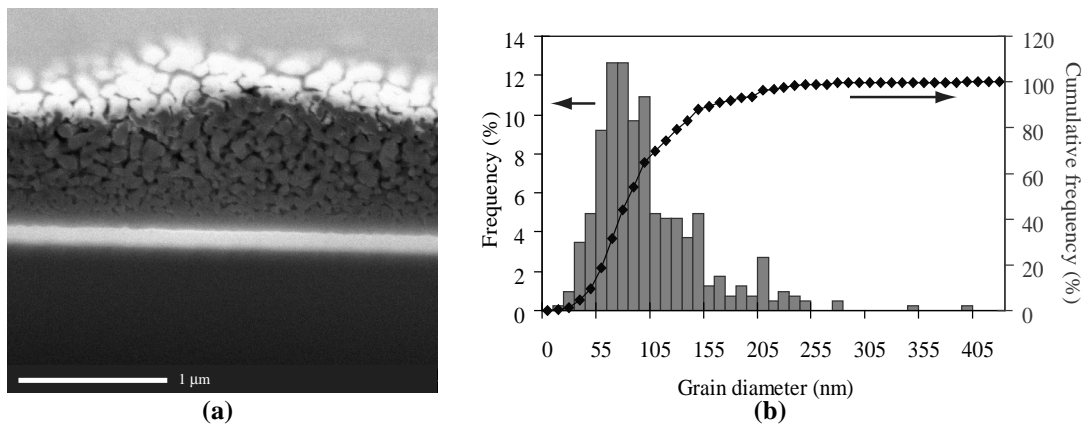
Figure 4-12 (a) SEM-micrograph of a non-reservoir layer on wafer support as obtained by FIB-milling for the grain size analysis. (b) number frequency distribution of the grain sizes in a non-reservoir TiO_2-coating, obtained by the analysis of the SEM-images after FIB milling.

Table 4-6 Characteristics of the TiO$_2$-films in the non-reservoir (NRL) and reservoir layer (*RL*) modifications. Films were sintered on silicon wafer supports, except f800NRL, which was sintered freely without support.

sample	S_{BET} (m^2/g)	d_{BET} (nm)	anatase (%wt)	ρ_{theo} (g/cm^3)	ρ_S (g/cm^3)
w730NRL	16.68 ± 1.07	91.35 ± 5.52	79.21 ± 6.86	3.95 ± 0.03	n.p.
w730*RL*	n.p.	n.p.	87.07 ± 2.04	3.92 ± 0.01	n.p.
w800NRL	10.82 ± 0.47	135.93 ± 6.55	41.13 ± 7.81	4.09 ± 0.03	3.58 ± 0.20
w800*RL*	n.p.	n.p.	56.6	4.03	n.p.
f800NRL	3.91 ± 0.34	365 ± 32.39	3.40 ± 1.35	4.23 ± 0.01	3.83 ± 0.06

n.p.: not possible to determine, because of a good adhesion or too small quantity of sample available.

Besides the characterization of the titania films, which were sintered at a maximum sintering temperature of 730 °C, films prepared at T$_{max}$ of 800 °C were also characterized for comparison. The structure of the NRLs sintered at 800 °C (w800NRL) is presented in Figure 4-13 (a). It featured a similar structure like w730NRL, comprising a high porosity and slightly connected TiO$_2$-particles. The mean grain diameter, d$_{BET}$, was bigger than the one of w730NRL: 135.93 ± 6.55 nm. The structure differed furthermore to the one of a film, which was scratched off the support prior to sintering at T$_{max}$ of 800 °C, f800NRL, in Figure 4-13 (b) and Table 4-6. f800NRL exhibited a 2.7 times greater d$_{BET}$: 365 ± 32.39 nm. A high porosity was still present in the freely sintered film.
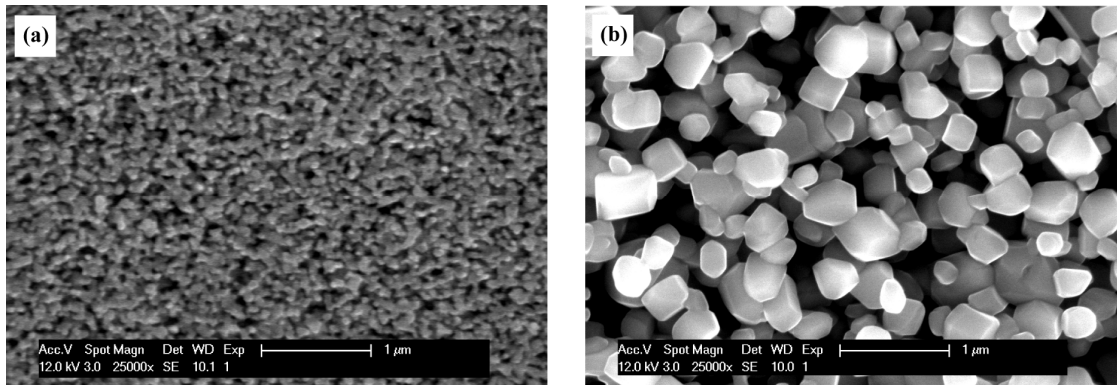
Figure 4-13 SEM-micrographs of (a) a top view of the titania coating sintered at 800 °C on wafer support and (b) of a NRL, which was sintered without the presence of the support at 800 °C.

It was demonstrated that the presence of the support during the heat treatment of the films has constrained the sintering of the films. This was furthermore reflected by the distribution of the crystal phases, anatase and rutile, in the coatings. The NRLs on wafers comprised an anatase content of 41.13 %wt after the consolidation, whereas the same film sintered without the presence of the support material had a residual amount of anatase left, Table 4-6 and Figure 4-14.
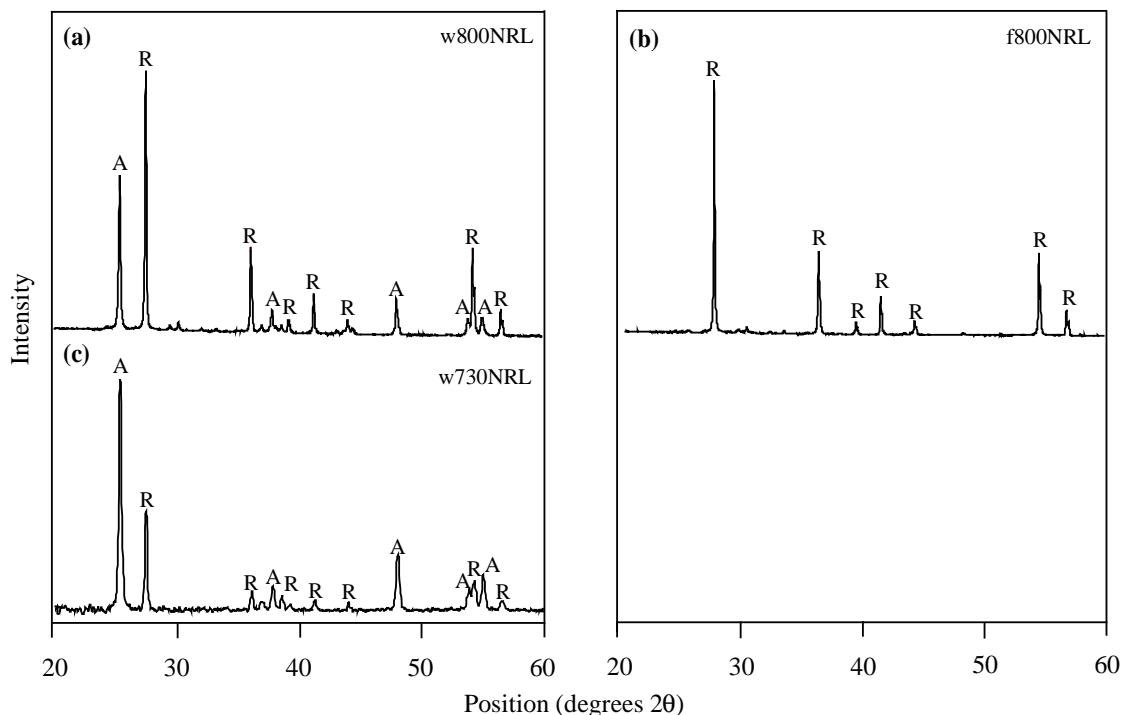
Figure 4-14 XRD spectra of the TiO_2-films (a) sintered on a wafer support at the maximum sintering temperature (T_{max}) of 800 °C, (b) sintered freely at T_{max} = 800 °C and (c) sintered on a wafer support at T_{max} = 730 °C. A: anatase, R: rutile.

The densification in the films, which were sintered at the same T_{max} of 800 °C, had progressed more in the freely sintered coating f800NRL compared to the one with the underlying support. This was verified by their densities. The theoretical and skeletal densities, ρ_{theo} and ρ_S, were both higher for f800NRL than for w800NRL, Table 4-6. It was impossible to determine the bulk densities of these samples by the Archimedes method. The films were either attached on the support or present as crushed fragments after their detachment from the support. For determining the bulk density by the Archimedes method, the specimens have to exhibit a block-shape.

The presence of the reservoirs in the coating w800*RL*, heat treated at T_{max} = 800 °C, created a slightly higher anatase content of 57 %wt compared to the NRL, Table 4-6. The same tendency was apparent for the samples sintered at 730 °C: 79 %wt vs. 87 %wt for w730NRL and w730*RL*, respectively.

To determine the porosity of the thin films, ellipsometric porosimetry (EP), small angle neutron scattering porosimetry (SANS) and mercury intrusion porosimetry (MIP) were chosen. The adsorption isotherms from the EP measurement of the sample w730NRL were deduced from the ellipsometric parameters, which are displayed in Figure A-3, Appendix. The isotherms reached no plateau at the high partial pressure domain, Figure 4-15 (a), (b).

The adsorption of toluene in the pores of the NRL-structure was incomplete. Hence the porosity of the sample could not be determined exactly. But it was estimated to be > 34.4 %. The pore size distribution (PSD) could not be accurately evaluated due to the incomplete adsorption, but the smallest pores in the coating had a width of 40 nm, Figure 4-15 (c).
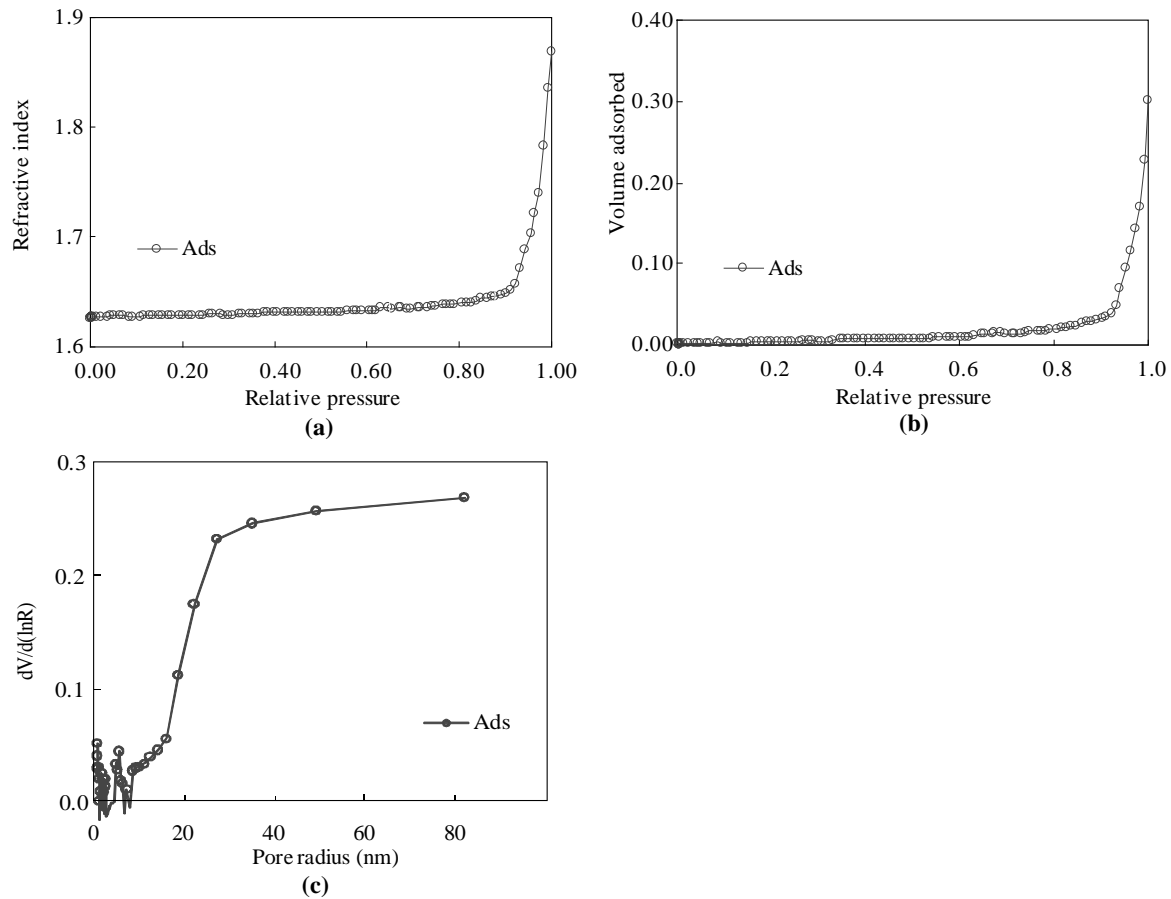
Figure 4-15 Graphs recorded during ellipsometric porosimetry. (a) the refractive index isotherm, (b) the volume adsorbed isotherm and (c) the pore size distribution of the TiO_2-non-reservoir layer on wafer, ("Ads": adsorption) [18].

The scattering intensity curves obtained by the SANS-porosimetry of the w730NRL and w730*RL* coatings are depicted in Figure 4-16. They could be fitted to a mathematical model, which describes the scattering intensity as a function of spherical voids in-between dilute particles. Applying this model was favorable, because the titania particles had a spherical shape and they were slightly connected, as was observed in the SEM-micrographs (Figure 4-10, Figure 4-11). The voids in between the grains represented the inverse of the TiO_2 and hence were assumed to be spherical.
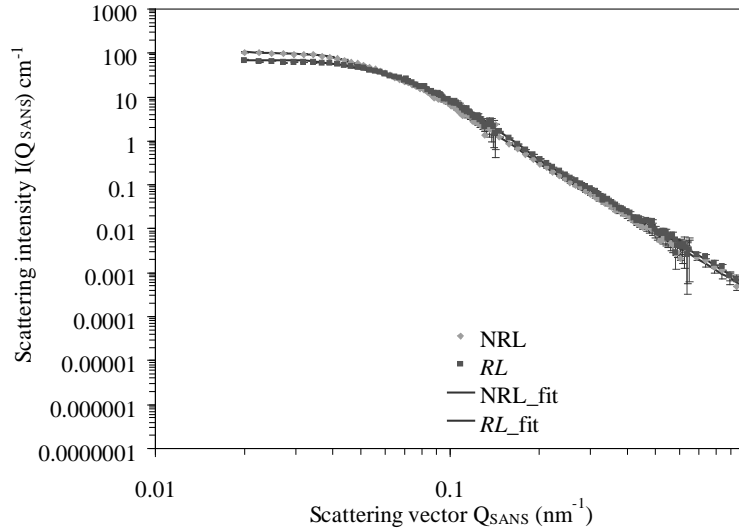
Figure 4-16 Scattering intensity curves of the TiO_2-coatings in the non-reservoir layer (NRL) and reservoir layer (*RL*) modifications on wafers and sintered at a maximum temperature of 730 °C, as obtained in the small angle neutron scattering (SANS) measurements. Represented are the measured data and their mathematical fits as a function of the scattering vector.

The PSDs of the NRLs and *RL*s on wafers could be deduced from the scattering curves, Figure 4-17 and Table 4-7. The pore sizes of the NRL ranged from 20-100 nm, whereas the median pore diameter, d_{v50}, was 45.21 nm. The *RL* was characterized by a broader pore size distribution of 17-200 nm and a d_{v50} of 60.39 nm.
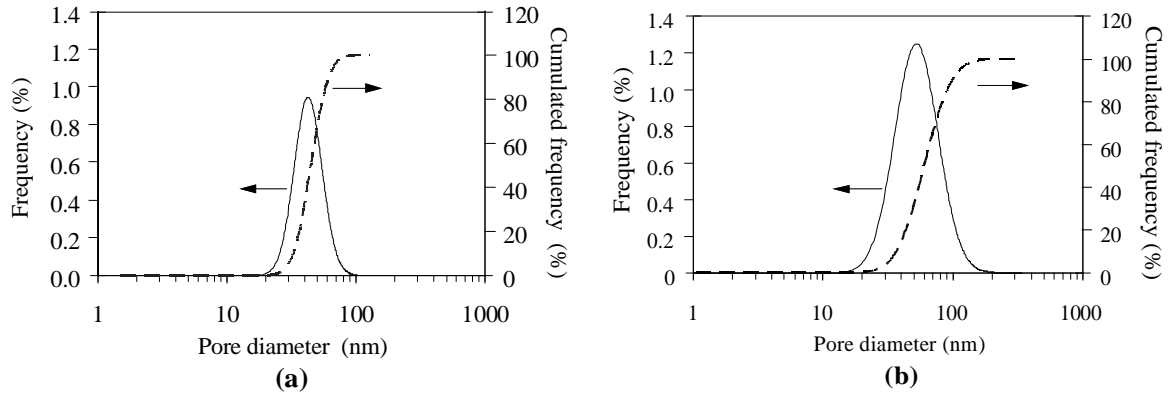
Figure 4-17 Pore size distributions of (a) the non-reservoir titania layer and (b) the TiO_2-reservoir layer on wafer supports, as obtained from the small angle neutron scattering porosimetry.

Table 4-7 Median pore diameters, d_{v50}, and most frequent pore diameters, d_{mode}, of several coatings, as measured by small angle neutron scattering (SANS), stereology and mercury intrusion porosimetry (MIP). Values were obtained in two different pore width regimes for MIP: (1) 0-100 or (2) 0-1000 nm.

sample	*method*	*range of pore diameters (nm)*	d_{v50} *(nm)*	d_{mode} *(nm)*	*porosity (%)*
w730NRL	SANS	0-100	45.21	44.11	-
w730*RL*	SANS	0-100	60.39	53.45	-
w730NRL	stereology	-	-	-	22.83 ± 6.78
w730NRL	MIP	0 – 1000	82.70	87.37	64.45
	MIP	0 - 100	76.34	87.37	41.91
w800NRL	MIP	0 – 1000	138.31 ± 15.11	180.68 ± 7.04	55.04 ± 8.19
	MIP	0 - 100	67.42 ± 4.15	95.69 ± 7.47	16.07 ± 2.33

The porosity obtained by stereology of w730NRL, in which SEM-micrographs of cross sections were evaluated by image analysis, was 22.83 %, Table 4-7. The recorded pore size distributions of w730NRL and w800NRL by MIP were bimodal, such as displayed in Figure 4-18. One peak was detected for all film specimens at pore diameters below 1000 nm and a second one above that value.
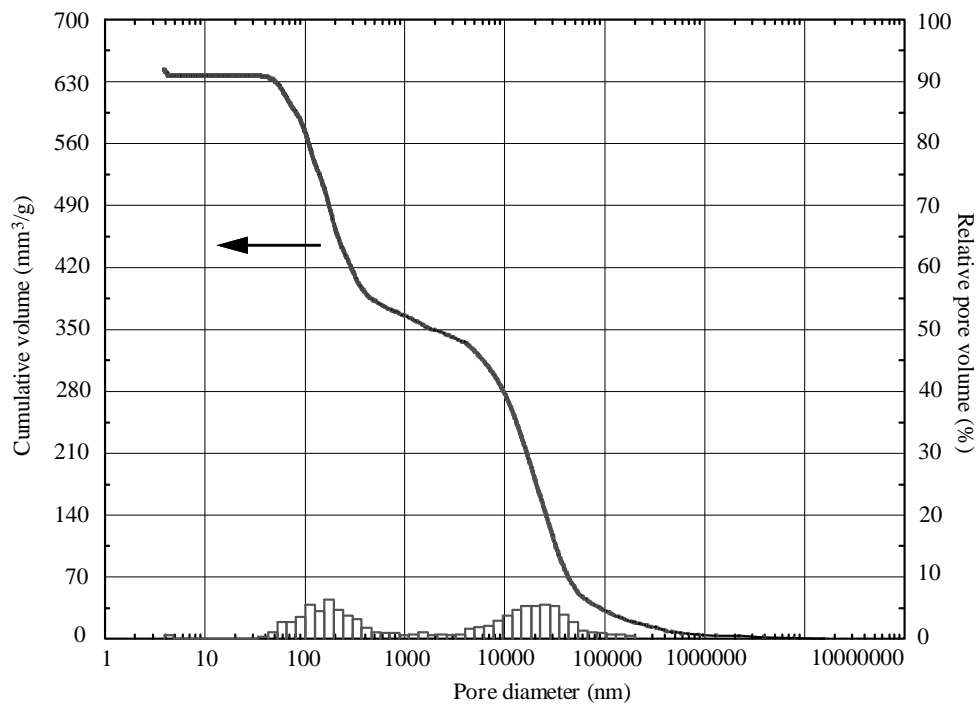
Figure 4-18 Graph of the bimodal pore size distribution of a non-reservoir titania layer, sintered with a maximum temperature of 800 °C, as obtained by mercury intrusion porosimetry.

The pore diameters in the region greater than 1000 nm were excluded from the PSD evaluation, because they were caused by an artifact. The films had to be scratched off the support prior to analysis and were given as a powder with unequal film fragments into the pressure capillary for MIP-analysis. The application of pressurized mercury caused the

compactation of the loosely packed fragments of the coatings at the beginning of the analysis and the filling of the inter-fragment voids. This generated the presence of the bigger pores in the PSD. The cut off pore diameter of 1000 nm for the analysis was chosen, because the coatings had a thickness of 1.2 µm and the pores could not exceed this length. This was furthermore validated by the SEM-images of the NRL in Figure 4-11 (a), where no continuous pores through the whole coating were visible.

The pore diameters of w730NRL in the PSD depicted in Figure 4-19 (a) extended from a few nanometers up to 250 nm. The coating was hence composed of mesopores, having pore widths of 2-50 nm, and macropores, with pores greater than 50 nm. The median pore diameter from the volume distribution, d_{v50}, of pores in the range of 0-1000 nm was 82.70 nm. The one of the smaller interval (0-100 nm pore diameter) was 76.34 nm, Table 4-7. The characteristic pore diameters in the range up to 100 nm were calculated to being able to compare them with the ones deduced by SANS. Because the maximum pore diameter, which could be detected by SANS, was ~100 nm.
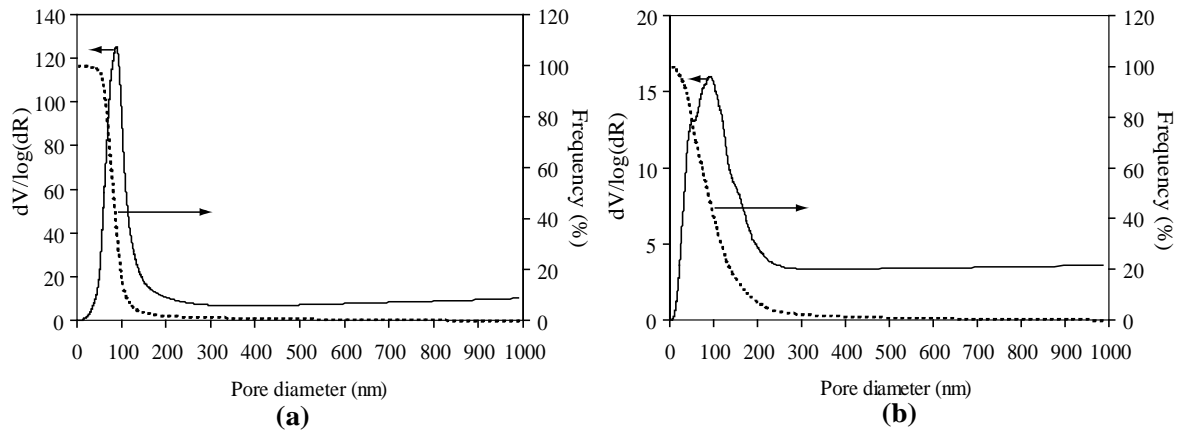
Figure 4-19 Pore size distributions of the non-reservoir layers sintered at a maximum temperature of (a) 730 °C and (b) 800 °C. Measurements were performed by mercury intrusion porosimetry.

The pore size distribution of the NRL, which was heat treated at 800 °C (w800NRL), in Figure 4-19 (b) was in the same range like the one of w730NRL, but not as narrow. In the pore diameter regime up to 1000 nm the d_{v50} was 138.31 nm, in the interval up to 100 nm, d_{v50} was 67.42 nm. The porosities of the coatings were not computed by the MIP software. Values, which were automatically calculated from the MIP-run, like the specific surface area and the density, were invalid. They included data points from the big pore sizes (> 1000 nm), which were artifacts due to the sample preparation. Hence the porosities for both types of NRLs were calculated from the density of a cylindrical bulk, representative for the coating, and from the pore volume measured up to the critical pore diameters of either 100 or 1000 nm. The density of the cylindrical bulk was 2.05 g/cm^3 (c.f. following chapter). The

cylindrical bulk was prepared by slip casting and sintered at a maximum sintering temperature of 740 °C (b740). A porosity of 64 % for w730NRL and of 55 % for w800NRL in the interval of 0-1000 nm was obtained, Table 4-7. The porosity in the smaller regime was accordingly lower: 42 and 16 %, respectively.

In all previously mentioned pore size evaluations NRL-modifications of the TiO_2-films were used except in SANS porosimetry. But SANS did not deliver the PSD of the reservoirs, because their size exceeded the maximum scattering length of 100 nm. The reservoirs in the MIP measurements were destroyed during the detachment of the films from the supports and thus delivered false results. To get an estimation, how the presence of the reservoirs in a certain density and size could influence the overall porosity of the titania films, calculations with the parameters listed in Table 4-8 were carried out. The values of the parameters are based on the porosity measurements performed on the NRLs and on the SEM-micrographs of cross sections of *RL*s, Figure 4-11. The reservoir size factors represent the ratio of the reservoir size after heat treatment in a certain direction, to the size of the initial spherical templates of 1 µm. The thickness of the nanoporous layer represents the distance between the upper edge of the reservoir to the top of the coating's surface, Figure 1-5. The base layer corresponds to the span between the lower edge of the reservoir to the surface of the support.

Table 4-8 Parameters used for the calculation of the total film porosity as a function of reservoir size and density.

entry values	
porous volume fraction	50 %
reservoir size factor after shrinkage, x direction	88 %
reservoir size factor after shrinkage, y direction	59 %
nanoporous layer thickness	0.329 µm
base layer thickness	0.250 µm

The results of the calculation are depicted in Figure 4-20. A higher reservoir density results in a higher total porosity of the film, Figure 4-20 (a). However, a lower density of bigger reservoirs significantly increases the porosity of the layers. This is moreover demonstrated in Figure 4-20 (b), where the ratio of the pore volume occupied *only* by the reservoirs to the total pore volume is plotted as a function of reservoir density. A *RL* with a reservoir width of 1 µm and a density of 150000 reservoirs/mm^2, which is the specification of the fabricated *RL*s in the present study, contains theoretically 3 % more porosity than the NRL. By increasing the size of the reservoirs to 2 µm and keeping the same reservoir density, the *RL*s occupy 16 % more pore volume than the NRLs. When increasing the reservoir width further, a lower macropore density can create high porosities. The overall porosity is then strongly influenced by the increase in layer thickness and consequently by the porosity of the porous structure surrounding the reservoirs.
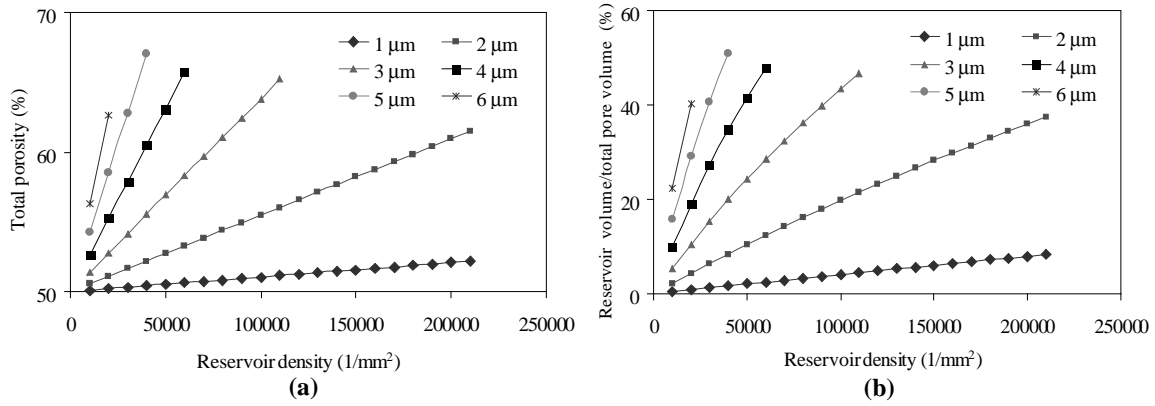
Figure 4-20 (a) total porosity of the TiO$_2$-films as a function of reservoir density and size. (b) Volume occupied by the reservoirs referenced to the total pore volume and as a function of reservoir density and size.

4.5.3   *Sintering behavior and structure of the bulks*

For understanding the sintering behavior of the TiO$_2$-nanoparticles in a bulk green compact, *in situ* X-ray diffraction (XRD) and dilatometry measurements were conducted. The XRD spectra in Figure 4-21, recorded during the sintering of a slip cast bulk cylinder, show the progress of the phase transition from anatase (A) to rutile (R) during the heat treatment. Until the end of the first temperature plateau of 500 °C, no initiation of the phase transformation was present. The crystal phase was anatase. The phase transition started at the second heating interval from 500 up to 800 °C. The amount of anatase present before the plateau at a maximum sintering temperature, T_{max}, of 800 °C of 56.2 %wt diminished until the end of the plateau to a value of 15.9 %wt. After the cooling to room temperature, rutile and a negligible amount of anatase (3.8 %wt) were remaining.
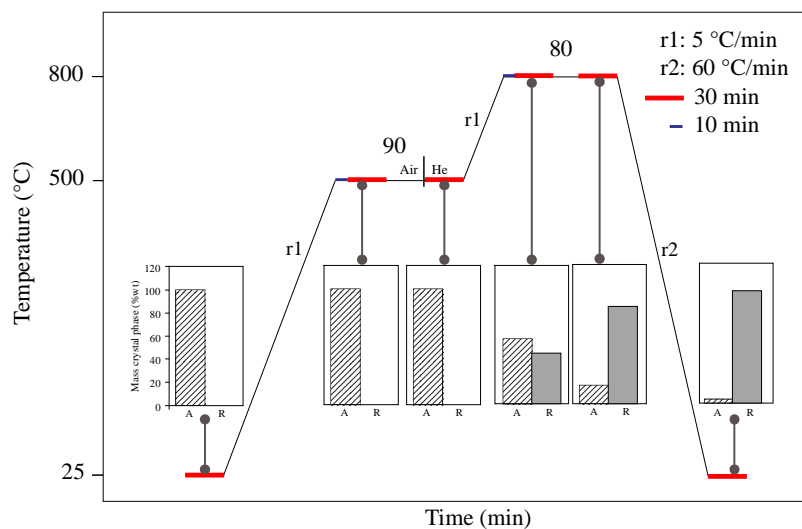
Figure 4-21 *In situ* XRD measurements of a bulk TiO$_2$-sample. The progress of the phase transformation from A: anatase to R: rutile as a function of temperature profile is illustrated (r1, r2: heating/cooling rate).

These findings were compared with the result from the dilatometry run of a cylindrical bulk TiO$_2$-specimen, Figure 4-22. The fist graph shows the relative change in length as a function of increasing temperature. Several rapid changes in length were observed and could be pointed out in more detail in the graph of the sintering rate, Figure 4-22 (b). By increasing the temperature from 23 °C to 500 °C, a slow, steady decrease in length of the bulk sample and changes in the sintering rate were recorded. This observation could be correlated to the evaporation of residual water from the specimen and to a re-orientation of the titania particles. Subsequently the shrinking rate slowed down until it increased at 780 °C, representing the phase transition from anatase to rutile, as was also detected by *in situ* XRD. From a temperature greater than 860 °C, the shrinkage rate augmented and reached its maximum of 7.1 µm/min at 1007 °C. The densification was taking place in that temperature regime.

In the following, TiO$_2$-bulks were to be prepared exhibiting identical properties like the thin NRLs on wafers. They were to be used for porosity and PSD determinations by MIP and NSP, representing the features of the films. Because the standardized measurements with the NRL-material were too elaborate: 10 coated wafers of a diameter of 12 cm had to be prepared for one measurement. The bulks, of which a high quantity could easily be prepared by slip casting, were hence favorable. *In situ* XRD and dilatometry limited the range of the maximum sintering temperature of the bulks to $700 < T_{max} < 800$ °C to yield anatase and rutile simultaneously in the bulks. Additionally this temperature range was in the focus of interest to study the mechanical properties of the coating, cf. Thesis A. Tourvieille de Labrouhe [14].
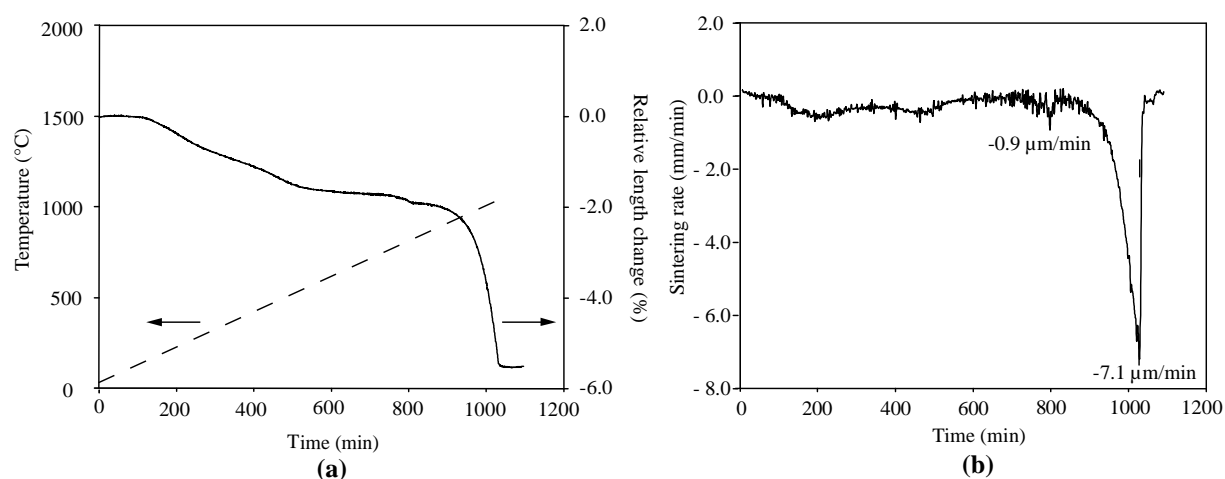
Figure 4-22 Dilatometry of a bulk TiO$_2$-sample in the NRL-modification. In (a) the relative change in length as function of time and temperature and in (b) the sintering rate are presented.

In a first step, the bulk samples produced by slip casting and sintered with T_{max} of

800 °C (b800) were characterized. The microstructure of b800 in Figure 4-23 looks alike the one of the freely sintered film (f800NRL), Figure 4-13 (b). The grains in the specimen were as big as 700 nm or much smaller. The mean grain size, d_{BET}, obtained from the specific surface area was 356 nm and was equal to the one of f800NRL, Table 4-6. Only rutile was present in b800. The theoretical density was accordingly 4.24 g/cm^3. Its skeletal density measured by pycnometry was 3.96 g/cm^3.
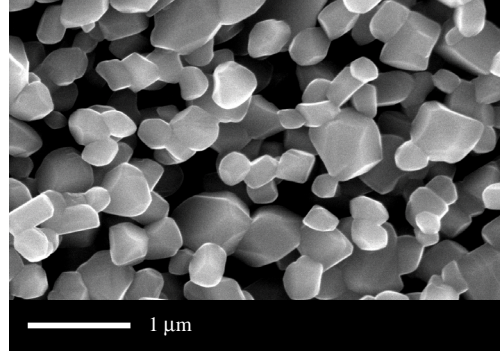
Figure 4-23 SEM-micrograph of the bulk TiO$_2$ sintered at a maximum temperature of 800 °C.

The dependence of the maximum sintering temperature of the bulks on their structural parameters is demonstrated in Figure 4-24. The grain size d_{BET} increased with augmenting T_{max} from smaller than 100 nm at 740 °C up to 360 nm at 770 °C. The shape of the curve of the anatase phase content was inversely. 70 %wt anatase were measured for the specimens sintered at 700 °C. With increasing T_{max}, the content decreased and only rutile was present in the bulks sintered at T_{max} of 800 °C. High standard deviations were recorded for the phase content in the temperature range of 700 to 750 °C. The grain size d_{BET} of the sample b750 exhibited a high standard deviation. But lower ones were recorded for the specimens sintered at T_{max} lower than 750 °C or higher than 770 °C. Hence the high standard deviations could be attributed to the region of the phase transformation of TiO$_2$.
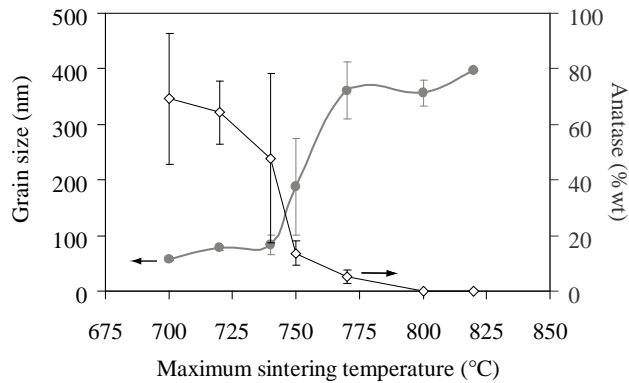
Figure 4-24 Grain size evaluation and anatase phase content of TiO$_2$-bulks with a NRL-structure as a function of maximum sintering temperature.

The porosities of the bulk samples could be deduced from their densities according to the formulas

$$total-porosity = 100 - \left(\frac{\rho_{Arch}}{\rho_{theo}} \cdot 100 \right)$$ (4-8),

$$closed-porosity = 100 - \left(\frac{\rho_S}{\rho_{theo}} \cdot 100 \right)$$ (4-9),

with ρ_{Arch}: Archimedes density, ρ_{theo}: theoretical density and ρ_S: skeletal density of the porous bulks. The total porosity of the sintered bulk samples of 50 % does not change significantly in the temperature interval of 700-800 °C, Figure 4-25. A slight decrease was recorded for the specimens sintered at 820 °C. The open porosity of 42 % stayed constant for the bulks in the whole temperature range of interest.
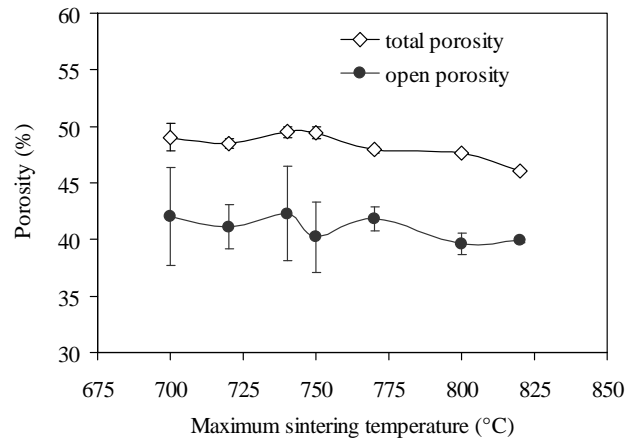
Figure 4-25 Total and open porosities of the bulk TiO_2-samples, as was calculated from their densities.

The following aim was to produce a high quantity of bulk material with identical properties like the NRLs, sintered on wafer with a maximum temperature of 730 °C (w730NRL) to perform porosimetry measurements. The knowledge of the sintering behavior of the TiO_2-bulks helped to select the production parameters of the bulks, which are to represent the NRLs. The specific surface area was the criteria chosen to select the equivalent bulks, because it is linked to the grain size and the phase composition. It was alike for the films w730NRL and the bulks b740, as depicted in Table 4-9. The bulk material calcined at 740 °C was hence used to measure the pore size distribution by MIP.

Table 4-9 Specific surface areas, S_{BET}, of the TiO$_2$-films on wafer supports and of the TiO$_2$-bulk samples, which hold equivalent properties.

sample	maximum sintering temperature (°C)	S_{BET} (g/m^2)
w730NRL	730	16.68 ± 1.07
b740	740	18.11 ± 3.72

A representative graph of the bimodal PSD of b740 obtained by MIP is pointed out in Figure 4-26. One peak of the volume distribution was detected below 100 nm, a second one above that value. The results of the three replicas are summarized in Table 4-10. Two pore diameter ranges were again accounted for in the evaluation: (1) 0-1000 nm and (2) 0-100 nm. They were selected to being able to compare the results with the ones of the films, which were measured by SANS and MIP. The pore widths exceeding 1000 nm are again excluded from the interpretation, because they represent artifacts in the PSD related to the compression of sample fragments. The median pore width, d_{v50}, of two replicas of b740 in the range of 0-1000 nm was 50 nm, whereas for the third one 270 nm was measured. The total pore volume of the first two replicas was predominated by the pores below 100 nm. The smaller pores below 100 nm occupied more pore volume in the third analogue. However, the total porosity of all replicas in the pore size interval up to 1000 nm was 47.10 ± 7.63 %.
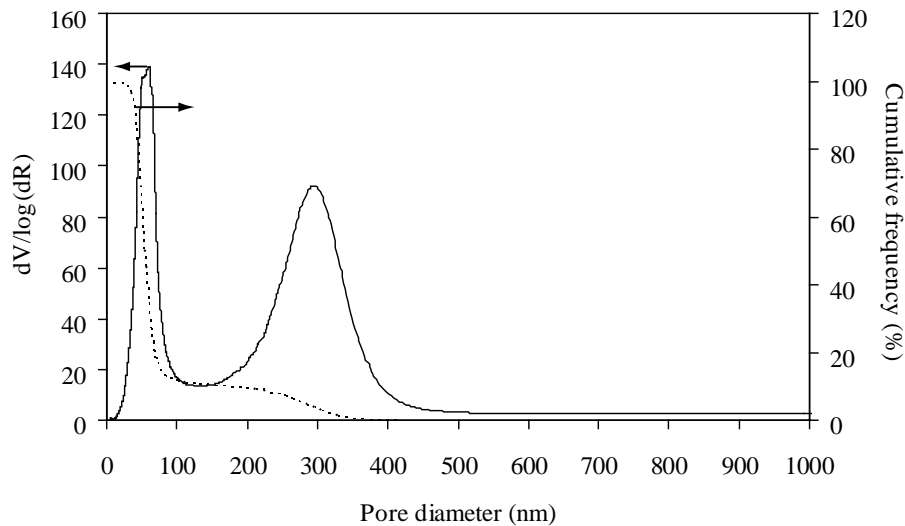
Figure 4-26 Pore size distribution of the TiO$_2$-bulks sintered at a maximum sintering temperature of 740 °C, as obtained by mercury intrusion porosimetry.

Table 4-10 Pore sizes and porosities as obtained by mercury intrusion (MIP) and nitrogen sorption porosimetry (NSP) of the bulk TiO$_2$-specimens sintered with a maximum temperature of 740 °C (d$_{v50}$: median pore diameter, d$_{mode1,2}$: most frequent pore diameter 1, 2).

sample	*method*	*range of pore diameters (nm)*	*d$_{v50}$ (nm)*	*d$_{mode1}$ (nm)*	*d$_{mode2}$ (nm)*	*porosity (%)*
b740_1	MIP	0-1000	45.61	43.97	290.52	50.45
		0-100	45.54	43.97	-	40.67
b740_2	MIP	0-1000	55.67	58.18	289.51	51.70
		0-100	53.79	58.18	-	28.32
b740-3	MIP	0-1000	271.47	47.16	271.47	52.52
		0-100	52.67	47.16	-	3.04
b740-1	NSP	0-100	59.47	52.10	-	38.86
b740-2	NSP	0-100	49.59	30.26	-	27.03
b740-3	NSP	0-100	65.90	28.77	-	8.64

The PSD of b740 was additionally measured by nitrogen sorption porosimetry (NSP) for comparison. The results are displayed in Table 4-10 and in Figure 4-27. The monomodal distribution exhibited a median pore diameter, d$_{v50}$, of 58.32 ± 8.21 nm. The porosity, deduced from the pore volume with pore diameters up to 100 nm, was 30 % for two of the replicas and as small as 9 % for the third specimen. In addition to the characterization of the intrinsic structure of the films and bulks, the surface properties of the coatings were analyzed.
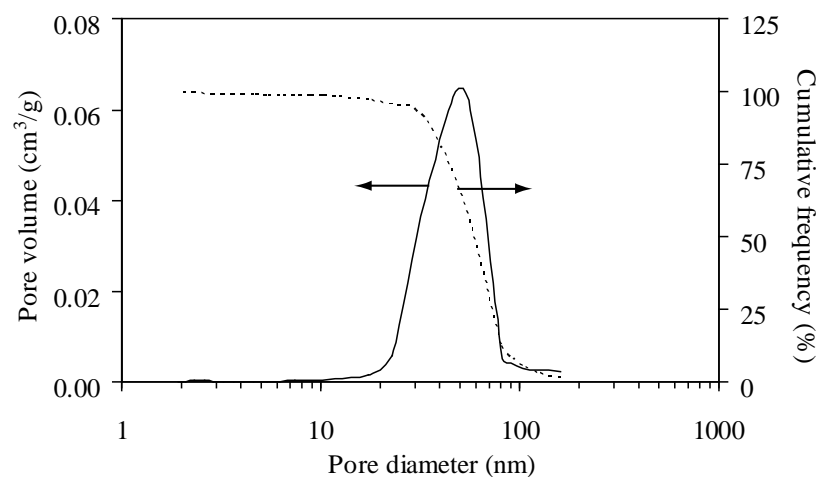
Figure 4-27 Pore size distribution of the TiO$_2$-bulk, sintered at a maximum temperature of 740 °C, as measured by nitrogen sorption porosimetry.

4.5.4   *Surface characterization of the thin films*

The findings of the chemical analysis of the TiO$_2$-coated stainless steel (SS) by X-ray photoelectron spectroscopy (XPS) are displayed in Figure 4-28. The intensity of emitted

photoelectrons from the sample as a function of their binding energy was recorded. The peaks labeled are consistent with the characteristic peaks of the electron configuration of the electrons within the specific atoms, e.g., O 1s or Ti 2p. The number of detected electrons in each of the characteristic peaks is directly related to the amount of element within the volume irradiated. The spectra of the NRL and *RL* featured peaks corresponding to titanium (Ti), oxygen (O), carbon (C) and nitrogen (N). Vanishing small peaks of chromium (Cr) and iron (Fe) were also detected. The following deconvolution of the peaks revealed that Ti is present in the coating as stoichiometric TiO_2. Cr and Fe were bound as metal oxides and were present as trace amounts. C and N were contaminations on the coating.
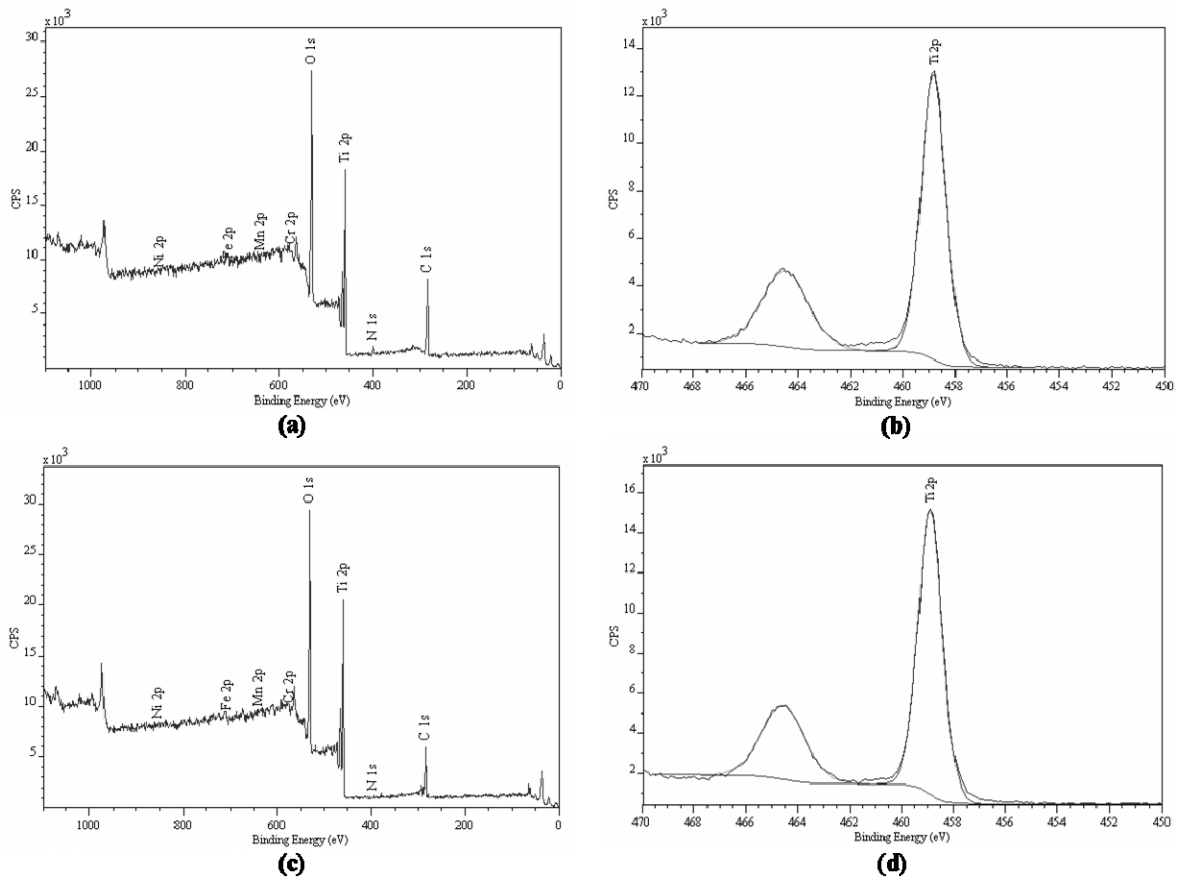
Figure 4-28 (a) X-ray photoelectron spectra of the TiO_2 thin films on stainless steel supports in the non-reservoir modification and sintered at a maximum temperature of 730 °C (ss730NRL), (b) the corresponding deconvolution of the Ti-peak. In (c), the spectra of the reservoir layer ss730*RL* and in (d) the deconvolution of the Ti-peak are represented.

The XPS spectra of the titania coatings calcined on the wafer support are depicted in Figure 4-29. The coating consisted of stoichiometric TiO_2, oxygen and carbon. The latter was contamination on the coating's surface.
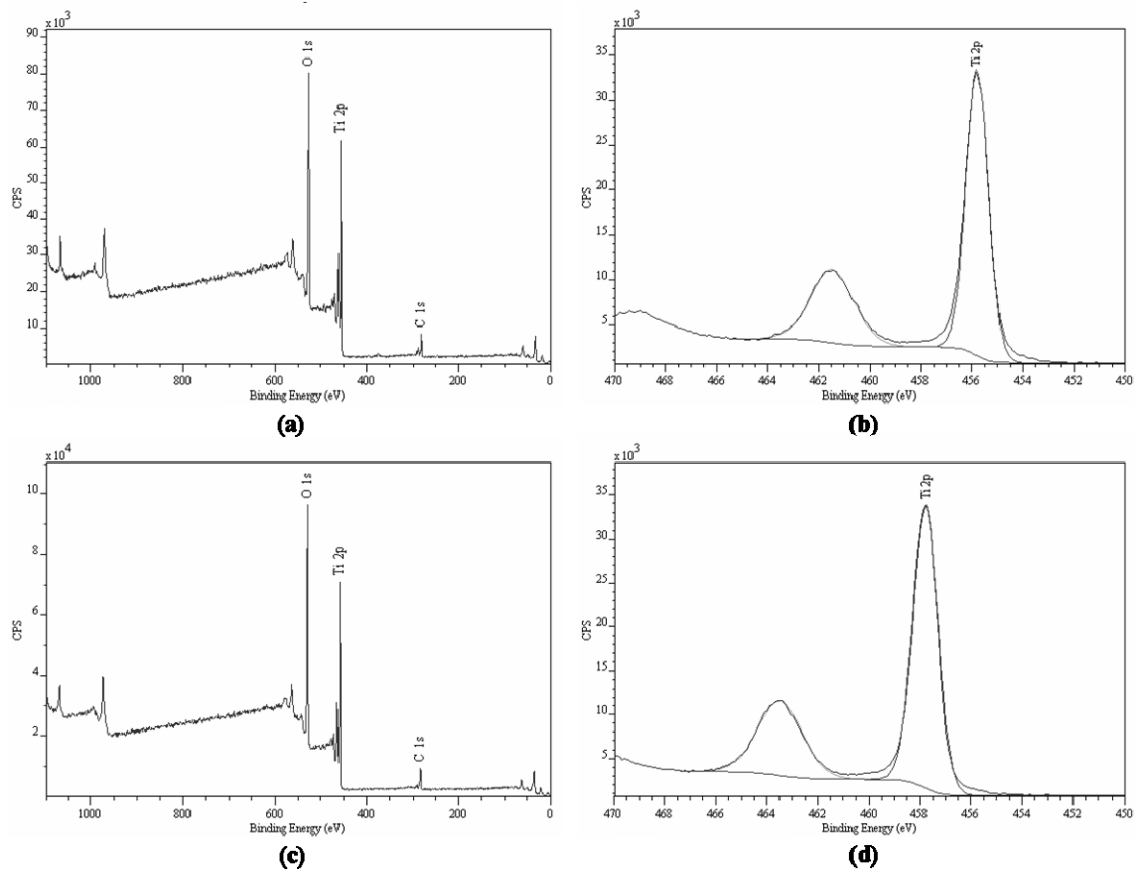
Figure 4-29 (a) X-ray photoelectron spectra of the TiO_2 thin films on wafer supports in the non-reservoir modification and sintered at a maximum temperature of 730 °C (w730NRL), (b) the corresponding deconvolution of the Ti-peak. In (c), the spectra of the reservoir layer w730*RL* and in (d) the deconvolution of the Ti-peak are represented.

The arithmetic mean roughnesses, R_a, of various titania coatings and of the supports are listed in Table 4-11. The coatings on SS exhibited a R_a of 76.38 nm and 54.13 nm for the NRL (ss730NRL) and the *RL* (ss730*RL*) modification, respectively. The roughness of the NRL on the wafer support was 16.70 nm and for the *RL* 25.30 nm. A mean roughness R_a of 22.74 nm of w730NRL was additionally deduced from AFM-microtopography, Figure 4-30. The roughness of the support materials influenced the coating's roughness. Whilst the wafer with R_a smaller than 5 nm had less impact on the film's roughness, the stainless steel support with R_a of 75.25 nm gave distinction to the topography of the titania coating in the sample ss730NRL, Table 4-11.

Table 4-11 Mean roughnesses, R_a, of the TiO_2-coatings on wafers and stainless steel, as well as of the supports. Contact angles, θ_c, of the coatings with water and of the supports with the TiO_2-suspension TP1.

sample	ss730NRL	ss730RL	w730NRL	w730RL	wafer	stainless steel
R_a (nm)	76.38 ± 5.19	54.13 ± 6.54	16.70 ± 1.96	25.30 ± 4.28	< 5	75.25 ± 19.19
θ_c (°), water	45.33 ± 22.70	53.06 ± 17.08	16.43 ± 3.63	17.91 ± 3.10	-	-
θ_c (°), TiO_2-suspension	-	-	-	-	35.05 ± 2.44	34.15 ± 5.38
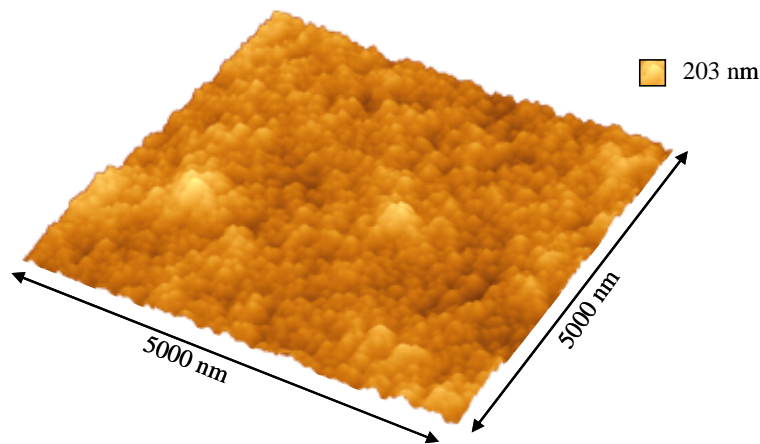
Figure 4-30 AFM-topography of the non-reservoir titania film on a wafer support, heat treated at a maximum temperature of 730 °C.

The contact angles θ_c of the NRL and *RL* titania coatings on wafers with water showed similar values: 16.43 ° and 17.91 °, respectively, Table 4-11. The TiO_2-coatings on stainless steel exhibited a more hydrophobic character with θ_c of 45.33 ° for ss730*RL* and of 53.06 ° for ss730*RL*. The high standard deviations of 20 ° of the coatings on steel resulted from the measurements of specimens produced in different batches. One sample itself did not exhibit these high deviations in θ_c. To check if the thickness of the TiO_2-film deposited by dip coating was influenced by the wettability of the colloidal TiO_2-suspension with the supports, their contact angles were measured. They were identical with θ_c of 35.05 for the wafer and of 34.15 ° for the stainless steel.

4.6   Discussion

4.6.1   Influence of the support type on the characteristics of the films

The thin nanostructured TiO_2-coatings were successfully created on 316L stainless steel (SS) or silicon wafer supports by multi-step dip coating followed by a heat treatment. They consisted of either a homogeneous meso- and macroporous non-reservoir layer (NRL)-structure or of drug reservoirs embedded in that structure to create a reservoir layer (*RL*). The ellipsoidal drug reservoirs featured a maximum elongation of 1 μm, equivalent to the diameter of the polymer templates used to produce them. The *RL* is to be applied on metal stents as a drug carrying matrix to create a drug-eluting stent (DES). It exhibited a good adhesion to the SS support, which is recommended for its usage in stents, because stents experience a deformation of max. 10 % during stenting [28, 29]. The adhesion of the film

might have been caused on one hand by the high contact area between the TiO_2-nanoparticles and the support. On the other hand, the built-up of an intermediate layer between the steel and the TiO_2 can have further endorsed the adhesion. This interlayer may be composed of chromium oxide and complexes made of iron and other elements, caused by diffusing metal atoms from the steel during the sintering [14]. This topic was in detail investigated by A. Tourvieille de Labrouhe [14]. Because of the strong adhesion, it was impossible to scratch the film off the steel support, which would have been necessary to conduct common analyses like BET, pycnometry or mercury intrusion porosimetry (MIP). Cutting the steel samples to produce cross sections, which would have given information about the thickness of the coating and the structure of the pores in thickness direction, failed.

The coatings produced on silicon wafer supports were a good model to represent the coating's structure on the steel support. They were used to acquire the structural information of the coating. The support material type itself did not have a significant influence on the structure of the coating, as was seen in the SEM-micrographs of the top views of the coatings on either steel or wafer supports in Figure 4-6 and Figure 4-10. The coatings produced on either type of support exhibited TiO_2-grain diameters smaller than 100 nm. They were slightly connected via neck formation created during sintering. Another parameter which proved the similarity of the coatings on wafers to the ones on steel was the anatase phase content measured by X-ray diffraction. It was 73.93 ± 13.22 %wt for the NRL on SS and 79.21 ± 6.86 %wt for the NRL on wafer support. The coatings, which contained reservoirs, exhibited 77.87 ± 23.05 %wt anatase when prepared on SS and 87.07 ± 2.04 %wt when fabricated on wafer. The high standard deviations of the films on SS were caused by the background signal from the steel support, which was recorded in the XRD spectra in Figure 4-8.

Small agglomerates of the TiO_2-nanoparticles with a size of 300 nm were detected in the micrographs of the coatings on either support, labeled as "sa" in Figure 4-6 and Figure 4-10. Agglomerates are unfavorable for the processing, since they can lead to differential sintering and therefore non-uniform microstructures [1]. The initial powder from the supplier had a mean particle size, d_{BET}, of 21.5 nm. It was electrostatically stabilized with ammonia in a water based phase at a pH of 10.5. The particles of this suspension possessed a monomodal particle size distribution with a median pore diameter, d_{v50}, of 60 nm, cf. Table 4-1 and Figure A-1 in Appendix. Small agglomerates of initial particles were hence formed in the suspension. However, some agglomerates detected in the coating after sintering had a diameter of 1 μm, delineated with "ba" in Figure 4-6 and Figure 4-10. These big agglomerates must have been present in the suspension and were deposited during dip coating. An increase in the time of ultrasonication of the titania suspension prior to usage did

not eliminate these residual agglomerates. The agglomerates might have been generated by the addition of the polyvinyl alcohol (PVA) binder into the suspension. It is a molecular binder, which adsorbs on the TiO_2-particles via hydrogen bonding between its OH-groups and the particle surface. An intermolecular bonding, due to the dipolar attraction of the OH-groups, builds additionally a polymer-polymer bonded network, in which the particles are dispersed [2]. PVA is a degradable polymer, which has good film forming properties. This makes it a favorable ingredient of the suspension for applying the TiO_2-films onto complex geometries like a stent [2]. The specific PVA used had a degree of hydrolysis of 96.8 to 97.6 %mol [30]. A higher hydrolysis rate promotes its tendency for crystallization [31]. Therefore the binder might have re-crystallized after a certain time in suspension. This might have resulted in a local segregation of the suspension and the TiO_2-particle clusters might have been formed, which were then deposited in the film. However, suspensions were prepared freshly before usage and it was assumed that PVA was perfectly dissolved. It is important in further studies to control the suspension's properties over time by thermogravimetric analysis (TGA) and particle size measurements. Maybe it would be optional to test other binders, like poly aspartic acid or PVA with a lower hydrolysis grade, to reduce its re-crystallization tendency.

Moreover, attention has to be given to the physical properties of the binder. The viscosity of the suspension depends besides its solid content on the type of binder used: a lower molecular weight of the binder reduces the viscosity [32]. This has an influence on the thickness of the films fabricated by dip coating, as can be deduced from the Landau-Levich equation, Equation (4-1). The thickness of the film decreases with lowering viscosity of the suspension, whilst the other parameters are kept constant. Equation (4-1) also illustrates that the liquid vapor surface tension, γ_{LV}, influences the thickness of the deposited film. It is related to the wettability of the suspension with the support and depends on the contact angle between them. The Young equation relates these parameters:

$$\gamma_{SV} = \gamma_{SL} + \gamma_{LV} \cdot \cos(\theta_c) \tag{4-10},$$

with γ_{SV} solid/vapor, γ_{SL} solid/liquid surface tension and θ_c contact angle [33]. The contact angles of the TiO_2-suspension with the wafer and steel were equal: 35 °. Therefore one would expect identical wetting properties and the same film thickness on the two types of supports. The films on steel nevertheless were 500 nm, the ones on wafers 1.2 μm in thickness. The process parameters were identical. It could be excluded that a small change in withdrawal speed, which was adjusted manually on the dip coater, could have caused this effect. Even if a small variation of ± 2 mm/min in the withdrawal speed of 90 mm/min can

cause a thickness change of the wet TiO$_2$-layer of ~ 20 nm, the evaporation of 90 %wt water from it would leave only a negligible change in thickness in the dried film. However, an effect observed by A. Tourvieille was the saturation of the film thickness on wire shaped steel supports after multiple dips. The phenomenon is not well understood, but might also have been the reason for the thinner coatings on the steel supports in this study.

The TiO$_2$-coatings produced on wafers instead of on SS initiated ways to characterize the NRL- and *RL*-structures, which were not viable when steel supports were used. It was feasible to easily cut cross sections with a diamond knife and consequently to acquire SEM-images of them. Hence one could measure the coating's thickness: 1.2 μm. The drug reservoirs were not spherical, but ellipsoidal with the shortest axis of 500 nm in the thickness (z) direction and the longest one of 1 μm in the plane parallel to the support. This phenomenon can be explained by constrained film sintering [34]. In presence of a substrate, the direction of the film shrinkage is the thickness direction due to the directed mass flow/diffusion during sintering [35]. Shrinkage does less occur in the planes parallel to the support (x and y direction, Figure 1-5).

The influence of constrained sintering on the film's structure was further pointed out by comparison of the properties of the films sintered without support (f800NRL) and with support (w800NRL). The freely sintered specimens showed a smaller specific surface area, a higher grain size and only a trace amount of anatase compared to w800NRL. The features of f800NRL equaled the properties of the NRL-structure in the bulk specimen b800: both were mainly composed of rutile and had a d$_{BET}$ of 360 nm. These samples were more progressed in sintering than the constrained films on the supports. In constrained film sintering, a geometrical constraint, such as the presence of the support, gives rise to bi-axial stresses in a coating [35, 36, 37, 38]. They can be caused on the one hand by the film forming process. Drying for instance results in shrinkage strains in particulate films on rigid supports. They will be increased by following densification. On the second hand, different expansion coefficients of the film and the support at elevated temperatures can contribute to directed strains in a film [34]. The rigid support, such as the silicon wafer or SS, can exert a tensile stress on the film at the interface between the substrate and the coating. It is opposed by the sintering stress acting to produce in-plane, that means parallel to substrate, shrinkage in the film [35, 37, 39, 40]. The sintering stress, as the driving force for densification, is the stress generated by interfacial energies acting over curved surfaces in a sintering system and can be described by the Laplace equation [2]:

$$\sigma = \gamma \cdot \left(\frac{1}{r_1} + \frac{1}{r_2} \right) \tag{4-11}$$

with σ: stress over a curved surface, γ surface energy, r_1 and r_2 the radii of curvature of the surface. If one now imagines the initial sintering of two identical spheres, a neck forms between them. The stresses arising from the curvature of the interparticle neck is different to the ones along the surface away from the neck. This stress gradient is the driving force of mass flow into the neck during sintering. As a result, the grains grow and the surface area is reduced. The system reduced its surface energy. However in the final stage of sintering, the sintering stress is composed of two terms: one is attributed to the grains and the second one to the pores:

$$\sigma = \frac{2 \cdot \gamma_{ss}}{d_g} + \frac{4 \cdot \gamma_{sv}}{d_P} \qquad\qquad (4\text{-}12),$$

with γ_{ss} solid/solid grain boundary energy, γ_{sv} solid/vapor surface energy, d_g: grain size, d_P: pore size. For small gain sizes, the first term is dominant. For small pore sizes, which arise when the sintering is progressed, the second term is dominant [41]. From this explanation it gets clear that the particle size and the particle arrangement in a powder compact play an important role in neck formation and thus in densification. It can be used to explain the phenomenon of delayed densification in the constrained films. The arrangement of the primary ceramic particles can be described by their coordination number. That is the number of nearest neighbors of a particle having actual physical contact [36]. The higher the coordination number is, the higher is the number of necks formed during sintering and thus the higher is the densification and the crystallite growth. A difference of the coordination numbers of the freely and the constrained sintered TiO_2-films in the present study have contributed to the different consolidation. This difference did not arise from the drying process, because both films were prepared by the same dip coating technique. The only difference between the both was that f800NRL was removed from the support prior to sintering. The difference of the coordination number aroused in the initial stage of sintering, where the necessary re-arrangement of the TiO_2-particles was partially inhibited in w800NRL by the particle-support interaction. This resulted in a relatively low number of physical contact points in the constrained film and consequently in a lower sintering activity, crystallite growth and phase transition [36]. Indeed a higher anatase content-the low temperature stable form of TiO_2-in w800NRL was detected compared to f800NRL. The anatase to rutile phase transition depends on the primary particle size, as well as on the coordination number [11]. This issue will be discussed later in this chapter. Besides the particle size and their arrangement, the stiffness of the support and the particle's attachment to it might have prohibited the phase formation to rutile, because it requires a contraction [42].

Another effect which is related to constrained film sintering is the development of a directional anisotropic structure in the film [43]. Garino and Bowen suggested that particle motion is prohibited laterally in the planes parallel to the support. This leads to directional pore growth, as the centers of two adjacent regions of relative high density remain separated [35]. Guillon *et al.* investigated the microstructure change in dip coated alumina thin films and reported an anisotropy. With increasing densification, the pores got anisomeric and oriented along the thickness direction [43], Figure 4-31. SEM-micrographs of the TiO_2-film on wafer support (w730NRL) in Figure 4-12 (a) revealed a homogeneous meso and macroporous structure with no directional pores. The formation of an anisotropy was not as progressed in the initial state of sintering, in which the present films were sintered, as in the intermediate or end phases of sintering. The TiO_2-films might furthermore have been too thin to observe an anisotropy. Because the films under investigation by Guillon *et al.* were sintered in the final stage of sintering and were 10 times thicker than the present ones. They recorded a well distinct anisomery with a lower pore density in the region distant to the support and an increased mean grain size compared to the structure close to the support. Moreover the pores oriented along the thickness-direction of the coating, Figure 4-31.
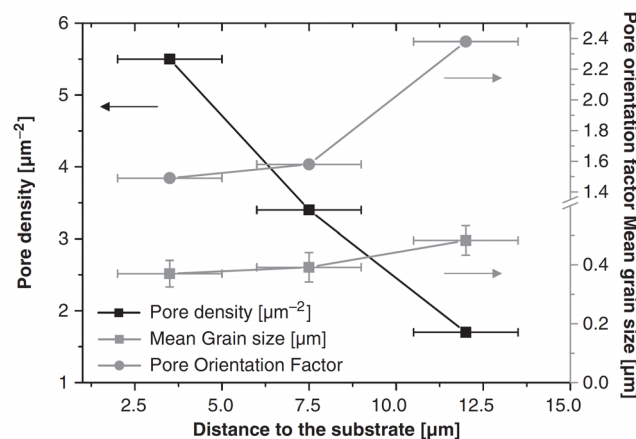
Figure 4-31 Gradients of the pore density and pore orientation along the thickness direction of an alumina thin film prepared by dip coating and having a relative density of 97 % [43].

The following aspects hence have to be kept in mind when optimizing the structured TiO_2-coating for its application in a stent. An increase in the film-thickness for achieving a higher drug-load, or an augmentation of the sintering temperature to improve the mechanical properties, can result in the generation of an anisotropy in the coating. Most likely different grain sizes and oriented pores will evolve. Directed pores in the films might increase the drug-release, because their smaller tortuosity will decrease the diffusion path of the drug molecules out of the coating.

In our days it is still a challenge to determine the pore size distribution (PSD) and porosity of thin, structured, highly porous films. Several methods were employed in the present study to ascertain these values, because they are essential to assess the drug-load and release capability of the coating. Ellipsometry porosimetry (EP) is a fast, cheap and non destructive method to determine open pore sizes in the range of pore diameters of 0.32 to 65 nm and the overall open porosity of thin films [16]. In this study EP did not reveal the exact PSD and porosity of the NRLs on SS and on wafer supports. Only the onset pore diameter of 40 nm was detected in the coating on the wafer, and a porosity of greater than 34 % was deduced. The porosity and the pore widths in the titania coatings exceeded the limit of detection. The adsorbate toluene did not saturate the total pore volume and the adsorption isotherms were incomplete. One way to measure the PSD by EP in the future might be to use another adsorbate, which has a longer carbon chain than toluene. This can be illustrated by the Kelvin equation in Equation (4-3). The Kelvin radius r_K of toluene at the pressure ratio p/p^0 of 0.8 is 10.9 nm. The r_K of decane at the same partial pressure is bigger: 16.8 nm [18]. Hence a smaller amount of adsorbate molecules is necessary to fill the pores, when the relative pressure is varied in the same range like for toluene. This should lead to complete adsorption isotherms and should give access to measure bigger pores and higher porosities. Analyses using decane will be performed in the future on the present specimens. EP can furthermore deliver information about the film thicknesses, refractive indices, extinction coefficients and the Young Moduli of the thin films. This makes it an interesting technique to be used later for the quality control of the thin TiO$_2$-films on flat supports.

Small angle neutron scattering (SANS) porosimetry gave structural information of the thin TiO$_2$-films when staying attached to the supporting wafer. The aim of the measurements was to detect a difference in the scattering patterns of the NRLs and *RL*s and to determine the PSDs of the thin films. The median pore diameter d_{v50} of the NRLs on wafer supports was lower than for the *RL*s: 45.21 nm and 60.39 nm, respectively. The scattering length of the voids, representing the PSD, and of the TiO$_2$-particles was evaluated during SANS. The reservoirs in the *RL* created a higher quantity of higher scattering lengths, shifting the median pore width to higher values than in the NRL. Another reason for the difference in the d_{v50} between the NRL- and *RL*-structures is, that in SANS the amount of open and closed pores were recorded. The distribution of small, closed pores was homogeneous in the isotropic NRL. In the big voids of the *RL* instead, this amount of small, closed pores was missing and thus shifting its PSD to higher pore diameters. For both measurements, the range of detectable pore diameters was limited to 0-100 nm, which was the maximum scattering length of the neutrons. The pore sizes evolving from pores greater than that critical size could therefore not be included as whole pores in the measurements. They were measured as multiple pores with a maximum length of 100 nm. Hence the reservoirs, with a

mean diameter of 800 nm, could not be evaluated. SANS is not the most common method to determine PSDs, because it is expensive, desires a high working effort and one has restricted access to the machines. However, this technique might be used in the future to study the dissolution of a drug, which is incorporated into the NRL TiO_2-coating, with time *in situ*. Neutrons are beneficial compared to the application of X-rays, because they have a neutral charge. They do not show electrostatic interaction with the electrons of the atoms in the coating and are scattered by the nucleus itself. X-rays in comparison interact with the atoms they pass through [44], resulting in a weakening of the beam intensity and possibly damaging the material. Neutrons on the contrary can pass through materials without harming them. This has directed the application of SANS for hard and soft matter characterizations [19]. Thus the observation of the dissolution of the "soft" organic drug in the "hard" TiO_2-coating seams feasible. A next SANS experiment could hence be the following. A NRL on wafer support, sintered at a maximum temperature of 730 °C, should be loaded with the drug. A recorded scattering pattern of that sample should be different to the one of the non-loaded samples obtained in this study. Then one could immerse the drug-loaded specimens into a mixture of water and deuterate-water (D_2O). The contrast variation of H_2O and D_2O during penetration should be recorded. Subsequent comparison of the scattering patterns with the ones of the dry, drug-loaded samples should give information about the diffusion of water in the coating and furthermore of the dissolution of the drug. This might give fundamental information of molecule transports in nanoporous, thin films and might be further applied to the transport of substances in membranes and filters.

Mercury intrusion porosimetry (MIP) is a standardized method for the determination of PSDs and porosities. This method covers the measurements of pores in the range of 5 nm up to several millimeter [9]. However, the preparation of the TiO_2-coatings for the measurements showed some disadvantages. The PSD by MIP could only be ascertained on coatings without reservoirs. Because the detachment of the coating from the support prior to analysis has created small fragments, which were preferably broken at sites of a high reservoir density. The reservoirs were destroyed and not incorporated in the measurement. MIP results were defined in two different pore diameter ranges: (1) between 0-100 nm to compare with the results of the SANS-measurements, (2) between 0-1000 nm, to incorporate all pores in the coating, Table 4-10. The median pore diameter, d_{v50}, of the NRL on wafer and sintered with a maximum temperature of 730 °C (w730NRL) was 76.34 nm in the range of 0-100 nm and 30 nm bigger than the one obtained in the SANS measurements. The reason for the difference lies in the various pore volumes accessible by the different methods. Whereas in MIP only the open pores were included in the measurement, in SANS open and closed pores were evaluated. The small, closed pores shifted the distribution to smaller values. Another factor for the deviation was addressed to the different models used for the

evaluation: in MIP a cylindrical pore model was applied, whereas in SANS spherical pores were assumed. In the wider pore diameter regime of 0-1000 nm the d_{v50} of w730NRL was only slightly bigger than for the smaller range. One could hence conclude that the void volume was predominantly occupied by pores with a diameter smaller than 100 nm. The porous structure of the NRL could be classified into meso and macroporous. The porosity occupied by pores up to 1000 nm was 64.45 %.

The PSD of the NRLs sintered at a maximum sintering temperature of 800 °C (w800NRL) was also evaluated by MIP. The d_{v50} in the range up to 100 nm was 67.42 nm and smaller than for the film sintered at 730 °C. However, when taking into account the bigger diameter range up to 1000 nm, a d_{v50} of 138.31 nm was obtained. The presence of more pores, which are smaller than in w730NRL sintered at a maximum temperature of 730 °C, and of a higher quantity of pores with a diameter greater than 100 nm, clearly showed the sintering progress of w800NRL compared to w730NRL. This phenomenon is described in literature. Allemann, Hofmann and Gauckler showed for zirconia that *small pores* shrink first when sintering a powder compact, followed by the *bigger ones* at a higher sintering temperature. This is related to the presence of small pores in agglomerates, the so-called intra-agglomerate pores, depicted in Figure 4-32. They disappear earlier during consolidation. The bigger inter-agglomerate pores get eliminated later in the sintering [45]. The presence of small agglomerates in the coating with a diameter of about 300 nm was shown by electron microscopy in the Figure 4-6 and Figure 4-10. Hence the findings of the pore size development in the present study correlates with the theory.
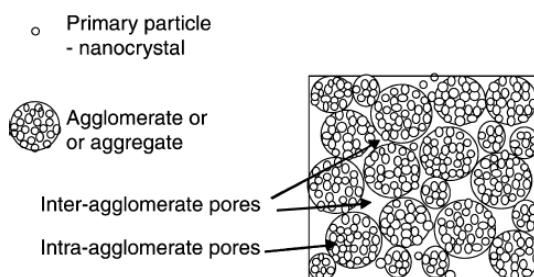
Figure 4-32 Illustration of primary particles, agglomerates and their packing in a powder compact [46].

The porosity in the pore diameter interval up to 1000 nm decreased from 64.45 % to 55.04 %, when increasing the maximum sintering temperatures of the films of 70 °C from 730 °C to 800 °C. This is coherent with the sintering theory, where an increase of densification is attended by porosity reduction [41]. This is related to re-orientation of the primary particles and to grain growth. Coarsening of the titania grains was observed: the mean grain diameter d_{BET} of w800NRL was 1.5 times the size of the one of w730NRL. Nevertheless the films w800NRL were still sintered in the initial stage. Because the SEM-

micrographs in Figure 4-13 (a) revealed that the TiO_2-particles were connected slightly via neck formation and a low densification has taken place [2]. This was furthermore coherent with the results of the dilatometry of the bulk titania cylinders in Figure 4-22.

During this study, the amount of pore volume occupied by the reservoirs was not measured, but calculated, like depicted in Figure 4-20. The *RL* applied in the present study contained 3 % more porosity than a NRL of the same thickness. The calculation has shown that an increase in reservoir size and density can significantly increase the porosity of the coating. For instance densely packed reservoirs of a diameter of 4 µm can create an overall porosity of 65 %. But an increase in reservoir size is related to an incorporation of bigger polymer templates, which need to be covered by the TiO_2-suspension. This is attended by an augmentation of the film's thickness and an accession of the porous ceramic structure surrounding the reservoirs. The amount of porosity occupied by the porous ceramic structure surrounding the reservoirs contributes significantly to the overall porosity. The density of reservoirs in the coating and their size might in the future need to be optimized for individual applications of the drug-eluting coating. Bigger reservoirs might be favored for incorporating sufficient amounts of therapeutical agents. But when aiming for a high porosity and greater film thicknesses, one has to consider that the coating's mechanical stability depends on these parameters and might deteriorate.

The sintering behavior of the thin titania films and their structural characterization have now been discussed. It was clear that the constrained sintering of the film creates less densification than in a bulk sample sintered at the same maximum temperature of 800 °C. A disadvantage observed during the characterization of the films was the high amount of coating necessary to perform analyses, such as the determination of the specific surface area or the porosity. Many supports had to be coated and fired to being able to perform one measurement. The characterization of the structure of the TiO_2-films on SS supports was only restricted possible. The aim in a next step was to produce a high amount of bulk material exhibiting equivalent properties like the NRLs.

4.6.2   *Sintering of titania nanoparticles in the bulks*

Dilatometry of the bulk samples showed that the sintering rate increased drastically exceeding 850 °C, which was the temperature where the intermediate stage of sintering started, Figure 4-22. That there was almost no densification happening before 850 °C was confirmed by the calculation of the total porosity of the bulk samples sintered between 700 and 820 °C, Figure 4-25. The total porosity remained constant until 800 °C. From these two experiments it could be concluded that until at least 800 °C, sintering was in its initial

stage. In this period, the necks between the grains in the powder compact formed by means of surface diffusion, as was also deduced from SEM-images, Figure 4-23. The pore shapes were randomly and not spherical, as they would be in the final stage of sintering [41]. The specific surface area of the bulk bodies changed drastically between 740 and 770 °C, although there has no densification occurred. The amount of anatase phase decreased with diminishing specific surface area, Figure 4-24. This was attributed to the growth of the titania particles, which from a critical size on trigger the transformation from anatase to rutile [11]. A strong drop in the anatase phase content took place when the titania particles reached a size of 190 nm at 750 °C, Figure 4-24. The anatase to rutile transformation is of reconstructive nature [47], meaning that bonds between atoms are cleaved, and rebuilt during the transition. This may lead to much more mobility of the atoms and one could imagine that this facilitates material transport and thus grain growth. A plot from Ranade *et al.* was modified to display not only the surface area as in the original paper, but also the mean grain diameter d_{BET} calculated with Equation (4-2), Figure 4-33 [11]. For small particles, anatase is the most stable phase. As soon as the particle size exceeds 120 nm, rutile is the most stable polymorph of TiO_2. The formation of brookite, which is displayed in Figure 4-33, was kinetically blocked.
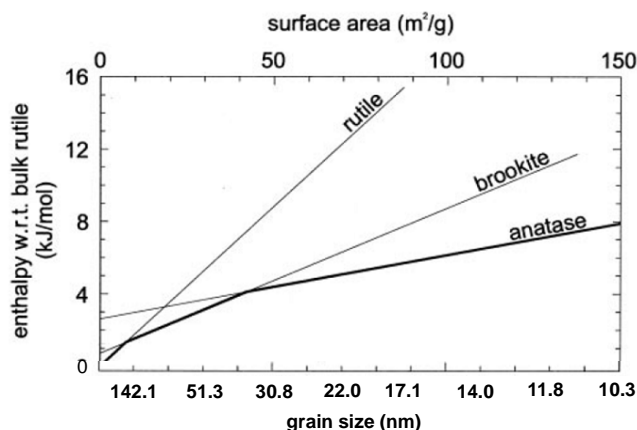
Figure 4-33 Polymorphs of TiO_2, anatase, rutile and brookite, at room temperature as a function of specific surface area and grain size, as modified from Ranade *et al.* [11].

The phase transition of TiO_2 at 750 °C sintering temperature of the bulks correlated further with work deduced by Kim and coworkers [48], who reported a start of the phase transformation of anatase particles with an initial size of 21 nm-such as in the present study-at 750 °C. It was completed at 800 °C.

From the *in situ* XRD measurements of the bulk titania compact it was clear that the phase transformation from anatase to rutile was initiated during the temperature ramp of 500 to 800 °C, proceeded during the plateau of the maximum sintering temperature of

800 °C and came to the end after cooling to room temperature, Figure 4-21. These findings fit the thermodynamic phase diagram of TiO$_2$, which shows that at atmospheric pressure the phase transformation of TiO$_2$ starts at 600 °C [49], Figure 4-34.
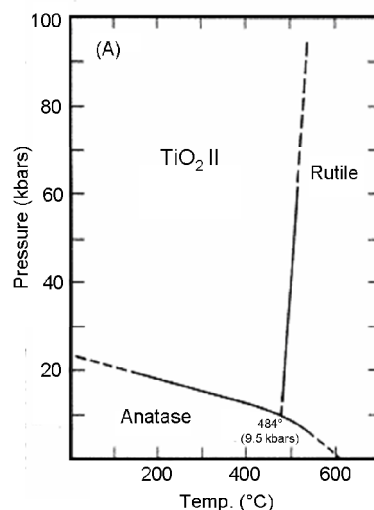
Figure 4-34 Phase diagram of the polymorphs of TiO$_2$: anatase and rutile [49].

The phase transition from anatase to rutile is a first order transition, represented as a line in the phase diagram. The transition should have been taking place simultaneously for all anatase particles. Nevertheless, a temperature region for the transformation was observed, represented by a temporary increase in the sintering rate between 760 and 800 °C, Figure 4-22. This fits the findings from XRD measurements (Figure 4-21), where the phase transformation was almost finished after the plateau of 800 °C. To correlate the increase in shrinkage rate in this temperature interval with the phase transformation is reasonable. It also was observed by Kim et al., who measured shrinkage curves with a hillock in the region of the phase transition from anatase to rutile [47]. Legros *et al.* suggested that in alumina the phase transformation is coupled with a grain rearrangement, which leads to a densification of the ceramic [50]. If the same happened in the titania powder compacts, this could explain the increase in shrinkage occurring at the phase transformation.

Furthermore a deviation between the temperature region of the phase transition of the bulk samples, heat treated during dilatometry and by the conventional method was observed. In dilatometry the phase transition was *initiated* at 760 °C. The bulk sample, which passed through the whole sintering cycle with the maximum sintering temperature of 770 °C, contained already mainly rutile. The higher amount of anatase in the dilatometry specimen compared to the conventionally sintered one was associated to the different heating cycles and to the time points when the XR-diffractograms were recorded [46, 50]. The ones of the conventionally fabricated bulks were recorded after the whole sintering cycle was complete.

The nucleation sites of rutile were initiated during the heating and grew bigger during the isothermal hold at the maximum sintering temperature T_{max} and the cooling. On the contrary, in dilatometry the temperature was increased continuously up to 1000 °C with the same rate and without any isothermal holds-the phase transition was hence more rapid. Significant high standard deviations were observed in the mean grain size d_{BET} and the phase composition of the conventionally sintered bulks in the temperature range of 700-770 °C. They might be related to the presence of agglomerates of different sizes in the titania green body. Gribb and Banfield showed that the phase transition, once initiated in a crystallite, proceeds rapidly through the entire crystallite. These seeds lower the energy needed for transformation, as they serve as nucleation sites. A higher concentration of seeds leads to a lowering of the phase transition temperature [51]. A variation of the number of seeds in the samples might thus have created the deviations. The number of seeds depends on the particle size distribution in the green compact and the presence of agglomerates in the specimens. Varying amounts of agglomerates in individual samples might have triggered the standard deviations.

The understanding of the sintering behavior helped to set the production parameters of cylindrical bulks, which are "equivalent" to the ones of the NRL-structured film sintered at a maximum temperature of 730 °C. The bulk samples sintered at 740 °C were selected to represent the structure of w730NRL. Their surface areas were almost identical with 17 and 18 m^2/g, respectively. The BET surface area was the used criterion to select the production parameters of the bulk, because it is linked to the grain size and the phase composition as was shown by Ranade *et al.*, Figure 4-33, and in the present study, Figure 4-24.

The PSD of the bulks sintered at 740 °C (b740) was measured by MIP and nitrogen sorption porosimetry (NSP). The obtained values of the median pore diameter d_{v50} in the range of 0-100 nm as a function of the two methods correlated: MIP revealed 51 nm and NSP 58 nm. The PSD by MIP was bi-modal for b740 when performing the same analyses taking into account the bigger pore size interval (0-1000 nm). Two most frequent pore diameters were detected, one at 58 nm and the second one at 283 nm. Hence pores exceeding a width of 100 nm existed, but most of them were smaller than 100 nm. For w730NRL a mono-modal distribution was obtained with a d_{v50} of 76 nm in the range of 0-100 nm, 83 nm in the range of 0-1000 nm, and a most frequent diameter of 87 nm. Mainly pores with a diameter smaller than 100 nm existed. The features of the bulks b740, which were to be equivalent to the films w730NRL, were not equal in regards to their PSD. The difference was associated to the production methods. The films were prepared by a multi-step dip coating procedure, in which the TiO$_2$-particles could get ordered during the withdrawal of the substrate from the suspension [52]. After the deposition of each thin layer the samples

were dried under controlled atmosphere in a climatic chamber. The aqueous phase evaporated quickly from the few microliter of suspension deposited as the thin film. The TiO_2-nanoparticles did not have time to re-arrange and to build up big agglomerates. Particles were densely and homogeneously packed in the films, as was seen in the SEM-micrographs. A few big agglomerates with a diameter of 1 μm were located, but they were already formed in the suspension prior to deposition. The situation was different for the bulks fabricated by slip casting. During slip casting, several milliliter of the TiO_2-suspension were poured into one opening of the mould to create cylindrical specimens. The evaporation of the aqueous phase took accordingly longer than for the films. The TiO_2-particles hence had time to re-arrange in the liquid phase and to build big agglomerates. The presence of these agglomerates caused the recorded bi-modal pore size distribution in the bulks.

The influence of agglomerates in a powder compact on the PSD was in more detail analyzed by J. Allaman *et al.* [45]. Smaller pores were attributed to be inter-particle pores, or "intra-agglomerate pores". The bigger ones were caused by the voids between the agglomerates and are termed inter-agglomerate pores, Figure 4-32. During consolidation, the intra-agglomerate pores get eliminated and bigger pores grow. This could be verified by the characteristics of the bulks sintered at different maximum temperatures. Up to 800 °C, the calculated open and closed porosities stayed constant at 50 and 42 % respectively, Figure 4-24. A slight decrease of the total porosity was obtained between b800 and b820, but the open porosity stayed constant. These findings can be explained by the elimination of closed intra-agglomerate pores upon proceeding neck formation between the particles in b820. The neck formation can be correlated with a lower specific surface area in b820 compared to b800.

When in the future bulks with equivalent properties like the films have to be produced, one might choose tape coating instead of slip casing. In tape coating a high area of support can be coated in a short period of time. The evaporation of the water phase is accordingly faster compared to slip casting. This might prevent the formation of big agglomerates and thus the formation of big pores. The tape coated films might be removed from the support prior to heat treatment. The maximum sintering temperature of the tape coated films can be the same as for the constrained films, as long as the sintering stays in the early initial stage. Because the present study has shown, that the influence of constrained film sintering on densification was less severe during the early initial stage of sintering. NRLs and bulk specimens sintered at the same temperatures below 750 °C exhibited the same specific surface areas and similar anatase phase contents.

In the future the properties of the films might need to be adapted to the desired application. For instance the sintering temperature might need to be increased to improve the mechanical stability. The problem to determine the PSD in the films will still exist. One might then use the equation established by Scherer and Garino, Equation (4-13), to predict the shrinkage of the constrained film compared to a freely sintered film, which can be prepared and characterized easily.

$$\left(\frac{\rho'}{\rho}\right)_c \bigg/ \left(\frac{\rho'}{\rho}\right)_u = (1 + \nu_p)/3 \cdot (1 - \nu_p) \tag{4-13}$$

with $(\rho'/\rho)_c$ the densification rate of the constrained film, $(\rho'/\rho)_u$ the densification rate of the unconstrained film and ν_p viscous Poisson's ratio, which is a function of porosity and the microstructural properties [35, 37]. The densification rate of the unconstrained film might be measured by dilatometry.

4.6.3   Surface properties of the films

Surface properties of implants are a key issue in the interaction of a biomaterial with the biological environment [3, 53]. The structural makeup of the implant's surface directs and influences the response of proteins, cells and the organism [3]. But besides the performance in the biological media, the surface properties of the titania coating can also influence the drug-load behavior, when it is to be applied in a drug-eluting stent. To evaluate the influence of the preparation methods of the TiO_2-coating on its surface structure, analyses concerning its chemical composition, topography and wettability were deduced.

The NRL and *RL* TiO_2-films on wafer supports were similar. They exhibited the same chemical composition on the outer 10 nm of the coating: stoichiometric TiO_2, as was determined by X-ray photoelectron spectroscopy (XPS). No diffusion of Si-ions from the support to the outer part of the coating was detected, if a maximum calcination temperature of 730 °C was applied. The determined mean roughness, R_a, of the two types of coatings was similar with a slightly higher value of the *RL* of 25.30 nm compared to 16.70 nm of the NRL. The reasons for the slightly higher R_a in the *RL*s were small elevations in the films, which were produced by the drug reservoirs, as was observed by SEM. The contact angles θ_c of these two types of coatings with water showed similar values with w730NRL: 16 ° and w730*RL*: 18 °. No significant influence of the presence of the reservoirs on the contact angles was deduced. The contact angles measured were comparable with the ones obtained in studies by Wu *et al*. [54], who reported a θ_c of an anatase crystalline surface of 24 ° and for rutile 58 °. In this study the coating was mainly composed of anatase and small amounts

of rutile were present. Therefore one has expected a θ_c dominated by the features of anatase. The slightly lower values obtained in this study compared to Wu and coworkers might be caused by the roughness of the surface. A *roughness factor f* can be included into Young's equation for the calculation of the contact angle, Equation (4-10). The factor f can be defined as

$$f = \frac{A_{\text{effective}}}{A_{\text{apparent}}}$$
(4-14),

with $A_{\text{effective}}$: the effective surface area of the rough sample and A_{apparent}: the apparent geometrical area. If the surface is rough, f   1. For a smooth surface, f =1. Modifying Equation (4-10) reveals

$$\cos(\theta_{c0}) = \frac{\gamma_{SV} - \gamma_{SL}}{\gamma_{LV}}$$
(4-15),

with θ_{c0} the ideal contact angle. It is connected to the effective contact angle by

$$\cos(\theta_c) = f \cdot \cos(\theta_{c0})$$
(4-16).

From these equations it gets obvious, that if $0\,° < \theta_{c0} < 90\,°$, $0 < \cos(\theta_{c0}) < 1$ and the surface gets more hydrophilic [3]. A higher roughness can increase the hydrophilicity of an otherwise hydrophilic smooth surface of the same material. The higher roughness on the TiO_2-coatings in this study, when compared to the findings of Wu *et al.*, might have increased the hydrophilicity.

The higher hydrophilicity of anatase compared to rutile is explained as follows. When water is brought into contact with the TiO_2-surface, its molecules form intermolecular interactions with the surface atoms. The degree of wetting is determined by a balance between adhesive and cohesive forces between the involved molecules. The TiO_2-molecule on the surface is a dipole with positive Ti^+ and negative O^- sites. In an aqueous environment OH^- bonds to the Ti cation form Ti-OH groups [55]. The OH-groups then can form hydrogen bonding with the water molecules from the liquid. The more –OH groups are formed on the surface, the more water can bind and thus the more hydrophilic is the system. The different behavior of anatase and rutile is caused by their different interfacial tensions with water. The interfacial energies of water with anatase and rutile, γ_{sl}, were determined by Wu *et al.* to be -12.1 and 11.1 mJ/m^2 respectively. The free energy of adhesion of water to a solid surface, ΔG, could be calculated by

$$\Delta G = \gamma_{sl} - \gamma_{sv} - \gamma_{lv} \qquad\qquad (4\text{-}17).$$

The free energy of anatase was evaluated to be -139.4 mJ/m^2 and for rutile -112.6 mJ/m^2 [54]. Because the free energy is lower for anatase, water molecules adhere more favorably on anatase and thus make it more hydrophilic. The free energy itself depends on the different crystal structures of the two TiO$_2$-morphologies.

The NRLs- and *RL*s on stainless steel supports exhibited differences to the coatings on the wafer supports. XPS revealed that Ti was bound as stoichiometric TiO$_2$. Trace amounts of iron in iron oxide and chromium in chromium oxide have been present in the upper layer of the coating on SS.

The roughnesses R$_a$ of the coatings were directed by the roughness of the underlying supports. R$_a$ of the wafer was below 5 nm and of the coatings on top 16.70 nm and 25.30 nm for the NRL and *RL*, respectively. The SS exhibited a R$_a$ of 75.25 nm and the coatings NRL and *RL* 76.38 nm and 54.13 nm, respectively. A thicker coating on the SS supports might decrease R$_a$.

The mean contact angles θ_c of the titania coatings on SS were higher than on the wafer supports: 45.33 ° and 53.06 ° for the NRL and *RL*, respectively. The presence of the vanishing amounts of iron and chromium oxides on top of the surface might have altered the wetting properties [56]. Significant variations of θ_c for the coatings on SS were observed. θ_c measured on different spots on one individual sample did not cause these deviations. But the wettabilities of samples produced in different batches with the same parameters were different. Therefore it is important to establish quality controls in several steps during the complex production cycle of the TiO$_2$-coatings. The surface roughness of the steel after electropolishing should always be measured for at least 3 samples from one batch. The additionally fast and inexpensive measurement of θ_c can give reliable information of the chemical state of the polished steel before the coating is applied. The determination of the microbeads' density by microscopy should in the future be followed for each batch of samples, like was done here. An automation using image processing to evaluate this characteristic might be advantageous. It might even be of advantage to control the atmosphere during the deposition of the beads to increase the reproducibility. Because it was impossible on some days to create the wanted microbeads-density of 150000 beads/mm^2. The environmental factors affecting the deposition of the templates were not systematically analyzed in the present study. In a last quality control step, the contact angle of the coating with water should be measured to get information about the quality of the nanoporous titania films.

4.7   Conclusion

The following conclusions could be drawn in respect to the production and characterization of the nanostructured titania (TiO_2) coatings for stent-implants. The thin TiO_2-coatings were successfully created on stainless steel (SS) and silicon wafer supports by a dip coating technique and a following sintering step. The micrometer-sized holes, which will serve as drug reservoirs, were surrounded by a porous ceramic structure with smaller pores. The characterization of the structure of the films on SS supports was not possible in terms of their specific surface area, porosity or density. The coatings fabricated on silicon wafer supports represented a good model to measure these parameters, which are important to be defined to apply the coating as a drug-eluting matrix in stents.

The specifications of the thin TiO_2-coatings, which were heat treated at a maximum sintering temperature of 730 °C and do not containing reservoirs (NRLs), were determined. Their properties are equivalent to the porous structure surrounding the reservoirs in a reservoir layer (*RL*). The pore size distribution (PSD) of the NRL-structure exhibited a median pore width below 100 nm and an open porosity of more than 50 %. The influence of the reservoir size and density in the coatings on the overall porosity could not be measured, but calculated. The used *RL*s in this study, which had a reservoir density of 150000 reservoirs/mm^2 and a reservoir size of 1 µm, increased theoretically the overall porosity of 3 % compared to an equivalent NRL. The calculations have shown that the pore volume can further be increased by creating thicker coatings with bigger reservoirs, as well as by increasing the reservoir density. In addition it could be deduced that the porous structure surrounding the reservoirs has a significant influence on the overall porosity.

In our days it is still a challenge to measure the PSD and porosity of thin ceramic films, which contain bimodal PSDs of different orders of magnitudes. Ellipsometric porosimetry is not yet advanced enough and the constraint of small angle neutron scattering and nitrogen sorption porosimetry is a pore diameter of 100 nm. A high quantity of NRLs was required to perform one measurement by mercury intrusion porosimetry (MIP). Hence bulk, cylindrical samples with a NRL-structure, representing the NRL-structure of the films, were easily and effectively prepared by slip casting. Their PSD and porosity were measured by MIP.

By comparing the results of the bulk specimens sintered at a maximum sintering temperature of 800 °C with the ones of a NRL, which was heat treated identically, it could be concluded that the bulks were more progressed in sintering than the films. The geometric constraint of the support has directed the film to constrained sintering and hence to a lower densification. The effect of constrained film sintering in the beginning of the initial stage of

sintering, represented by lower sintering temperatures, was not as progressed as in the end of the initial stage, the intermediate or the final stage. Hence similar properties of the TiO_2-bulks and the NRLs, which were sintered with the same method and with a maximum sintering temperature of 730 °C, in regard to their specific surface area and porosity were detected. Only the PSD of the bulks was shifted to higher values compared to the one of the films. This could be correlated to the presence of agglomerates of the TiO_2-primary particles in the bulks, which were formed during the drying after slip casting.

The TiO_2-films, which were fabricated on either silicon wafer or SS and heat treated at a maximum sintering temperature of 730 °C, were composed of mainly anatase. The residual amount was rutile, which is the high temperature stable morphology of TiO_2. Whilst the surface of the titania coatings on wafer supports contained only stoichiometic TiO_2, the same coatings on SS supports exhibited in addition trace amounts of iron oxide and chromium oxide. The roughness of the porous NRLs and *RL*s depended on the roughness of the underlying support material. Hence the roughness of the films on the smooth silicon wafers exhibited a lower mean roughness than the films on SS.

The TiO_2-coatings on wafers were hydrophilic, as was deduced from contact angle measurements with water. The titania films on SS featured a more hydrophobic character, which was most probably affected by the presence of the metal ions in the coating. The presence of the drug reservoirs in the coating did not significantly change the wettability behavior of the films.

For the application of the nanostructured titania coating in a medical implant it might be necessary to adopt some characteristics of the coating, such as the porosity to create a higher drug-load capacity or a higher densification for a better mechanical stability. These features can easily be modified by changing the process parameters, such as increasing the sintering temperature. But one has to be aware, that with increasing sintering temperature and increasing film thickness an anisotropy in the film might arise due to the effect of constrained film sintering. This can be beneficial, if aligned pores are wanted to increase the drug diffusion out of the coating. But this is also accompanied by a reduction in porosity and hence a lower drug-load capability. Inhomogeneous, bigger grain sizes are then formed and they might be unfavored in regard to the mechanical stability. One also needs to pay attention to the behavior of the underlying support material during heating, because metals can form precipitates in their grain boundaries leading to lower corrosion protection.

A change in calcination temperature can also affect the surface properties of the coating. A higher sintering temperature might change the morphology of TiO_2 to consisting

of a higher amount of rutile and thus creating a higher hydrophobic character of the surface. Furthermore the diffusion of metal ions from the stainless steel support along the titania grains, which depends on the temperature, increases. The presence of these ions on the upper layer of the coating might alter its performance in the biological environment. This will be evaluated in future tests.

4.8   References

[1]   R.E. Loehman, "Characterization of ceramics", *Butterworth-Heinemann*, 1993.

[2]   J.S. Reed, "Principles of Ceramics Processing", *John Wiley and Sons*, 1995.

[3]   B.D. Ratner, A.S. Hoffman, F.J. Schoen, J.E. Lemons, "Biomaterials Science: An Introduction to Materials in Medicine", *Elsevier Academic Press*, 2004.

[4]   F. Zhang, Z. Zheng, Y. Chen, X. Liu, A. Chen, Z. Jiang, "*In vivo* investigation of blood compatibility of titanium oxide films", *Journal of Biomedical Materials Research*, Vol. 42, 1998, pp. 128-133.

[5]   F. Akin, H. Zreiqat, S. Jordan, M. Wijesundara, L. Hanley, "Preparation and analysis of macroporous TiO_2 films on Ti surfaces for bone-tissue implants", *Journal of Biomedical Materials Research*, Vol. 57, 2001, pp. 588-596.

[6]   N. Huang, P. Yang, Y.X. Leng, J.Y. Chen, H. Sun, J. Wang, G.J. Wang, P.D. Ding, T.F. Xi, Y. Leng, "Hemocompatibility of titanium oxide films", *Biomaterials*, Vol. 24, 2003, pp. 2177-2187.

[7]   J. Liu, D. Yang, F. Shi, Y. Cai, "Sol-gel deposited TiO_2 film on NiTi surgical alloy for biocompatibility improvement," *Thin Solid Films*, Vol. 429, 2003, pp. 225-230.

[8]   L. D. Landau, V. G. Levich, "Dragging of a Liquid by a Moving Plate", *Acta Physicochimica URSS*, Vol. 17, 1942, pp. 42–54.

[9]   F. Schüth, K.S. Sing, J. Weitkamp, "Handbook of Porous Solids", *Wiley-VCH*, 2002.

[10]   J. Rouquerol, D. Avnir, C.W. Fairbridge, D.H. Everett, J.H. Haynes, N. Pernicone, J.D.F. Ramsey, K.S.W. Sing, K.K. Unger, "Recommendations for the characterization of porous solids", *Pure and Applied Chemistry*, Vol. 66, 1994, pp. 1739-1758.

[11]   M.R. Ranade, A. Navrotsky, H.Z. Zhang, J.F. Banfield, S.H. Elder, A. Zaban, P.H. Borse, S.K. Kulkarni, G.S. Doran, H.J. Whitfield, "Energetics of nanocrystalline TiO_2", *Proceedings of the National Academy of Sciences of the United States of America*, Vol. 99, 2002, pp. 6476-6481.

[12]   D. Peckner, I.M. Bernstein, "Handbook of Stainless Steels", *McGraw-Hill Inc.*, 1977.

[13]   I. De Scheerder, J. Sohier, L. Froyen, J. van Humbeeck, E. Verbeken, "Biocompatibility of coronary stent materials: Effect of Electrochemical Polishing", *Materialwissenschaft und Werkstofftechnik*, Vol. 32, 2001, pp. 142-148.

[14]   A. Tourvieille de Labrouhe, " Nanostructured ceramic coatings for deformable medical

implants such as stents", Thesis, Ecole Polytechnique Fédérale de Lausanne, 2009.

[15] H.M. Rietveld, "A profile refinement method for nuclear and magnetic structures", *Journal of Applied Crystallography*, Vol. 2, 1969, pp. 65-71.

[16] M.R. Baklanov, "Determination of pore size distribution in thin films by ellipsometric porosimetry", *Journal of Vacuum Science Technology B*, Vol. 18, 2000, pp. 1385-1391.

[17] H. G. Tompkins, W. A. McGahan, "Spectroscopic Ellipsometry and Reflectometry", *John Wiley & Sons Inc.*, 1999.

[18] Private communication A. Burgeois, Sopra SA., France.

[19] Y.B. Melnichenko, G.D. Wignall, "Small-angle neutron scattering in materials science: Recent practical applications", *Journal of Applied Physics*, Vol. 102, 2007, pp. 021101-021124.

[20] W. Wu, W.E. Wallace, E.K. Lin, G.W. Lynn, C.J. Glinka, E.T. Ryan, H. Ho, "Properties of nanoporous silica thin films determined by high-resolution X-ray reflectivity and small-angle neutron scattering", *Journal of Applied Physics*, Vol. 87, 2000, pp. 1193-1200.

[21] O. Glatter, O. Kratky, "Small Angle X-ray Scattering", *Academic Press Inc.*, 1982.

[22] H. Brumberger, "Modern Aspects of Small-Angle Scattering", *Kluwer Academic Publishers*, 1993.

[23] Private communication J. Kohlbrecher, Paul Scherrer Institute (PSI), Villigen, Switzerland.

[24] R. Richardson, ed. T. Cosgrove, "Scattering and Reflection Techniques", *Blackwell Publishing*, 2005.

[25] J.F. Moulder, W.F. Stickle, P.E. Sobol, K.D. Bomben, "Handbook of X-ray Photoelectron spectroscopy", *Perkin-Elmer Corporation*, 1992.

[26] "NIST X-ray Photoelectron Spectroscopy Database", available at: http://srdata.nist.gov/xps/, December 2008.

[27] A. Tourvieille de Labrouhe, " Nanostructured ceramic coatings for deformable medical implants such as stents", Thesis, Ecole Polytechnique Fédérale de Lausanne, 2009.

[28] N. Kukreja, Y. Onuma, J. Daemen, P.W. Serruys, "The future of drug-eluting stents," *Pharmacological Research*, Vol. 57, 2008, pp. 171-180.

[29] F. Migliavacca, L. Petrini, V. Montanari, I. Quagliana, F. Auricchio, G. Dubini, "A predictive study of the mechanical behavior of coronary stents by computer modeling",

Medical Engineering and Physics, Vol. 27, 2005, pp. 13-18.

[30] Mowiol 3-96®, Product Specification Sheet, available at: http://www.sigmaaldrich.com/catalog/ProductDetail.do?N4=51438|ALDRICH&N5=SEARCH_CONCAT_PNO|BRAND_KEY&F=SPEC, Mai 2009.

[31] ''Mowiol® and Kuraray Poval - materials for 1001 applications'', available at: http://www.kuraray-pva-pvb.eu/start?open&&3, Mai 2009.

[32] D.F. Evans, H.Wennerström, "The Colloidal Domain: Where physics, chemistry, and biology meet", *Wiley-VCH*, 1999.

[33] C.J. Brinker, G.W. Scherer, "Sol-gel science: the physics and chemistry of sol-gel processing", *San Diego, Academic Press Inc.*, 1990.

[34] W.E. Lee, "Ceramic Films and Coatings" *British Ceramic Proceedings Series No. 54, Institute of Materials, Minerals and Mining*, 1995.

[35] T.J. Garino, H.K. Bowen, "Kinetics of constrained-film Sintering", *Journal of the American Ceramic Society*, Vol. 73, 1990, pp. 251-257.

[36] K.P. Kumar, K. Keizer, A.J. Burggraaf, T. Okubo, H. Nagamoto, "Textural evolution and phase transformation in titania membranes: Part 2.-Supported membranes", *Journal of Materials Chemistry*, Vol. 3, 1993, pp. 1151-1159.

[37] G.W. Scherer, T. Garino, "Viscous Sintering on a rigid substrate", *Journal of the American Ceramic Society*, Vol. 68, 1985, pp. 216 – 220.

[38] R.K. Bordia, G.W. Scherer, "On constrained sintering-II. Comparison of Constitutive Models", *Acta Metallurgica*, Vol. 36, 1988, pp. 2399-2409.

[39] T. Garino, B. H. Kent, "Deposition and Sintering of Particle Films on a Rigid Substrate", *Journal of the American Ceramic Society*, Vol. 70, 1987, pp. C-315–317.

[40] R. K. Bordia, A. Jagota, "Crack Growth and Damage in Constrained Sintering Films", *Journal of the American Ceramic Society*, Vol. 76, 1993, pp. 2475–2485.

[41] R.M. German, "Sintering Theory and Practice," *John Wiley & Sons Inc.*, 1996.

[42] M. Stech, P. Reynders, J. Rödel," Constrained Film Sintering of Nanocrystalline TiO_2", *Journal of the American Ceramic Society*, Vol. 83, 2000, pp. 1889-1896.

[43] O. Guillon, L. Weiler, J. Rödel, "Anisotropic Microstructural Development During the Constrained Sintering of Dip-Coated Alumina Thin Films", *Journal of the American Ceramic Society*, Vol. 90, 2007, pp. 1394-1400.

[44] C.G. Windsor, "An Introduction to Small-Angle Neutron Scattering", *Journal of Applied Crystallography*, Vol. 21, 1988, pp. 582-588.

[45] J. Allemann, H. Hofmann, L. Gauckler, "Sintering behaviour of tetragonal zirconia polycrystalline powders", *Ceramic Forum International*, Vol. 67, 1990, pp. 434-442.

[46] P. Bowen, C. Carry, "From powders to sintered pieces: forming, transformations and sintering of nanostructured ceramic oxides", *Powder Technology*, Vol. 128, 2002, pp. 248-255.

[47] D.W. Kim, T.G. Kim, K.S. Hong, "Origin of a Shrinkage Anomaly in Anatase", Journal of the American Ceramic Society, Vol. 81, 1998, pp. 1692-1694.

[48] C. Kim, I. Kwon, B.K. Moon, J.H. Jeong, B. Choi, J.H. Kim, H. Choi, S.S. Yi, D. Yoo, K. Hong, J. Park, H.S. Lee, "Synthesis and particle size effect on the phase transformation of nanocrystalline TiO_2", *Materials Science and Engineering: C*, Vol. 27, 2007, pp. 1343-1346.

[49] E.M. Levin, C.R. Robbins, H.F. McMurdie, "Phase Diagrams for Ceramists", Figure 4258, *The Amercian Ceramic Society*, 1975.

[50] C. Legros, C. Carry, P. Bowen, H. Hofmann, "Sintering of a transition alumina: effects of phase transformation, powder characteristics and thermal cycle", *Journal of the European Ceramic Society*, Vol. 19, Sep. 1999, pp. 1967-1978.

[51] A.A. Gribb, J.F. Banfield, "Particle size effects on transformation kinetics and phase stability in nanocrystalline TiO_2", *American Mineralogist*, Vol. 82, 1997, pp. 717–728.

[52] F. Juillerat, "Self-assembled nanostructures prepared by colloidal chemistry", Thesis, Ecole Polytechnique Fédérale de Lausanne, 2005.

[53] D. Brune, R.Hellborg, H.J.Whitlow, O.Hunderi, "Surface Characterizaion: A User's Sourcebook", *Wiley-VCH*, 1997.

[54] W. Wu, G.H. Nancollas, "Kinetics of Heterogeneous Nucleation of Calcium Phosphates on Anatase and Rutile Surfaces", *Journal of Colloid and Interface Science*, Vol. 199, 1998, pp. 206-211.

[55] R. Rohanizadeh, M. Al-Sadeq, R.Z. LeGeros, "Preparation of different forms of titanium oxide on titanium surface: Effects on apatite deposition", *Journal of Biomedical Materials Research Part A*, Vol. 71A, 2004, pp. 343-352.

[56] T. Shozui, K. Tsuru, S. Hayakawa, Y. Shirosaki, A. Osaka, "XPS study on potential suppression factors suppressing *in vitro* apatite formation on anatase films prepared on various substrates", *Surface and Coatings Technology*, Vol. 203, 2009, pp. 2181 – 2185.

CHAPTER V

5 DRUG-LOADING OF THE THIN TITANIA FILMS AND DRUG-RELEASE

5.1 Background and introduction

This chapter focuses on the loading of the previously presented thin, nanostructured titania (TiO_2)-films with the therapeutical agent paclitaxel (PTX). PTX served as a model drug, because it is used in commercially available drug-eluting stents (DESs) and drug-release studies are available for comparison [1, 2, 3]. Solvent evaporation methods were chosen to incorporate the agent into the coatings. The targeted load was 1 µg/mm^2 geometric surface area of the coating, which is a value consistent with the load of PTX in the commercially available Taxus^{TM} stent [1]. The release of the drug should last several months, corresponding to a release rate smaller than 1 % of initially incorporated drug per day. These specifications were predetermined by the industrial partner of this project and were educed from the Taxus^{TM} stent.

The implantation of the Taxus^{TM} stent into patients suffering from atherosclerosis reduced the restenosis rate to 7.9 % after 6 month of implantation. For comparison, it was as high as 26.5 % for the application of bare metal stents [1, 2]. The *in vitro* release kinetics of PTX from the titania coatings into water and into bovine plasma will be presented and evaluated in the present chapter.

When working with PTX as a pharmacological agent to being incorporated into a drug-delivering coating for stents, one has to consider its chemical and physical features for the processing. PTX has a molecular weight of 853.9 g/mol and a melting point of 213-216 °C. It hydrolyzes in aqueous solutions and undergoes transesterification in methanol [4]. The application of methanol during processing was thus not recommended. The drug exhibits a lipophilic character, which makes it well soluble in different types of glycols or oils, like depicted in Table 5-1. For instance it is soluble in a concentration of 1400 µg/ml in 75 % propylene glycol, 300 µg/ml in soybean oil and 74000 µg/ml in Triacetin. The PTX-molecule, which is shown in Figure 5-1 (a), does not possess suitable chemical functionality, such as having an amine or carboxylic acid for salt formation. Hence it is badly soluble in water and reported solubility concentrations range from 0.3 to 30 µg/ml. The recorded values vary greatly in literature and depend on the experimental conditions [5, 6].

Table 5-1 PTX-solubilities in different solvents and oils.

solvent	*solubility concentration (µg/ml)*
dimethyl sulfoxide (DMSO)	50000 [4]
dichloromethane (DCM)	> 19000 [5]
ethanol	ca. 39000 [5]
acetone (ACET)	not known
ethyl acetate (EA)	103610*
75 % propylene glycol	< 1400 [5]
75% polyethylene glycol 400	31000 [5]
35 % polyethylene glycol 400	30 [5]
soybean oil	300 [5]
triacetin	74000 [5]
water	< 30 [5]
	0. 7; 6; 30; 0. 34 [6]

* determined in the present study as will be explained in Chapter 5.4.2.2

The variations in the PTX-solubilities can be explained by the existence of paclitaxel polymorphs. PTX-dihydrate has an aqueous solubility lower than the anhydrous form, as was reported by Burt *et al*. [6]. The dissolution measured depended on the time PTX was exposed to water and the time when the data points were recorded. A short time after anhydrous crystalline PTX is immersed into water, it has the apparent solubility of the anhydrous form, which is as high as 3 µg/ml. After 12 h it decreases to 1 µg/ml, which corresponds to the solubility of the dihydrated crystalline form [6].

$x=1.299\ nm$
$y=1.020\ nm$
$z=1.609\ nm$

(a)   **(b)**
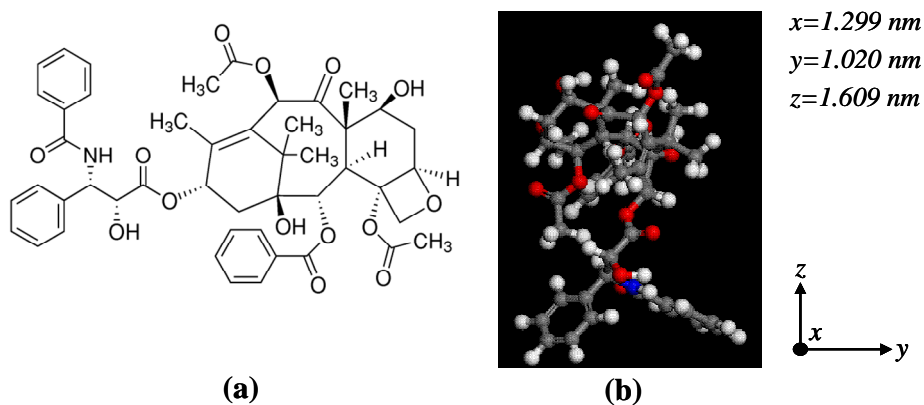
Figure 5-1 (a) molecular structure of paclitaxel [4], (b) 3D-structure and dimensions of a PTX-molecule.

Many pharmaceuticals exist as polymorphs, having different crystalline or an amorphous morphology. The drug molecules in the particular *crystalline* morphologies exhibit different arrangements or conformations in the crystal lattices. The solid *amorphous* drugs feature a disordered arrangement of the molecules. The polymorphs can hence have different chemical and physical properties, such as a different melting point, chemical reactivity, solubility and dissolution rates. Generally, an amorphous form is thermodynamically less stable than any crystalline form. It exhibits a higher apparent aqueous solubility and a higher dissolution rate. In the pharmaceutical industry the most stable polymorph is used to ensure the stability of the drug with time and under environmental conditions [7, 8, 9].

To optimize the PTX-release from the TiO$_2$-coatings, it was therefore interesting to evaluate the effect of the specific PTX-morphology on the release kinetics. The production of the PTX-polymorphs by mainly solvent evaporation procedures has been described in different studies [6, 10, 11]. Lee *et al.* and Burt *et al.* used simple methods, such as infrared-spectroscopy (IR) and differential scanning calorimetry (DSC), to determine the polymorphs of the drug. Typical Fourier-transform IR (FT-IR) spectra of the polymorphs are depicted in Figure 5-2 (a). They clearly show differences in the absorption at several wave number regions. Amorphous PTX exhibits only one carbonyl absorption near 1720 cm^{-1}, whereas all the others show 2 carbonyl absorptions. Other absorption peaks at 1650 and 1522 cm^{-1} also show differences. The thermograms of the PTX-polymorphs displayed in Figure 5-2 (b) illustrate the transitions of PTX during heating. The anhydrous crystalline form of PTX exhibits one endothermic peak in the DSC-thermogram at 224 °C, representing the melting. The decomposition of PTX is shown by the second peak at 240 °C. The plot of the amorphous PTX is characterized by a glass transition at 140 °C before the peak of the exothermic decomposition at 220 °C. The DSC-curve of dihydrated crystalline PTX holds two endothermic peaks close to 100 °C, referring to the PTX-dehydration and the

vaporization of residual solvents. A solid-solid transition is recorded at 160 °C and a melting endothermal peak at 220 °C, before its decomposition. The IR- and DSC-graphs, which are depicted in Figure 5-2, will be used as reference-curves for comparison.
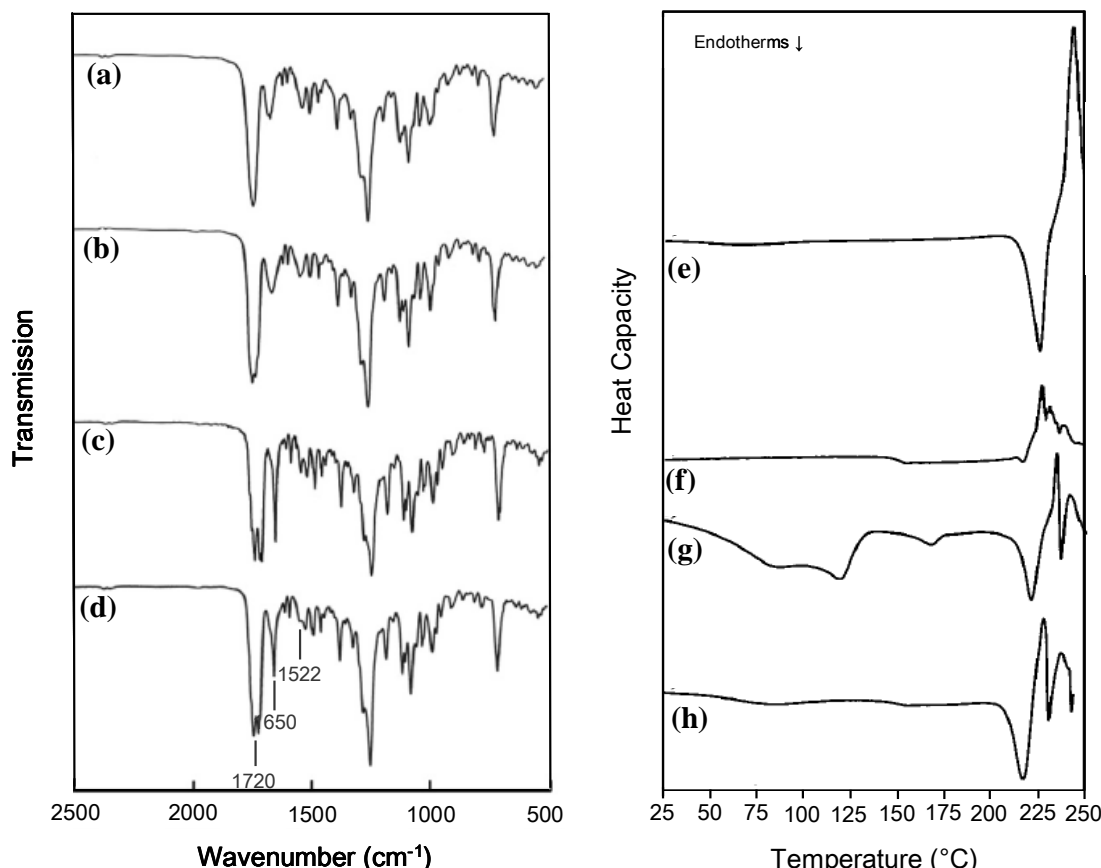
Figure 5-2 Left: IR spectra of PTX-polymorphs (a) amorphous, (b) dihydrated crystalline, (c) anhydrous crystalline and (d) anhydrous crystalline, modified from [11]; right: DSC thermograms of (e) anhydrous crystalline, (f) amorphous, (g) dihydrate crystalline PTX and (h) anhydrous crystalline PTX, modified from Burt *et al.* [6].

When wanting to incorporate PTX into the porous TiO_2-network of the coating, the pore width-to-PTX-size ratio has to be considered. A study of Kuroda *et al.* has shown that PTX was adsorbed in 2-D hexagonal, mesoporous silicas exhibiting pore diameters larger than 1.8 nm. It did not adsorb into channels having pore width less than 1.6 nm [12]. The reason was the size exclusion of PTX by the pores. The longest dimension of the molecule was measured in Figure 5-1 (b) to be 2.067 nm. Hence the molecule was too big to enter the silica pores. In the present study, the pores in the ceramic structure surrounding the reservoirs were bigger, like was shown in Chapter 4.5.2. The median pore width of the porous structure was 76 nm, leading to a ratio of molecule-to-pore diameter, χ, of 0.027. No steric hindrance of the PTX-molecule to penetrate the porous TiO_2-network of the films during drug-loading was therefore expected [13].

The aim of the drug-load and release study was to establish methods and to prove the feasibility to load the nanostructured TiO$_2$-coatings with PTX. The factors influencing the drug-release had to be identified, to eventually adapt the coating to create a sustained drug-release. The target was not to optimize the coating. This will be the scope of future work and depends on the individual application.

5.2   Theory of drug-release kinetics

The measured amount of drug released from a pharmaceutical dosage form as a function of time is a so-called drug-release profile. By applying different mathematical models to the drug-release profiles, the transport mechanisms involved in the drug-liberation can be identified. Some models will now be introduced.

5.2.1   *Korsmeyer-Peppas model*

The Korsmeyer-Peppas model is a semi-empirical model, which can be used to analyze the data of the controlled release of water-soluble drugs from polymers [14, 15]. The model is generally employed when the release mechanism is not well known or when more than one type of release phenomenon could be involved. In the Korsmeyer-Peppas model the fractional release of the drug, M_t/M_0, is exponentially related to the release time t by

$$\frac{M_t}{M_0} = k_{KP} \cdot t^n$$

(5-1),

with M_t: amount of drug released at time t, M_0: the initial amount of drug incorporated into the system and k_{KP} is the Korsmeyer-Peppas release constant, incorporating structural and geometric characteristics of the device. The release exponent n can give information about the transport mechanisms involved. If the drug-delivery occurs from a slab, a release exponent n of 0.5 indicates Fickian diffusion, n between 0.5 and 1 indicates anomalous or non-Fickian transport, which is often termed first-order release. If n equals 1, the transport equates a zero-order release, also known as case-II-transport. A value of n greater than 1 describes a super case II transport, in which the drug-release is faster than in the release following Fickian diffusion or case II transport [14].

By applying this model, the drug amount released as a function of time is fitted by an exponential approximation, which delivers n. Caution has to be given to the following restrictions to apply this model:

- ▪ For the determination of n, only the initial portion of the release curve should be used, in which $M_t/M_0 < 0.6$.

- ▪ Perfect sink conditions during the analysis are required. Thus the concentration in the release media at time t, C_t, should be much smaller than the drug's maximum solubility concentration in that media, C_s. In the present study, sink conditions were set to be fulfilled for C_t $1/3 \cdot C_s$.

- ▪ The diffusion coefficient is concentration-independent.

- ▪ The diffusion occurs one-dimensional, that means that the aspect ratio of the slabs, width over thickness, is at least 10/1.

5.2.2 *Zero order release kinetics*

The release mechanism, in which the drug dissolution and release from the dosage form is constant, is called zero order kinetics. It is the ideal method of drug-release in order to achieve a pharmacological prolonged action. These kinds of formulations are used in some transdermal systems, in matrix tablets with low soluble drugs or in osmotic and reservoir systems. For instance in a reservoir system, the drug is surrounded by a film. The diffusion of the agent through that film is the rate-limiting factor. To maintain a constant flux out of the reservoir systems, the concentration gradient across the membrane needs to be constant. It can be achieved by keeping a constant high drug concentration at the internal wall of the membrane. This is possible by loading a powdered drug into the reservoir, whose concentration at the internal wall of the membrane will be the saturation concentration C_s [15, 16, 17, 18].

The same premises apply for the pure dissolution of a low soluble drug. If the concentration of the drug in solid form is high during a certain period of time, C_i, a constant concentration gradient exists between the saturation concentration at the surface of the solid drug, C_s, and the bulk concentration in the surrounding media, Figure 5-3 (a).

The flux J of the drug can then be described by Fick's law as

$$J = \frac{dM_t}{dt} = -D_{eff} \cdot \frac{dC}{h} \tag{5-2},$$

with M_t: amount of drug dissolved in time t, D_{eff}: effective diffusion coefficient of the drug, dC: concentration difference of the drug between the surface of the solid drug and the surrounding release media, and h: thickness of the stagnant diffusion layer.
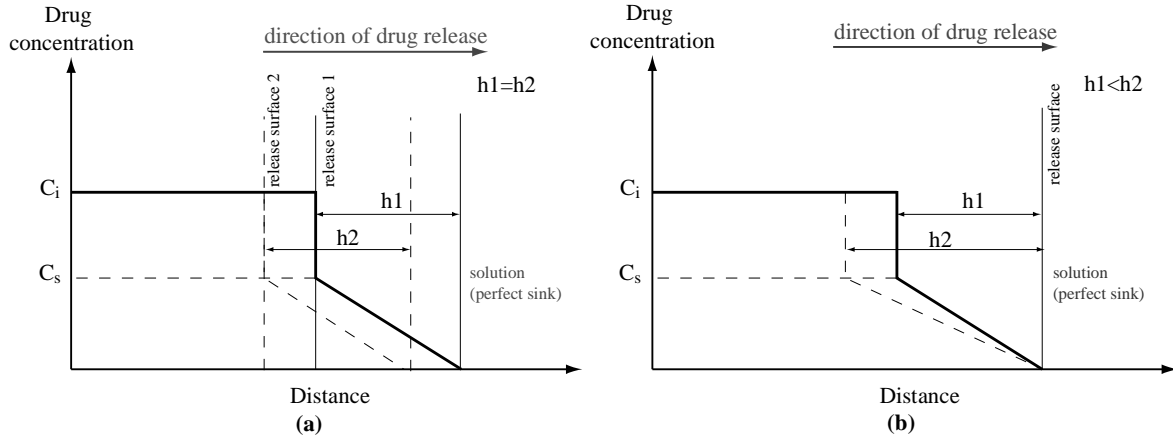
Figure 5-3 Theoretical drug concentration profiles. (a) zero order release, where the concentration gradient and hence the flux into the sink release media is constant. In (b) the Higuchi model, where the release from a matrix in direct contact with the release media, is illustrated ((b) modified from [15]). h represents the thickness of the diffusion layer with h1 at release time t1 and h2 at release time t2, whereas t1 < t2. C_i: initial drug concentration; C_s: saturation concentration.

For the dissolution of a low soluble drug, $D_{eff} \approx D_{SE}$. D_{SE} is the Stokes Einstein diffusion coefficient expressed as

$$D_{SE} = \frac{k_B \cdot T}{6 \cdot \pi \cdot \eta \cdot r_h} \qquad (5\text{-}3),$$

and it describes the self diffusion of a molecule in a media. k_B is thereby the Boltzman constant of $1.381 \cdot 10^{-23}$ J/K, T: temperature, η: dynamic viscosity of the media and r_h: hydrodynamic radius of the molecule [19]. For the drug-release from reservoir systems, another D_{eff} needs to be applied. For microporous membranes in reservoir systems, the flux is then dependent on

$$D_{eff} = \frac{D_{SE} \cdot \varepsilon}{\tau} \qquad (5\text{-}4).$$

The effective diffusion coefficient incorporates structural parameters of the membrane, such as the porosity of the membrane ε and the tortuosity τ of the pores [17]. Integrating Equation (5-2) by keeping the concentration gradient constant and the concentration in the bulk media time-independent, the zero order release model can be deduced as

$$M_t = M_{is} + k_0 \cdot t \qquad (5\text{-}5),$$

with M_{is}: initial amount of drug in solution and k_0: zero order release constant [15], containing D_{eff}. Therefore the plot of M_t as a function of t reveals a straight line with the

slope of k_0. For employing this model the following restrictions exist:

- The pharmaceutical dosage form should not disaggregate,

- The drug is released slowly,

- The area, from which the drug gets released, does not change,

- Perfect sink conditions prevail,

- The diffusion coefficient is independent of the concentration and time,

- And it is valid as long as the saturation concentration is present at the formulation's surface.

5.2.3   *First order release kinetics*

This type of release kinetics is the most common one to describe the dissolution of drugs from pharmaceutical formulations. The Noyes-Whitney equation describes the dissolution of a solid in a liquid media:

$$\frac{dC_t}{dt} = K \cdot (C_s - C_t) \tag{5-6}$$

with C_t: time dependent concentration of the drug in the bulk media, K: first order proportionality constant and C_s: maximum solubility concentration of the drug in the release media. This equation was modified by several scientists assuming that under steady state conditions a thin stagnant fluid layer at the solid surface is build. With the incorporation of Fick's law of diffusion and subsequent integration, Equation (5-7) is derived:

$$\log M_t = \log M_{is} + \frac{k_1}{2.303} \cdot t \tag{5-7}$$

with M_t: amount of drug released at the time t, M_{is}: initial concentration of drug in solution and with the first order release constant

$$k_1 = \frac{D \cdot S}{h \cdot V} \tag{5-8}$$

D is the diffusion coefficient in the dissolution media ($\approx D_{SE}$), S: the solid area accessible to dissolution, h: width of the diffusion layer and V: volume of the liquid release media [15]. A graph of the decimal logarithm of the released amount of drug versus time will be linear and the slope will represent $k_1/2.303$. The premises to apply this model are:

- The released amount of drug decreases with time,

- A constant area is accessible to dissolution,

- And perfect sink conditions exist during the experiment.

5.2.4   *Higuchi model*

The last model of interest in this study is the Higuchi model. It describes the release of solid drugs incorporated into solid matrices. The release from a planar system, which has a granular matrix from which the drug diffusion occurs through intergranular openings, can be described by

$$\frac{M_t}{M_0} = \sqrt{\frac{D \cdot U}{\tau}\left(2 - U \cdot C_s\right) \cdot C_s \cdot t} = k_h \cdot \sqrt{t} \tag{5-9},$$

with M_t: amount of drug released in the time t, M_0: initial amount of drug incorporated into the matrix, D: diffusion coefficient of the drug in the permeating liquid, U: specific volume of the drug in the porous structure (1/density of the drug, when M_0 is expressed in mass per volume), C_s: solubility of the pharmaceutical in the media, τ: tortuosity of the pores and k_h: Higuchi dissolution constant [20]. Therefore a plot of the fractional amount of drug released as a function of square root of time should yield a straight line, in which the slope represents k_h. Some restrictions to apply the model have to be made:

- The elution test should be performed in perfect sink conditions,

- The cross sectional area of the diffusion path is reduced by a porosity factor and the diffusion front in the matrix changes as is illustrated in Figure 5-3 (b),

- The model is valid as long as $C_i > C_s$.

5.3   Materials and methods to quantify paclitaxel and to characterize its solid state

The quantification of paclitaxel (PTX) in the liquid phase by high performance liquid chromatography (HPLC) and extraction will be described in the first part of this section. The production of PTX-polymorphs will further be documented, the methods for the drug-load and release studies explained.

5.3.1 Paclitaxel

Paclitaxel (PTX) as a white powder was purchased from Sigma-Aldrich (T1912, min. 97 % purity by HPLC) and used in pre-tests of the drug-load and release studies. It was named PTX_S. A second batch of PTX, PTX_K, was bought from Knowshine (Shanghai) Pharmachemicals Inc. (99.8 % purity by HPLC) and applied in the main drug-load and release experiments.

5.3.2 Quantification by high performance liquid chromatography

When PTX was dissolved in ultrapure water (UP-water, MilliQ-Systems), acetonitrile (AcN, Biosolve, HPLC grade), or a mixture of both, it was quantified by high performance liquid chromatography (HPLC). The HPLC-system consisted of an Alliance 2690 pump module (Waters) connected to the analytical column ODS-3 (Inertsil®, particle size 5 µm; 4.6 x 150 mm), which was protected with an ODS-3 conventional guard column (Inertsil®, particle size 5 µm; 4.6 x 50 mm). The analysis procedure applied in this study was adapted from S.-H. Lee *et al*. [21] and M.S. Alexander *et al*. [22]. The mobile phase consisted of UP-water and AcN in a gradient elution, Table 5-2. The flow rate was set to 1 ml/min. Detection was performed at 227 nm with a Photodiode Array Detector 996 (Waters) with connection to the Millenium 3.05.01 software data station (Waters). 100 µl of each sample were injected via autosampler for analysis. The absorption of PTX as a function of retention time was recorded in the chromatograms.

Calibration curves of PTX_S and PTX_K were obtained either in pure AcN, a mixture of AcN/water of 50/50 %vol or in UP-water. Therefore a stock solution of ~ 500 µg/ml PTX was prepared by weighing the appropriate amount of PTX with a thermo-balance (TG50, Mettler) and diluting it in AcN in a 10 ml glass screw vial. This solution was mixed by a vortex mixer (REAX 2000, Heidolph) for 2 min prior to its application. Standard solutions in known concentrations were prepared from the stock solution by dilution with the appropriate solvent or solvent/UP-water mixture. They were injected into the HPLC-system by an autosampler. The PTX-peak in the recorded chromatogram was integrated to obtain its area, which was proportional to the concentration of PTX in the standard. Standards were each prepared and measured in triplicates. Calibration curves were finally deduced from the linear regression of the mean measured peak areas of the standards as a function of the defined concentrations of PTX. Sample analysis was performed in the same way. During the continuous analyses, an external standard was analyzed each 5 injections to evaluate eventual drifts of the PTX-peak positions and areas.

Table 5-2 Elution gradient used for the quantification of PTX by high performance liquid chromatography.

time (min)	AcN (%vol)	UP-water (%vol)
0	20	80
2	20	80
20	80	20
22	100	0
24	40	60
26	20	80

5.3.3   *Liquid-liquid extraction from bovine plasma*

If PTX was incorporated into bovine plasma, a liquid-liquid extraction had to be performed prior to the quantification by HPLC. If this step would not have been accomplished, the ions, proteins and other components of the plasma would have blocked the analytical column during the HPLC-analysis. The extraction method to transfer PTX from bovine plasma (2-18F00-I, Amimed) into AcN for HPLC analysis was adopted from S.H. Lee *et al.*, who reported a PTX-recovery rate of greater than 97 % [21].

In order to determine the recovery efficiency of PTX from the plasma, preliminary tests were performed, in which plasma samples were spiked with known concentrations of the drug. A *stock solution S1* of PTX in AcN at a concentration of 520 µg/ml was prepared like described in the previous section. In a next step, *standard solutions* in the concentrations of 10.4; 1.04; 0.83; 0.62; 0.42; 0.21; 0 µg/ml PTX in plasma were prepared in 10 ml glass screw flasks. Each *standard solution* was vortex mixed for 1 min to disperse PTX well in the plasma. 750 µl were each pipetted into 2 ml cryogenic vials (Nalgene) and the same volume of tert.-butyl methyl ether (TBME, Riedel-de-Haën, min. 99.7 % purity) was added to each of the aliquots, Figure 5-4. The following procedure was composed of two identical cycles. After mixing the two phases TBME and plasma with PTX and centrifugation, the organic phase, which was enriched with PTX, was pipetted into a 2 ml HPLC glass vial (Infochroma AG). The residual PTX in plasma was subjected again to the extraction cycle. The organic phase with PTX of the second run was added to the one of the first run. After TBME was evaporated at room atmosphere for 120 h, the dry PTX in the vial was reconstituted with 1.5 ml AcN and then injected into the HPLC for quantification.

The percentage extraction recovery of PTX was determined by comparing the PTX-peak-area ratios from standard solutions of the appropriate concentrations (PTX in AcN) with those obtained in the samples subjected to the complete extraction procedure. Extraction recovery was determined as the mean (± SEM) of 3 samples after ANOVA statistical analysis using the software of Statistical Design of Experiment by J. Lemaître, EPFL [23]. The error risk was set to 5 %. The PTX-plasma-eluates from the release test

R_LP$_{EA}$1_plasma were exposed to the same procedure prior to quantification by HPLC.
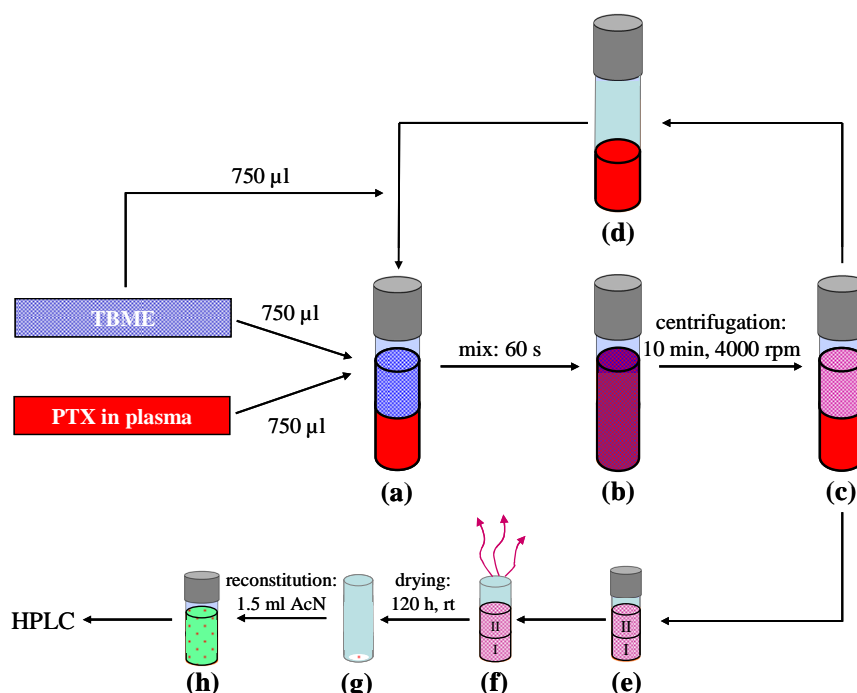
Figure 5-4 Schemata of the extraction of PTX from plasma. 750 µl of each, PTX in plasma (red) and TBME (blue) were transferred into a cryo vial (a). They showed separated phases with TBME being at the top. After mixing for 60 s, both phases were well dispersed (b). The phases were again separated after centrifugation (c) with PTX in the TBME-organic phase on top, plasma plus residual PTX at the bottom. The organic phase was transferred with a pipette into the 2 ml HPLC vial (e, I) and the residual PTX in plasma (d) reconstituted with 750 µl TBME (a). The steps up to (d) were repeated. The second PTX-TBME organic phase (II) was added to the fist one (e). TBME was then evaporated (f) for 120 h at room temperature (rt) and dry PTX was left in the vial (g). It was re-constituted with 1.5 ml AcN (h) and analyzed by HPLC.

5.3.4 *Solid state of paclitaxel by infrared spectroscopy and differential scanning calorimetry*

PTX can exist in different polymorphs, like anhydrous crystalline, dihydrous crystalline or amorphous [6, 10, 11]. It is crucial to know the solid state of PTX to understand and modify its release behavior from the thin porous TiO$_2$-films. IR-spectra of the drug were accomplished with a powder *FT-IR spectrometer* (Spectrum One, Perkin Elmer Instruments). The spectra were obtained by placing the powder or the drug-loaded coatings onto the sample holder. A spectral width of 4000-500 cm^{-1} and a spectral resolution of 4 cm^{-1} were applied to record the spectra.

Differential scanning calorimetry (DSC)-measurements were employed to determine the crystallinity of PTX. Samples were placed in an aluminum crucible, in which two

pinholes were made on top. The cell of the calorimeter (DSC 25, Mettler Toledo) was purged with nitrogen flow of 20 ml/min and the samples were heated with a rate of 5 °C/min. The flux of heat was recorded as a function of time. The DSC-measurements were performed using only one replica, because the available amount of PTX was limited.

5.3.5   *Production of paclitaxel polymorphs by solvent evaporation*

Assays were performed to modify the PTX-morphology by solvent evaporation [10, 11]. The drug was dissolved in a concentration of 50 mg/ml in different solvents and pipetted onto a TiO$_2$-surface, Table 5-3. The solvents of interest were dichloromethane (DCM, VWR/Prolabo, min. 99.5 %), acetone (ACET, Fluka, min. 99.5 % purity), ethyl acetate (EA, Fluka, min. 99.5 % purity) and dimethyl sulfoxide (DMSO, CHROMASOLV, Sigma-Aldrich, min. 99.7 % purity). In addition to the usage of the pure solvents, 1 ml UP-water (MilliQ-system) was dispersed on the TiO$_2$-coating and the same volume of PTX/solvent mixture added to it. PTX as a solid was obtained by evaporating the solvent or solvent/water mixtures at 60 °C for 48 h in a heat and drying cabinet (Rumed®). PTX was then scratched off the TiO$_2$-coating with a spatula prior to its chemical analysis by FT-IR spectroscopy and the analysis of its physical properties by DSC.

Table 5-3 Solvents and solvent/water mixtures, which were used to prepare PTX-polymorphs by a solvent evaporation technique.

sample	*solvent*	*concentration of solvents (%vol/%vol)*
DMSO_w730NRL	DMSO	100/0
WDMSO_w730NRL	DMSO/water	50/50
DCM_w730NRL	DCM	100/0
WDCM_w730NRL	DCM/water	50/50
ACET_w730NRL	ACET	100/0
WACET_w730NRL	ACET/water	50/50
EA_w730NRL	EA	100/0
WEA_w730NRL	EA/water	50/50

5.4   Materials and methods for the drug-loading of the films and the drug-release

5.4.1   *Titania films*

Two different nanostructured titania coatings were prepared on wafer supports and used to study the drug-loading. One type was the non-reservoir layer (NRL) w730NRL, the second one was the reservoir layer (*RL*) w730*RL*s. Both films were sintered at a maximum

sintering temperature of 730 °C. The structures of both were well characterized, Chapter 4. The NRLs were used to establish the drug-loading procedure and to test the reproducibility of the PTX-load in the coating in *pre-tests*. *RL*s, which are to be applied on the stent-implant, were finally loaded with PTX in *main tests*.

5.4.2 *Drug-loading procedures*

To load PTX into the titania layers, parameters of two loading procedures were varied arbitrarily in the initial steps of development. In the first procedure, PTX was dissolved in different solvents and loaded into the coating at atmospheric pressure. In the second method, PTX was dissolved in two selected solvents and incorporated into the coating at lower pressure.

5.4.2.1 *Drug-loading at atmospheric pressure*

The objective of applying atmospheric pressure during the drug-loading was to form different morphologies of PTX in the coatings [11]. In the present test, only NRL titania films were employed. No *RL*s were applied, to avoid deviations in the PTX-load caused by variations in the reservoir densities. The preparation of the drug/solvent solutions involved the dissolution of 50 mg PTX_S in 1 ml of each of the solvents: dichloromethane (DCM), acetone (ACET) or ethyl acetate (EA) at room temperature. The rectangular shaped TiO_2-coated plates, which had a size of $1.5 \times 4 \times 7 \cdot 10^{-5}$ cm, Figure 5-5, were first dried at 100 °C in a dry and heat cabinet (TC100, Thermocenter) to evaporate adsorbed water from the porous structure (step 1, Table 5-4). They were then manually immersed into the PTX/solvent solutions, step 2.
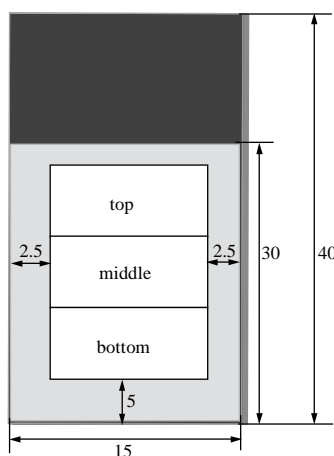
Figure 5-5 Schemata of a TiO_2-coated silicon wafer plate, which was cut after drug-loading to obtain small samples (top, middle, bottom) for the drug-load quantifications and the drug-release experiments (all dimensions in mm).

After 48 h the PTX/solvent solution penetrated throughout the capillaries of the coating and the specimens were pulled out of the solution manually. They were dried for 10 min at room atmosphere, step evaporation 1 in Table 5-4. To then trigger a certain morphology of the drug in the coating, some of the samples were immediately immersed into UP-water for 30 s, while manually agitating. Samples, which were loaded with PTX dissolved in ACET and rinsed in UP-water, were called WACET_w730NRL, the ones loaded with PTX in DCM and rinsed with water WDCM_w730NRL, and the ones loaded with PTX dissolved in EA and rinsed with water WEA_w730NRL. Drug-loaded specimens, which were not rinsed with water, were termed ACET_w730NRL if a solution of PTX in ACET was applied, DCM_w730NRL when PTX in DCM was used and EA_w730NRL when PTX in EA was employed during the drug-loading. A second drying step in the climatic test cabinet (RUMED®) at 37 °C and 10 % relative humidity in the dark followed for all samples. Blank reference specimens, which did not contain PTX, underwent the same drug-loading procedure, except that pure solvents were applied.

Prior to the determination of the quantity of loaded drug, the plate shaped samples in Figure 5-5 were cut by a diamond knife into small pieces called top, middle and bottom. Only these parts of the plates were used for the drug quantification and release experiments. The residual parts close to the edges of the plates were not applied, because they contained an inhomogeneous PTX-content, as will be demonstrated later.

5.4.2.2   Drug-loading with a low pressure technique

The objective of the drug-loading using a low pressure technique was to better control and to increase the PTX-load compared to the one achieved by the atmospheric pressure technique. Attention had to be given to the solvent's boiling point when exposing the PTX/solvent solution to low pressure. Because if one would apply a pressure lower than the saturation pressure of the PTX/solvent solution, it will boil and thus might lower the activity of the pharmaceutical. The saturation pressures of the different solvents were estimated by the Clausius Clapeyron equation

$$\ln\left(\frac{p}{p_2}\right) = \frac{\Delta H_v}{R} \cdot \frac{(T_1 - T_2)}{T_1 \cdot T_2}$$

(5-10),

with p: atmospheric pressure of 1.0133 bar, p_2: saturation pressure of the solution at the temperature T_2, ΔH_v: evaporation enthalpy of the solution, R: gas constant of 8.3145 J/(mol · K), T_1: boiling point of the solution at room temperature, T_2: room temperature. The results listed in Table 5-5 clearly showed that the saturation pressures of

DCM, ACET and DMSO were already reached at 593, 327 and 522 mbar. For EA a lower
saturation pressure of 150 mbar was calculated. The parameters in the drug-loading
procedure were thus adapted to not reach the solvents' boiling points.

Table 5-4 Parameters of the drug-loading at atmospheric pressure.

name of procedure	AP_{DS}	
coating specification	NRL	
step	parameter	value
1 drying	time (h)	48
	temperature (°C)	100
2 immersion	solvent	DCM, ACET, EA
	type of PTX	PTX_S
	concentration PTX (mg/ml)	50
	time (h)	48
	temperature (°C)	22 ± 2
	pressure (bar)	1
3 pull	method	manual, sequentially
4 evaporation 1	time (min)	10
	temperature (°C)	22±2
	pressure (bar)	1
5 rinsing	solvent	H_2O
	time (s)	30
	temperature (°C)	22 ± 2
	pressure (bar)	1
6 evaporation 2	time (min)	30
	temperature (°C)	60
	pressure (bar)	1
7 repetition	number of total dips	1
8 drying 2	temperature (°C)	37
	time (h)	24
	relative humidity (%)	10
	dark (y/n)	y

Table 5-5 Calculated saturation pressures of the solvents, which were applied in the drug-loading procedures.
ΔH_v: evaporation enthalpy of the solution; T_1: boiling point of the solution at 20 °C and 1 bar; p_2: saturation
pressure of the solution.

solvent	ΔH_v (J/mol K) [24]	$T_{1(20°C, 1bar)}$ (°C) [24]	$p_{2(25°C)}$ (bar)
DCM	28.1	40	0.593
ACET	29.7	56	0.327
EA	32.1	77	0.148
DMSO	52.9	189	0.522

Drug-loading of the titania coatings was performed at lower pressure in a modified
embedding chamber (Epovac, Struers), like illustrated in Figure 5-6. Plate shaped samples
were prepared by a drying step at 100 °C in a dry and heat cabinet, to evaporate water in the
porous structure (step 1 in Table 5-6). They were then mounted-without cutting-onto the

holder in the embedding chamber and a low pressure was applied to "evacuate" the porous structure (step 2 in Table 5-6). By dipping the samples into the PTX/solvent solution at low pressure (step 3) and applying atmospheric pressure (step 4), the liquid was forced to penetrate the porous network. The samples were pulled out either all at ones (LP$_{DMSO}$) or consecutively (LP$_{EA}$) manually after a certain time (step 5 in Table 5-6). The solvent was evaporated at varying conditions (steps 6 to 8). Upon completion of the drug-loading and in order to preclude undesirable PTX clusters on top of the TiO$_2$-surface, specimens in LP$_{EA}$2 were immersed into solutions of different concentrations of AcN in UP-water. They were manually agitated for 30 s before they were pulled out (step 11). Accordingly specimens were dried in a final step (step 12). Blank reference samples without PTX were prepared by performing exactly the same drug-loading, except that a pure solvent was applied instead of the PTX/solvent solution.
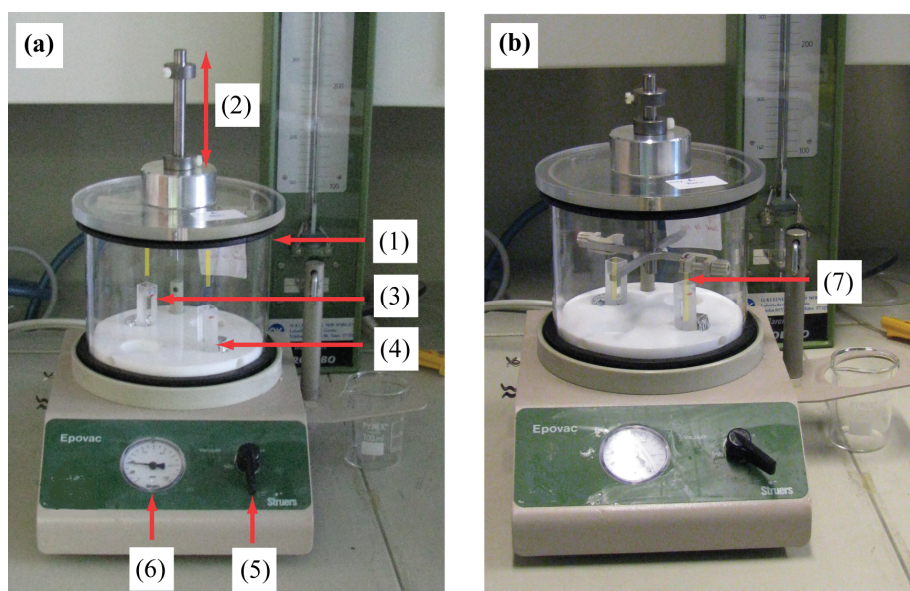
Figure 5-6 Chamber to perform drug-loading at lower pressure. (a) preparation of samples under low pressure in a plexi-glass chamber (1) with an elevating mechanism (2) in the lid of the chamber, on which the samples (yellow) were attached. The solutions in the cuvettes or beakers, (3) PTX-solution and (4) solvent solution as a reference, were mounted in a base plate in the chamber. With the pressure regulator (5) the pressure in the chamber was adopted (6). In (b) a dip of the samples (7) into the solutions is illustrated.

Three different drug-loading methods were applied to study the influence of different process parameters on the drug-load, Table 5-6. The method LP$_{DMSO}$ was used to study the reproducibility of the PTX-load into the NRLs and to evaluate the effect of 1 compared to 4 consecutive dips into the PTX/DMSO solution, which had a concentration of 10 mg/ml. Dimethyl sulfoxide (DMSO) was used, because it is commonly employed as a carrier for pharmaceuticals in medicine, it is water soluble and the maximum solubility of PTX in it was known to be 50 mg/ml [4].

The drug-loading method $LP_{EA}1$ was applied to study the effect of the immersion time, step 4 in Table 5-6, onto the total drug-load. The maximum solubility concentration of PTX in EA was not found in literature. It was determined by consecutively adding PTX_K into EA, stirring the solution for 5 min with a magnetic stirrer at 300 rpm at room temperature and observing the opacity of the solution. If the solution was transparent after each stirring period, more PTX was added. As soon as the solution stayed cloudy, it was assumed to be saturated. Thus the saturation concentration was deduced to be 103.61 mg/ml.

In $LP_{EA}2$ the effect of rinsing after the drug-loading to remove undesired PTX on top of the surface was evaluated. The PTX-loaded coatings were therefore immersed into a solution of acetonitrile (AcN) and UP-water in different concentrations or into EA for 3 s. SEM-micrographs were taken and the residual quantity of PTX in the coatings determined by HPLC, cf. Chapter 5.4.4.

Because the PTX/solvent solution already had to be situated in the embedding chamber at lower pressure during step 2, a suitable time had to be chosen for that step to avoid the total evaporation of the solvent and hence an up-concentration of PTX in the solution. The time for step 2 in the methods $LP_{EA}1$ and $LP_{EA}2$ was set by performing an evaporation experiment of EA. Therefore two quartz cuvettes (Hellma) with each an open area of 1 cm^2 were filled with 1.6 g of EA. They were then exposed to 350 mbar in the embedding chamber. After each 20 min, up to a total time of 120 min, the cuvettes were taken out and weighted. A curve of the mean mass of EA as a function of time it was exposed to lower pressure was plotted. Its slope correlated to the evaporation rate of EA.

Table 5-6 Parameters used for the drug-loading with the low pressure technique.

Name of procedure			*LP$_{DMSO}$*	*LP$_{EA}$1*	*LP$_{EA}$2*
coating specification			*NRL*	*NRL, RL*	*NRL, RL*
step	*parameter*		*value*		
1 drying 1	time (h)		24	24	24
	temperature (°C)		100	100	100
2 low pressure	time (min)		30	10	10
	temperature (°C)		22±2	22±2	22±2
	pressure (bar)		0.200	0.350	0.350
3 immersion	solvent		DMSO	EA	EA
	concentration PTX (mg/ml)		10	103.61 ± 21.82	103.61 ± 21.82
	time (s)		30	60	60
	temperature (°C)		22 ± 2	22 ± 2	22 ± 2
	pressure (bar)		0.200	0.35	0.35
	position sample		in solution		
4 high pressure	time (h)		0.02	0.02; 0.5; 1; 5; 24	24
	temperature (°C)		22 ± 2	22 ± 2	22 ± 2
	pressure (bar)		1	1	1
	position sample		in solution		
5 pull	method		manual, all at once	manual, sequentially	manual, sequentially
6 evaporation 1	time (min)		2	2	2
	temperature (°C)		22±2	22±2	22±2
	pressure (bar)		1	1	1
7 evaporation 2	time (min)		25	60	60
	temperature (°C)		22±2	22±2	22±2
	pressure (bar)		0.200	0.350	0.350
8 evaporation 3	time (min)		30	30	30
	temperature (°C)		60	60	60
	pressure (bar)		1	1	1
9 repetition	number of total tips		1; 4	1	1
10 drying 2	time (h)		24	24	24
	temperature (°C)		37	37	37
	relative humidity (%)		10	10	10
	dark (y/n)		y	y	y
11 rinsing	solvent		-	-	AcN in UP-water (%vol): 0; 20; 40, 60; 80; 100 EA: 100 %vol
	time (s)		-	-	3
	temperature (°C)		-	-	22
	pressure (bar)		-	-	1
12 drying 3			-	-	cf. step 10

5.4.3   Microscopy

Photos of the drug-loaded coatings, which were cut from the top, middle and bottom position of the plate shaped samples illustrated in Figure 5-5, were taken by a light microscope (MZ8, Leica). The correct, geometric area of these samples was subsequently determined analyzing the images by the imaging software ImageJ (V 1.38x). The drug-loaded films were furthermore examined at higher resolution by an optical microscope (Olympus B071). Micrographs of the cross sections of the drug-loaded, nanostructured titania film samples were taken by a high resolution scanning electron microscope (HRSEM, XL-30SFEG, Philips).

5.4.4   Quantification of the total drug-load

After the plate shaped specimens depicted in Figure 5-5 were loaded with PTX, the amount of pharmaceutical in the porous coating was determined. Simple weighing was not possible, because the amount of PTX was below the detection limit of the balances. The only way to quantify was by first cutting the big plates in Figure 5-5 into the small pieces called top, middle and bottom with a diamond knife. Their geometric area was determined by microscopy, cf. Chapter 5.4.3. No slices, which were cut close to the edges of the plates, were employed for the quantification. The droplet formation of the PTX/solvent solution on the edges of the sample after withdrawal from the solution has caused an inhomogeneous PTX-load in the region close to the edges. The small samples were then each transferred into a 2 ml, glass HPLC vial and 1.5 ml AcN added to any of them. After 1 hour of agitation with 250 1/min (VIBRAX VXR basic, IKA) at 37 °C, PTX was dissolved in the coating and was diffused into the surrounding AcN. The titania coated supports were removed from the HPLC vial and the PTX/AcN solution stored at -81 °C (-86 Ultralow freezer, NUAIRE[TM]) prior to their analysis by HPLC. From the determined concentration of PTX in AcN by chromatography, the PTX-load as mass per geometric area was calculated.

That the total amount of PTX was diffused out of the coating into AcN after 1 h of agitation was verified at the early stages of this study. Thereby the drug-loaded specimens were exposed to AcN for 3 h, whereas AcN was re-freshed every hour. The PTX in all of these solutions was quantified. PTX was only measured in the eluate after 1 h. The concentrations in the eluates after 2 and 3 h were below the detection limit of the HPLC and were estimated to be maximal 0.0015 % of the initially incorporated amount of PTX, and hence negligible.

5.4.5   Drug-release tests into water and bovine plasma

The PTX-release from the titania coatings was studied in elution tests, using either UP-water or bovine plasma as elution media. Water was applied for simplification, because the eluates did not need to be subjected to the extraction step prior to the injection into the HPLC. Hence the results were obtained in a reasonable time and could be compared to simulations. PTX, which was eluted into plasma, had to be extracted from the plasma prior to the analysis by HPLC. This was accompanied by a bigger working effort and only selected titania coatings were used for this test.

After the drug-loaded plates were cut into small pieces from the regions top and middle of the plates in Figure 5-5, their geometric area was determined by microscopy as was previously described in Chapter 5.4.3. Each small drug-loaded sample was transferred into a 2 ml HPLC glass vial and 1.5 ml media, UP-water or plasma, added. After slight agitation at 250 1/min at 37 °C in the dry and heat cabinet for a designated time, the specimens were each transferred into a fresh HPLC vial and reconstituted with 1.5 ml fresh media. They were again placed into the dry and heat cabinet for the next time interval. This procedure was repeated multiple times, according to Table 5-7. The time points for the total exchange of the media were varied from test to test, because appropriate time spans for each interval had to be found. They depended on the maximum dissolution concentration of PTX in that particular media and on the detection limit of PTX by the HPLC method. Furthermore the diffusion of PTX from the films depends on a concentration gradient of the drug between the coating's surface and the surrounding media. To not limit the diffusion, the gradient had to be kept at perfect sink conditions. Those were defined in Chapter 5.2: the concentration of PTX in the media should always be lower or at most 1/3 of its maximum solubility concentration in that media.

The PTX/media solutions, obtained in each elution interval between the total exchange of the media, were stored at -81 °C prior to extraction and/or analysis by HPLC. Because PTX strongly adsorbs on various surfaces, each eluate was vortex mixed for 30 s to detach it from the glass vial before the analysis [25]. 750 µl of each eluate of PTX in water were transferred into a 2 ml HPLC glass vial. The same volume of AcN was added to stabilize the drug in solution and to keep it detached from the vial's wall to allow the application of the auto-sampler of the HPLC.

The quantification of PTX in the plasma-eluates of the test R_LP$_{EA}$1_plasma was achieved by performing a liquid-liquid extraction (cf. Chapter 5.3.2) followed by HPLC-analysis. A Taxus Express^{2TM} stent (Boston Scientific) was also subjected to the release test into bovine plasma for comparison. In each drug-release test, drug-loaded and non-drug-

loaded coatings were used, each in triplicates, Table 5-7.

Table 5-7 Parameters of the *in vitro* drug-release tests of PTX from the TiO$_2$-coatings.

release test	*loading procedure*	*sample*	*release media*	*time points*
R_AP$_{DS}$	AP$_{DS}$	DCM_w730NRL ACET_w730NRL EA_w730NRL WDCM_w730NRL WACET_w730NRL WEA_w730NRL w730NRL (blank)	UP-water	1; 5; 10 h; 1; 2; 3; 4 d
R_LP$_{EA}$1_water	LP$_{EA}$1, 24h	EA_w730*RL* w730*RL* (blank)	UP-water	1; 2; 3; 4; 5; 6; 7; 8; 9; 10; 11 h 1; 1.5; 2; 3; 4; 6; 7; 8; 9; 10; 11; 13; 14; 15; 16; 17; 18; 20; 21; 22; 23; 24; 25; 27; 28; 29; 30; 31; 32 d
R_LP$_{EA}$1_plasma	LP$_{EA}$1, 24h	EA_w730*RL* w730*RL* (blank) Taxus^{TM} stent*	plasma	0.5; 1; 2; 3; 4; 5; 6; 7 d

* specification: Taxus Express^{2TM}, Monorail, 3.5 x 24 mm, Boston Scientific

5.4.6   *Surface wettability by contact angle measurements*

The contact angles of the PTX-loaded coatings with water were measured with an OCA 35 (Data Physics Instrument GmbH). 2 µl of water were placed manually on the surface of the sample. After 20 s, a photo was taken and the contact angle automatically evaluated by the software SCA20.

5.4.7   *Simulation of the diffusion coefficient*

Simulation of the free diffusion coefficient of PTX in water was performed by U. Aschauer, LTP, using the molecular dynamics software MS Modeling v4. (Accelrys Software Inc). One molecule of PTX was placed into a cubic amorphous cell of water molecules. The cell had a side length of 2.9 nm. The mean square displacement of PTX in the amorphous water during 0.5 ns was simulated. The self diffusion coefficient of PTX could then be calculated from that value.

5.5   Results

5.5.1   *Validation of the high performance liquid chromatography and the extraction methods*

A representative chromatogram of paclitaxel (PTX) in acetonitrile (AcN), as obtained by high performance liquid chromatography (HPLC), is presented in Figure 5-7. PTX eluted with a single sharp peak from the analytical HPLC-column at a retention time of 18.6 min.
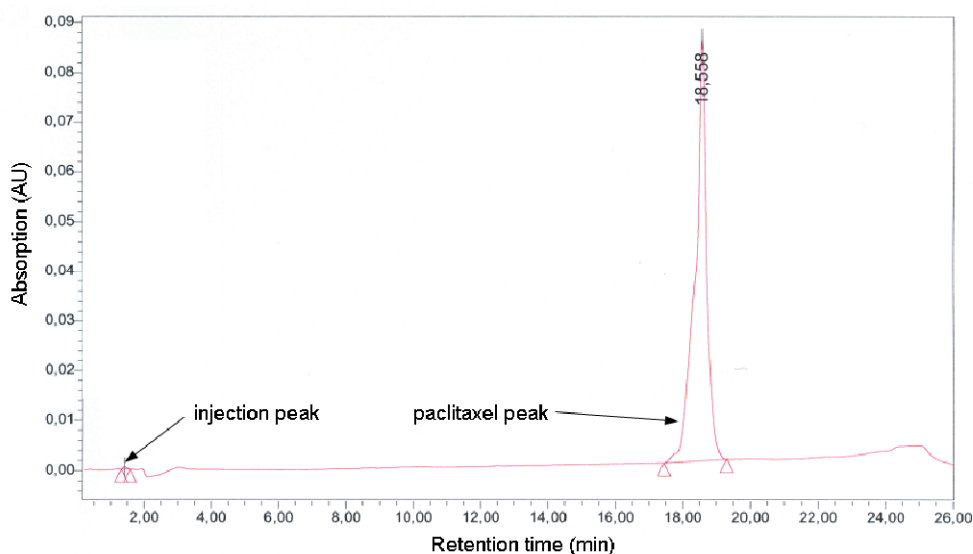
Figure 5-7 Chromatogram of a paclitaxel standard in acetonitrile.

Calibration curves were measured for each of the two types of PTX applied, PTX_S and PTX_K, in ultra pure (UP)-water, AcN and in AcN/UP-water in a mixing ratio of 50/50 vol%. To establish the calibration curves in various solvents was necessary, because they were employed to quantify the PTX-loads in the nanostructured titania coatings, as well as to study its drug-release in *in vitro* release tests. Examples of the calibration curves of PTX_K in AcN and AcN/UP-water are depicted in Figure 5-8. Linearity between the PTX-peak areas and its concentrations were accepted, when the correlation coefficient R^2 between the measured data and the linear regression was bigger than 0.9900. Typical equations of the linear regression and the regression coefficients are pointed out for the particular calibration curve in the graphs. Depending on the concentrations of PTX detected in the media of the drug-release tests, additional calibration curves to the ones in Figure 5-8 were measured, to quantify in this particular PTX-concentration range. The limit of detection of PTX in AcN/UP-water was measured to be at a concentration of 0.02 µg/ml. This was the concentration, at which the signal to noise ratio was 3:1 [26].
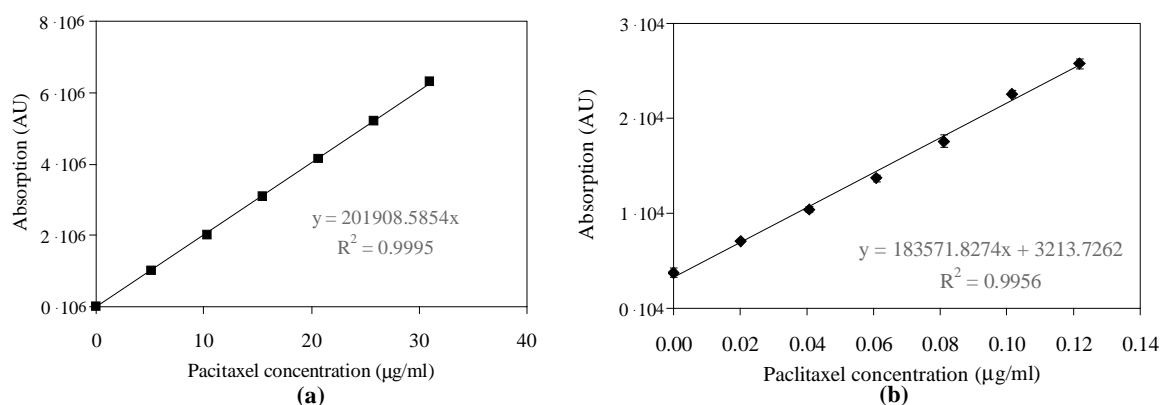
Figure 5-8 Calibration curves of paclitaxel in (a) acetonitrile and in (b) a mixture of acetonitrile and water.

To evaluate the efficiency of the extraction of PTX from plasma, the plasma, which was spiked with known concentrations of PTX, was subjected to the liquid-liquid extraction. The PTX-concentrations of these extracts were then analyzed by HPLC and linear related to the known peak areas. A typical equation obtained by regression of the data points was $y = 193887 \cdot x$ with a correlation coefficient of 0.9958. The extraction recovery of PTX with the applied method was 96.54 % for a concentration range of spiked plasma of 0.2 to 1 µg/ml, Figure 5-9. The detected recovery rate was similar to the one recorded by Lee *et al.* [21]. No significant differences of the PTX-recovery between the measured mean values at the particular concentrations were detected after analysis of variance (ANOVA) with an error risk of 5 %. Hence the extraction efficiency was alike at the depicted concentration interval. The method of liquid-liquid extraction hence could be applied for the quantification of PTX in plasma in the *in vitro* drug-release tests.
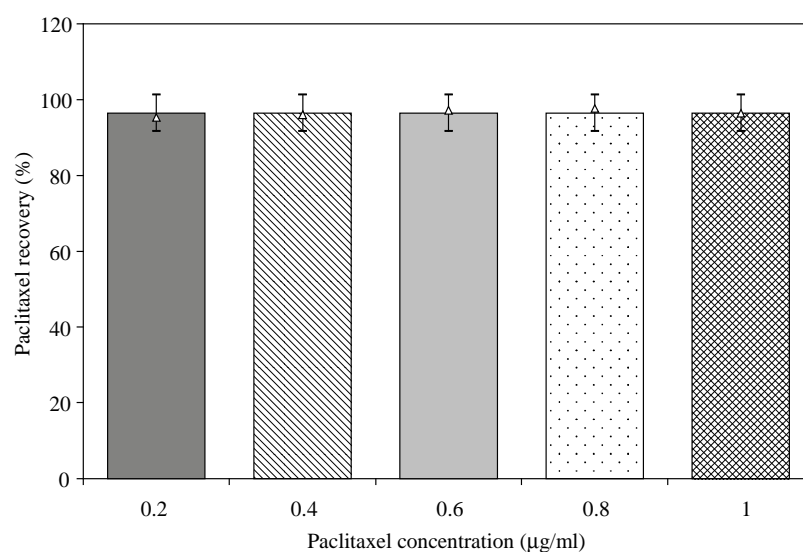
Figure 5-9 Recovery rate of PTX after extraction from plasma. Displayed are the adjusted mean values (columns), the non-adjusted mean values (Δ) and the standard deviations (-) after ANOVA analysis with $p < 0.05$.

5.5.2 *Solid states of the polymorphs of paclitaxel*

Solid PTX can have different morphologies. The as-received forms of PTX, PTX_S and PTX_K, were characterized to be anhydrous crystalline, when comparing their FT-IR-spectra and DSC-thermograms with the findings of Lee *et al*. and Pyo *et al*., Figure 5-10 and Figure 5-2 [10, 11]. Both IR-spectra in Figure 5-10 (a) show the same characteristic bands at wave numbers between 2500 and 500 cm^{-1}. Those are particularly the two characteristic carbonyl absorptions in the region of 1720 cm^{-1} and a sharp long band at 1650 cm^{-1}.
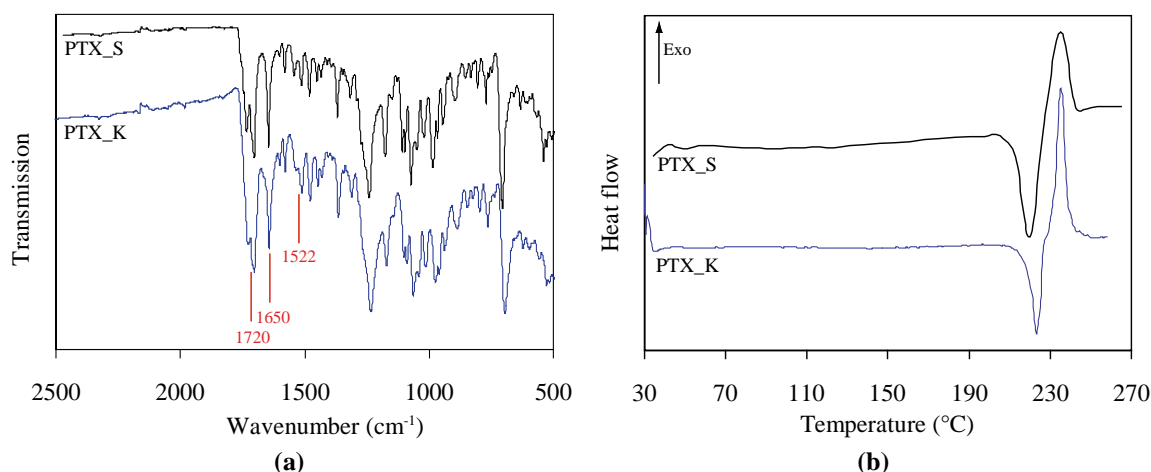
Figure 5-10 FT-IR spectra of (a) the as-received forms of paclitaxel PTX_S, PTX_K and (b) DSC-thermograms of PTX_S and PTX_K.

The recorded DSC-thermograms of the as-received types of PTX in Figure 5-10 (b) exhibited the same characteristic peaks representing phase transitions. No transitions were observed up to 220 °C. At 222.04 °C an endothermic peak was recorded, which denoted the melting of the drug. The melting point correlated with the one in literature [4, 6]. The heat of fusion, ΔH, was calculated from the peak area to be 77.86 ± 0.17 J/g. The adjacent exothermic peak at 230 °C was representative of the decomposition of PTX.

The morphology of PTX, which was formed by solvent evaporation, was also determined by FT-IR- and DSC-measurements. The FT-IR spectra of the PTX-polymorphs are pointed out in Figure 5-11. The labeling of the samples was the following. Samples, which were loaded with PTX dissolved in ACET and rinsed in UP-water, were called WACET_w730NRL. The ones loaded with PTX in DCM and rinsed with water were termed WDCM_w730NRL, and the ones loaded with PTX dissolved in EA and rinsed with water WEA_w730NRL. Drug-loaded specimens, which were not rinsed with water, were termed ACET_w730NRL if a solution of PTX in ACET was applied, DCM_w730NRL when PTX in DCM was used and EA_w730NRL when PTX in EA was employed during the drug-

loading. The spectra of the individual morphologies clearly showed differences in several wave number regions. DCM_w730NRL, WDCM_w730NRL and EA_w730NRL showed one carbonyl absorption near 1720 cm^{-1}, whereas all the others exhibited two carbonyl absorptions. Other absorption bands near 1650 and 1522 cm^{-1} also featured differences in their shape. While at 1650 cm^{-1}, DCM_w730NRL, WDCM_w730NRL, WACET_w730NRL, EA_w730NRL and WEA_w730NRL held a small, round shaped band, the other samples exhibited a long, sharp band.

Figure 5-12 presents the DSC-thermograms of PTX formed by the evaporation of different solvents. A glass transition was observed at 144 °C in the graph of DCM_w730NRL and an exothermic peak at 230 °C, representing the decomposition of PTX. The morphology of PTX was identified with the reference spectra and thermograms in Figure 5-2 to be amorphous, Table 5-8.
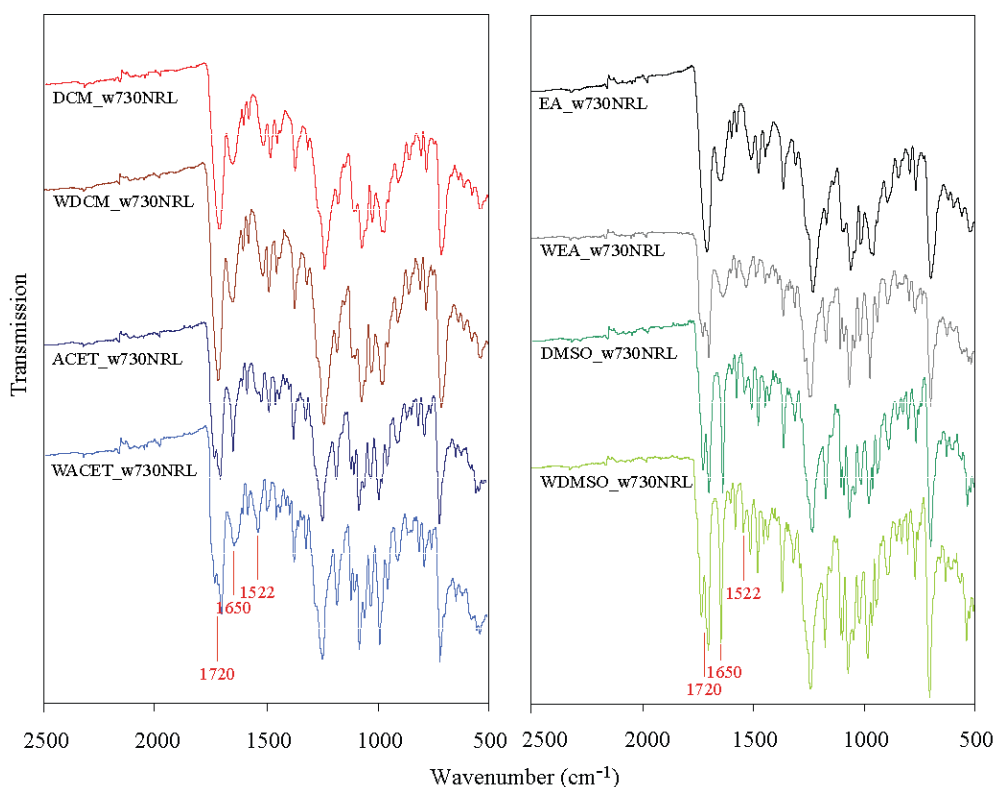
Figure 5-11 IR spectra of paclitaxel-polymorphs, which were formed by solvent evaporation.
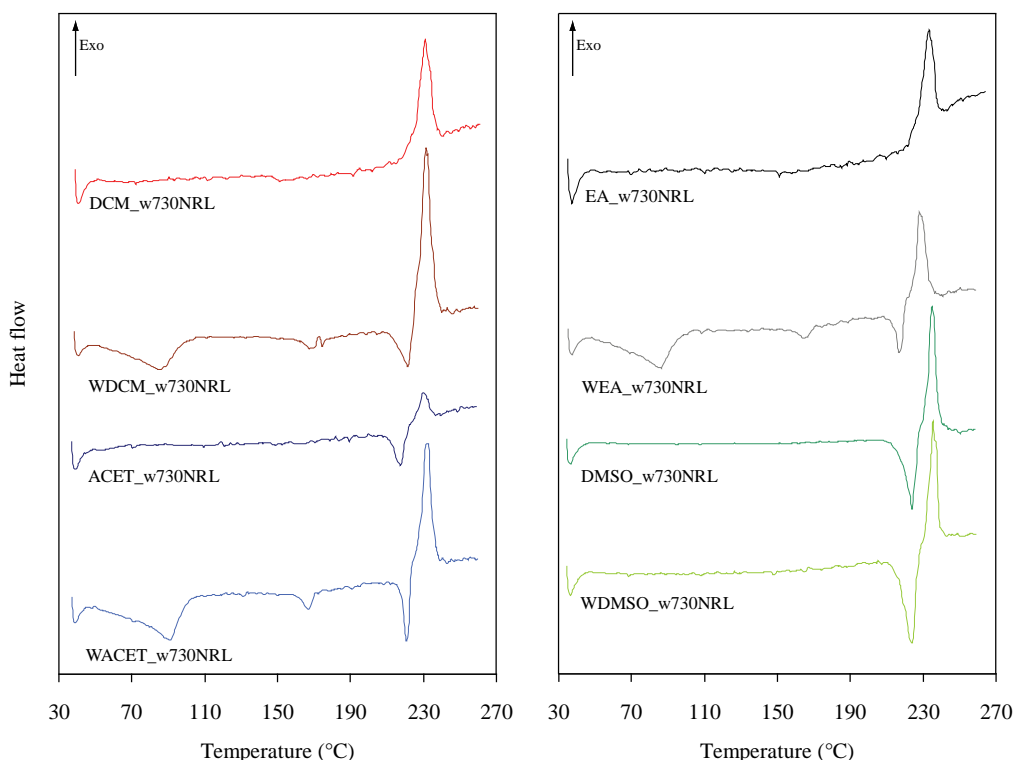
Figure 5-12 DSC-thermograms of paclitaxel-polymorphs, which were formed by solvent evaporation.

An endothermic dehydration and vaporization peak with its maximum at 81 °C was detected for the PTX in WDCM_w730NRL. The intermediate PTX, which was formed after the dehydration, was identified to be dehydrated paclitaxel dihydrate, when comparing with literature [6]. At higher temperatures, two small endothermic peaks occurred. They were solid-solid transitions at 164 °C and 171 °C, in which the intermediate PTX was converted to a semi-crystalline material. This semi-crystalline PTX melted at 218 °C with a heat of fusion, ΔH, of 20.28 J/g, like pointed out in Table 5-8. A glass transition could not be identified by DSC measurements, but the IR spectrum of WDCM_w730NRL in Figure 5-11 exhibited at 1720 cm^{-1} and 1650 cm^{-1} characteristic bands for the amorphous form of PTX. Therefore PTX created from H_2O and DCM was composed of amorphous and dihydrated crystalline PTX-morphologies. The DSC-thermogram of ACET_w730NRL was characterized by a single melting endotherm at 215 °C with ΔH of 55.78 J/g. PTX was hence classified as anhydrous crystalline, which is in accordance to the findings from the IR-measurements. WACET_w730NRL exhibited a similar DSC-curve like WDCM_w730NRL. The endothermic peak with its maximum at 88 °C represented the dehydration/evaporation of residual water and solvent and the formation of the intermediate form of PTX. At 164 °C, a solid-solid transition was detected. A melting transformation at 218 °C followed, which consumed the heat of fusion of 28.25 J/g. WACET_w730NRL was hence dihydrated crystalline, as was also proven by the IR-measurements. EA_w730NRL exhibited a glass transition at 147.83 °C and a decomposition peak at 230 °C. It was amorphous. By adding

water to the PTX/EA solution on the titania coating, the dihydrated morphology of PTX was created. The corresponding DSC-thermogram showed a dehydration/evaporation endotherm, a solid-solid transition and a melting endotherm, Figure 5-12. The IR-spectrum was also characteristic for that morphology. DMSO_w730NRL and WDMSO_w730NRL exhibited only a melting transition in the thermograms at 222 °C. Both forms were identified as anhydrous crystalline. A summary of the formed morphologies of PTX can be found in Table 5-8. Various PTX-polymorphs were formed by simply applying various solvents or solvent/UP-water mixtures. Their influence on the drug-load and release will be explored in the following.

Table 5-8 Polymorphs of paclitaxel, which were formed by solvent evaporation.

sample	*morphology*	*Transition T ($^{\bullet}$C)/ΔH (J/g)*			
		peak I	*glass transition*	*solid-solid*	*melting*
DCM_w730NRL	amorphous	-	143.94/-	-	-
WDCM_w730NRL	amorphous + dihydrated crystalline	80.93/-48.33	-	163.81/-7.12 171.14/-1.32	218.45/-20.28
ACET_w730NRL	anhydrous crystalline	-	-	-	215.21/-55.78
WACET_w730NRL	dihydrated crystalline	87.61/-84.99	-	164.17/-12.17	218.39/-28.25
EA_w730NRL	amorphous	-	147.83/-	-	-
WEA_w730NRL	dihydrated crystalline	84.30/-79.82	-	163.85/-9.67	215.28/-21.94
DMSO_w730NRL	anhydrous crystalline	-	-	-	222.61/-71.62
WDMSO_w730NRL	anhydrous crystalline	-	-	-	222.25/-82.82

5.5.3 *Preliminary tests to identify parameters influencing the drug-load and release*

Preliminary tests were performed to identify factors, which influence the drug-loading into the porous TiO_2-coating. Some errors occurring during these tests were not systematically analyzed. Although the results are presented at this point, because some findings might be relevant for the optimization of the coating for drug-eluting stents (DESs) in future studies.

5.5.3.1 *Polymorphs of paclitaxel*

Drug-loading at atmospheric conditions with the method AP_{DS} was chosen to create different polymorphs of PTX in the coating. The amounts of drug in the non-reservoir layers (NRLs) as a function of applied solvent are pointed out in Figure 5-13. For DCM_w730NRL and WDCM_w730NRL an amount of 1.241 ± 0.257 µg/mm^2 geometrical surface area of the coating was obtained. For ACET_w730NRL and WACET_w730NRL 1.094 ± 0.443 µg/mm^2 and for EA_w730NRL and WEA_w730NRL 0.411 ± 0.128 µg/mm^2 were detected. The polymorphs, which were formed by the evaporation of the solvents and solvent/water mixtures, were identical to the ones characterized in the previous chapter:

DCM_w730NRL and EA_w730NRL: amorphous, WDCM_w730NRL: amorphous and dihydrated crystalline, ACET_w730NRL: anhydrous crystalline, WACET_w730NRL and WEA_w730NRL: dihydrated crystalline. High standard deviations in all of the measured loads were discovered, but not systematically investigated at this stage of development.
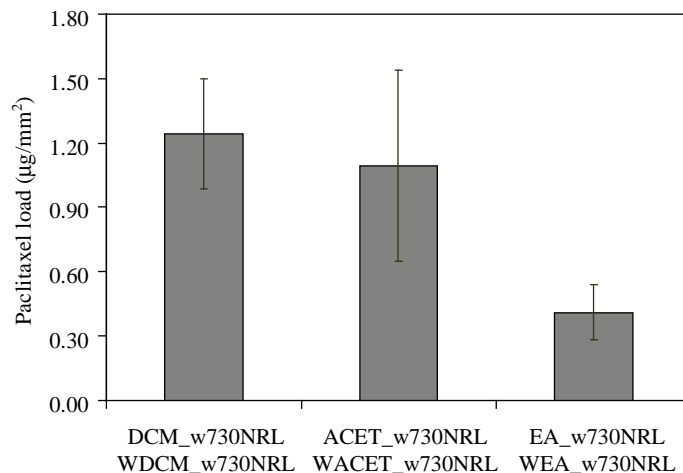
Figure 5-13 Paclitaxel-loads of the non-reservoir titania layers as a function of applied solvent, solvent/water mixture.

The release profiles of PTX from these drug-loaded NRLs into water clearly showed differences one to each other, like depicted in Figure 5-14. The samples not rinsed in water after the loading were characterized by a fast release at the beginning up to 10 h, followed by a continuous, slower release up to 4 d, Figure 5-14 (a). At the beginning of elution, EA_w730NRL released the highest amount of drug in the so-called burst-release, compared to the other specimens. After 4 d, 33 % of initially incorporated drug, were released. The profile of DCM_w730NRL was similar, but with a lower burst-release. ACET_w730NRL was characterized by the slowest liberation of the pharmaceutical: 16 % of totally incorporated drug eluted after 4 d. The shapes of the release curves of the specimens rinsed with water after loading in Figure 5-14 (b) were similar and with a lower burst-release compared to the samples not rinsed in water. The quantities of released PTX up to 4 d were different: WEA_w730NRL: 12 %, WDCM_w730NRL: 10 % and WACET_w730NRL: 5 %. The test was stopped after 4 d of elution, because it was a preliminary test. Even if the dissolution yielded an incomplete drug-release from the coating after these 4 d, the release kinetics were analyzed. The mathematical models, which were introduced in Chapter 5.2, were employed.

The release data of all samples were fitted to the Korsmeyer-Peppas, Higuchi, zero-order and first order models. Only data from selected time intervals of the release curves were chosen because of the following. The concentrations of PTX detected in the aqueous

media for DCM_w730NRL, ACET_w730NRL and EA_w730NRL were as high as 10 µg/ml after 1 h, and 5 µg/ml after 5 h of elution.
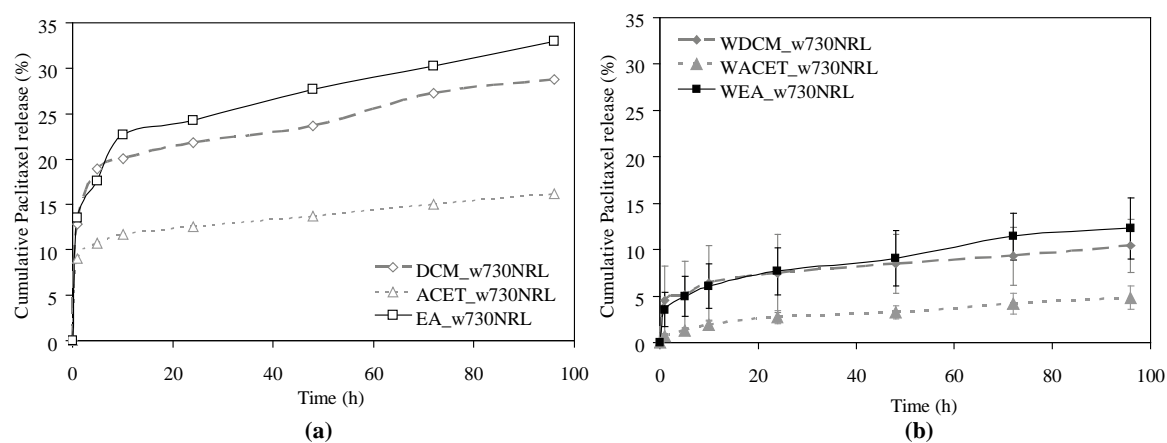
Figure 5-14 *In vitro* release of paclitaxel from non-reservoir titania coatings into water as a function of time and PTX-morphology.

These values exceeded the maximum solubility concentration of PTX in water of 3 µg/ml, which was deduced from literature, cf. Table 5-1. Hence perfect sink conditions, which are required for the application of the mathematical models, were not fulfilled. The detected high PTX-concentrations were caused by the breaking of loose PTX-fragments on top of the titania coating. The same phenomenon of high PTX-concentrations in water was observed for WDCM_w730NRL, WACET_w730NRL and WEA_w730NRL. The drug concentrations in the media up to 10 h of elution were then as high as 6 µg/ml for WDCM_w730NRL and 1 and 3 µg/ml for WACET_w730NRL and WEA_w730NRL, respectively. The data points of the release up to 10 h of elution were *excluded* from the evaluation. Only the part of the release curve between 24 to 96 h was employed in the analysis. The PTX-concentrations in water were smaller than 1 µg/ml in this interval and hence fulfilled perfect sink conditions.

The exponent n of the Korsmeyer-Peppas model, the release rate constants k and the correlation coefficients R^2 for all samples are depicted in Table 5-9. The Korsmeyer-Peppas model revealed for the drug-release from any coating n < 0.5 and thus predicted a diffusion transport. The kinetic model that best fitted the experimental data was deduced by R^2. The samples DCM_w730NRL, ACET_w730NRL, WDCM_w730NRL, WACET_w730NRL exhibited the best linearity for the zero-order approach with regression coefficients of 0.973, 1.000, 0.997, 0.991. The highest regression coefficients for EA_w730NRL and WEA_w730NRL were evaluated for the Higuchi model with R^2 of 0.998 and 0.989, respectively.

Table 5-9 *In vitro* release kinetics of PTX from the TiO$_2$-coatings. Shown are the release exponent n, the regression coefficients R^2 of the mathematical fits and the release constants k of the individual models.

sample	morphology	Korsmeyer-Peppas		Higuchi		zero order		first order	
		n	*R^2*	$k_h \cdot 10^{-5}$ $(\mu g/(mm^2\,s))$	*R^2*	$k_0 \cdot 10^{-5}$ $(\%/s)$	*R^2*	$k_1 \cdot 10^{-6}$ $(\%/s)$	*R^2*
DCM_w730NRL	amorphous	0.206	0.950	30.732	0.967	**2.819**	**0.973**	1.122	0.971
ACET_w730NRL	anhydrous crystalline	0.181	0.974	13.530	0.990	**1.415**	**1.000**	0.990	0.999
EA_w730NRL	amorphous	0.218	0.991	**14.986**	**0.998**	3.330	0.996	1.172	0.988
WDCM_w730NRL	amorphous, dihydrated crystalline	0.236	0.974	12.344	0.985	**1.136**	**0.997**	1.285	0.996
WACET_w730NRL	dihydrated crystalline	0.416	0.962	7.979	0.973	**0.838**	**0.991**	2.273	0.990
WEA_w730NRL	dihydrated crystalline	0.312	0.984	**5.827**	**0.989**	1.293	0.984	1.672	0.975

By comparing these findings it seems that the drug-release from the coatings depended on the dissolution rate of the drug rather than on the diffusion of PTX from the porous structure, except for the EA_w730NRL and WEA_w730NRL. An effective diffusion coefficient, D$_{eff}$, was not calculated from the release constants, because the precise transport mechanisms involved in the drug-release were unknown. PTX was present in the pores of the NRLs as well as in a so-called burst-layer on top of the coating, which will be illustrated later in this chapter. Hence it was unclear, from which position of the coating PTX was released. A D$_{eff}$ of PTX dissolved from the burst-layer must be different to a D$_{eff}$ when PTX is diffused through the porous structure of the coating. The geometric factors to calculate D$_{eff}$ were hence inexplicit. But the release constants k could be evaluated. The higher k$_0$ in the zero order release is, the faster is the release. For amorphous PTX in DCM_w730NRL and EA_w730NRL, k$_0$ of $2.819 \cdot 10^{-5}$ and $3.330 \cdot 10^{-5}$ %/s (% of initially loaded drug released from the matrix per second) was obtained, respectively. The zero order constants of the anhydrous crystalline PTX in ACET_w730NRL was $1.415 \cdot 10^{-5}$ %/s and smaller than for the amorphous forms. WACET_w730NRL and WEA_w730NRL with dihydrate crystalline morphologies exhibited k$_0$ of $0.838 \cdot 10^{-5}$ and $1.293 \cdot 10^{-5}$ %/s, respectively. The release rates were smaller than the ones of the anhydrous crystalline and amorphous forms of PTX. WDCM_w730NRL, as an amorphous and dihydrate crystalline form, exhibited k$_0$ of $1.136 \cdot 10^{-5}$ %/s. Thus the dissolution rate is coherent with the physical properties of the different morphologies of PTX. The amorphous forms dissolved faster than any crystalline ones. The dihydrate crystalline polymorph, which has a lower aqueous solubility than the anhydrous crystalline one (cf. Chapter 5.1), showed the smallest dissolution rate.

5.5.3.2 *Dip coating and number of dips*

The relatively distinct standard deviations in the PTX-loads, which were observed in the previous test, were connected to a non-uniform PTX-load in the big TiO_2-plates. A systematic analysis of the PTX-quantity loaded into the small pieces cut from the positions top, middle and bottom of the big plates, illustrated in Figure 5-5, was carried out. The big titania coated plates with a NRL-structure were hence drug-loaded with the low pressure technique LP_{DMSO}. One single dip of the plates into the PTX/DMSO solution was performed.

The amount of medicament loaded into the small pieces, which are located in the top and middle of the big plates, was equal: 0.016 µg/mm^2, like depicted in Figure 5-15. The samples from the bottom, 5 mm distant from the lowest edge of the plates, held a PTX amount of 0.159 µg/mm^2. This value was of an order of magnitude of 1 bigger than for the other specimens. The same tendency of inhomogeneous drug-load was detected for samples loaded with 4 consecutive dips into the PTX/DMSO solution. Specimens from the top position of the plates contained 0.016 µg/mm^2, from the middle location 0.022 µg/mm^2 and from the bottom region 0.110 µg/mm^2. Whereas the quantity in the top piece did not increase after 4 consecutive dips, the amount in the middle piece contained 37.5 % more drug than after 1 single dip. The PTX-load in the bottom piece decreased after 4 dips compared to 1 dip, but was still much higher than for the other specimens. This accumulation of PTX at the bottom was caused by the droplet formation of the PTX/DMSO solution after withdrawal of the plate-samples. This effect was still significant on the drug-load in regions of the NRLs, which were 5 mm distant from the bottom edge of the plate. In future drug-loading tests, only 1 dip into the PTX/solvent solution was performed. Quantification of the drug-load was only performed on small specimens cut from the top and middle regions of the big plates, because the drug-load was there reproducible.
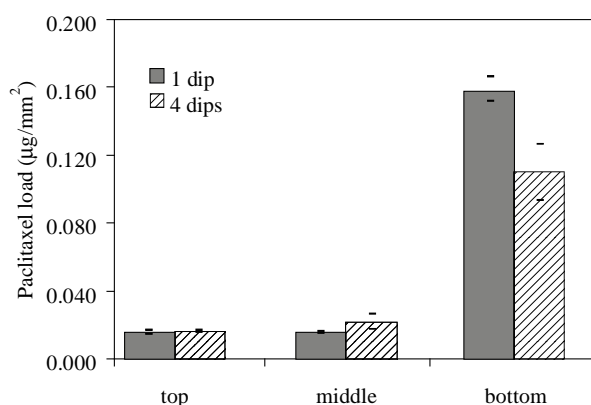
Figure 5-15 PTX-loads of non-reservoir layers as a function of the position on the big, drug-loaded plates and of the number of dips into the PTX/DMSO solution. Shown are the mean values and the two individual data points.

5.5.4   Optimization of the drug-load using a low pressure technique

The objectives to apply low pressure during drug-loading were (1) to evacuate the pores of the titania coating prior to immersion into the PTX/solvent solution and (2) to apply a pressure gradient, which forces the solution into the coating. Small tests were performed first, to set parameters of the drug-loading.

A test to determine the evaporation rate of the solvent EA at 350 mbar was deduced to set the preparation time of the NRLs at lower pressure, step 2 in Table 5-6. The pressure of 350 mbar was chosen instead of the solvent's saturation pressure of 150 mbar, to provide reliability by reducing the evaporation rate and hence by keeping the level of solvent in the glass beakers constant for a longer period of time than at 150 mbar. A glass cuvette was filled with EA and exposed to 350 mbar. At certain times the mass of EA in the cuvette was measured. A linear decrease of the solvent's mass in the cuvette as a function of time was recorded, Figure 5-16. After 120 min, 45 %wt of the initial EA in the quartz cuvette was left. For the methods $LP_{EA}1$ and $LP_{EA}2$ a time span of 10 min was applied to prepare the NRLs at low pressure. Because after that time, 95 %wt of the EA initially poured into the cuvette was still present. The up-concentration of the drug in the PTX/solvent solution due to the evaporation of the solvent was hence negligible.

Another parameter changed for these drug-loading procedures, compared to the ones previously used, was the concentration of PTX in the solvent. The *saturation concentration* of PTX in EA of 103.61 ± 21.82 µg/ml was applied in the following.
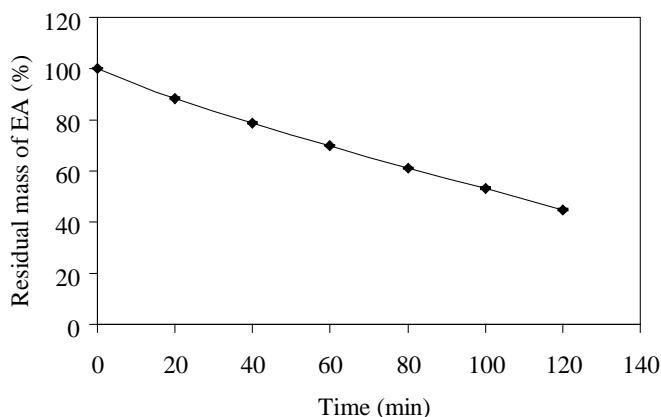
Figure 5-16 Mass of EA as a function of time, in which it was exposed to a pressure of 350 mbar.

5.5.4.1 Influence of the coating's structure and the immersion time

The immersion time of the NRLs into the PTX/EA solution was varied in the test $LP_{EA}1$: 1 min, 0.5 h and 5 h. Two big titania coated plates were loaded with the same method to check the reproducibility of the drug-loading. From each one, three small samples from the top and middle position were cut and the PTX-quantity determined, Figure 5-17. Each of the columns of the PTX-loads in Figure 5-17 corresponds to the mean value of drug-loads of one big plate. The two columns at one immersion time represent plate 1 and 2, which were drug-loaded identically. No significant differences in the mean values of the PTX-loads of plate 1 and 2 at each immersion time were deduced after ANOVA analysis with an error risk of 5 %. The drug-loading was hence reproducible. Significant differences of the PTX-loads as a function of immersion time were recorded. The adjusted mean value for an immersion time of 0.02 h (1 min) was 0.706 µg/mm^2, for 0.5 h 0.504 µg/mm^2 and for 5 h 0.818 µg/mm^2, Table 5-10.

The PTX-load in the NRLs depended on the immersion time of the specimens into the PTX/EA solution during the drug-loading. After 1 h of immersion, a load of 0.472 µg/mm^2 and after 24 h 1.056 µg/mm^2 was measured, Table 5-10. Starting the drug-load with an immersion time of 1 min and increasing it to 1 h decreases the PTX-load in the coating, whereas the opposite behavior was expected. The decrease in drug-load might have been caused by the different thicknesses of the PTX-layer, which was build on top of the porous coating, Figure 5-18. The NRL, which was loaded with an immersion time of 1 min exhibited the thickest layer of PTX, whereas the layers were thinner after 0.5 and 1 h of immersion.
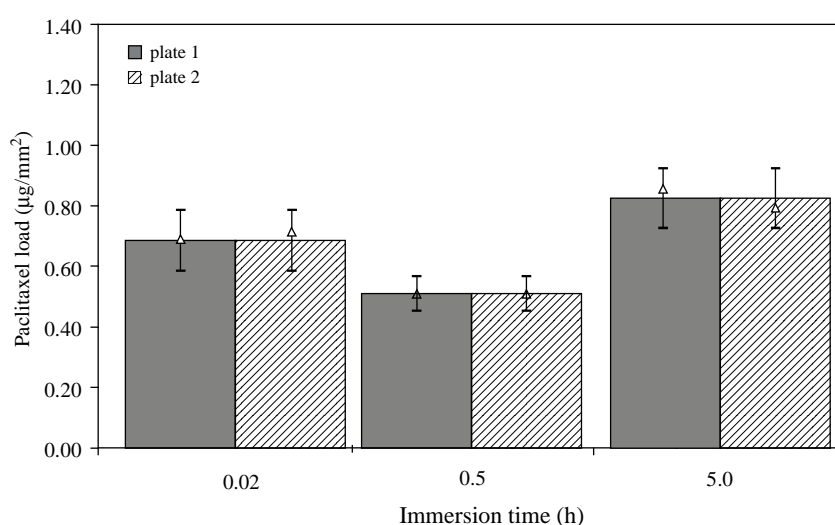
Figure 5-17 PTX-loads as a function of immersion time. Shown are the adjusted mean values (columns), the mean values as obtained (Δ), the standard deviations (-) after ANOVA analysis with $p < 0.05$.

Table 5-10 Adjusted mean values of the PTX-loads as a function of immersion time and coating type. Values were obtained after ANOVA analysis with an error risk of $p < 0.05$.

sample type	*coating specification*	*immersion time (h)*	*PTX-load ($\mu g/mm^2$)*
EA_w730NRL	NRL	0.02	0.706 ± 0.055
	NRL	0.5	0.504 ± 0.055
	NRL	1	0.472 ± 0.055
	NRL	5	0.818 ± 0.055
	NRL	24	1.056 ± 0.055
EA_w730*RL*	*RL*	5	0.941 ± 0.066
	RL	24	1.211 ± 0.066

By increasing the immersion time above 1 h, the PTX-quantity in the coating increased. The maximum PTX-load of 1.056 $\mu g/mm^2$ in the NRL was obtained after 24 h. Up to now, only NRLs were used for the drug-loading and release tests. The objective of the study was to incorporate PTX into the *RL*s and to accumulate the pharmaceutical agent in its reservoirs. A calculation was first deduced to estimate the PTX-load in the *RL*s. If a prismatic envelope around the PTX-molecule in Figure 5-1 (b) is drawn, one can calculate the volume in that envelope to be 2.132 nm^3. This represents the volume of one PTX-molecule. This approximation, as well as the determined structural parameters of the coating, served to estimate the amount of drug, which could theoretically be loaded into the coating. The input parameters, which were used for the calculation, are listed in Table 5-11. It was assumed that 50 % of the volume of the pores in the coating were filled with the drug. The application of this value gets reasonable, if one takes a look at the cross sections of drug-loaded *RL*s in Figure 5-20.

The results of the calculation are displayed in Figure 5-19. The theoretical load of a NRL was estimated to be 0.195 $\mu g/mm^2$. The theoretical load of a *RL*, which has a reservoir density of 150000 reservoirs/mm^2 and a reservoir size of 1 μm, was 0.201 $\mu g/mm^2$. The *RL* theoretically would contain 3.08 % more drug than the NRL. By increasing the reservoir size, a smaller density of them is necessary to augment the PTX-load. But by enlarging the reservoirs, the TiO_2-layer gets thicker and also the pore volume in the porous structure surrounding the reservoirs. The amount of PTX in that structure significantly influences the total PTX-load in the coating.

Figure 5-18 SEM-micrographs of cross sections of paclitaxel-loaded, non-reservoir layers. Immersion time into the PTX/solvent solution was (a) 1 min, (b) 0.5 h and (c) 1 h.

Table 5-11 Parameters used to calculate the theoretical PTX-load in the TiO_2-coatings.

entry values		
PTX	molecular weight PTX	854 g/mol
	PTX unit volume = volume 1 molecule	$2.13 \cdot 10^{-9}$ μm^3
	PTX reservoir and void fill	50 %
	Avogadro's constant	$6.02 \cdot 10^{23}$ 1/mol
porous TiO_2-coating	TiO_2 porous volume fraction	50 %
	reservoir size factor after shrinkage, x direction	88 %
	reservoir size factor after shrinkage, y direction	59 %
	nanoporous layer thickness	0.329 μm
	base layer thickness	0.250 μm

The calculation revealed that it would be impossible to load the targeted amount of 1 µg/mm² PTX into the *RL*s. The experiments proved differently: this load was obtained for the NRLs loaded with immersion times of 5 or 24 h. These two immersion times were hence chosen to perform the drug-loading on *RL*s. The presence of the reservoirs promoted a higher drug-load in both cases compared to the NRLs. The *RL* contained 14.63 % more drug after 5 h and 14.15 % more PTX after 24 h of immersion compared to the NRLs, Table 5-10. The total loads after 5 h and 24 h were significantly different one to another in the coatings: 0.941 µg/mm² and 1.211 µg/mm², respectively. Electron microscopy verified that PTX was

accumulated in the drug reservoirs, Figure 5-20. Moreover it was present in the porous structure surrounding the reservoirs and on top of the coating as a so-called burst-layer.
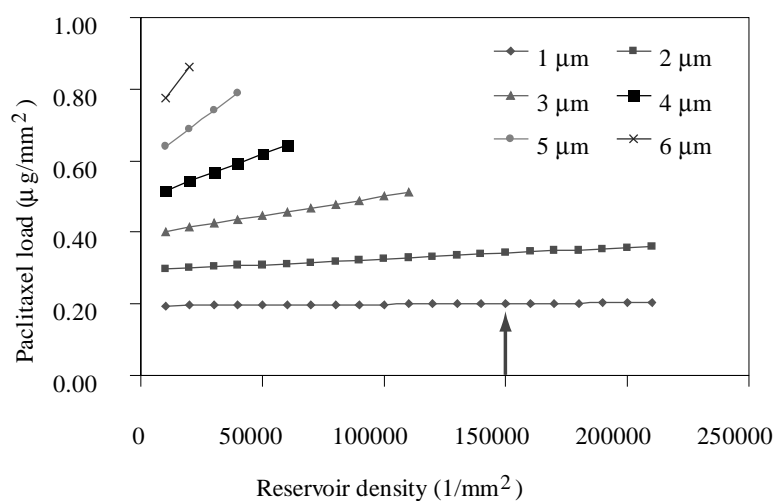
Figure 5-19 PTX-load as a function of reservoir density and reservoir size, as was obtained from calculations. The red arrow indicates the properties of the titania reservoir layer used in this study.
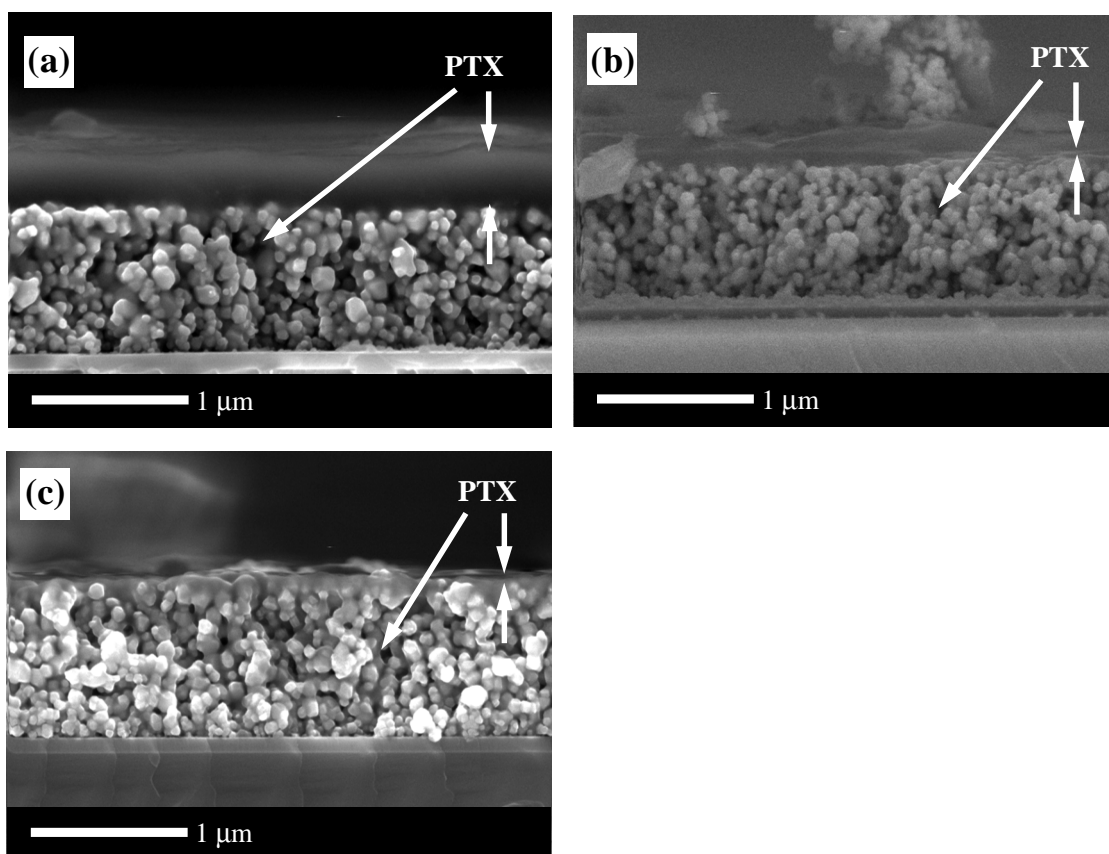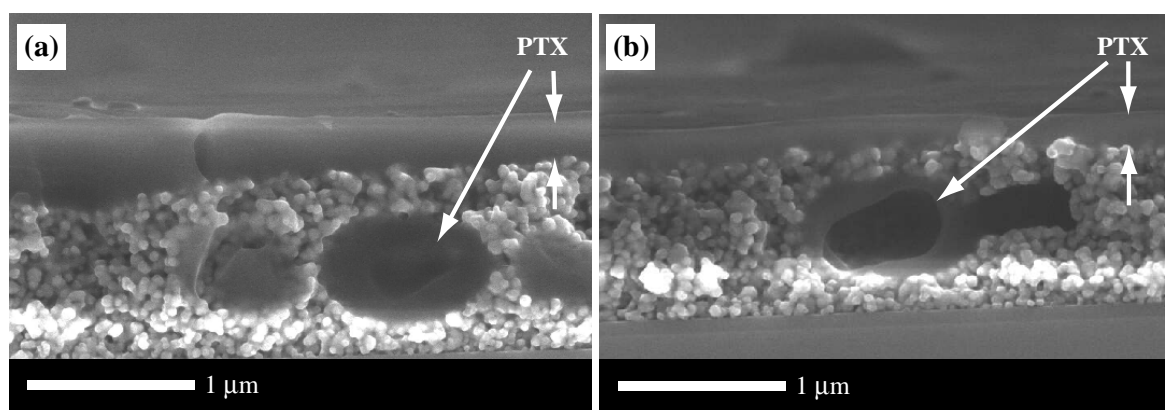

Figure 5-20 SEM-micrographs of cross sections of paclitaxel-loaded reservoir layers. The immersion time into the paclitaxel/solvent solution was 24 h. In (a) reservoirs totally filled with the drug are shown. In (b) only partially filled reservoirs are depicted.

5.5.4.2   *Influence of the paclitaxel burst-layer on the wettability*

Because PTX has an extremely hydrophobic character, the presence of the PTX-burst-layer on top of the titania coatings influenced their wettability with water, Table 5-12. The mean contact angles for the drug-loaded NRLs and *RL*s with water were 50.36 ° and 66.74 °, respectively. They were much higher than the contact angles of the native coatings with water, Table 4-11 in Chapter 4.5.4. A standard deviation of 22 ° was recorded for the drug-loaded NRLs. This deviation was caused by different wettabilities of the coating with water

on various spots of *one* sample.

Table 5-12 Contact angles θ_c of the PTX-loaded non-reservoir layers (NRL) and reservoir layers (*RL*) with water.

sample	*EA_w730NRL*	*EA_w730RL*
θ_c (°), water	50.36 ± 22.20	66.74 ± 6.41

5.5.4.3 Rinsing

The total drug-load of the titania coatings was affected by the amount of PTX accumulated in the burst-layer. Up to now it was not measured, how much PTX was present *only* in the porous network and how much was localized in the burst-layer. The rinsing test $LP_{EA}2$ to remove the PTX-burst-layer from the coating was therefore accomplished. PTX is well soluble in acetonitrile (AcN) and less soluble in water. Rinsing solutions of different volumetric concentrations of AcN and UP-water were prepared. They were applied in a rinsing step, step 11 in Table 5-6, after the titania coatings were drug-loaded at lower pressure with the method $LP_{EA}2$ and with an immersion time of 24 h.

The influence of the rinsing with the AcN/UP-water mixtures on the total load of PTX in the NRLs and *RLs* can be found in Figure 5-21. If only water was employed for rinsing, the total PTX-load in the coatings did not change and was equal to the amount of initially loaded PTX. If a mixture of 20 %vol AcN in UP-water was applied, the PTX-load did not change. No PTX was dissolved from the coating. However, the top views of the coatings, which were observed by an optical microscope, changed, Figure 5-22 (a)-(i). Whereas the surface of the water-washed sample looked like the one of the initially drug-loaded sample, the PTX in the coating after rinsing in a mixture of 20 %vol AcN showed the formation of big, star-like PTX-crystals, (g), (h). They were not only seen on top of the coating, but also in the reservoirs, (i). PTX was not as compact as it was in the initial drug-loaded coating (f). The morphology of crystal-like PTX was determined by IR spectroscopy as dihydrated crystalline. Thus it was possible to change amorphous PTX into a crystalline form in the film, by applying an AcN/water mixture for a short period of time to the coatings.
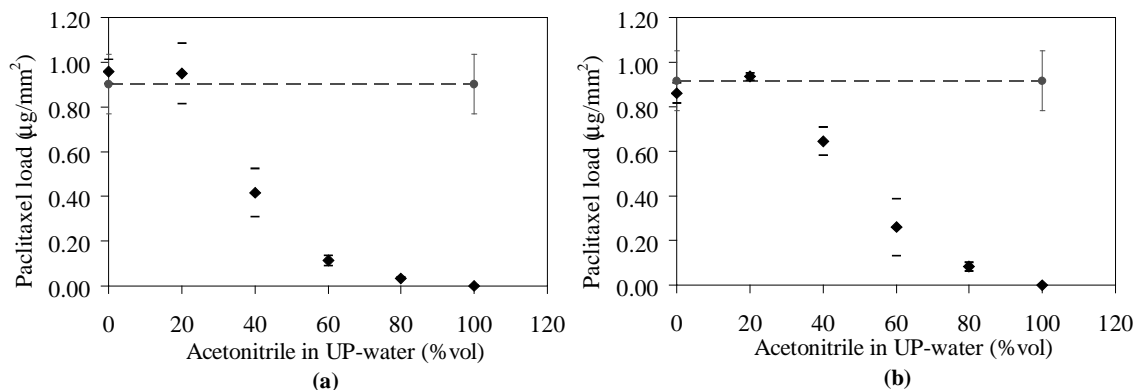
Figure 5-21 PTX-load in (a) a NRL and in (b) a *RL* after washing for 3 s in solutions of different concentrations of AcN and UP-water. Shown are the mean values and the individual two data points.

When a mixture of 40 %vol AcN in water was used, the PTX-load in the coating decreased more than 50 % in the NRL and of 30 % in the *RL,* Figure 5-21. The photos (j) to (l) in Figure 5-22 show that the amount of crystals on top of the coating was depleted compared to the samples washed with 20 %vol AcN. PTX did not occupy as much space in the reservoirs as before and showed long, needle shaped crystals. By using a rinsing solution of 60 %vol AcN, only 10 % of the initial PTX-load was left in the NRLs, 30 % in the *RL*s. A less amount of crystals was localized on top of the coating's surface and no PTX was detected in the reservoirs, images (m) to (o) in Figure 5-22. If the amount of AcN in water was 80 %vol, a trace amount of PTX was left in both types of coatings. No medicament was detected in the reservoirs by microscopy. A solution of 100 % AcN caused the total amount of PTX being eluted from the coating during only 3 s of rinsing.

Because it was impossible to just remove the upper PTX-burst-layer from the TiO_2-coating using solutions of water and AcN, one assay was performed applying 100 % EA as a rinsing solvent, cf. drug-loading method $LP_{EA}2$, Table 5-6. Only trace amounts of PTX were left in the layers: 0.020 µg/mm^2 for the NRLs and 0.019 µg/mm^2 for the *RL*s. No PTX was seen by electron microscopy in the coatings.

native coating
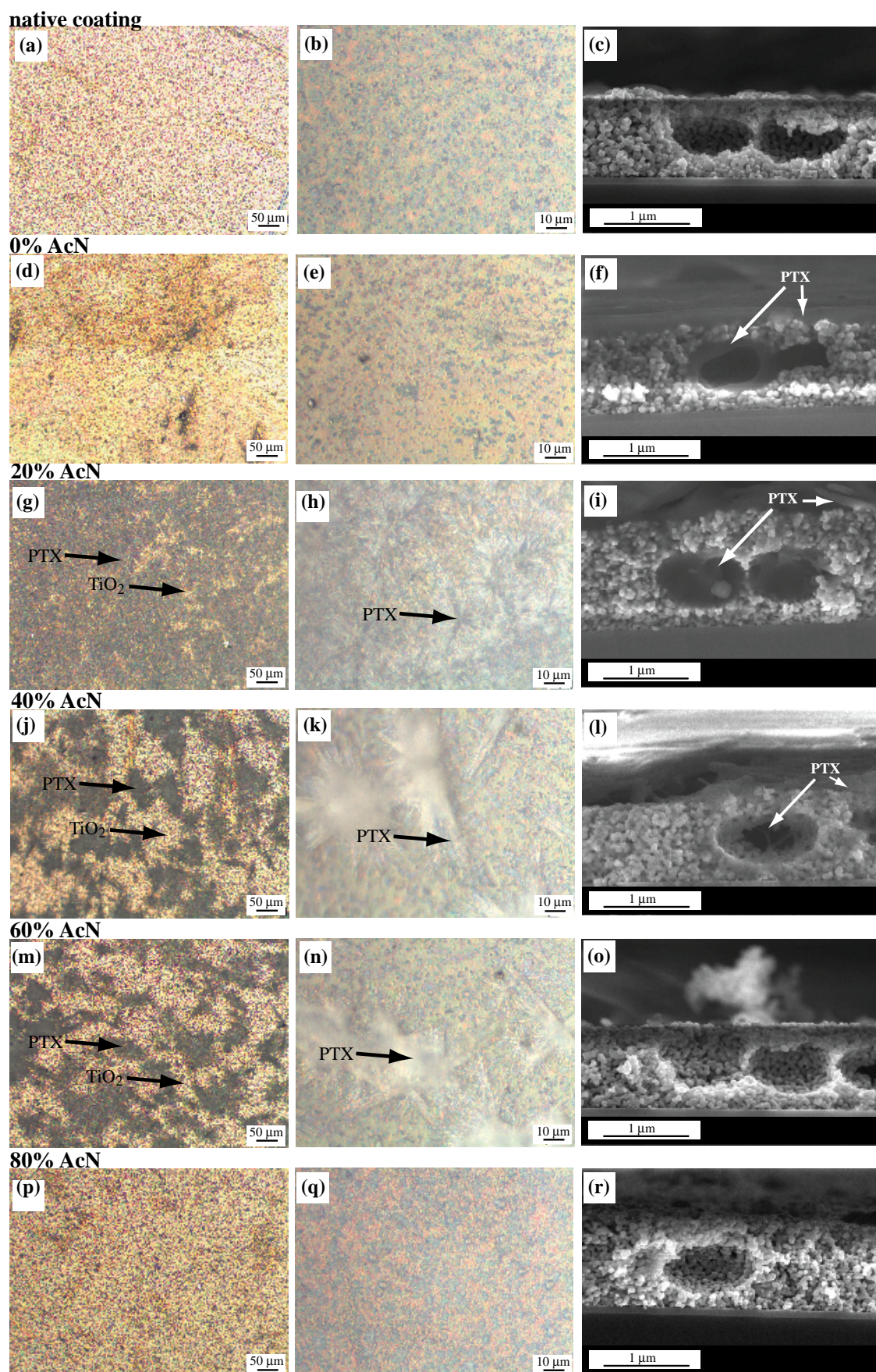
Figure 5-22 Optical micrographs and SEM-micrographs of cross sections of drug-loaded *RLs* after washing in solutions of different concentrations of AcN and UP-water.

5.5.5   *Drug-release of Paclitaxel from the films into water and bovine plasma*

The *RL*s with a drug-load of 1.21 µg/mm^2 and an amorphous PTX-morphology, Table 5-8 and Table 5-10, were exposed to drug-release tests. The medium was either water in the test R_LP$_{EA}$1_water or bovine plasma in the experiment R_LP$_{EA}$1_plasma.

The PTX-liberation from the *RL*s into water was continuous up to 32 d, by which only 11 % of the initially incorporated quantity of drug were released, Figure 5-23. The test was still continuing at the time of writing this chapter. It is expected that the drug-release follows this linear behavior until 100 % are released. Different mathematical models were applied to the release data. The release constants k were evaluated in the time interval of 24-768 h of elution. The kinetic model with the best fit to the release profile was evaluated by the correlation coefficient R^2, Table 5-13. The zero order release kinetic, with a release constant k$_0$ of 0.335 %/s, best described the data. This model predicts a slow, continuous release of low water-soluble drugs, cf. Chapter 5.2.2.
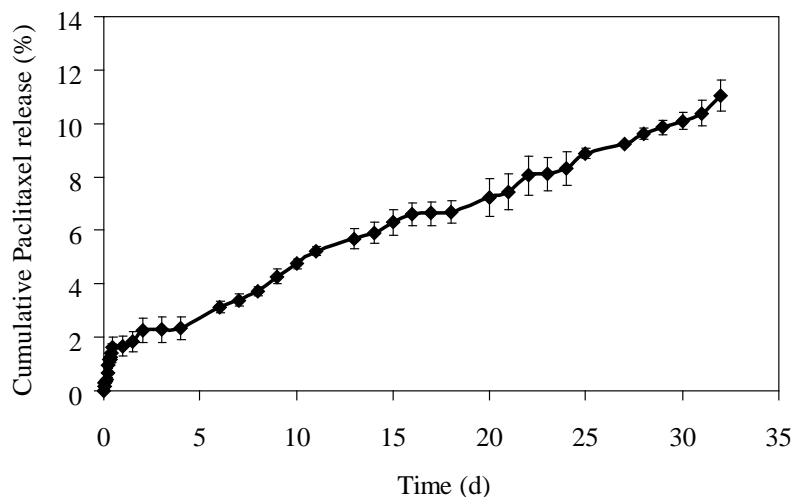
Figure 5-23 *In vitro* paclitaxel-release from a reservoir layer. The test was still continuing at the time of report.

Table 5-13 Drug-release kinetics of amorphous paclitaxel from a reservoir layer and from the commercially available Taxus Express^{2TM} stent into water or bovine plasma.

release test (time interval)	coating specification	Korsmeyer		Higuchi		zero order		first order	
		n	*R^2*	*k$_h$ · 10^{-5} (µg/(mm^2·s))*	*R^2*	*k$_0$ · 10^{-5} (%/s)*	*R^2*	*k$_1$ · 10^{-6} (%/s)*	*R^2*
R_LP$_{EA}$1_water (24 – 768 h)	*RL*	0.581	0.969	6.426	0.974	**0.335**	**0.994**	0.638	0.919
R_LP$_{EA}$1_plasma (0-7d)	*RL*	0.171	0.698	**50.494**	**0.715**	4.839	0.454	0.606	0.419
R_LP$_{EA}$1_plasma (0-7d)	Taxus^{TM} stent	0.504	0.976	**2.769**	**0.964**	0.319	0.857	2.061	0.784

The PTX-release from the *RL*s into bovine plasma exhibited a different release curve than the one into water, Figure 5-24. After one day of elution, 43 % of the initial PTX-load were liberated. After 4 d, no more pharmaceutical was released and 54 % stayed trapped in the coating. No kinetic model introduced in Chapter 5.2 fitted well the data, Table 5-13. All correlation coefficients were far below 0.900. Nevertheless, the highest correlation coefficient was obtained for the Higuchi-kinetic, with a R^2 of 0.715. This model describes the release of a solid drug from a solid, porous matrix.

That more than 50 % of the drug stayed trapped in the coating was also observed by electron microscopy of the cross sections of a drug-loaded *RL*, which was exposed for 38 d to the elution into plasma, Figure 5-25 (a). The reservoirs of the titania layers were still filled with PTX. The morphology of PTX in the reservoirs looked alike the one of the "freshly" drug-loaded coatings shown in Figure 5-20.
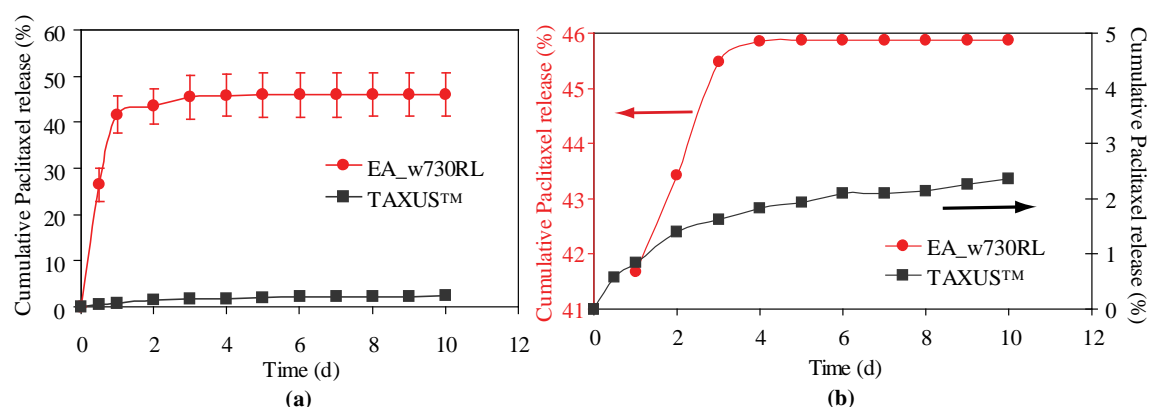
Figure 5-24 (a) *In vitro* release of PTX from reservoir layers and from the commercially available Taxus[TM] stent. (b) shows a higher resolution of the release curves.
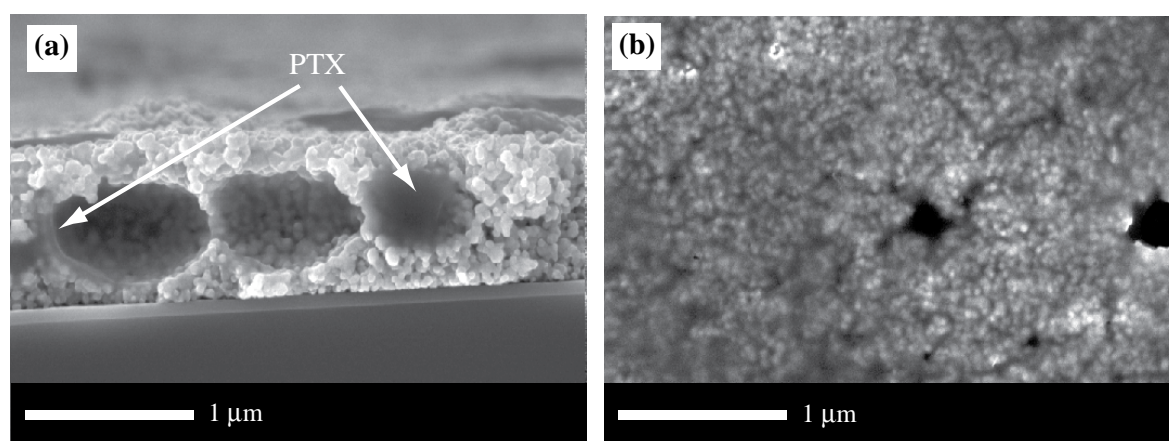
Figure 5-25 SEM-micrographs of a reservoir layer, which contains paclitaxel after 38 d of elution into bovine plasma. (a) cross section and (b) top view.

The SEM-micrographs revealed further that a layer on top of the TiO_2-film was built, Figure 5-25 (b). This layer was not observed in the SEM-micrographs of drug-loaded *RL*s exposed to the drug-release into water. It could be deduced from this experiment that ~ 0.6 µg/mm^2 PTX were present in the porous structure of the *RL*s. The residual ~ 0.6 µg/mm^2, which were released up to 4 d, equaled the quantity of PTX in the burst-layer.

The *in vitro* drug-release curve of the Taxus^{TM} stent into bovine plasma is pointed out in Figure 5-24. The PTX-release from this drug-eluting stent (DES) is slower than the release from the *RL*s. Only 2 % of initially incorporated drug-referenced to a load-concentration of 1 µg/mm^2 and a total load of 85 µg [1, 2]-were eluted into plasma up to 7 d. The release up to that time was continuous and did not contain a burst-effect at the beginning. The release data were best described by the Higuchi model, Table 5-13, with the regression coefficient R^2 of 0.964. Also in literature it was described that the Higuchi kinetic model best describes the PTX-release from the Taxus^{TM} stent [1, 2]. The release was thus determined by the diffusion of PTX through the polymer matrix system. This was verified further by the release exponent n of 0.504 of the Korsmeyer-Peppas model, which predicts a diffusion controlled release mechanism.

The detailed transport mechanisms of PTX from the *RL*s into water or bovine plasma could not be deduced. The system was too complex to correlate appropriate release kinetics to the release data. PTX was present in the reservoirs, in the pores of the surrounding ceramic structure and it was present as a burst-layer on top of the coating. It was unknown at which time PTX got eluted from the burst-layer or from the reservoirs. Hence parameters which would have an impact on the effective diffusivity D_{eff}, such as the diffusion layer thickness h or the porosity, were not specified. It was not possible to calculate the correct D_{eff} from the data and to compare it with the free diffusivities of PTX represented in Table 5-14. The Stoke's Einstein diffusion coefficient of PTX in water, D_{SE}, of $3.86 \cdot 10^{-10}$ m^2/s was calculated with Equation (5-3). The simulated diffusion coefficient D_{sim} of $5.50 \cdot 10^{-10}$ m^2/s was equal to D_{SE}.

Table 5-14 Stoke's Einstein diffusion coefficient (D_{SE}) and simulated diffusion coefficient (D_{sim}) of paclitaxel (PTX) in water.

Diffusion coefficients of PTX $\cdot 10^{-10}$ (m^2/s)	
D_{SE}	3.86
D_{sim}	5.50 [27]

5.6   Discussion

The feasibility to use the nanostructured titania coatings as drug-eluting films for stent-implants will be discussed. The influence of the structure of the TiO_2-layer and the process parameters of the drug-loading on the drug-load are depicted. Factors, which influence the PTX-release kinetics into UP-water or bovine plasma, will be pointed out.

5.6.1   *Characterization of the polymorphs of paclitaxel*

In the present study, various PTX-polymorphs were formed on the nanostructured titania coatings. The polymorphs of PTX were varied by dissolving the as-received anhydrous crystalline form in different solvents or solvent/water mixtures and evaporating the liquid phase [6, 10]. PTX constituted from dichloromethane (DCM) was amorphous, which is in accordance with the results from Pyo *et al*. and Lee *et al*. [6, 10, 11]. The addition of water to PTX, which was dissolved in DCM, changed its morphology to co-existing forms of amorphous and dihydrated crystalline. This result was comparable with the findings of Pyo *et al*., who observed this kind of morphology after spray drying of PTX dispersed in DCM. If acetone (ACET) was employed, the constituted PTX was anhydrous crystalline. A combination of water and PTX dissolved in ACET generated a dihydrated crystalline morphology of PTX on the titania coating. If the solvent ethyl acetate (EA) was utilized, the resulting PTX was amorphous. This was in discrepancy with the findings of Pyo *et al.* and Lee *et al*., who observed the anhydrous crystalline form [10, 11]. The differences of the findings in literature and to the ones in the present study might have been caused by the purity grades of the solvents, because impurities can influence the nucleation of drug crystals. For instance residual water in the solvent can attach to the drug molecules to form hydrogen bonding. This can alter the conformation of the drug molecules in the solvent and can contribute to generate a certain drug morphology, e.g. the dihydrated crystalline form of PTX instead of the anhydrous crystalline one. This effect, the partial charge distribution between the particular solvent and the drug molecules, as well as the different supersaturating conditions of PTX in the solvent system have caused the formation of the different PTX-morphologies by single solvent evaporation [9, 28].

If PTX in EA was added to water and the liquid phase was evaporated, dihydrated crystalline PTX evolved. PTX dissolved in pure dimethyl sulfoxide (DMSO) or DMSO and water, yielded the anhydrous crystalline morphology in both cases. Hence the production of certain PTX-polymorphs on the titania coating could be controlled simply by varying solvents or solvent/water mixtures. The influence of the PTX-polymorph on the drug-load and release from the coating will now be discussed.

5.6.2 Factors affecting the drug-load capacity

The drug-load capacity of the TiO_2 nanostructured coatings can be influenced by two types of factors: one type is related to the *structure of the ceramic coating* and the second type to the *process parameters* used during the drug-loading.

5.6.2.1 Structural parameters of the titania coating

Structural factors, which influence the overall drug-load, are the thickness of the coating and its porosity, like was illustrated in Figure 5-19. By increasing the thickness of the coating, the amount of porous structure surrounding the reservoirs increases. This structure was characterized by 50 % porosity. Thus a duplication of the film's thickness will add 50 % more pore volume accessible to store a drug and will hence double the drug-load. The influence of the reservoir density in the coating and their size on the drug-load capability is also evident: increasing each of them increases the drug-load. Nevertheless, the amount of porous structure surrounding the reservoirs significantly influences the total drug-load, as was deduced from the theoretical calculations. The reservoirs with a diameter of 1 μm and a density of 150000 reservoirs/mm^2 in the coating, which equals the specification of the used reservoir layer (*RL*), added *theoretically* 3 % more drug into the coating compared to a coating with a non-reservoir structure (NRL). 14 % more PTX were loaded in the experiments into the *RL*s compared to the NRLs. This value was much higher than predicted by the calculations and this can be explained by the following. One has to consider that PTX was present in the reservoirs of the coating, in the pores of the surrounding ceramic and as a burst on top of the coating. When subtracting the amount of PTX in the burst-layer, a total load of ~ 0.6 μg/mm^2 is obtained in the *RL*s. This value is still 3 times the value obtained by the calculations. One has to take into consideration that the calculation of the theoretical load contained assumptions. For instance the volume of one PTX-unit was approximated to be identical to the volume of one PTX-molecule. In reality, the drug molecules might have arranged themselves densely to create small PTX-units containing more than one molecule. One can hence use 2 or 3 molecules of PTX in a unit volume in the calculations to correlate the theoretical PTX-load in the *RL*s with the one obtained by the experiments.

5.6.2.2 Process parameters of the drug-loading

In preliminary tests, drug-loading was performed using an atmospheric pressure technique and different solvents, in which PTX was dissolved. The loads of the coatings were different. The coatings with a NRL-structure, loaded with PTX dissolved in either DCM, ACET or in addition rinsed in water, contained 1 μg/mm^2 PTX. This drug-load is

comparable to the one applied in the commercially available Taxus[TM] drug-eluting stent (DES) [1, 29]. The PTX-load of the NRLs, loaded by dissolving PTX in EA, or additionally rinsing it in water, was lower: 0.4 µg/mm^2. The standard deviations obtained for the PTX-loads in the titania coatings were as high as 0.443 µg/mm^2 for the NRL loaded with ACET, Figure 5-13. The process parameters, which influence the drug loading hence had to be investigated.

Influence of the wettability and the process pressure on the penetration speed

The wettability of the PTX/solvent solution with TiO$_2$ can influence the penetration depth of the solution into the pores of the titania coating. It was not possible to measure the wettability of the solvents with the TiO$_2$-coating using the contact angle method. The deposited solvent-droplets spread on the surface leading to a total wettability. The penetration depth or the position of PTX in the pores of the coating could not be deduced by electron microscopy. But one could make estimations of the filling velocity of the NRL-porous structure by applying the Washburn equation

$$p_c = \frac{2 \cdot \gamma_{LV} \cdot \cos \theta_c}{r_p} \tag{5-11},$$

with p_c: capillary pressure, γ_{LV}: surface tension of the liquid, θ_c: contact angle and r_p: radius of the cylindrical pore. It describes the dynamic filling of a capillary with a circular cross section under non-slip conditions [30]. The meniscus velocity v, referred to as the filling rate, is given by

$$v = \frac{r_p \cdot \gamma_{LV} \cdot \cos \theta_c}{4 \cdot \eta} \cdot \frac{1}{l} \tag{5-12},$$

with η: dynamic viscosity of the liquid and l: distance between the capillary meniscus and the capillary inlet [31, 32]. If one assumes a good wettability, $\theta_c \to 0$ and $\cos \theta_c \to 1$. Thus the Equation (5-12) simplifies to

$$v = \frac{\gamma_{LV}}{4 \cdot \eta} \cdot \frac{r_p}{l} \tag{5-13}.$$

The ratio r_p/l was calculated from the mean pore radius of the NRL of 46.68 nm and the total thickness of the titania coating of 1200 nm, cf. Chapter 4.5.2, to 0.04. If this ratio is kept constant, the velocity is a function of the surface tension and the viscosity of the solvents. If one now inserts the solvent parameters listed in Table 5-15 into Equation (5-13), one can calculate the filling velocities of the capillaries. This NRL-structure equals the porous

structure surrounding the reservoirs in a *RL*.

Table 5-15 Dynamic viscosities and surface tensions of various solvents. Values for 20 °C unless stated otherwise [33, 34, 35].

solvent	*η (Pa·s)*	*γ_{LV} (mN/m)*	*v (m/s)*
DCM	$0.44 \cdot 10^{-3}$ [33]	23.70 [34]	0.51
ACET	$0.33 \cdot 10^{-3}$ [33]	26.50 [34]	0.78
EA	$0.45 \cdot 10^{-3}$ [33]	23.70 [35]	0.51
DMSO	$1.99 \cdot 10^{-3}$ (25 °C) [33]	43.50 [34]	0.21

The obtained filling velocities of the NRLs are equal for DCM and EA with 0.51 m/s. The filling velocity of ACET is higher: 0.78 m/s and for DMSO lower with 0.21 m/s. About half a meter of a capillary in the NRL-structure of the coating could be filled in only one second. Thus all types of PTX/solvent solutions should have well penetrated throughout the porous structure of the coating during the drug-loading. PTX should have been present in all pores of the ceramic structure. However, PTX was not detected by SEM in cross sections of the NRL, drug-loaded with PTX dissolved in EA in the preliminary test using the atmospheric pressure technique. Either PTX was adsorbed as a thin layer on the pore's walls and could not be detected by SEM. Or residual air in the pores built a counterforce to the capillary pressure of the penetrating PTX/solvent solution and no PTX was present in the pores of the coating.

The reasons to apply low pressure in the low pressure drug-loading technique were hence the following: a better control of the drug-loading and the "evacuation" of the porous structure prior to its immersion into the PTX/solvent solution. An additional effect was to force the penetration of the PTX/solvent solution into the porous coating by applying a pressure gradient. This pressure gradient was generated by applying atmospheric pressure, after the samples were immersed into the PTX/solvent solution at lower pressure. The laminar flow of the PTX/solvent solution through the coating as a function of applied pressure gradient can be expressed by the Carman equation [36]:

$$\frac{\Delta p}{L} = K'' \cdot \frac{(1-\varepsilon)^2}{\varepsilon^3} \cdot S_{BET}^{\;2} \cdot \eta \cdot (\varepsilon \cdot v_p) \qquad (5\text{-}14),$$

with Δp: pressure drop, L: thickness of the porous coating, K'': dimensionless constant, ε: fractional porosity, S_{BET}: specific surface area, η: dynamic viscosity of the fluid and v_p: average velocity through the pore channels. To apply this equation, the flow is approximated to be one-dimensional in the z direction of the coating, Figure 1-5 in Chapter 1.2. In many materials, $3.5 < K'' < 5.5$ is valid and a value of 5 was applied in the calculation. For spherical particles in the porous solid, like the slightly connected titania

grains which were observed in the NRLs and *RL*s in the present study, S_{BET} equals $6/d_g$. d_g is the grain diameter. With these two assumptions Equation (5-14) simplifies to [36]

$$\frac{\Delta p}{L} = 180 \cdot \frac{(1-\varepsilon)^2}{\varepsilon^3} \cdot \frac{1}{d_g^2} \cdot \eta \cdot (\varepsilon \cdot v_p) \qquad \text{(5-15).}$$

Usually a pressure drop Δp occurs naturally if a liquid flows through a porous structure. In the present study, Δp was represented by the applied pressure gradient. At the point, at which the atmospheric pressure is applied in the drug-loading (step 4 in Table 5-6), the pressure difference is at its maximum. Thus one can calculate the average velocity of the PTX/solvent solution in the pore channels with Equation (5-15). For simplification, the parameters of the pure solvents and not of the PTX/solvent solution were applied. The parameters of the coating, depicted in Table 5-16, were employed and the parameters η and γ_{LV} of the solvents EA and DMSO, Table 5-15. The pressure gradient Δp for the loading with the PTX/EA solution was $0.663 \cdot 10^5$ Pa and for PTX in DMSO $0.813 \cdot 10^5$ Pa. The velocity of EA to penetrate the entire coating was 0.0059 m/s and of DMSO 0.0017 m/s. This velocity corresponds to the penetration velocity only caused by the pressure gradient and it does not contain the velocity component generated by the capillary forces.

Table 5-16 Structural parameters of the NRL-titania coatings, which were applied to calculate the velocity of the fluid flow through the coating.

parameter	value
h	1.2 μm
ε	0.5
$d_g = d_{BET}$	93 nm

The penetration velocity generated from only the capillary forces was of a factor of 100 higher for EA. It can therefore be concluded that in the present case the dominant driving forces for the solvent penetration into the titania coatings were the capillary forces. The pressure difference, which was additionally applied in the low pressure technique, did not significantly alter the penetration velocity. But because the coating was subjected to lower pressure before immersion into the liquid, a smaller amount of residual air was present in the coating as compared in the atmospheric pressure technique. Thus the penetration of the PTX/solvent solution was not hindered by residual gas in the pores. PTX was detected in the coating by SEM, Figure 5-20.

Parameters related to dip coating

Dip coating in combination with low pressure was the favored method to load PTX into the titania coatings. Indeed it was possible to achieve reproducible drug-loads as high as

1.21 µg/mm^2 for *RL*s. However, process parameters, which influence the drug-load, had to be identified in this context. They were in particular the *droplet formation*, the *number of dips*, the *immersion time* and the *withdrawal velocity* from the PTX/solvent solution.

Droplet formation

First tests using the low pressure technique were accounted for the establishment of reproducible drug-loads. NRLs were hence loaded with a solution of PTX in DMSO. It was found that the PTX-load in one plate-shaped sample with the NRL-structure was inhomogeneous. The small specimens, which were cut from the top and middle region of the drug-loaded plates as shown in Figure 5-5, contained 0.016 µg/mm^2 PTX after one dip, the ones cut from the bottom were characterized by a 10 times higher amount, Figure 5-14. The droplet formation of the PTX/DMSO solution on the bottom of the big plates after withdrawal still had an influence 5 mm distant from the bottom edge. The high standard deviations in the drug-loads discovered at the beginning of the studies could therefore be addressed to the droplet generation and hence the accumulation of PTX at the bottom. For further testing, only samples cut from the middle and top piece of the plates were applied. The problem could thus be easily solved for the rectangular, TiO$_2$-coated plates. But it has to be accounted for when using this dip coating, drug-loading technique to create the DES. The stent has a complex geometry with interconnecting metal struts, cf. Figure 2-1. Using the dip coating technique for drug-loading can create droplets at the connection-points of the stent's struts and at the stent's bottom edge. This can create an inhomogeneous PTX-load in the stent and can result in a non-homogeneous drug-release later. One has to think about methods to remove the droplets after drug-loading, like rotating the stent around its axis with a high speed. The thus created centrifugal force might detach the droplets. Another method would be to remove the PTX-droplets in a washing procedure following the drug-loading. But washing is not as trivial as it seems, as was observed in the experiments to remove the PTX-burst-layer, Chapter 5.5.4.3.

Number of dips

Multiple dips into the drug/solvent solution can increase the drug-load in a porous coating [37]. Four dips sequentially into the PTX/DMSO solution increased the load of the middle part of the drug-loaded plates in Figure 5-5 from 0.016 µg/mm^2 after 1 dip to 0.022 µg/mm^2 after 4 dips. One can compare the findings with the theoretical PTX-load in the NRLs after 4 consecutive dips into the PTX/solvent solution. The calculation for the theoretical load was the following. The solvent should have completely penetrated the coating, as was obtained from the calculations of the penetration velocities. Assuming that the pores of the coating were totally filled with the PTX/DMSO solution of a concentration of 10 mg/ml, 0.006 µg/mm^2 PTX should have been left in the coating after 1 dip. After 4

dips, 4 times that value, which equals $0.024\ \mu g/mm^2$, should have been present in the coating. This value is only valid, if one assumes that the amount of adsorbed PTX in the pores did not change the pore volume and that *no* PTX got desorbed from the pore-walls in the subsequent dips. The measured value of $0.022\ \mu g/mm^2$ thus fitted well to the calculation.

The PTX-load of the small pieces at the top position of the plates did not change, Figure 5-15. It might have been caused by the 30 min of time, in which the samples were exposed to low pressure before getting immersed into the liquid. After 4 times that time span (120 min), the level of the PTX/DMSO solution in the glass beaker might have decreased. No more PTX/solvent solution was added to again increase the liquid level. Thus the liquid did not totally cover the plates any more for drug-loading. Hence no more PTX could be loaded into the top area of the plates. This has illustrated that it was important to set the correct immersion time for drug-loading to avoid the evaporation of the solvent.

Immersion time

The drug-loading tests of the nanostructured titania coatings revealed a dependence of the PTX-load on the time, during which the samples were immersed into the PTX/EA solution at high pressure, step 4 of procedure $LP_{EA}1$ in Table 5-6. For an immersion time between 1 min and 1 h, the overall load decreased. For immersion times between 1 h and 24 h, the PTX-load increased, as depicted in Table 5-10. By applying 24 h, the maximum PTX-loads of $1.056\ \mu g/mm^2$ for NRLs and of $1.211\ \mu g/mm^2$ for *RL*s were obtained.

It is not totally clear why with increasing immersion time from 1 h to 24 h the PTX-quantity in the coating increased. The PTX/EA solution should have fully penetrated the entire porous NRL in $2.3\ \mu s$, as was calculated earlier. In the calculation for the capillary driven penetration, straight cylindrical pores with a median pore diameter, d_{v50}, of 76 nm were applied. In reality, the pores showed a pore size distribution with pore widths as small as 20 nm and as big as 120 nm. Additionally, pores were not straight, but exhibited a tortuosity and they were interconnected, as was seen in Chapter 4.5.2. The presence of smaller pores as well as a longer distance between the capillary meniscus and the capillary inlet caused by the tortuosity (parameter l in Equation (5-13)), can decrease the filling velocity. A longer immersion time might hence have triggered a "deeper" penetration and higher loads after 24 h of immersion compared to 1 h. The incoherence with the immersion time and the PTX-load of the samples loaded with immersion times below 1 h is not totally clear, but might be associated to different thicknesses of the PTX-burst-layer on top of the coating, as was demonstrated in Figure 5-18. The thickness of this layer is influenced by the withdrawal velocities, a factor which was not exactly controlled during the drug-loading.

Withdrawal velocity

The withdrawal velocity in dip coating has an influence on the thickness of the deposited liquid layer on the substrate, as was depicted in the Equation of Landau-Levich, Equation (4-1) in Chapter 4.1. This equation was used to approximate, how much PTX was deposited on top of the TiO$_2$-coating. Calculations of that amount were performed using the specifications of the PTX/DMSO and PTX/EA solutions, which were applied in the drug-loading. The parameters in the calculation applying the PTX/DMSO solution were the dynamic viscosity of DMSO, η_{DMSO}, the liquid vapor surface tension of DMSO, $\gamma_{LV,DMSO}$, listed in Table 5-15, the density of DMSO, ρ_{DMSO}, of 1.100 g/cm^3, the withdrawal velocity of 1.0 ± 1 cm/s, the acceleration due to gravity of 9.81 m/s^2 and the concentration of PTX in DMSO of 10 mg/ml. For PTX/EA the same parameters were applied, except that the values of η_{EA} and $\gamma_{LV,EA}$ listed in Table 5-15 were applied, the density of EA was ρ_{EA} of 0.897 g/cm^3 and the concentration of PTX in EA was 103.61 mg/ml. The withdrawal velocity of the titania coatings from the drug/solvent solutions was not controlled in the present study, except for the samples produced with the method LP$_{EA}$1 with immersion times of 5 h and 24 h and with the method LP$_{EA}$2. For these samples, the pulling speed was adjusted to count 3 s to withdraw the plate of a length of 3 cm from the solution. Thus the resulting withdrawal velocity of ~ 1 cm/s was applied in the calculations.

The amount of PTX in the liquid film on top of the TiO$_2$-coating after withdrawal from the PTX/DMSO solution was calculated to be 0.112 µg/mm^2 for 1 cm/s, Figure 5-26. This amount was bigger than the total load in the films, which was obtained in experiments. If the withdrawal velocity was as small as 0.1 cm/s, 0.024 µg/mm^2 would have been deposited on the top of the NRLs, Figure 5-26. That the withdrawal velocity needs to be well controlled in the drug-loading procedure gets clearer if one uses the solution of a high concentration of PTX in EA. The amount of PTX in the burst-layer after withdrawal with 1 cm/s is 0.530 µg/mm^2, Figure 5-26. An increase of the withdrawal speed from 1 to 2 cm/s adds 59 % more PTX on top of the coating. To avoid variations in the drug-load in the PTX-burst-layer, always the same withdrawal velocity should be used. The thickness of the burst-layer can be reduced, if a lower withdrawal velocity is applied.

However, the PTX-loads after 5 h and 24 h of immersion into the PTX/EA solution were reproducible for the NRLs and the *RL*s. PTX was accumulated in the drug reservoirs, in the pores of the structure surrounding the reservoirs and as a burst-layer, Figure 5-20. The therapeutical agent was preferentially localized at the edges of the reservoirs. This can be explained by the drying of the coating after drug-loading. During the drying, the solvent gets evaporated through the small pores of the porous structure surrounding the reservoirs. Capillary forces, as well as surface tensions directed the PTX/solvent solution towards the

edges of the reservoirs.
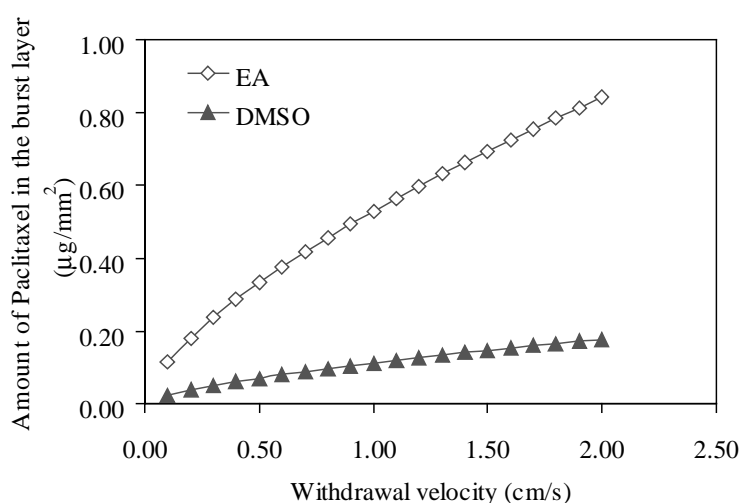
Figure 5-26 PTX-load in the liquid film on top of the TiO$_2$-coating as a function of the withdrawal speed from the PTX/DMSO solution with 10 mg/ml or from the PTX/EA solution with a concentration of 104 mg/ml.

5.6.2.3 Rinsing

The rinsing of the PTX-loaded titania coatings, which was performed to remove the burst-layer, has shown that the PTX-morphology in the coatings can be changed by various concentrations of acetonitrile in UP-water. Amorphous PTX from EA_w730RL was transformed into the dihydrated crystalline form in, and on top of the coating. The crystals were long and needle-shaped, like depicted in Figure 5-22. The applied rinsing methods need future improvement to just dissolve PTX from the top of the surfaces. In the present study, PTX was not at all removed from the coating after rinsing in water for 3 s. The presence of PTX generated a hydrophobic character of the coating compared to the native coating without drug. This was shown by comparing the contact angles with water: 25.30 ° for the native *RL* and 66.74 ° for the drug-loaded *RL*, Table 4-11 and Table 5-12. This hindered the penetration of water. Mixtures of high concentrations of non-polar acetonitrile in water increased the PTX-solubility. Hence the entire drug was dissolved from the coating and not just from the burst-layer. When the coatings were immersed into bovine plasma for a drug-release test, only the PTX-burst-layer was released after 4 d of testing. PTX is lipophilic and gets well dissolved in bovine plasma, which contains lipoproteins, cholesterol and fatty acids amongst other constituents, Table 5-17. But it is not recommended to use plasma as a rinsing agent, because it contains many other components, like proteins and ions, which can contaminate the coating.

Table 5-17 Main constituents and ionic concentrations of blood plasma [26].

major proteins and organic constituents of blood plasma		*ionic concentrations in blood plasma*	
albumin	30-55 g/l	Cl^-	96-111 mM
α-globulins	5-10 g/l	HCO_3^-	16-31 mM
β-globulins	6-12 g/l	HPO_4^{2-}	1-1.5 mM
γ-globulins	6.6-15 g/l	SO_4^{2-}	0.35-1 mM
α-lipoproteins	3.5-4.5 g/l	$H_2PO_4^{2-}$	
fibrinogen	1.7-4.3 g/l	Na^+	131-155 mM
total cholesterol	1.2-2.5 g/l	Mg^{2+}	0.7-1.9 mM
fatty acids	1.9-4.5 g/l	Ca^{2+}	1.9-3 mM
glucose	0.65-1.1 g/l	K^+	3.5-5.6 mM
lactate	0.5 2.2 mM		
urea	3-7 mM		

Further studies are hence necessary to optimize the rinsing procedure. Another method to reduce the thickness of the PTX-burst-layer is to apply a reduced withdrawal velocity of the titania coatings from the PTX/solvent solution, like was pointed out earlier in this discussion.

5.6.3   *Factors influencing the in vitro release kinetics of Paclitaxel*

In the present study it has been observed that many factors can influence the drug release from the thin, nanostructured titania coatings. They belong to the three categories depicted in Table 5-18: the structure of the TiO_2-coating, the drug's properties and the parameters of the in vitro *drug-release* experiments. They will be discussed in the following.

Table 5-18 Parameters influencing the PTX-release from the thin nanostructured TiO_2-films.

category	*parameter*
structure of the TiO_2-coating	pore diameter
	pore tortuosity
	pore interconnectivity
	thickness of the nanoporous layer
	size of the reservoirs
features of the drug	morphology
	dissolution rate
	size of drug particles
drug-release experiment	solubility in media
	time intervals
	temperature
	agitation speed

5.6.3.1 *Structures of the TiO$_2$-coating and of paclitaxel*

The various polymorphs of PTX in the drug-delivering NRLs directed the release velocities of the therapeutical agent into water, Figure 5-14 and Figure 5-28. The highest cumulative release of PTX after 4 d of elution was recorded for amorphous PTX, lower ones for the anhydrous crystalline and dihydrated crystalline morphologies. The release was thus dominated by the dissolution of PTX rather than by its diffusion from the porous TiO$_2$-structure during the considered time interval. This gets clear if one considers the zero order release constants, k$_0$, which depended on the PTX-morphology: amorphous > anhydrous crystalline > dihydrated crystalline, Table 5-9.

The explanation of the dependence of the k$_0$ on the PTX-morphology is the following. The drug molecules in the amorphous form of PTX are randomly arranged and not well ordered like in the case of the crystalline forms. Water can penetrate with less resistance than in the crystalline structures and dissolves the PTX-molecules. In the crystalline structures, the molecules are densely packed and ordered. The water penetration as well as the dissolution of the molecules from the crystal lattices is hindered, leading to a lower release constant. The higher release constant k$_0$ of the anhydrous crystalline compared to the dihydrated crystalline forms of PTX is in addition related to their dissolution concentrations. The saturation concentration of the anhydrous crystalline PTX in water is 3 µg/ml, and for the dihydrated crystalline one 1 µg/ml [6]. At the beginning of the immersion into the water up to 10 h, more PTX got dissolved from the anhydrous crystalline form than from the dihydrated crystalline one, which has the lower saturation concentration. This shifted the release curve of the anhydrous crystalline form (ACET_w730NRL) to higher values compared to the dihydrated crystalline ones of WACET_w730NRL and WEA_w730NRL. In the proceeding elution, the anhydrous crystalline form got converted into the dihydrated crystalline one, which is the stable form in equilibrium with water [6]. Hence the release slowed down.

A release test of amorphous PTX from a *RL* (EA_w730*RL*) into UP-water was performed during a longer period of time than 4 d to study the release kinetics. 11 % of the total PTX-load were continuously released up to 32 d. The zero-order model best fitted the data. From the performed release tests into water it was unclear, when the PTX-burst-layer was totally released from the coating, at what time the pharmaceutical got transported out of the pores or if both mechanisms took place simultaneously. The Korsmeyer-Peppas model predicted with a high correlation coefficient the diffusion dependence of the drug-release from the coating. The highest correlation coefficient of EA_w730NRL was obtained for the Higuchi model, Table 5-9. It describes the diffusion of a drug through a porous solid. A good fit to the zero order release kinetic was also determined in the release test of EA_w730*RL* up

to 32 d. It is described in literature, that this mechanism is observed for low-soluble drugs or drugs released from a reservoir system [15]. These two premises fit our system: PTX has a low solubility in water and the structured TiO_2-coating can be characterised as a combination of a *matrix system* and a *reservoir system*. A *matrix system*, because the drug is partially dispersed in the porous TiO_2-structure surrounding the reservoirs. And like described by Higuchi, the release depends then on the porosity ε of the solid structure and the tortuosity τ of the pores. In these systems, the concentration gradient of the drug changes with increasing release time. The *RL*s are also a *reservoir system*, because the drug is present in solid form in the reservoirs. And as described in Chapter 5.2 for the zero order release from reservoir systems, the release depends on the effective diffusivity of the drug through the surrounding membrane, thus the porous TiO_2 surrounding the reservoirs. The combination of the burst-layer, the matrix system and the reservoir system in the TiO_2-drug-delivering coating represents a complex drug-delivery system. Hence it was not possible in the present feasibility study to identify the detailed mechanisms directing the drug flux out of the coating and to determine an effective diffusion coefficient. They should be analyzed in following studies, whereas the results of the structural characterization of the coating and the drug-load/release results from the present study should serve as a basis for understanding. In future drug-release studies, samples should be taken out of the release test at certain time points, dried and the cross sections observed by HRSEM. It should then be possible to detect, when the PTX-burst-layer was completely removed, when the PTX in the structure surrounding the reservoirs was eliminated and when the dissolution of PTX from the reservoirs takes place. This should be correlated to the shape of the release curves. To remove the PTX-burst-layer prior to analysis, and thus to focus just on the release from the porous TiO_2, would be the ideal condition.

By analyzing theoretically the possible transport mechanisms involved in the drug-release from the TiO_2-coatings, one can summarize structural factors influencing the release kinetics. To *decrease* the flux of drug out of the coating, the following changes of the structural parameters can be done.

- A higher tortuosity factor of the pores in the ceramic structure surrounding the reservoirs should be applied (τ in Equations (5-4), (5-9)). It increases the diffusion path.

- The higher the initial porosity of the system, e.g. the higher the density of the big reservoirs, the more drug can be loaded into the coating. Thus the density of the drug, the so-called drug size in Table 5-18, in the porous structure increases. The specific volume of the drug U in Equation (5-9) decreases and thus the release diminishes.

- Shifting the ratio of molecule-to-pore diameter, χ, to a higher values will decrease the flux. That means the pore size distribution of the TiO_2-structure surrounding the

reservoirs should be shifted to smaller pores. A median pore diameter, d_{v50}, of 76 nm like applied in the present study, reveals a χ of 0.027. A new d_{v50} of 7.6 nm reveals a χ of 0.275. Pore size effects on the apparent diffusion coefficient can then be quiet large and can slow down the drug-release. It is reported in literature that a χ larger than 0.1 greatly slows down the molecular flux [38]. One can compare these effects with the gaseous flow in porous materials. Three regimes with different diffusivities, depending on the pore diameter, are depicted in Figure 5-27. For macropores, collisions between the molecules occur much more frequently than collisions with the pore wall and molecular diffusion is the dominant transport mechanism. As the size of pores decreases, the number of collisions with the wall increases and Knudsen diffusion takes over. The mobility of the molecules starts to depend on the dimension of the pore, and the effective diffusion coefficient, D_{eff}, reduces. At smaller pore sizes, when the pore diameter is similar to the molecule size, the molecules will constantly experience an interaction with the pore surface. Thus they will be in the configurational diffusion regime and D_{eff} decreases further [39]. If investigations of the influence of the pore diameter on D_{eff} should be deduced in future studies, one can precede as follows. One could think of using NRLs with various pore sizes. The pore sizes can be reduced by applying smaller primary TiO_2-nanoparticles. For instance to create pores of a width of 10 nm, the initial particles should exhibit a diameter of 5-10 nm. Another method to reduce the pore size is to increase the sintering temperature, whereas this is attended by a reduction in overall porosity. The produced NRLs should then be loaded with PTX by methods which were described in the present study and the PTX-burst-layer should be removed. The drug-loaded NRLs should be subjected to the release tests. The obtained release profiles should fit well the Higuchi and/or the zero order kinetics and should reveal D_{eff} as a function of pore diameter, according to Figure 5-27. Thus one can determine pore sizes triggering a certain drug-release and a critical pore size, which prevents diffusion at all.

▪   Another option to decrease the PTX-flow from the coating is related to treating the system as a reservoir system. An increase in the thickness of the nanoporous TiO_2-layer on top of the reservoirs, parameter Δx in Equation (5-2), increases the diffusion path of the molecules and hence retards the drug-release.

▪   The change of amorphous PTX to the dihydrated polymorph decreases its dissolution and hence the PTX-release out of the coating into water. If this effect is still significant when the coating is exposed to plasma instead of water needs to be investigated further.
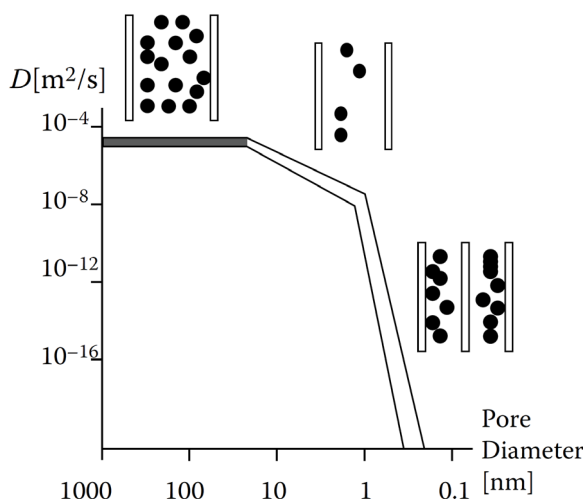
Figure 5-27 Relation between diffusivity and pore size for gaseous molecules. In the range of the highest diffusion coefficients, collisions between the molecules occur more frequently than with the wall (molecular diffusion). If the pore size gets smaller, the number of collisions with the walls increases (Knudsen diffusion). In the regime of the smallest diffusion coefficients, the molecules constantly interact with the pore's surface. Adapted from [39].

5.6.3.2   Parameters of the drug-release experiments and relation to literature findings

The obtained release profiles of the PTX-polymorphs from the TiO_2-coatings into water were similar to the ones obtained by Kamath *et al.* [1]. He and co-workers examined formulations of PTX in non-degradable styrene-isobutylene-styrene copolymer matrices, Figure 5-28, for the commercially available Taxus[TM] stent. The total PTX-load in the polymers was 1 µg/mm^2 and the release was performed into phosphate buffered saline (PBS), supplemented with Tween 20. Tween 20 as a surfactant was used to increase the aqueous solubility of PTX and to prevent drug loss through passive adsorption on the vial's wall. The preparations of the eluates of PTX from the titania coatings for HPLC-analysis in the present study were also adjusted to detach PTX from the vial's wall. Eluates were vortex mixed for 30 s prior to mixing them with acetonitrile and subjecting them to HPLC-analysis.

The release profiles of PTX from the polymer matrices of the Taxus[TM] stent depend on the drug-concentration in the polymers. A high PTX-concentration triggers a fast release, a lower concentration a moderate release and the lowest drug-concentration a slow release, Figure 5-28. The slow release was characterized by releasing much less than 5 % of total drug-load within 10 d, the moderate by releasing about 5 % and the fast release by liberating 70 % [1]. The slow release formulation is used in the commercially available Taxus[TM] stent. A certain quantity of therapeutical agent stays trapped in the polymers of each of the formulations [2].
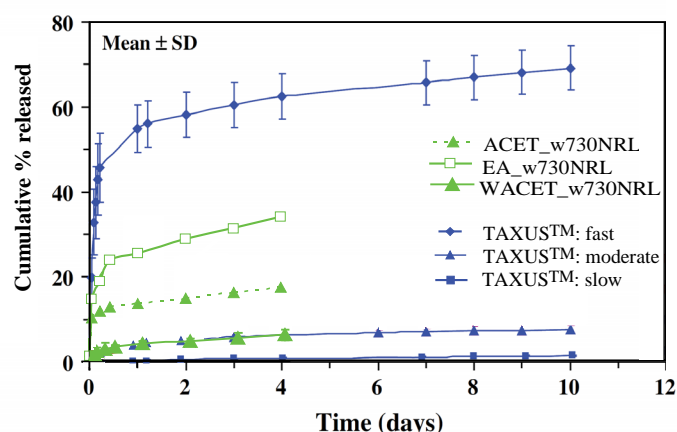
Figure 5-28 Cumulative PTX-release from different polymer matrices for the Taxus[TM] stent and of selected nanostructured titania coatings of the present study (graph modified from [1]). The release profiles of the polymer coatings were obtained in PBS supplemented with Tween 20 at 37 °C. The ones of the TiO_2-coatings in water at 37 °C.

Three representative release curves of PTX from the titania coatings recorded in the present study were added to the ones of the Taxus[TM] stent in Figure 5-28. Dihydrated crystalline PTX from WACET_w730NRL exhibited a moderate release when compared to the Taxus[TM] stent. The release of the amorphous PTX from EA_w730NRL and of anhydrous crystalline PTX from ACET_w730NRL were in between the moderate and fast release after 4 d of testing. Similar release profiles from the PTX-loaded NRLs to the ones of Kamath *et al*. were thus obtained with the restriction that in the present study pure water was applied. The solubility of PTX in water was different to the one of PBS supplemented with Tween 20. Different time intervals to renew the elution media also affect the drug-release profile and thus can restrict the comparison of the release kinetics between different studies. If diffusion is the driving force of drug-release, more frequent changes in the surrounding media create more frequently a higher concentration gradient between the drug-eluting matrix and the media. This can trigger a faster diffusion and thus a higher flux of the drug, except when always perfect sink conditions are applied. That means, that the concentration of drug in the release media should always be lower than 1/3 of the maximum solubility concentration.

The last, but not negligible factor influencing the release profiles, and thus the comparison between studies performed by different research groups, is the agitation of the media during the release test. Depending on the way of agitation and the agitation speed, convection needs to be added to the pure diffusion and dissolution models mentioned in Chapter 5.2. Then two characteristic liquid layers exist at the surface of the drug-eluting matrix: a diffusion boundary layer and further distant to the surface a hydrodynamic

boundary layer [40]. The thickness of the diffusion layer thus depends on the velocity of the surrounding, moving release media. If one assumes a laminar flow of the media and the drug-dissolution from a rotating disk specimen-or vice versa if the media is rotating over the pharmaceutical formulation with an angular velocity ω-the thickness of the diffusion layer, h, is calculated by

$$h \cong 0.5 \cdot \left(\frac{D}{v}\right)^{\frac{1}{3}} \cdot d_h \qquad (5\text{-}16),$$

with D the free diffusion coefficient of the drug, ν the kinematic viscosity of the media and d_h the thickness of the hydrodynamic layer, which is derived by [40]

$$d_h = 3.6 \cdot \left(\frac{v}{\omega}\right)^{\frac{1}{2}} \qquad (5\text{-}17).$$

If thus the angular speed of the media on top of the matrices' surface increases, the diffusion layer thickness h decreases, like is depicted in Figure 5-29. This augments the flux of medicament from the dosage form. This gets clearer if one inserts the diffusion layer thickness h in Equation (5-16) into the flux of the drug for the zero-order release kinetics in Equation (5-2) or into Equation (5-8) of the first order release constant.

When further studying the development of the Taxus[TM] stent, one gets to know that the slow and moderate formulations displayed in Figure 5-28 were applied in clinical trials. Even if the moderate release-modification did not reveal a compromise in stent-safety, the slow release formulation was commercialized [1]. Thus it needs to be investigated in future studies, if a moderate release of PTX from the TiO_2-coating is appropriate or if a slower release is preferential. Then the structural parameters of the titania film need to be modified as was described at the end of Chapter 5.6.3.1.

The release kinetics of PTX into water were discussed up to now. They were performed to accomplish release profiles in a reasonable time and to compare the effective diffusion coefficients-which could finally not be deduced-with the theoretical ones and the ones from simulations in Table 5-14. But UP-water did not represent physiological fluids.

One release experiment was hence performed with a selected drug-loaded *RL* and a Taxus[TM] stent into bovine plasma. The Taxus[TM] DES exhibited a continuous release without burst-effect up to 7 d, by which only 2 % of loaded drug was released. 46 % of the total drug-load in the titania *RL* was released within the first 4 d. After 4 d, no more PTX was liberated from the nanostructured coatings, Figure 5-24. More than 50 % of initially incorporated pharmaceutical hence stayed trapped in the coating. This could be verified by

electron micrography, Figure 5-25 (a). The quantity of released PTX from the coatings within the first days of elution corresponded to the amount of PTX present in the PTX-burst-layer on top of the coating.
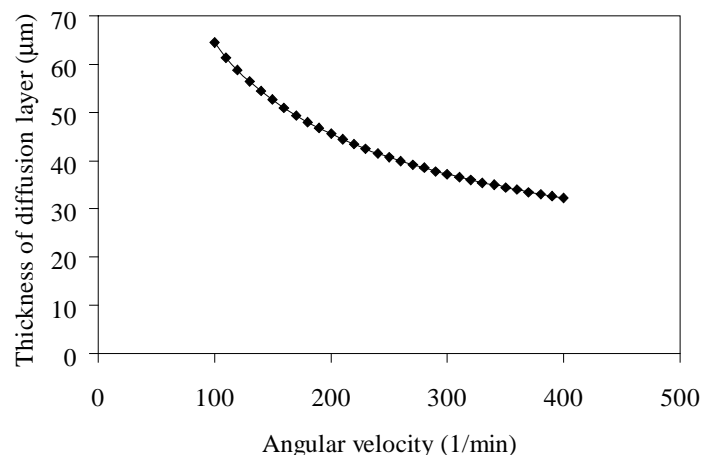
Figure 5-29 Influence of the angular velocity of agitation on the thickness of the diffusion layer at the release matrices' surface.

Since PTX is lipophilic, the applied plasma containing fatty acids, cf. Table 5-17, increased the drug's solubility compared to the one in water. This caused more rapid drug dissolution from the burst-layer. That the major amount of PTX stayed in the TiO_2-coating was generated by the built-up of a layer composed of plasma components on top of the coating, Figure 5-25 (b). It blocked the pores of the TiO_2-structure surrounding the reservoirs and hence the diffusion of the pharmaceutical out of the coating. The composition of that layer was not analyzed. But it is described in literature that proteins and calcium phosphates tend to adhere on TiO_2-surfaces [26, 41, 42, 43]. Immediately after implantation of a material, proteins adsorb on it surface. Fibrinogen and albumin represent adhesion proteins and are an essential component in the blood plasma, Table 5-17. Their presence on the implant's surface can trigger the adhesion of other proteins and can strongly influence the adhesion of blood platelets and other cells [26].

The calcification due to the deposition of calcium phosphate apatite is often observed on vascular implants. TiO_2-and more preferentially crystalline anatase-has a tendency to reinforce apatite formation [41, 42]. The net charges of the titania surface in contact with an aqueous media depends on the pH of the media, which transforms the Ti-OH groups to the following [41]:

- pH < 4: formation of $[Ti-OH_2]^+$ bonds creating a positive charged surface,

- pH > 9: $[Ti-O]^-$ creates a negatively charged surface.

Between both pH-ranges, the acidic and basic groups coexist. At the isoelectric point of TiO_2, at a pH of 5-6, the surface exhibits a net charge of 0. Thus at physiological conditions at pH 7.4 the surface is slightly negatively charged. The negative charge attracts cations like Ca^{2+} or Na^+ and the positive charge attracts anions like $H_2PO_4^-$. These ions are all components present in the blood plasma, Table 5-17, and their presence on the titania surface represents nucleation sites for the apatite formation. This happens more preferentially on anatase then on rutile when supersaturated calcium phosphate solutions are applied [41]. It is related to their different surface energies, cf. Chapter 4.6.3.

It has to be pointed out that the main phase present in the applied TiO_2-coatings was anatase. If the calcium phosphate precipitation on the titania films turns out to be a problem for their application in DESs, a higher sintering temperature can easily create rutile and thus decrease the calcification tendency of the coating. Lately it was reported by Osaka *et al.*, that the presence of some transition metal ions, like Cr^{3+}, Fe^{2+}/Fe^{3+} were effective to depress the bioactivity of the anatase layer on stainless steels supports [44]. The nanostructured TiO_2-coating will be applied on 316L SS supports in a DES and not on silicon wafers. During the heat treatment, to densify the primary TiO_2-nanoparticles in the coating, metal ions from the support might also migrate to the top of the films. Their presence might limit the apatite formation on top of the coatings [44]. On the contrary, the existence of the layer formed by plasma components can decrease the flux of the drug from the coating in such a way, that a sustained drug-release can be achieved. If the formation of that protein/calcium phosphate layer will have an influence on the drug-release under *in vivo* conditions, needs to be found out in future studies.

5.7   Conclusions

PTX was successfully loaded into the nanostructured TiO_2-coatings. The load of the drug into a layer of 1.2 µm thickness and not containing reservoirs (NRL) can be varied from as small as 0.06 µg/mm^2 to a maximum load of 1.06 µg/mm^2. The PTX-loads depend on the parameters applied in the drug-loading procedures. The maximum PTX-load in a titania layer containing drug reservoirs (*RL*) was 1.21 µg/mm^2 and higher than for the NRLs. PTX was accumulated in the drug reservoirs, in the porous structure surrounding the reservoirs and it was present as a burst-layer on top of the coating. The quantity of pharmaceutical agent loaded into the NRL or *RL* was comparable with the PTX-concentration in the commercially available Taxus^{TM} stent [1, 29].

Different factors influencing the drug-load capacity of the titania coating were identified during the experiments. They were separated into the two categories (1) structure of the TiO$_2$-coating and (2) process parameters used during the drug-loading. A higher porosity in the coating increases the PTX-load. The presence of the reservoirs in the *RL*s added 14.63 % more PTX into the porous film compared to the NRLs. Bigger reservoirs as well as a higher density of them will further increase the PTX-load, as was obtained from theoretical calculations. An increase of the thickness of the coating will also increase the space available to store PTX. But one has to be cautions to change the structure of the coating in needs of the drug-load capacity, because they are linked to the mechanical stability of the coating [45]. A solvent evaporation method was chosen to incorporate the pharmaceutical into the coating. This method has proven to be powerful to adapt the PTX-loads for different needs. Different PTX-polymorphs could be created by the application of various solvents, in which PTX was dissolved. For instance the evaporation of ethyl acetate (EA) from PTX created amorphous PTX, the evaporation of acetone (ACET) the anhydrous crystalline and of an ACET/UP-water mixture the dihydrated crystalline morphologies. The increase of the number of dips into the PTX/solvent solution during drug-loading augmented the PTX-load. Various PTX-loads in the coatings could be achieved by applying different immersion times of the specimens into the PTX/solvent solutions. After 5 h of immersion, 0.82 µg/mm^2 for the NRL and 0.94 µg/mm^2 for the *RL* were measured. After 24 h of immersion, 1.06 µg/mm^2 for the NRL and 1.21 µg/mm^2 for the *RL* were obtained. Besides PTX being present in the porous structure of the coating, it was detected on its top as a burst-layer. The burst-layer was formed by the withdrawal of the specimens from the PTX/solvent solutions, which created a liquid layer on top of the coating. After evaporation of the solvent, a solid PTX-layer was present, which occupied 50 % of the total PTX-load in the coating. Because the withdrawal velocity of the specimens was not precisely controlled in the present feasibility study, it is recommended to do so in future studies. The thickness of the PTX-burst-layer can be decreased by lowering the withdrawal velocity of the specimens from the PTX/solvent solution. Experiments to remove the PTX-burst-layer from the coating have shown that PTX an be removed from the coating, but the method needs further improvement.

The drug-loaded *RL*s were subjected to drug-release experiments into either ultra-pure (UP)-water or bovine plasma. The obtained release profile into water fitted the moderate and sustained release formulations of PTX investigated for the Taxus^{TM} drug-eluting stent (DES) [1, 2]. The detailed transport mechanisms involved in this nearly zero-order release from the *RL*s could not be identified, because during the tests PTX could have been released from the drug reservoirs, the porous structure surrounding the reservoirs and from the PTX-burst-layer on top of the coating. It is suggested that in future studies the burst-layer should be removed before the release experiments are started.

The parameters influencing the drug-release were in this study evaluated experimentally and theoretically. They can be categorized into belonging to the structure of the coating, the features of PTX and the set-up of the release experiments. A decrease in the pore size of the structure surrounding the reservoirs, a tortuosity increase of them and an increase of the thickness of the nanoporous coating on top of the reservoirs can diminish the diffusion of PTX out of the coating. The pore sizes can thus take effect on the effective diffusivities of the drug from the coating. Smaller pores increase the interaction of the drug molecules with the pore walls and lower the molecular flux out of the coating [38]. A median pore diameter of an order of magnitude of 1 smaller than the one in the coatings under investigation would reveal a molecule-to-pore ratio of 0.208. Molecules would hence collide more frequent with the pore walls and thus decrease the diffusivity. Smaller pores in the coating can be formed by decreasing the diameter of the primary TiO_2-nanoparticles to about 5-10 nm. If the drug particle size in the coating increases, which can be realized by completely filling the pores with PTX, a prolonged drug-release can be supported. The drug's morphology can modify the drug-release, as was seen in the drug-release experiments of PTX into UP-water. The amorphous PTX was released faster from the NRL than the anhydrous and dihydrated crystalline forms. If this effect will be still significant when performing the elution in a physiological media like plasma, needs to be investigated further.

In a release test of PTX-loaded *RL*s into bovine plasma, 46 % of the PTX-quantity loaded into the coating were released after 4 d of elution, the rest stayed trapped in the coating. The released amount was correlated to the quantity of PTX in the burst-layer on top of the coating. Hence ~ 0.6 µg/mm^2 PTX were present in the porous structure of the *RL*s. If the drug-release from the *RL*s gets blocked by the deposition of a layer of plasma components on top of the coating, like was observed in the present study, under *in vivo* conditions needs to be further examined. The drug-release from the Taxus^{TM} stent into bovine plasma for comparison was continuous up to 7 d, by which 2 % were released.

5.8   Reference

[1]   K.R. Kamath, J.J. Barry, K.M. Miller, "The Taxus^(TM) drug-eluting stent: A new paradigm in controlled drug delivery", *Advanced Drug Delivery Reviews*, Vol. 58, 2006, pp. 412-436.

[2]   S. Venkatraman, F. Boey, "Release profiles in drug-eluting stents: Issues and uncertainties", *Journal of Controlled Release*, Vol. 120, 2007, pp. 149-160.

[3]   G. Mani, M.D. Feldman, D. Patel, C.M. Agrawal, "Coronary stents: A materials perspective", *Biomaterials*, Vol. 28, 2007, pp. 1689-1710.

[4]   Paclitaxel   product   information   sheet,   Sigma   Aldrich,   available   at: http://www.sigmaaldrich.com/catalog/ProductDetail.do?N4=T1912| SIGMA&N5=SEARCH_CONCAT_PNO|BRAND_KEY&F=SPEC, February 2009.

[5]   V. Farina, "The chemistry and pharmacology of Taxol® and its derivatives", *Pharmaco Chemistry Library, Vol. 22, Elsevier Science B.V.*, 1995.

[6]   R.T.L.H. M. Burt, W.L. Hunter, "Solid-State Characterization of Paclitaxel," *Journal of Pharmaceutical Science*, Vol. 86, 1997, pp. 1458-1463.

[7]   V.R. Thalladi, M. Dabros, J.R. Cox, "Selective Growth of stable Polymorphs", *Patent WO2007109651(A2)*, 2007.

[8]   I. Karabas, M. Orkoula, C. Kontoyannis, "Analysis and stability of polymorphs in tablets: The case of Risperidone", *Talanta*, Vol. 71, 2007, pp. 1382-1386.

[9]   H.G. Brittain, "Polymorphism and Solvatomorphism 2005, Review", *Journal of Pharmaceutical Sciences*, Vol. 96, 2007, pp. 705-728.

[10]   J.H. Lee, U. Gi, J. Kim, S. Kim, H. Oh, B. Min, "Preparation and Characterization of Solvent Induced Dihydrated, Anhydrous, and Amorphous Paclitaxel", *Bulletin of the Korean Chemical Society*, Vol. 22, 2001, pp. 925-928.

[11]   S.-H. Pyo, J.-S. Cho, H.-J. Choi, B.-H. Han, "Preparation and Dissolution Profiles of the Amorphous, Dihydrated Crystalline, and Anhydrous Crystalline Forms of Paclitaxel", *Drying Technology*, Vol. 25, 2007, pp. 1759-1767.

[12]   H. Hata, S. Saeki, T. Kimura, Y. Sugahara, K. Kuroda, "Adsorption of Taxol into Ordered Mesoporous Silicas with Various Pore Diameters," *Chemistry of Materials*, Vol. 11, 1999, pp. 1110-1119.

[13]   I.A. Kathawalla, J.L. Anderson, "Pore Size Effects on Diffusion of Polystyrene in Dilute Solution", *Industrial and Engineering Chemsitry Reserarch*, Vol. 27, 1988, pp.

866-871.

[14] N.A. Peppas, "Analysis of Fickian and Non-Fickian Drug Release from Polymers", *Pharmaceutica Acta Helvetica*, Vol. 60, 1985, pp. 110-111.

[15] P. Costa, J.M.S. Lobo, "Modeling and comparison of dissolution profiles", *European Journal of Pharmaceutical Sciences*, Vol. 13, 2001, pp. 123-133.

[16] A.C. Tanquary, R.E. Lacey, "Advances in Experimental Medicine and Biology: Controlled release of biologically active agents", *Plenum Press*, Vol. 47, 1974.

[17] R.S. Langer, N.A. Peppas, "Present and future applications of biomaterials in controlled drug delivery systems", *Biomaterials*, 1981, Vol. 2, 201-214.

[18] P.J. Sinko, A.N. Martin, "Martin's physical pharmacy and pharmaceutical Sciences", *Lippincott Williams & Wilkins*, 2005.

[19] D.F. Evans, H. Wennerström, "The Colloidal Domain: Where physics, chemistry, and biology meet", *Wiley-VCH*, 1999.

[20] T. Higuchi, "Mechanism of Sustained-Action Medication: Theoretical Analysis of Rate of Release of Solid Drugs Dispersed in Solid Matrices", *Journal of Pharmaceutical Sciences*, Vol. 52, 1963, pp. 1145-1149.

[21] S.-H. Lee, S.D. Yoo, K.-H. Lee, "Rapid and sensitive determination of paxlitaxel in mouse plasma by high performance liquid chromatography", *Journal of Chromatography B*, Vol. 724, 1999, pp. 357 – 363.

[22] M.S. Alexander, M.M. Kiser, T. Culley, J.R. Kern, J.W. Dolan, J.D. McChesney, J. Zygmunt, S.J. Bannister, "Measurement of paclitaxel in biological matrices: high-throughput liquid chromatographic-tandem mass spectrometric quantification of paclitaxel and metabolites in human and dog plasma", *Journal of Chromatography B*, Vol. 785, 2003, pp. 253-261.

[23] J. Lemaître, Design of Experiment, available at: http://ltp.epfl.ch/page14769.html, February 2009.

[24] A.F.M. Barton, "Handbook of solubility parameters and other cohesion parameters", *CRC Press Inc.*, 1991.

[25] D. Song, L.-F. Hsu, J.L.-S. Au, "Binding of taxol to plastic and glass containers and protein under *in vitro* conditions", *Journal of Pharmacological Science*, Vol. 85, 1996, pp. 29-32.

[26] D.A. Skoog, D.M. West, F.J. Holler, "Fundamentals of Analytical Chemistry", *Sounders College Publishing*, 1996.

[27] Personal communication U. Aschauer.

[28] S. Khoshkhoo, J. Anwar, "Crystallization of polymorphs: the effect of solvent", *Journal of Physics D: Applied Physics*, Vol. 26, 1993, pp. B90-B93.

[29] S.V.Ranade, K.M. Miller, R.E. Richard, A.K. Chan, M.J. Allen, M.N. Helmus, "Physical characterization of controlled release of paclitaxel from the TAXUS[TM] Express[2TM] drug-eluting stent", *Journal of Biomedical Materials Research Part A*, Vol. 71A, 2004, pp. 625-634.

[30] J.S. Reed, "Principles of Ceramics Processing", *John Wiley and Sons*, 1995.

[31] A. Han, G. Mondin, N.G. Hegelbach, N.F. de Rooij, U. Staufer, "Filling kinetics of liquids in nanochannels as narrow as 27 nm by capillary force", *Journal of Colloid and Interface Science*, Vol. 293, 2006, pp. 151-157.

[32] D.I. Dimitrov, A. Milchev, K. Binder, "Capillary Rise in Nanopores: Molecular Dynamics Evidence for the Lucas-Washburn Equation", *Physical Review Letters*, Vol. 99, 2007.

[33] D. Stoye, "Solvents", Ullmann's Encyclopedia of Industrial Chemistry", *John Wiley and Sons Inc.*, 2009.

[34] A. W. Adamson, A. P. Gast, "Physical chemistry of surfaces", *Wiley-Interscience*, 1997.

[35] "Surface Tension of Pure Liquids and Binary Liquid Mixtures", *Landolt-Börnstein - Group IV Physical Chemistry*, Vol. 16, *Springer*, 2006.

[36] F. Schüth, K.S. Sing, J. Weitkamp, "Handbook of Porous Solids", *Wiley-VCH*, 2002.

[37] A. A. Ayon, M. Cantu, K. Chava, C. M. Agrawal, M.D. Feldman, D. Johnson, D. Patel, D. Marton, "Drug loading of nanoporous TiO_2 films", *Biomedical Materials*, Vol. 1, 2006, pp. L11-L15.

[38] I.A. Kathawalla, J.L. Anderson, "Pore Size Effects on Diffusion of Polystyrene in Dilute Solution", *Industrial and Engineering Chemsitry Reserarch*, Vol. 27, 1988, pp. 866-871.

[39] R.M.A. Roque-Malherbe, "Adsorption and Diffusion in Nanoporous Materials", *CRC Press*, 2007, pp. 121-162.

[40] H. Grijseels, D.J.A. Crommelin, C.J. de Blaey, "Hydrodynamic approach to dissolution rate", *Pharmaceutisch Weekblad Scientific Edition*, Vol. 3, 1981, pp. 129-144.

[41] R. Rohanizadeh, M. Al-Sadeq, R.Z. LeGeros, "Preparation of different forms of

titanium oxide on titanium surface: Effects on apatite deposition", *Journal of Biomedical Materials Research Part A*, Vol. 71A, 2004, pp. 343-352.

[42] W. Wu, G.H. Nancollas, "Kinetics of Heterogeneous Nucleation of Calcium Phosphates on Anatase and Rutile Surfaces", *Journal of Colloid and Interface Science*, Vol. 199, 1998, pp. 206-211.

[43] S. Sousa, P. Moradas-Ferreira, M. Barbosa, "TiO$_2$ type influences fibronectin adsorption", *Journal of Materials Science: Materials in Medicine*, Vol. 16, 2005, pp. 1173-1178.

[44] T. Shozui, K. Tsuru, S. Hayakawa, Y. Shirosaki, A. Osaka, "XPS study on potential suppression factors suppressing *in vitro* apatite formation on anatase films prepared on various substrates", *Surface and Coatings Technology*, Vol. 203, 2009, pp. 2181 – 2185.

[45] A. Tourvieille de Labrouhe, " Nanostructured ceramic coatings for deformable medical implants such as stents", Thesis, Ecole Polytechnique Fédérale de Lausanne, 2009.

CHAPTER VI

6   PRELIMINARY *IN VITRO* CYTOTOXICITY TESTS

6.1   Background and Introduction

Evaluating a material's biocompatibility comprises complex testing. For a stent in particular, it has to be ensured that it resists the mechanical deformation accompanied by the stenting process and the dynamic movement of the coronary artery after implantation. The material-host responses need to be investigated prior to clinical trials. Those are for stents *in vitro* tests regarding cytocompatibility, hemocompatibility, as well as *in vivo* animal testing. Preliminary *in vitro* cytotoxicity tests of non-PTX-loaded, nanostructured TiO_2-coatings have been performed in the present study and the results are presented in the following.

Cytotoxicity in general means that a substance causes toxic effects at a cellular level, e.g. cell death, alterations in cell membrane permeability or enzymatic inhibition. A *toxic material* is defined as a material that releases a chemical in sufficient quantities to kill cells either directly or indirectly through inhibition of key metabolic pathways [1]. The titania coatings, which are not filled with PTX, should *not* exhibit cytotoxicity. They should be cytocompatible and should promote the fast adhesion and proliferation of endothelial cells (ECs). Long-term clinical outcomes of the implantation of stents have proven that the re-endothelialization plays an important role in preventing late and very late stent thrombosis. Late stent thrombosis occurs later than 30 d, very late stent thrombosis later than 1 year after stenting. ECs are involved in the regulation of thrombosis and in the regulation of the proliferation of adjacent smooth muscle cells (SMC) [2, 3, 4]. Hence *in vitro* cell tests were

performed, in which the material was brought into direct contact with primary bovine ECs. The proliferation of the ECs was evaluated. Experiments were performed on the basis of the regulations described in the ISO 0993-5 for "Biological evaluation of medical devices-Part 5: Tests for *in vitro* cytotoxicity" [5]. The use and interpretation of *in vitro* cell tests is often controversially discussed, because they do not deliver information about the situation in the more complex *in vivo* environment. At the implantation-site more than just one cell type is involved, the immune system is active and metabolites can be transported to specific organs and be metabolized. However, *in vitro* tests are the primary biocompatibility screening tests for a wide variety of materials. They minimize the use of animals in research, they are required by most regulatory agencies and are much less expensive than *in vivo* tests [1].

The documentation of the preliminary cytotoxicity tests will be shown in chronological sequence. This will help to better understand, why certain process parameters of the titania coatings on stainless steel supports had to be changed during ongoing cell testing to create a better cytocompatibility. Also information obtained from the Thesis of A. Tourvieille de Labrouhe [6], which was performed in parallel to the present work, were taken into account for certain parameter changes. For a better overview, the used specimens and their specifications are summarized in Table 6-1.

Table 6-1 Specimens applied in the cell tests. They differ in the support material and the sintering method.

		sintering method		
		conventional	HT1	HT2
support material	*wafer* "w"	w730NRL, w730*RL*	-	-
	flat stainless steel "ss"	ss730NRL ss730*RL*	ss820NRL(H1), ss820(H1)	ss730NRL(H2), ss730*RL*(H2)
	wire shapes stainless steel "ssWire"	-	ssWire820NRL (HT1), ssWire820	-

"conventional": sintering as described in Chapter 4.2.5; "HT1": sintering up to 450 °C in air, in the second cycle up to 820 °C in hydrogen/argon/oxygen; "H2": two sintering cycles with the first one from room temperature up to 450 °C in air, the second one from room temperature to the maximum temperature 730 °C encapsulated under 300 mbar argon

6.2   Materials and Methods

6.2.1   *Substrates applied in the cell testing*

The preliminary *in vitro* cytotoxicity tests were performed using titania coatings on either wafer or on 316L stainless steel (SS) supports. None of the samples were loaded with Paclitaxel (PTX). The cell tests were performed to *just* evaluate the cell responses to the

titania coatings in the non-reservoir layer (NRL) and the reservoir layer (*RL*) modifications.

6.2.1.1 *TiO$_2$-coatings on silicon supports*

NRL- and *RL*-titania coatings on plate-shaped wafer supports, which were heat treated with the conventional method described in Chapter 4.2.5 and with the maximum sintering temperature of 730 °C (w730NRL and w730*RL*), were employed in the test CTSi1, Table 6-2. The negative references, defined as a material not creating any cytotoxic response under the *in vitro* conditions [5], consisted of microscope glass cover slips (Menzel Gläser, Gerhard Menzel, Glasbearbeitungswerk GmbH & Co. KG) [7]. To fit the samples into the 24 well culture dishes, they were cut with a diamond knife to exhibit an area of ~ 1 cm^2. It was necessary to know the exact areas of these specimens to refer the determined cell number to them. The areas were hence measured like was described previously in Chapter 5.4.3: photos of the cut workpieces were taken by a light microscope (MZ8, Leica) equipped with a JVC TK C1380 CCD camera. The geometric surface area was subsequently determined employing the imaging software ImageJ (V 1.38x). The cell test of the titania coatings on wafers served to establish the methods for further cell testing.

Table 6-2 Summary of *in vitro* cytotoxicity tests of the titania coatings on either wafer or steel supporting materials.

cell test	*samples*	*heat treatment*	*shape*
CTSi1	w730NRL, w730*RL*, cover slip (negative control)	conventional, cf. Chapter 4.2.5	flat
		-	
CTssWire	ssWire820NRL(HT1), ssWire, ssWirePS, ssWireSIBS	HT1 (partially in Ar/H$_2$ atmosphere)	wire
		-	
CTssFlat1	ss730NRL, ss730*RL*	conventional, cf. Chapter 4.2.5	flat
CTssFlat2	ss730NRL(HT2), ss730*RL*(HT2), ssFlat, cover slip (negative control)	HT2 (partially encapsulated)	flat
		-	

6.2.1.2 *TiO$_2$-coatings on stainless steel wires*

In the cell test CTssWire, stainless steel wires (Heraeus Material S.A.) with a diameter similar to the one of stent's struts of 300 µm and pre-treated with a special annealing by the company Meko GmbH, Germany, were applied. They were electropolished and cleaned according to the methods specified in Chapter 4.2.2 and in the thesis of A. Tourvieille de Labrouhe [6] prior to dip coating with TiO$_2$.

The titania coated wires in a NRL-modification and heat treated with a special sintering method with a maximum sintering temperature of 820 °C were termed

ssWire820NRL(HT1). They were prepared by dipping each wire into a TiO_2-nanoparticle suspension and withdrawing it two times at 90 mm/min and one time at 250 mm/min to achieve a decisive coating thickness, cf. methods described in Chapter 4.2.3. They were subsequently heat treated with a method different to the conventional one applied before, to reduce the amount of precipitated iron oxide on the steel's surface. Specimens were heated with a rate of 4.5 °C/min in a tubular furnace up to 450 °C and isothermally held for 60 min. The atmosphere was then changed from air to a combination of argon, hydrogen and air* to limit the oxidation of the steel's surface, whereas the flow was kept constant at 0.342 l/min. A second heating step was conducted applying a rate of 4.5 °C/min to a maximum sintering temperature, T_{max}, of 820 °C. The dwell time was 80 min before it was cooled to room atmosphere with 4.5 °C/min. Names of the samples heat treated with this method contain the abbreviation "HT1".

Besides the titania coated wires, native, not heat treated stainless steel wires were employed in the cell test, ssWire in Table 6-2. Two types of polymers were coated onto the native SS wires in order to test their application as negative controls in the cell tests on wires. They were termed ssWirePS and ssWireSIBS. The SS wires coated with polystyrene (PS), ssWirePS, were fabricated as follows. A solution of 26.73 %wt polystyrene (PS-storing tube, Semadeni) was prepared by dissolving PS in toluene (ACS reagent, purity 99.5 %, Sigma-Aldrich) in a glass bottle (Schott) and stirring it at 300 rpm (RCT classic, IKA®) at 80 °C for 12 h. SS wires were after cleaning dipped into the PS/toluene solution and withdrawn with 250 mm/min (Precision dip coating system PL 3201, Speedline Technologies). After drying for 10 min at 37 °C in a climatic test cabinet (RUMED®), the dip coating was repeated twice. The samples were subsequently dried for 19 h at 60 °C to completely evaporate the solvent. The ssWireSIBS specimens were prepared accordingly, except that a solution of 10 %wt styrene-isobutylene-styrene (SIBS, Albemarle Europe SPRL Belgium) in toluene was used. SIBS is a non-degradable, thermoplastic elastomer, which is used in the drug-eluting Taxus™ stent by Boston Scientific Corp.

6.2.1.3 TiO_2-coatings on flat stainless steel supports

Because the homogeneous cultivation of the cells on the wire substrates has been proven to be difficult, cf. Chapter 6.3.4, titania coatings on flat SS supports were investigated in the tests CTssFlat1 and CTssFlat2.

---

* The exact composition of the atmosphere was not determined, because the oven's tube exhibited a leakage.

CTssFlat1

The titania coatings in the NRL- and *RL*-modifications were produced as was described in detail in Chapter 4.2.3. The conventional heat treatment was applied with a T_{max} of 730 °C and the samples were termed ss730NRL and ss730*RL*. Specimens were not cut prior to the incubation with endothelial cells and held a rectangular shaped surface with the size of 1 x 5 cm.

CTssFlat2

The TiO$_2$-coated specimens applied in the assay CTssFlat2 were dip coated as was described earlier for the NRLs and the *RL*s in Chapter 4.2.3. The heat treatment was performed with a new method, called HT2, to limit the build up of iron oxide on the steel's surface and to obtain a good mechanical stability of the films (cf. Thesis A. Tourvieille [6]). The sintering was accomplished by applying two heating cycles. During the first cycle, specimens were mounted on an aluminum support in the tubular furnace and heated to 450 °C with 4.5 °C/min. The time of the isothermal hold at this temperature was 60 min before cooling with 4.5 °C/min to room temperature. The flow of air was 0.342 l/min. The samples were afterwards encapsulated into a quartz glass tube (VQT SA, Switzerland) with an atmosphere of 300 mbar argon and no residual air (more details in Thesis A. Tourvieille [6]). A second sintering cycle was carried out by increasing the temperature with 4.5 °C/min up to 730 °C, keeping this T_{max} constant for 80 min, before cooling to room atmosphere with the same rate. All samples with a rectangular surface of 1 x 5 cm were then cut into quadratic pieces with a surface area of 1 cm^2 by electro erosion. The specimens were cleaned by rinsing them in acetone for 5 min and additionally in UP-water for 20 min. Native SS substrates, ssFlat, were also applied in the test. They were subjected to the same cutting and cleaning process like the titania coated samples. The negative references in this test were glass cover slips.

6.2.2   Cells and cell viability testing

6.2.2.1   Primary endothelial cells and incubation

Primary bovine endothelial cells (ECs), which were isolated from a bovine aorta, were chosen in this test. Primary cells usually exhibit a higher specific sensitivity than some established cell lines [5, 8]. Prior to use, cells were de-frozen, the number of living and dead cells determined and the concentration of the cells in suspension adapted to 50000 cells/ml. The cell medium was Dulbecco's Modified Eagle Medium (DMEM, Invitrogen), supplemented with 10 % Fetal Bovine Serum (FBS, Invitrogen) and Penicillin, Streptomycin, Amphotericin (PSA, Invitrogen). All materials, which were to be tested, were

heat sterilized for 30 min at 121 °C prior to incubation (Dampfsterilisator HST 23/20, Zirbus GmbH).

Samples with a cubic surface area of 1 cm^2 of the tests CTSi1, CTssFlat2, as well as of CTssWire were each transferred into one well of the 24-wells tissue culture plastic plates (Zellkulturtest Platte 24, TPP). Cells were seeded at a concentration of 50000 cells per sample. After incubation at 37 °C, 5 % CO_2 (Nuaire DHD Autoflow, CO_2 Air-Jacked Incubator, Nuaire TM) in DMEM medium (DMEM, 10% FBS and PSA, Invitrogen) for 8 d, the analysis of the cytotoxicity was accomplished. This incubation period was chosen to ensure an adequate time for the formation of a cell monolayer, and in the view of future cell tests, in which paclitaxel (PTX) gets released from the titania films. The culture medium was completely replaced every 2 d of incubation. Samples of the test CTssFlat1 were incubated in a tissue culture dish (60 x 15 mm, Falcon), after 4 ml of the cell suspension were added. The test was stopped after only 2 d.

6.2.2.2 Determination of the cell number

By determining the number of living and dead cells present on the material, its toxicity can be estimated. Each substrate was after incubation for 8 d transferred into one well of the new 24 well plate and washed twice with fresh medium. 200 µl trypsin solution (Trypsin in ethylenediaminetetraacetic acid (EDTA) 0.05%, Invitrogen) was added and then stored in the incubator at 37 °C for 5 min. After trypsination and the incorporation of 400 µl medium to each sample, the cells were detached from the substrates and homogenated in the solution with a pipette. The solution composed of cells, media and trypsin was diluted with a trypane blue solution (Fluka) for 10 min. The dilution was adjusted to count 20 to 50 cells per quadrant in the hemocytometer (Neubauer Improved, 0.0025 mm^2, Brand). Non-living cells were stained dark blue, because the color dye could migrate into the damaged cells. The living cells appeared transparent, because they excluded trypane blue [9].

6.2.2.3 Photometric determination of the cell viability

The MTT-assay is a colorimetric method to measure the proliferation and viability of cells. In *living cells*, uptaken tetrazolium-salts like 3-(4,5-Dimethylthiazol-2-yl)-2,5-diphenyltetrazoliumbromid (MTT), which is a yellow, water-soluble salt, will be converted by the mitochondrial dehydrogenases to formazan, a dark blue, water insoluble substance, by reductive cleavage of the tetrazolium ring. This transformation will not take place in dead cells. The concentration of the formazan can be detected by a UV/VIS spectrophotometer in a cell suspension and correlates to the number of living cells and their cellular activity [9, 10].

A stock solution of MTT (Thiazolyl Blue Tetrazolium Bromide, TLC 98%, Sigma) in Phosphate Buffered Saline (Dulbecco's PBS 1x, Gibco, Invitrogen) was prepared at a concentration of 5 mg/ml. The substrates under investigation were transferred into fresh 24 well plates and washed two times with medium. 1 ml medium was added to each substrate and 160 µl of the MTT stock solution was incorporated. The well plates were stored in the incubator for 2 h. Afterwards the medium was removed and the samples were washed twice with fresh medium. 1 ml of a 39 mM isopropanol/hydrochloric acid solution was added to each substrate to destroy the cells, which were attached to them, and to release formazan. After incubating again for 15 min, 500 µl of the solution containing isopropanol, hydrochloric acid and formazan was each transferred into one well of a 48 well plastic culture plate and the absorbance measured at 540 nm with a microplate reader (Infinite M200, TECAN).

6.2.2.4   *Detection of the cell membrane permeability*

Glucose-6-phosphate (G-6-P) is produced in the cytoplasm of the cells. If the cell membrane is damaged, the G-6-P is released into the culture medium. In the resazurin essay the released G-6-P will be enzymatically transferred: the resazurin, which is blue and non-fluorescent, is reduced with diaphorase to resorufin. Resorufin is pink and highly fluorescent and can be detected in fluorescence and photometric measurements. The greater the permeability of the cell membrane, and hence its damage, the higher is the amount of fluorescent resorufin in the media [11, 12, 13].

A stock solution of resazurin (Resazurin Sodium Salt, Sigma) in ultra pure water was prepared with a concentration of 1 mg/ml. After stirring for 5 min, the solution was filtered with a 0.45 µm cellulose acetate filter (Semadeni) to remove possible big agglomerates. After incubation, substrates with the attached cells were transferred into fresh 24 well plates and twice washed with fresh medium. 1 ml medium was then added to each, before 10 µl of the resazurin stock solution were incorporated. After 4 h of incubation at 37 °C, 500 µl of the solution, containing media, resazurin and resorufin, were each transferred into a well of a new 48 well plate. The concentration of resorufin was measured by fluorescence spectroscopy with a microplate reader. An excitation wavelength of 560 nm was applied and the emission of resorufin measured at 590 nm.

6.2.2.5   *Cell morphology by microscopy*

It is important to use visual methods to analyze the morphology, adhesion and growth of the cells on the substrates [5, 9]. In the present study, optical and electron microscopy

were the methods of choice. The electron microscopy combined with focused ion beam milling gave further insight into the adhesion of the cells onto the substrate by observing cross sections.

Optical microscopy

A staining of the adherent cells on the substrates was done before optical microscopy using Giemsa staining. After the substrates with attached cells were transferred from the incubation well plates into wells of a new culture dish, they were each rinsed two times with phosphate buffered saline (DPBS 1x, Gibco). A solution of 1 ml PBS in methanol of a concentration of 50/50 %vol was added. After 2 min the solution was taken out and 2 ml of pure methanol were given to each substrate and removed after 2 min. Furthermore 2 ml of anhydrous methanol was pipetted to each substrate and taken out after 10 min, to finish the dehydration of the cells. 1 ml of the Giemsa solution (Giemsa Stain, Modified Solution, Riedel-de-Haën) was added to each substrate, waited for 2 min and then it was removed. 1 ml of a 5 x diluted Giemsa solution in water was each added. After 2 min the color dye solution was taken out and the substrates washed twice with ultra pure water. They were then fixed on a microscope slide and observed by light microscope (Olympus B071 with an Altra Soft Imaging System 20 camera and the software Analysis get it).

Scanning electron microscopy

Sample preparation for scanning electron microscopy (SEM) was performed in collaboration with the Center for Electron Microscopy, EPF Lausanne (CIME) and the Center of Electron Microscopy, Faculty of Biology and Medicine of the Université de Lausanne/Centre Hospitalier Universitaire Vaudois, Lausanne (CME, CHUV).

Substrates with attached ECs were transferred from the incubation culture dishes into fresh 24 well plates and rinsed twice with 1 ml PBS-solution. 1 ml fixation solution, composed of 2.5 % glutaraldehyde and 2 % paraformaldehyde in 0.1 M PBS, was given to each sample and left for 30 min. Specimens were thereafter dehydrated by putting them sequentially for each 5 min in solutions of ethanol and water in different concentrations: 50/50; 70/30; 90/10; 100 %vol. Samples were then dried with a critical point drying method (critical point dryer CPD 030, Baltec) at the CME, CHUV. The ethanol was thereby replaced by liquid CO_2, which was then evaporated from the cells without damaging their morphology. Specimens were fixed on a holder for electron microscopy and sputter coated (MED 010, Baltec) with platinum to yield a coating thickness of 10 nm. The cells on the substrates were then observed with an XLS 30 scanning electron microscope (Philips).

Scanning electron microscopy combined with focused ion beam (FIB)

The preparation of the samples for SEM-analysis, combined with focused ion beam (FIB) technique, was performed in collaboration with G. Knott, CIME, EPF Lausanne. The titania coated wires ssWire820NRL(HT1), to which cultured ECs adhered, were fixed with a solution of 2.5 % glutaraldehyde and 2 % paraformaldehyde in 0.1 M PBS for 4 hours. After fixation, the wires were washed thoroughly with cacodylate buffer (0.1 M), postfixed for 40 min in 1.5% potassium ferrocyanide and 1% osmium tetroxide, then 1 hour in 1% osmium tetroxide alone, and finally stained further with 1% uranyl acetate for 40 minutes. They were dehydrated through increasing concentrations of ethanol and finally embedded in Durcupan ACM resin (Fluka, Switzerland). The resin was hardened for 24 hours at 65 °C. Resin blocks, with the samples uppermost, were trimmed to a size of approximately 5 x 5 mm using a diamond wire saw. The upper surface of the block was then further trimmed with an ultramicrotome (Leica UCT) and a glass knife until the wire with the attached cells was not more than 20 μm distant from the surface. Specimens were then glued to SEM-stubs using carbon paint. The whole surfaces of the blocks were coated with a gold layer of 30 nm to avoid charging effects under the electron beam.

Manipulation of the electron microscopes and image processing were performed by M. Cantoni, CIME, EPFL. A NVision 40 CrossBeam (Zeiss) was used for the milling and imaging of the titania coated wires embedded in the resin blocks. In the FIB, a masking layer of about 1 μm platinum was deposited locally with the ion beam on the area to be milled, in order to prevent a roughing on the milling front. Cross sections of the wires with cells were prepared every 20 nm using the FIB, generated by a gallium liquid metal ion source, at 30 kV and a beam current of 700 nA. After each milling process, backscattered electron scanning images were recorded at accelerating voltages of 2 kV. The whole set of ~ 600 2D images were compiled to a 3D stack and processed using the software ImageJ.

6.2.2.6 Statistics

All data from the cell tests were statistically analyzed using analysis of variance, ANOVA, from the Statistical Design of Experiment provided by J. Lemaître, EPFL [14]. The number of replicas for each testing was 4, except for microscopy.

6.2.3 Preliminary elution test for the corrosion tendency of the steel supports

As will be seen in the results' section of this chapter, iron oxide was built on the SS supports after particular heat-treatments. A preliminary test was thus performed to determine, if iron oxide was only precipitated on the steel's surface, or if it was also build at

the interior of the steel samples. Therefore the following specimens were tested: native, non-heat treated SS (native ss), SS heat treated with the method HT1 and then grinded to remove the oxide layer (ss820(HT1)_poli), heat treated SS and not grinded (ss820(HT1)_nonpoli) and a titania coated SS and heat treated with the method HT1 (ss820NRL(HT1)), Figure 6-1 (a). They were each placed into a tissue culture dish of a size of 60 x 15 mm (Falcon) and 4 ml deionized water with a conductance below 0.1 µS/cm was added to totally cover them. The culture dishes were closed to avoid water evaporation and left at room atmosphere. After 96 h, photos were taken (Cyber-shot, Sony) and the distribution of iron oxide around the samples evaluated visually. The same methods were applied to SS wires, which are depicted in Figure 6-1 (b). The sample ssWire820(HT1)_poli was electropolished and not grinded like the flat analogue.
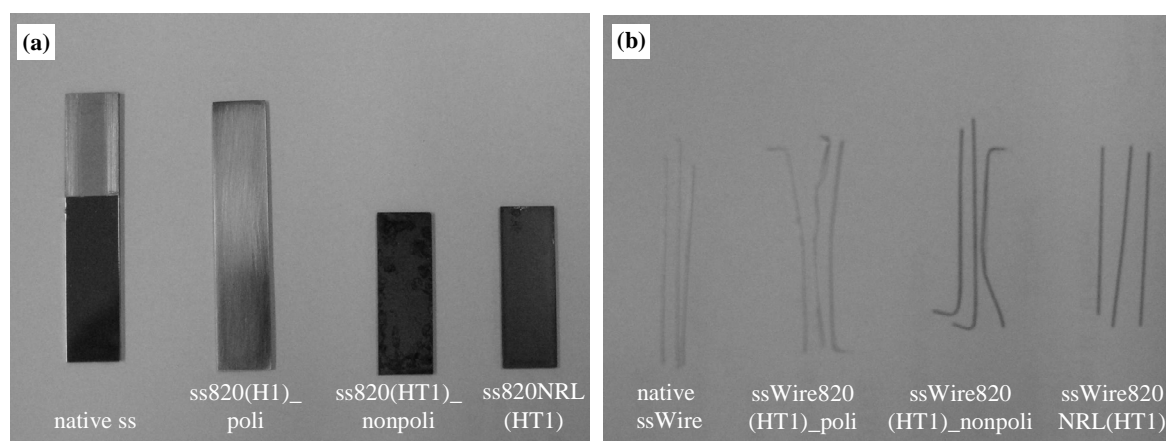

Figure 6-1 Samples used in the preliminary corrosion tests of the stainless steel supports: (a) rectangular and (b) wire steel samples.

6.2.4   *Methods for the surface characterization*

6.2.4.1   *X-ray photoelectron spectroscopy*

To determine the elemental composition of the substrate's surfaces after heat treatment, X-ray photoelectron spectroscopy (XPS)-measurements were carried out. The detailed analysis method is described in Chapter 4.4.1. Only the samples ss820NRL(HT1) and ssWire820NRL(HT1) were analyzed. The samples, which were heat treated with the method HT2, were further characterized by A. Tourvieille de Labrouhe [6].

6.2.4.2   *Contact angle measurements*

The contact angles of the negative reference cover slip and the titania coated SS-supports ss820NRL(HT2), ss820*RL*(HT2), were measured by the sessile drop method. This

method was described in detail in Chapter 4.4.2.

6.2.4.3   Roughness determinations

The roughnesses of the negative reference cover slip and the titania coated SS supports ss820NRL(HT2) and ss820*RL*(HT2) were measured using the mechanical profilometer Alpha Step 200 (TENCOR INSTRUMENTS). The procedure was explained in detail in Chapter 4.4.3.

6.3   Results

6.3.1   Cytocompatibility of the TiO$_2$-coatings on silicon supports

A smaller living cell density (LCD) was detected on the titania coated wafers with a NRL- and *RL*-modification as compared to the glass cover slip negative references, Figure 6-2 (a). The lowest LCD of 2000 living cells per 1 mm^2 substrate area was recorded for the *RL* w730*RL*. No significant differences of the cell's viability on the different substrates were obtained, when considering the mitochondrial activity depicted in Figure 6-2 (b) and the cell membrane permeability displayed in Figure 6-2 (c). ECs were present as a monolayer on the *RL*s. Parts of the negative reference and the NRLs were covered by a monolayer, others by a multilayer of ECs, Figure 6-3. The cells on the *RL*s were slightly bigger than on the negative references and the NRLs.
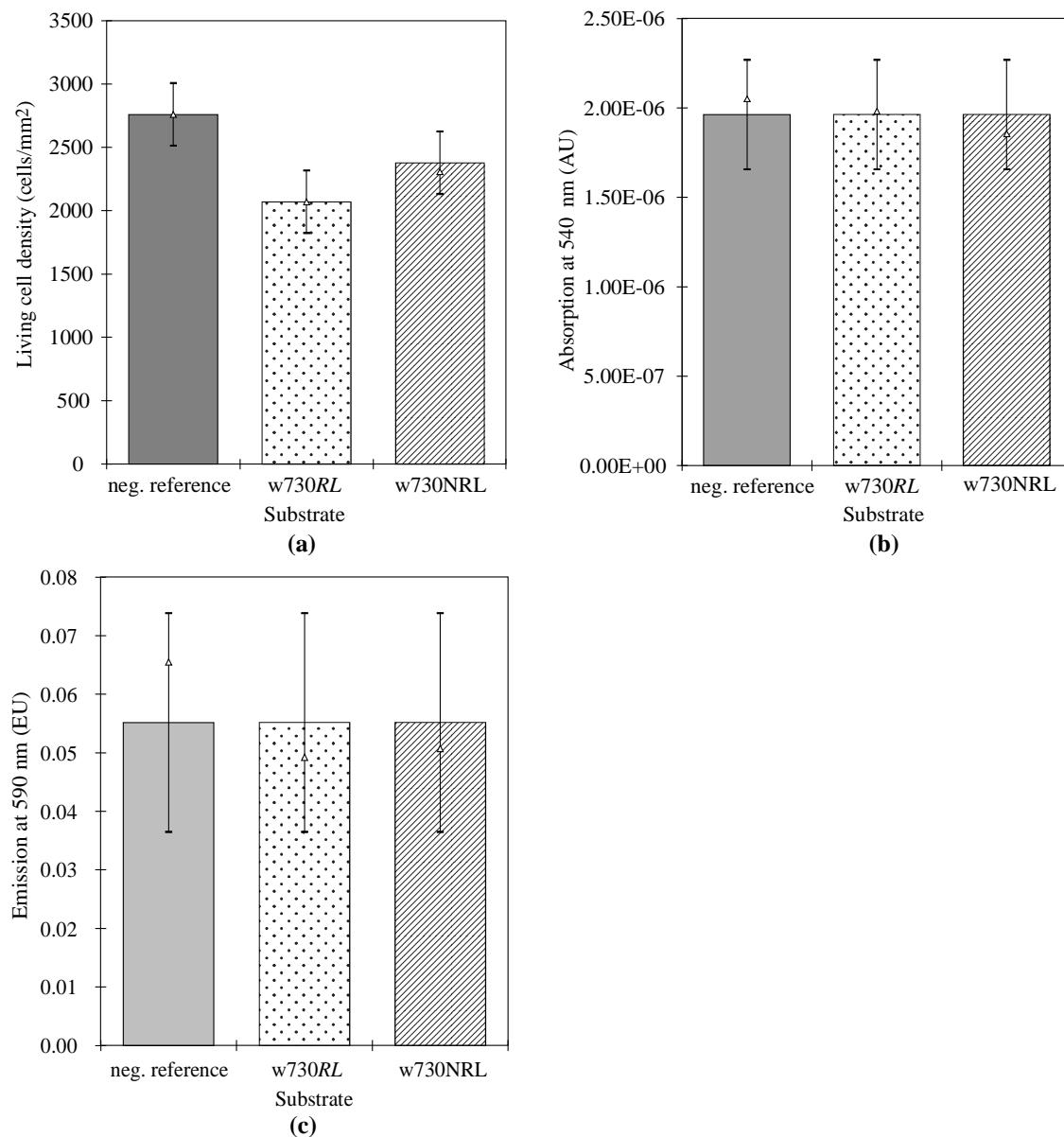
Figure 6-2 (a) The living cell density, (b) the mitochondrial activity and (c) membrane permeability of the primary bovine endothelial cells after 8 d of incubation on the titania coated wafer supports of test CTSi1. Displayed are the adjusted mean values (columns), the non-adjusted mean values (Δ), the standard deviations (-) after ANOVA analysis with $p < 0.05$.
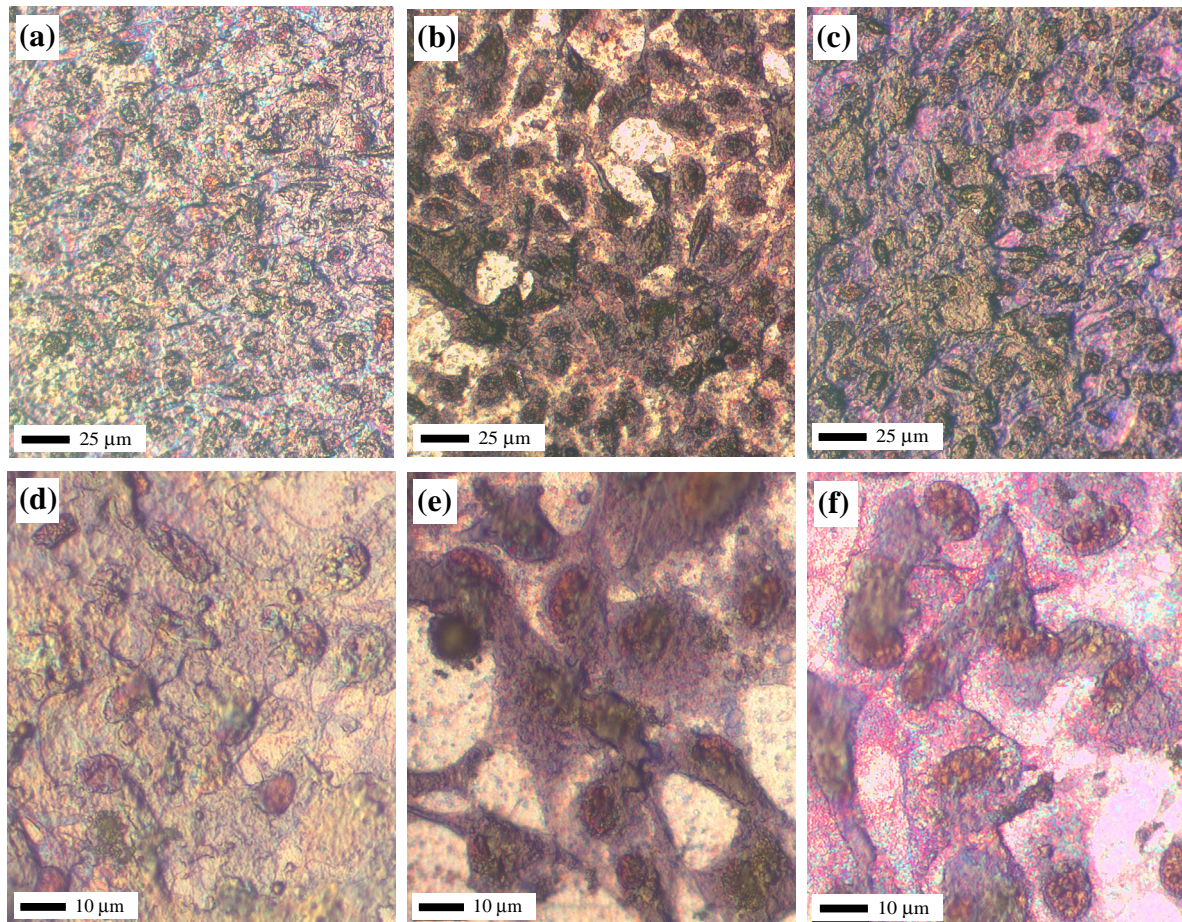
Figure 6-3 Optical micrographs of (a), (d) negative reference, (b), (e) titania reservoir layer on wafer support and (c), (f) titania non-reservoir layer on wafer support, all belonging to the cell test CTSi1. Samples were incubated for 8 d with primary bovine endothelial cells and stained by Giemsa staining method.

6.3.2 Cytocompatibility of the TiO₂-coatings on flat stainless steel after conventional sintering

The SS supports with a rectangular surface and coated with a titania NRL or *RL* exhibited after 2 d of cultivation with the ECs a pink culture medium, which is indicative for an alkaline environment. In addition, brown precipitates near the samples were detected, Figure 6-4. They represent iron oxides, which got dissolved from the steel's surface. After subjecting the samples to Giemsa staining, only a few ECs and cell debris were found on the titania surfaces, Figure 6-5. These results were the reason, why different heat treatments of the SS specimens had to be applied instead of the conventional sintering. The new methods were employed to limit the formation of iron oxides and hence cell death.
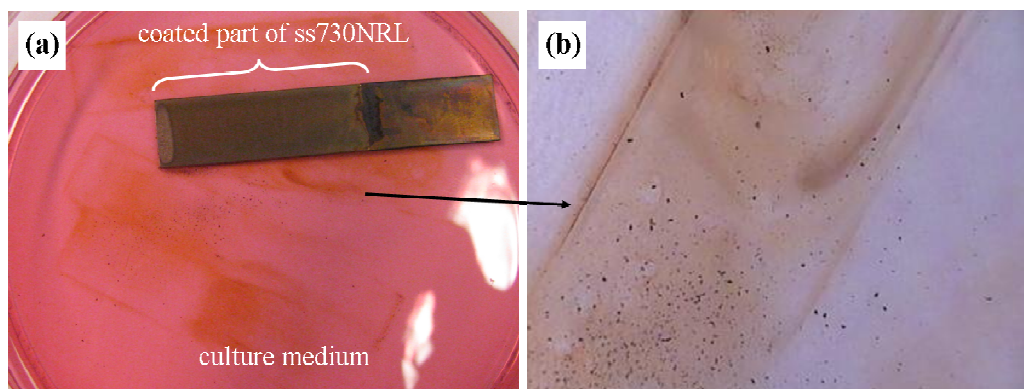
Figure 6-4 Iron oxide liberation from a titania non-reservoir layer on a flat SS support, sintered with the conventional heat treatment. After 2 d of cultivation with endothelial cells. The arrow indicates iron oxides.
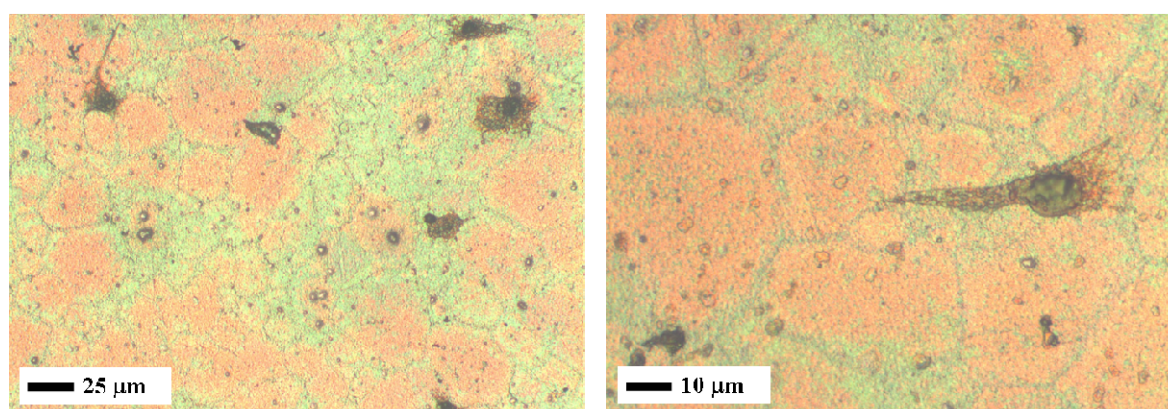

Figure 6-5 Optical micrographs of a titania non-reservoir layer on a flat SS support, sintered with the conventional heat treatment. After incubation for 2 d with the endothelial cells. Only a few endothelial cells (dark spots) were detected.

6.3.3   *Corrosion tendency of the specimens*

6.3.3.1   *Elution test*

Non-coated SS samples, which were subjected to the heat treatment HT1 involving a partial sintering in argon/hydrogen/air atmosphere, showed a black color. Grinding of the sample to remove the black surface revealed the silver color of the SS, Figure 6-1. After immersion of the specimens for 96 h into water, the native SS and the grinded heat treated one, ss820(HT1)_poli, did not show the release of iron oxide, Figure 6-6. The non-grinded ss820_nonpoli and the titania coated ss820NRL(HT1) exhibited a brown coloration around them, which is representative for iron oxide.

The findings of the wire samples were similar: the native SS, the grinded heat treated as well as the titania coated specimens did not show the release of iron oxide, Figure 6-7. Only ssWire820(HT1)_nonpoli exhibited the dissolution of iron oxides. From these two tests

it could be concluded that iron oxides were build on the steel's surface during heat treatment. They were not formed in the bulk of the steel. Iron oxides precipitated because a residual amount of oxygen was present in the oven's atmosphere. In future studies the heat treatment HT2, in which the specimens were encapsulated during the heat treatment at elevated temperatures, was applied. They did not exhibit the elution of iron oxides when they were immersed into water, as can be extracted from the Thesis of A. Tourvieille de Labrouhe [6]. For subsidiary information of the elemental composition of the specimens sintered with the sintering method HT1, X-ray photoelectron spectroscopy (XPS) measurements were realized.
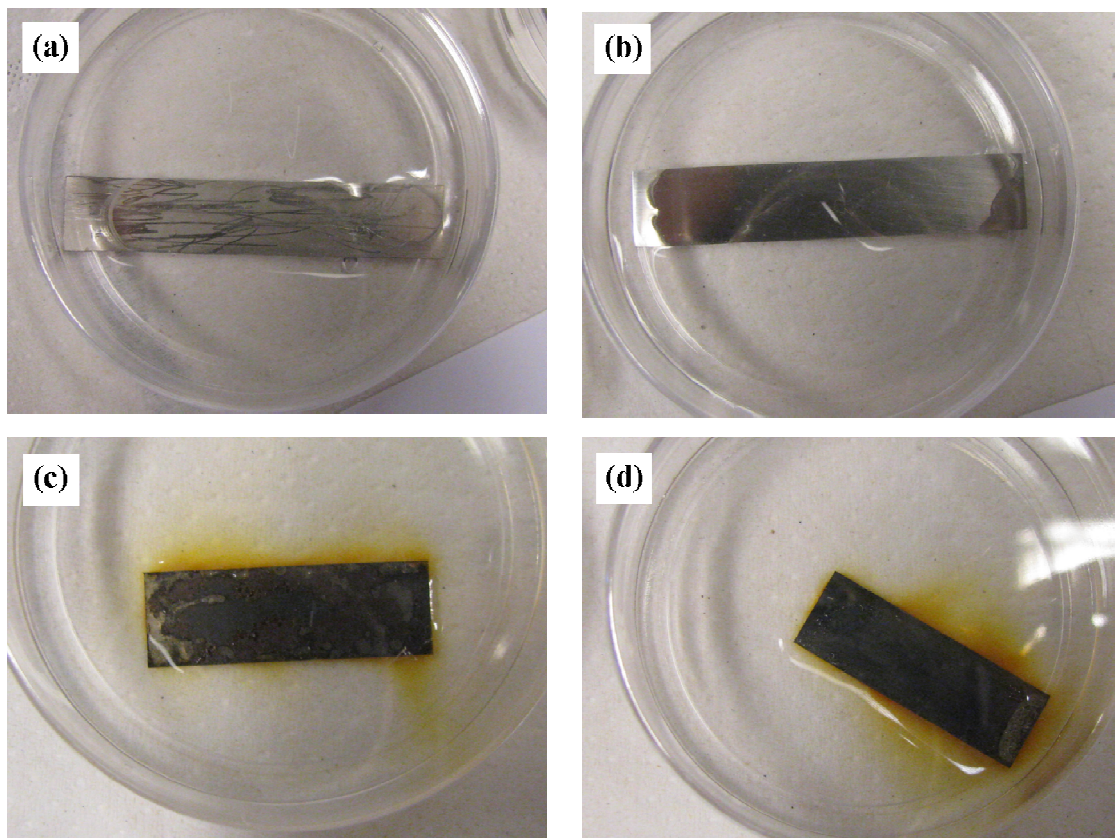
Figure 6-6 Samples from the preliminary corrosion test show for (a) native ss and (b) ss820(HT1)_poli no iron oxides, whereas for the samples (c) ss820(HT1)_nonpoli and (d) ss820NRL(HT1) iron oxides in the medium surrounding the specimens was detected.
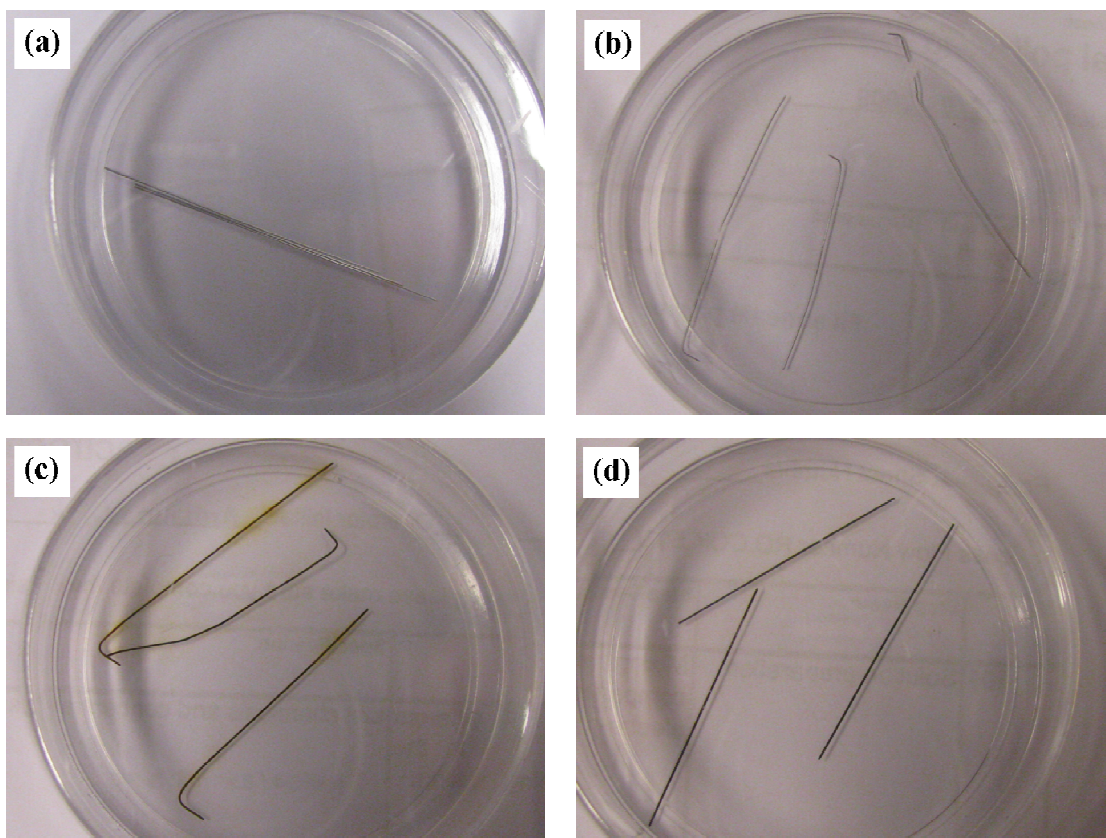
Figure 6-7 Samples from the preliminary corrosion test show for (a) native ssWire, (b) ssWire820(HT1)_poli and (d) ssWire820NRL(HT1) no iron oxides. For (c) ssWire820(HT1)_nonpoli iron oxides in the medium surrounding the specimens were visible.

6.3.3.2 Elemental composition

The elements present in the titania coatings on SS supports and heat-treated with the method HT1 (ss820NRL(HT1)) were nickel oxide, iron oxide, chromium oxide and TiO_2, Figure 6-8. If these oxides might also have existed as complex oxides combining Fe, Cr, Ni and O was not clear from the XPS data. A carbon peak was recorded in all spectra referred to being contamination. The findings for the titania NRL on SS wire (ssWire820NRL(HT1)) were similar, except that no Ni was found, Figure 6-9.
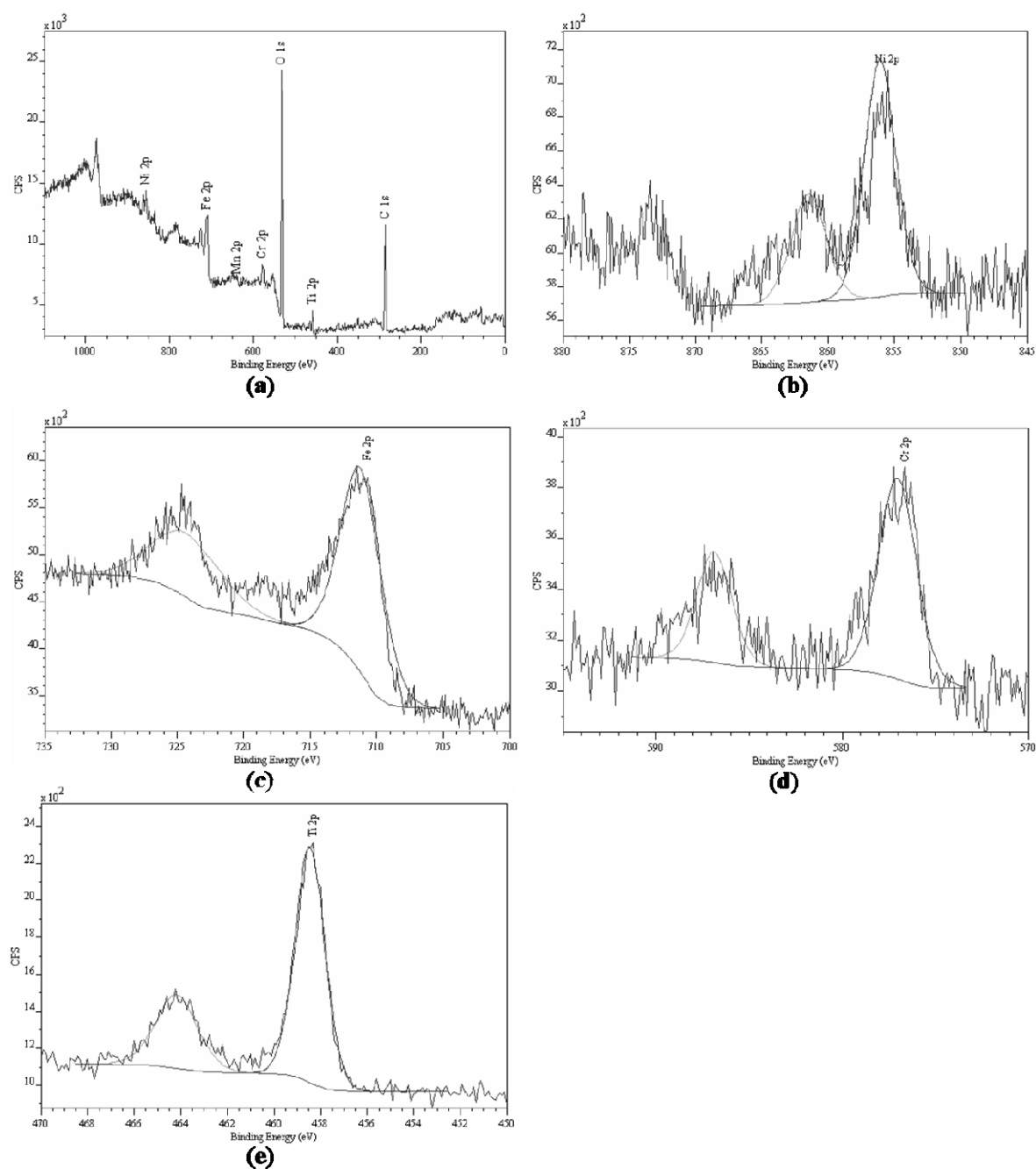
Figure 6-8 (a) XPS-spectrum of a titania coated stainless steel plate, which was sintered with the method HT1 (ss820NRL(HT1)).(b)-(e) represent the peak-deconvolutions of Ni, Fe, Cr and Ti.
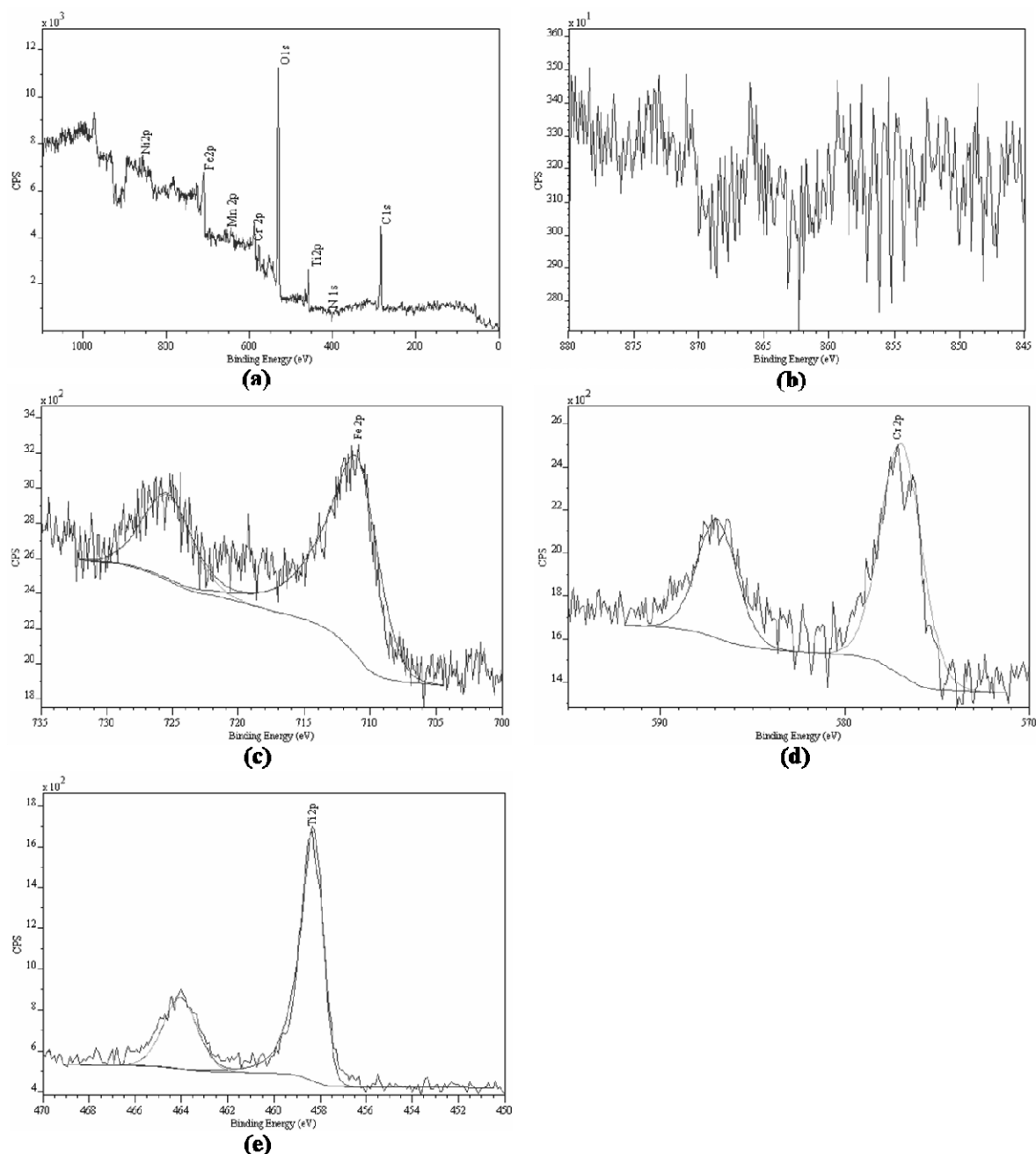
Figure 6-9 (a) XPS-spectrum of a titania coated stainless steel wire, which was sintered with the method HT1 (ss820NRL(HT1)).(b)-(e) represent the peak-deconvolutions of Ni, Fe, Cr and Ti.

6.3.4   *Cytocompatibility of the TiO$_2$-coatings on stainless steel wires after modified sintering*

Titania NRLs on SS wires and heat treated with the new method HT1 were subjected to an *in vitro* cell test. The ECs attached well on parts of the titania coated wires, as is depicted in Figure 6-10 and Figure 6-11. However, it was difficult to achieve a homogeneous cultivation of the ECs on the wires and hence a quantitative evaluation of the

cytocompatibility.

In a first test, only 1 wire of each kind with a length of 1 cm was inserted into one of the 24 wells of the culture dish for cultivation. Cells attached on the NRLs, Figure 6-10 and Figure 6-11. The number of cells on the wires was too small to be counted with the hemocytometer-method. Even an up-concentration of the cells in the suspension, which was obtained after trypsination of the cells from the wire and centrifugation, did not reveal the cell number. Theoretically, if the whole wire would have been covered by cells with a diameter of 30 µm, a density of 1415 cells/mm^2 should have been deduced. Hence it should have been possible to determine the living and dead cell numbers of this sample. By looking at the photos made by SEM in Figure 6-10, it gets obvious why the number of cells was lower than the theoretically expected one and hence non-detectable. The cells were only attached at the side of the wire, which was facing the top of the culture well during incubation. On the opposite side, which was facing the bottom of the plastic culture plate, almost no cells were present.
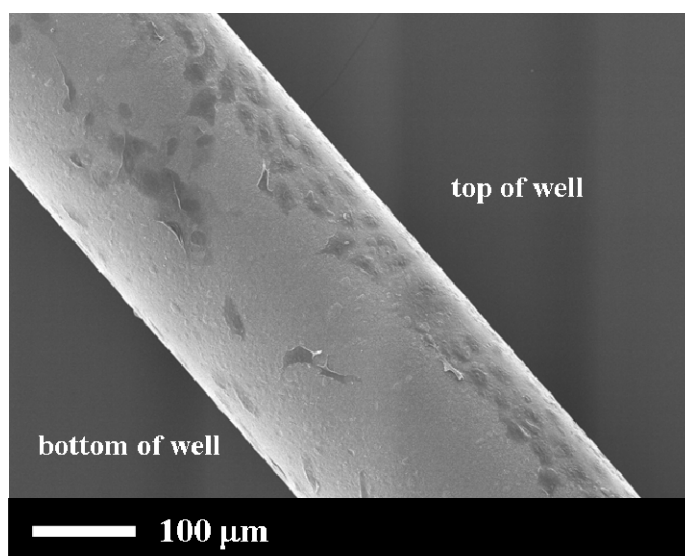
Figure 6-10 SEM-micrograph of ssWire820NRL(HT1) showing the inhomogeneous attachment of the endothelial cells on a wire.

This problem was addressed in following smaller tests, in which the wires in the culture well were rotated every 24 h. But cells were still only present on one side of the wire. The viability of the cells attached to the wire could not be evaluated by spectroscopic methods. The amount of metabolized MTT and resazurin was still below the detection limit. Small tests applying 10 wires placed in parallel into one well of the 24 well culture plate to increase the number of adherent cells and hence to increase the spectroscopic signals, failed. Only the cell morphology could be evaluated on the different types of specimens, Figure 6-11 and Figure 6-12. On the surface of the PS-coated native SS wires (ssWirePS) no

cells attached and only cell debris were observed. Thus the PS-coated wires could not be employed as negative controls in the present study. The surface of the wire, which was coated with the SIBS-polymer, was well covered with ECs. They were well spread on the surface. The cell density on the native SS support (ssWire) observed by optical microscopy was smaller than for the SIBS-wire and the titania coated wire (ssWire820NRL(HT1)). The shape of the ECs cultivated on the titania coated wire exhibited a more round shape than the ones on the native SS wire, Figure 6-11 (c, g, d, h). SEM further elucidated the shape of the cells on the titania coated wires ssWire820NRL(HT1) at higher magnification, Figure 6-12. One could see filopodia of the cells interacting with the surface, which is a good sign for the cell attraction by the substrate. The preparation of the samples on the polymer coated, as well as on the native steel wires, failed.
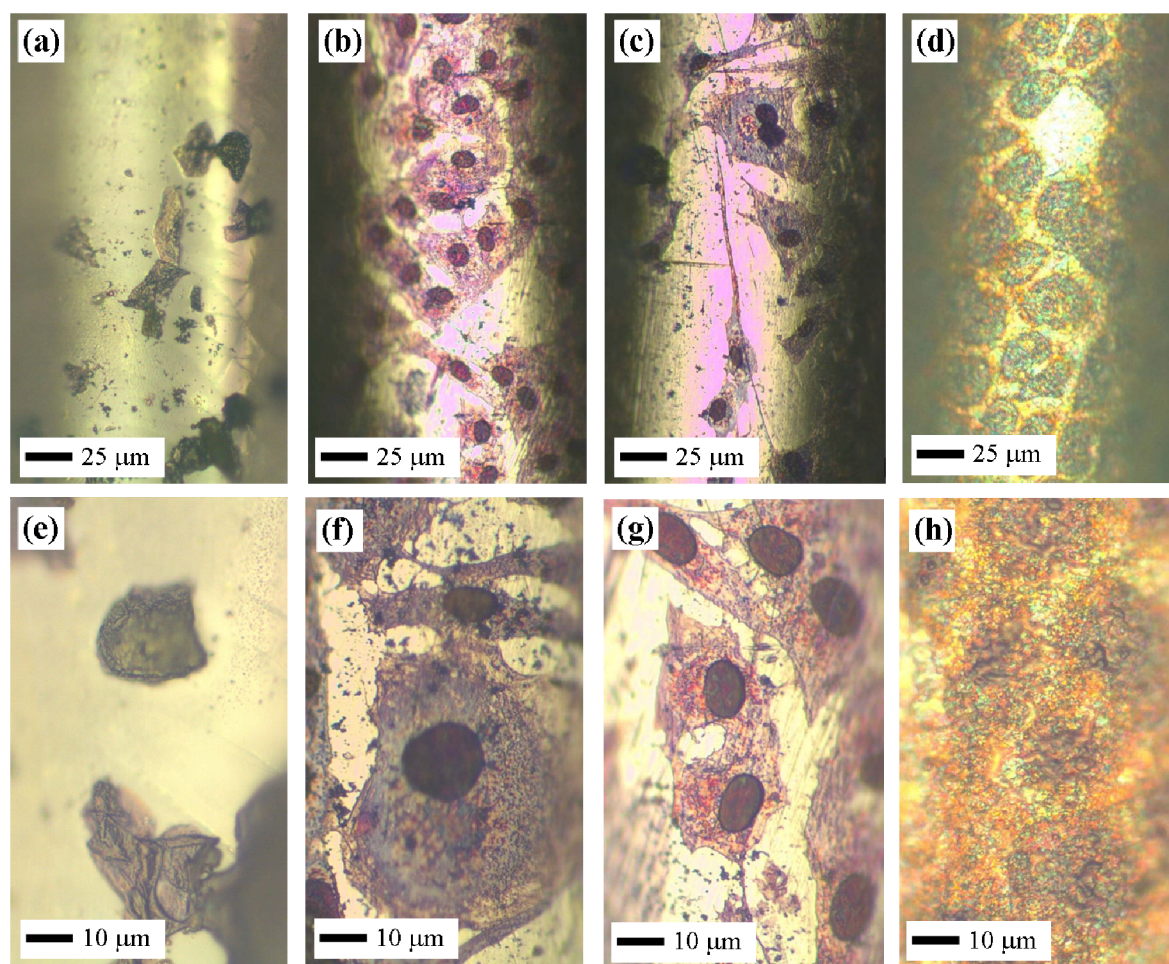
Figure 6-11 Optical micrographs of (a), (e) a polystyrene coated SS wire, (b), (f) a SIBS coated SS wire, (c), (g) a native SS wire and (d), (h) a SS wire coated with a titania NRL and heat treated with the method HT1. After incubation with the primary endothelial cells for 8 d.
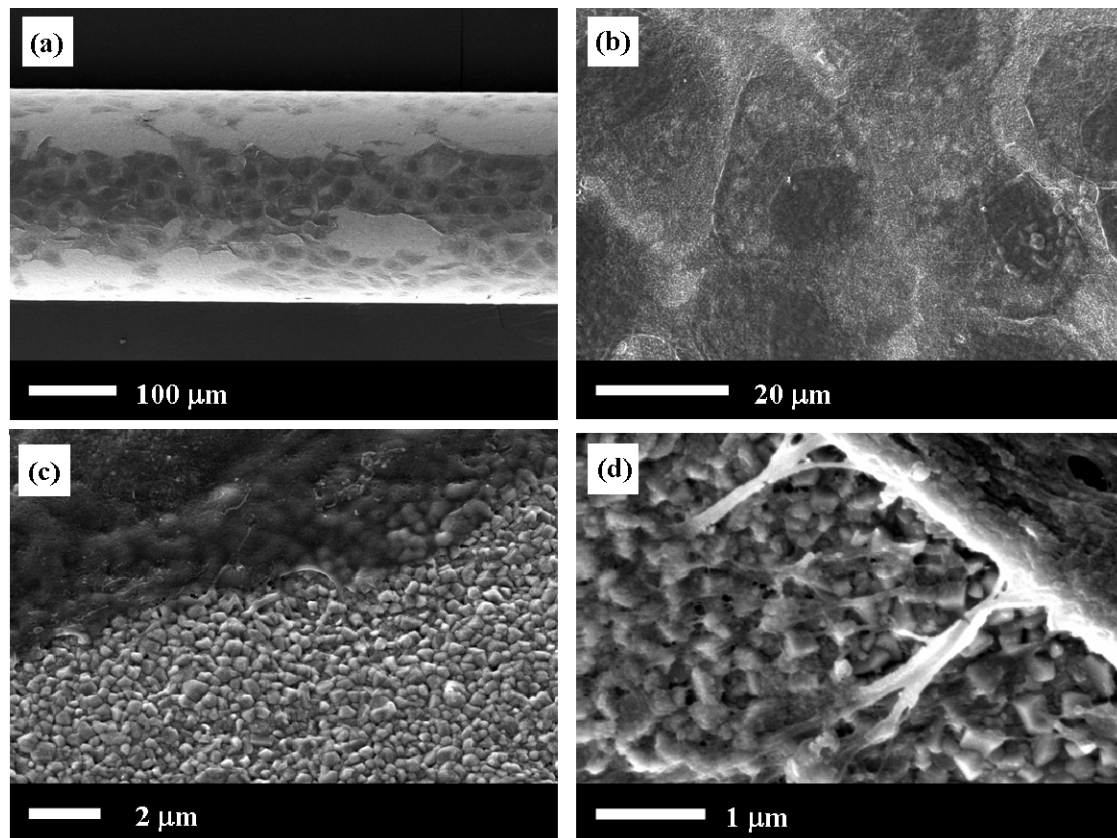
Figure 6-12 SEM-micrographs of a titania NRL on a SS wire, which was incubated for 8 d with endothelial cells. (a) to (d) show different magnifications.

By applying focused ion beam (FIB) milling to cut cross sections of the NRL-coated SS wires exposed to the cell test, more insight into the attachment of the cells onto the TiO_2-coating could be deduced, Figure 6-13. The ECs were in contact with the coating only at certain points, whereas at others a distance between the coating and the specimen's surface was observed. No additional substrates from the cell test were analyzed for comparison, because their preparation failed. In addition to the cell-substrate interaction, information about the substrates themselves could be gained by FIB. The thickness of the TiO_2-coating could be measured to be 300 nm. The grains of the underlying SS wire were visible exhibiting different grey scales. Their sizes can hence be measured. This gives information of the influence of the heat-treatment on the SS composition.
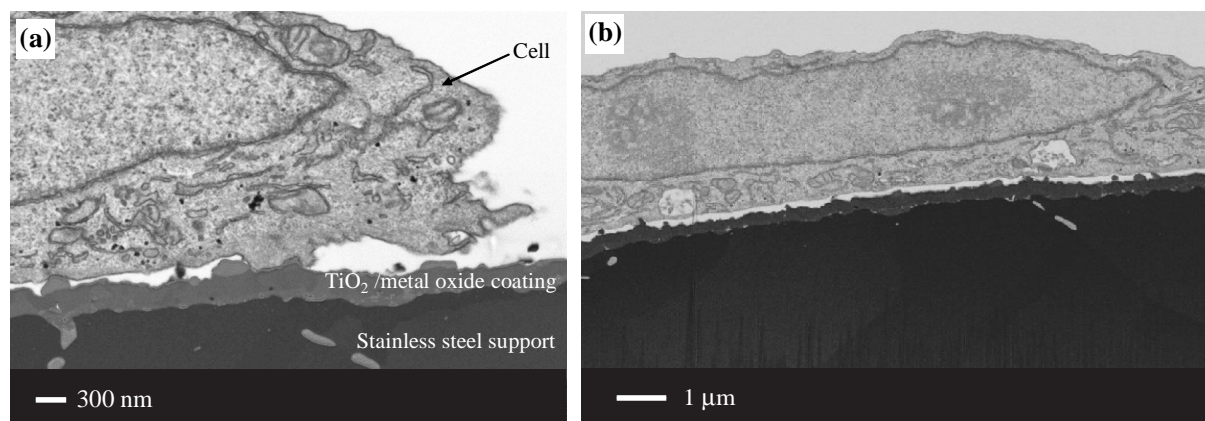
Figure 6-13 Electron micrographs of a cross section of a titania coated stainless steel wire, which was incubated with endothelial cells for 8 d.

6.3.5 *Cytocompatibility of the TiO₂-coatings on flat stainless steel after modified sintering*

Titania NRLs and *RL*s on flat SS supports, which were heat treated with the method HT2, were applied in this cell test. No significant differences of the living cell densities (LCD) as a function of substrate type was ascertained after ANOVA analysis of the data with an error risk of 5 %, Figure 6-14 (a). A high standard deviation was recorded for all of the samples. It was hence impossible to evaluate the cell test quantitatively, because the measured absorptions in the MTT assay (Figure 6-14 (b)) as well as the fluorescent signals in the resazurin test (Figure 6-14 (c)) are referenced to the adjusted mean values of the LCDs. The detected standard deviations in the LCDs propagated in the evaluation of the cell viability. This gets clearer if one compares the results of the MTT and resazurin tests. The MTT test and the resazurin assay are complementary tests. The lowest viability of the cells on ss730NRL(HT1) detected in the MTT experiment should lead to a high resorufin concentrations in the cell media. This was not the case: the membrane permeability did not show significant differences for all of the substrates.

Even if the quantitative results of this test were not distinct and the assay needs to be repeated, essential information was gained regarding the cell attachment. All substrates under investigation were covered with widely spread, adherent ECs, like was observed in the optical micrographs in Figure 6-15 and the SEM-micrographs in Figure 6-16. On the negative reference and the native SS cells have build a multilayer coverage. The cells on the *RL*s and NRLs were present as a monolayer. Filopodia were expressed by the cells on all substrates.
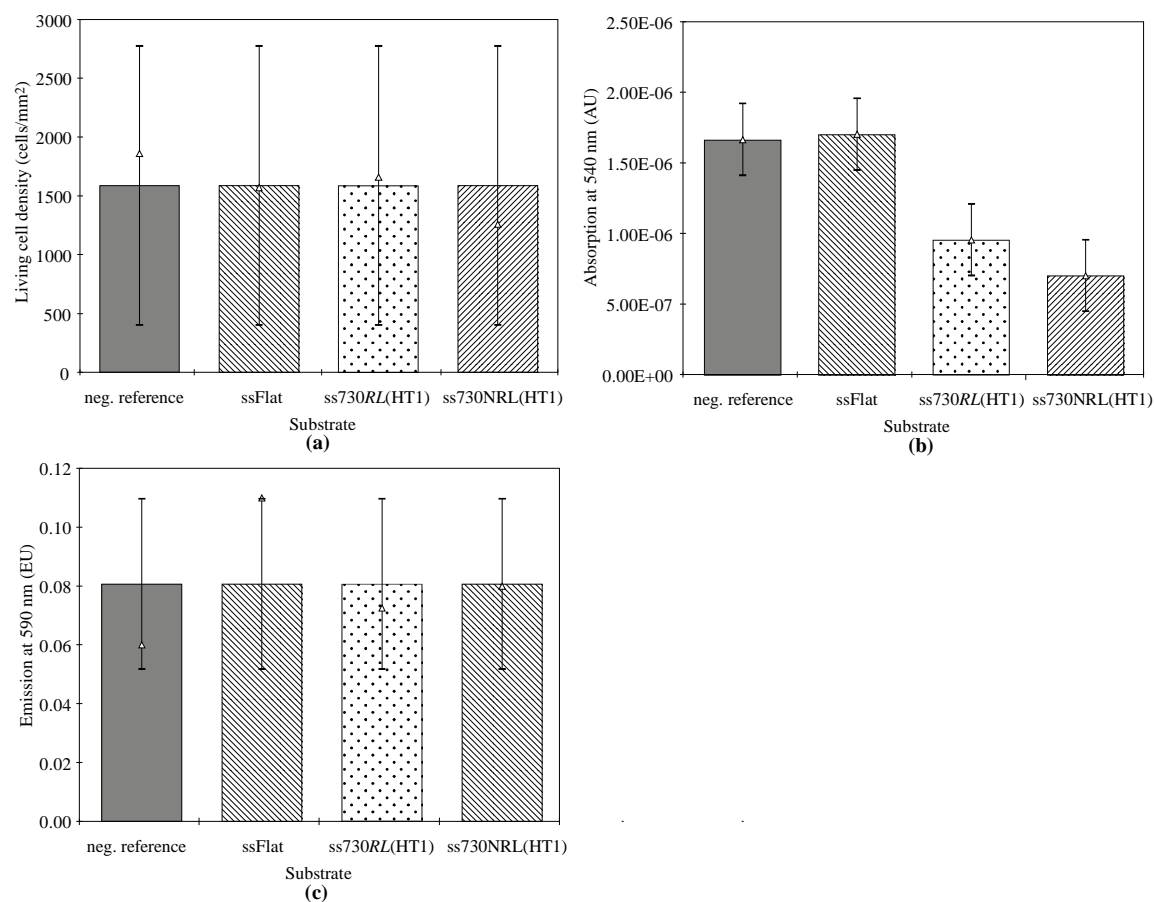
Figure 6-14 (a) The living cell density, (b) the mitochondrial activity and (c) membrane permeability of the primary endothelial cells after 8 d of incubation on the substrates of test CTssFlat2. Displayed are the adjusted mean values (columns), the non-adjusted mean values (Δ) and the standard deviations (-) after ANOVA analysis with $p < 0.05$.
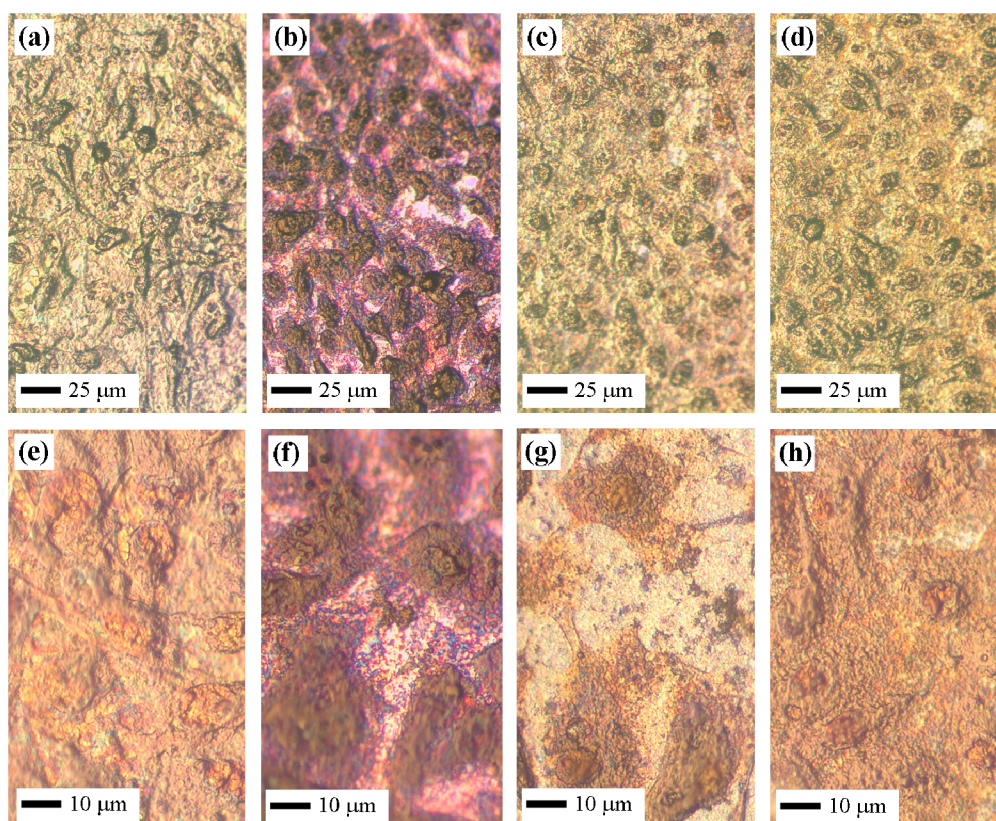
Figure 6-15 Optical micrographs of (a), (e) the cover slip negative reference, (b), (f) native stainless steel (SS), (c), (g) a titania *RL* on flat SS, (d), (h) a titania *RL* on flat SS, after incubation with endothelial cells for 8 d.
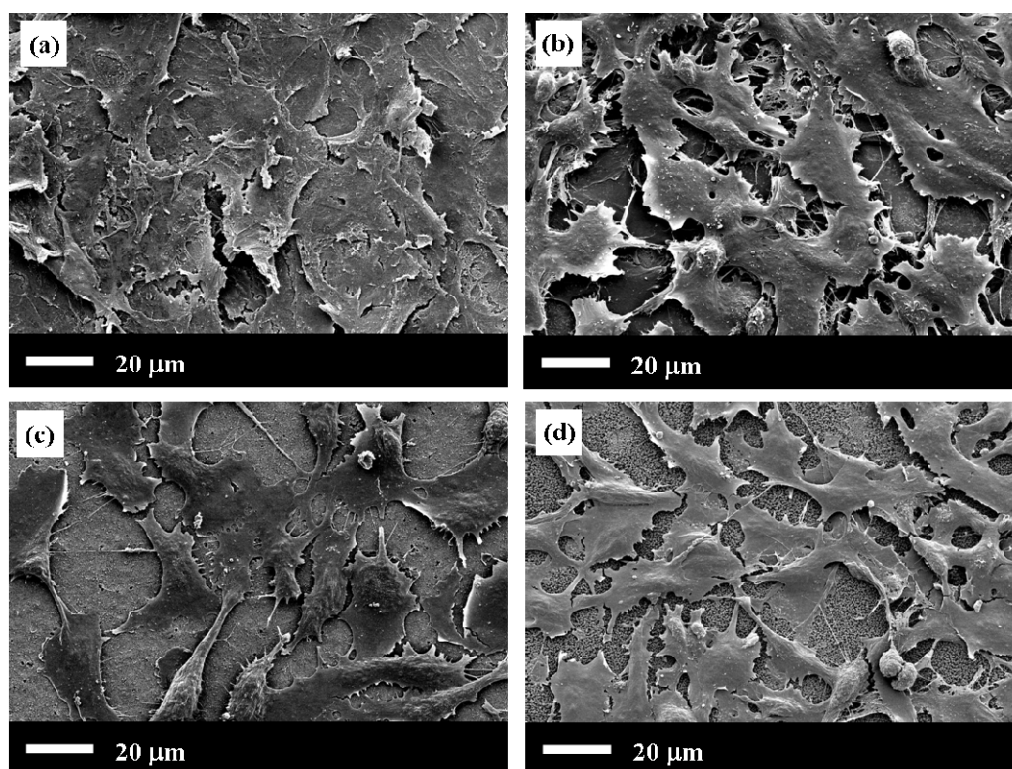
Figure 6-16 SEM-micrographs of (a) the cover slip negative reference, (b) native stainless steel (SS), (c) a titania *RL* on flat SS, (d) a titania *RL* on flat SS, after incubation with endothelial cells for 8 d.

6.3.6   *Roughnesses and contact angles*

The glass cover slip, which was applied as a negative reference in the cell tests, exhibited a smooth surface with a mean roughness, R_a, of 8.88 nm. The roughnesses of the NRLs on flat SS supports and heat treated with method HT2 (ss730NRL(HT2)) and of the equivalent *RL*s (ss730*RL*(HT2)) were 99.50 nm and 80.25 nm, respectively. The contact angle θ_c of the cover slip with water was measured to be 40.58 °. The titania coatings featured high standard deviations in the contact angles. They varied with the position on the substrates, at which the measurements were deduced. The middle of the quadratic surfaces of both sample-types exhibited a hydrophobic character with θ_c of 83.09 ° and 133.88 ° for the NRLs and *RL*s, respectively. At the border area, which is up to 3 mm distant from the sample's edges, smaller contact angles were detected: 48.58 ° for NRLs and 63.57 for the *RL*.

Table 6-3 Mean roughnesses R_a and contact angles θ_c with water of samples applied in the cell tests.

| *sample*	*cover slip*	*ss730NRL(HT2)*	*ss730RL(HT2)*
R_a (nm)	8.88 ± 4.96	99.50 ± 4.20	80.25 ± 25.44
θ_c (°), water: middle / border*	40.58 ± 2.32 / -	83.09 ± 10.72 / 48.58 ± 8.75	133.88 ± 6.94 / 63.57 ± 14.62

* the position of the measurement of the contact angle of a specimen of 1 cm^2 surface area

6.4   Discussion

The cytocompatibility of the nanostructured titania coatings with primary endothelial cells (ECs) was evaluated. Non-reservoir layers (NRLs) and reservoir layers (*RL*s) were fabricated on either silicon wafer or 316 L stainless steel (SS) supports and tested.

The well characterized titania coatings on wafer supports were sintered with the conventional heat treatment introduced in Chapter 4.2.5 and with the maximum sintering temperature of 730 °C. They were used to evaluate the influence of the topography of the NRLs and *RL*s on the cell proliferation and to establish the cell testing methods. A smaller living cell density (LCD) was detected on the surfaces of the TiO$_2$-coated samples, as compared to the glass cover slip negative references, Figure 6-2. This behavior might be related to two issues. The higher LCD might have been caused by multilayer cell coverage of the negative reference and the monolayer coverage on the titania coatings. Secondly it might be related to the cell's morphology. One could detect slightly bigger, more elongated ECs on the *RL*s compared to the NRLs and the negative reference in the micrographs of the cells on the surface. Bigger cells occupy a bigger area and hence fewer cells can attach to the surface. The different morphologies of the ECs were created by the reaction of the cells to the

material's surface. On one side, the borosilicate glass cover-slip exhibited a different chemical composition at the surface than stoichiometric TiO_2. It is known that TiO_2 promotes a good adhesion of osteoblasts in orthopedic and dental applications, and of ECs for stents [1, 15, 16]. The fast and good cell attachment on the TiO_2-surfaces is supported by their hydrophilicity, because a hydrophilic surface enhances the cell attachment rather than a hydrophobic one [1]. The contact angles of the titania coated wafers with water were below 20 ° (Table 4-11), the surfaces therefore hydrophilic. On the other side, the nanotopography of a surface can significantly change a cell's shape and vitality. In the field of dental and orthopedic medicine, it is well demonstrated that the nanotopography, which spans length scales of 0-100 nm, can trigger protein adsorption followed by osteoblast adhesion [17, 18]. A study of Dalby *et al.* with ECs on polymer surfaces of different roughnesses revealed that after 1 week of incubation, the cells were more spread on the manufactured rough topographies than on chemically similar flat surfaces. Of all nanotopographies investigated in their study, islands of a size of 13 nm gave the largest cell response. The cells exhibited highly spread morphologies containing well-defined cytoskeletons. The effect of the surfaces with higher roughnesses was less distinct. The samples investigated in the present test fit into the same roughness interval. The cover slip negative reference had a mean roughness, R_a, of 8.88 nm and the NRLs R_a of 16.70 nm (Table 6-3, Table 4-11). For the *RL*s, 25.30 nm was detected. Hence a good cell spreading on these types of surfaces could have been expected when compared to the findings by Dalby *et al*. Future testing with systematically varying the nanotopography of the TiO_2-coating is necessary to study the ECs-adhesion on the titania coatings. ECs should adhere fast to the coating, proliferate and hence prevent thrombosis and restenosis.

For the application of the coatings in a drug-eluting stents (DESs), SS supports instead of wafers will be applied. Titania NRLs and *RL*s on SS supports and heat treated with the conventional method and a maximum sintering temperature of 730 °C were subjected to a cell test. They were cytotoxic-only a few cells were present on the coating and iron oxides from the metal's surface were released into the culture medium, Figure 6-4, Figure 6-5. The presence of small amounts of iron oxides on the top-surface of the titania films was detected by X-ray photoelectron spectroscopy (XPS) analysis, Figure 4-28. The elemental composition of the underlying steel's surface could not be evaluated, because the escape depth of the photoelectrons was smaller than 10 nm and smaller than the thickness of the coating.

The conventional heat treatment was then modified to avoid the iron oxide formation on the steel's surface. Instead of using argon and oxygen in the high temperature region of the sintering cycle, a reducing atmosphere of argon, hydrogen and oxygen was applied. The

maximum sintering temperature was 820 °C and the method termed HT1. A preliminary corrosion test of SS-samples and NRL-coated SS, which were sintered with method HT1, in UP-water revealed the presence of iron oxides on top of the steel's surface, Figure 6-6 and Figure 6-7, and not in the bulk of the SS. The formation and release of iron oxides can be explained by the following. The presence of a natural, thin metal oxide layer of the elements chromium and nickel creates a passivation of the native, low carbon, austenitic 316L SS. Hence it gets corrosion resistant against many aggressive media, e.g. body fluid. The formation and growth of this oxide layer can be provoked by a chemical treatment of the SS and by heating the SS in air atmosphere. [19, 20, 21; 22]. But the temperature of the heating in air is crucial to the performance of the SS. As described by Nomura *et al.* [20], the oxide films on SS, heated above 800 °C, were not protective against inner corrosion and iron oxide formation. Fine metal oxide particles, made of chromium oxides and nickel oxides, grew bigger on top of the coating with increasing oxidation time and heating temperature. The presence of these large oxide particles as well as a depletion of Cr and Ni in the underlying SS, destroyed the protective films of SS and iron oxides get released from SS. In the present study, they diffused from the steel's surface through the porous titania coating into the surrounding medium. Their concentration in the culture medium was high enough to cause cell death. The mechanisms of the corrosion were in detail studied by A. Tourvieille de Labrouhe [6].

The presence of different metal oxides on top of the titania coated SS, heat treated with method HT1, were confirmed by XPS-analyses, Figure 6-8, Figure 6-9. The metal cations diffused into the coating from the SS due to the heat treatment with a maximum sintering temperature of 820 °C and were present on top of it. This was observed on both, flat SS coated with TiO_2 ss820NRL(HT1) and wire shaped SS coated with TiO_2 ssWire820NRL(HT1). Iron oxides and chromium oxides were present, besides stoichiometric TiO_2. The flat specimen showed additionally nickel oxide. The migration of Cr^{3+}, Fe^{2+}, Fe^{3+} from a 316 L stainless steel support through a 300 nm thick anatase layer after heating at 500 °C was recently also recorded by Shozui *et al.* [23].

In the preliminary corrosion test, the NRL-coated wire (ssWire820NRL(HT1)) did not show the release of iron oxide. Hence it was subjected to a cytotoxicity test. Flat, spread and inter-connected ECs were present on one side of the titania coated wire as was observed by microscopy. The opposite side, which was facing the bottom of the culture dish during cultivation, did not contain cells. The reason lies in the nature of the ECs, which are adherent growing cells. Once the cell suspension was added to the wires in the well plate, cells attached to the top of them, not at the bottom. During the cultivation for 8 d, they did not migrate to completely cover the wire and preferentially proliferated on top. When looking at

the cross sections of the NRL-coated wires seeded with ECs obtained by FIB, one could observe that the cells were interacting with the substrate at some points, at others they were distant. Well pronounced filopodia were seen in the SEM-images, which indicate cell attraction by the substrate. Cells interact with biomaterials via so called focal adhesions, which comprise an assembly of intra- and extracellular proteins, coupled to each other by transmembrane integrins. The focal adhesions were seen in the SEM-micrographs of the FIB-cross sections. Cell-surface integrin receptors promote furthermore the cell attachment to substrates. These receptors transduce biochemical signals to the nucleus by activating the same intracellular pathways that are used by growth factor receptors. The more the cells spread, the higher their rate of proliferation [1]. A quantitative evaluation of the cell numbers on the wires and their viability could not be deduced. The number of cells attached to them was too small to get signals in the spectroscopic measurements of the cell viability. If the observed contacts between the cells on titania NRLs on wires were an indicator for a better cell spreading than on a positive reference, or less good compared to the negative reference could not be deduced. On the one hand, the elaborate preparation of the specimens failed. On the other hand, it was difficult to find an appropriate negative reference for the test with the SS wires. Only dead cell debris were present on the polystyrene (PS)-coated wires, whereas on the styrene-isobutylene-styrene (SIBS)-coated ones more cells were detected. SIBS is the polymer applied in the commercially available Taxus^{TM} stent. Maybe in future studies the SIBS-coated stainless steel wires can be used as a negative reference, but it has to be checked if their usage fulfills the demanded regulations.

In future studies it might be of interest to use the FIB-method to study the close contact between the cells and the titania coating. If process parameters of the coating, such as a change in sintering temperature to modify the pore size, porosity or phase of TiO_2 will be applied, the cell response will certainly differ [1, 17]. How a pore size and shape can influence the cell attachment and where the focal adhesions of the cells are located in the highly porous coating might be accomplished with the help of FIB. Because by conventional SEM, one gets only a top view of the cells attached to the support and not of the region below the cell. To understand, how to trigger a fast, continuous re-endothelialization of the highly porous TiO_2-coating is beneficial to its application in a DES. A fast re-endothelialization is recommended for stents. Because ECs are involved in the regulation of thrombosis and in the proliferation of subjacent smooth muscle cells, when a stent is implanted into the coronary artery. An incomplete endothelialization of the stents struts is recognized as being a major cause of late stent thrombosis [2, 3, 4], which can lead to severe side effects in patients after 1 year of stenting. Besides the information of the cell-surface interaction in cross sections by FIB, one can get information about the coating's thickness, the size of the steel's grains and-if once cell testing will be performed on drug-loaded

coatings-the position of the drug in the coating. FIB might be a powerful tool for future investigations of the coating's performance.

The *in vitro* cell test on wires could not be optimized in the present feasibility study. A further cytotoxicity test was performed using flat SS supports and renouncing the effect of curvature existing on the wires on the cell attachment. In the last preliminary assay, specimens were prepared under well controlled sintering atmosphere with a so-called HT2-method. The heating was performed in two cycles: a first one in air up to 450 °C to remove the binder and a second one from room temperature up to 730 °C. The samples were encapsulated in the second cycle in a quartz tube, in which reducing atmosphere of 300 mbar argon was present. This special atmosphere was applied to limit the iron oxide formation on the steel's surface. The in such a way treated SS samples did not exhibit the release of iron oxide, as was deduced by A. Tourvieille [6]. Cells could be seeded on the native SS, on flat SS coated with NRLs or *RL*s. The optical micrographs of the negative references, the native SS and the two titania coatings showed all a good coverage with flat, spread ECs. On the negative reference and the SS, even multi-layered cell coverage was detected, Figure 6-16. A comparison of the viabilities of the different specimens by spectroscopic methods could not be deduced. A high standard deviation in the LCD, Figure 6-14, was detected. Applying the adjusted LCDs to calculate the signals form the spectroscopy data delivered the lowest viability of the NRL and the highest for the SS. The resazurin assay, as a complementary study, did not fit well with the MTT testing. Hence the errors in the LCD were assigned to the viability results and one could not perform a quantitative evaluation of the cytotoxicity. Factors, which might have caused the remarkable standard deviations, were identified. One might be related to inhomogeneities of the TiO_2-coatings on the flat SS. It was found that the contact angles of the quadratic SS samples coated with NRLs and *RL*s with water varied on different positions of one specimen. Whereas in the middle of the 1 cm^2 piece a contact angle θ_c of 83.09 ° for the NRL and of 133.88 ° for the *RL* was measured, the contact angles at the border area were 48.58 ° and 63.37 ° for NRLs and the *RL*s, respectively. The border area was the area of the specimen up to 3 mm distant to its edges. The different properties at the border area compared to the middle position were linked to varying thicknesses of the coating. They were created by the edge effect of the TiO_2-suspension after dip coating, by which more suspension accumulated at the edges of the sample creating a thicker TiO_2-coating. A second factor causing the deviations of the LCDs was related to the cutting of the big rectangular specimens by electro erosion. Even after cleaning of the workpieces in acetone and water, some metal ions, which were released from the steel during cutting, might have been left in the porous structure of the TiO_2-coating and promoted a certain cell response. However from this preliminary test it was shown that ECs grew on the NRLs and *RL*s on flat SS-supports, which were heat treated with the new method HT2. An analysis of

the elemental composition of the specimen's surface and the analysis of the steel regarding corrosion can be found in the Thesis of A. Tourvieille in conjunction with the analysis of their mechanical stability. A future test is planned to proof the cytocompatibility of the nanostructured TiO$_2$-coatings on stainless steel, which was indicated in the last preliminary cell test. The *in vitro* cell testing methods were established and the identified problems connected to the sample preparation will be accounted for in the following test.

In the near future, further application-relevant *in vitro* testing might be of interest. One should study the hemocompatibility of the NRLs and *RL*s on SS, which were heat treated with the method HT2, to evaluate platelet adhesion and the tendency of thrombus formation. This is important for implants in contact with blood, such as stents. TiO$_2$ is negatively charged when it is implanted. It should retard the attachment of blood components with a negative charge, e.g. platelets, and thus should help against thrombus formation, as is suggested by Liu *et al.* [24]. Another interesting study would be related to the study of the PTX-release from the coating. One can think of applying eluates of PTX from a titania *RL* into bovine plasma, like was discussed in Chapter 5, in a cell migration assay with SMCs [25]. It should help to evaluate the efficiency of the PTX-eluting titania coatings towards neointimal hyperplasia, which is characterized by an overproliferation of SMCs.

6.5   Conclusion

Several preliminary *in vitro* cytotoxicity tests were performed applying primary bovine endothelial cells (ECs) to different titania coated substrates. A first assay was accomplished with the coatings in the non-reservoir layer (NRL) and reservoir layer (*RL*) modifications on wafer supports, and sintered with the conventional heat treatment with a maximum sintering temperature, T$_{max}$, of 730 °C. A good cytocompatibility of the ECs after 8 d of incubation in regard to their living cell density and their viability was detected. The established cell-test methods could be used for further assays, because in reality the coating will be applied to metal supports, such as stainless steel (SS).

Surveys using the TiO$_2$-coated SS supports prepared by the conventional heat treatment and with T$_{max}$ of 730 °C exhibited cytotoxicity after 2 d of incubation. Corrosion testing revealed that it was associated to the dissolution of iron oxides from the steel's surface and their diffusion through the porous TiO$_2$-structure to the ECs. It was hence necessary to change the sintering atmosphere of the TiO$_2$-coated SS supports to reduce the iron oxide formation. Specimens were fabricated with a special sintering method termed HT1, in which a reducing atmosphere of argon, hydrogen and air during the high

temperature cycle of the sintering was applied. The ECs attached well to the titania coated wires and proliferated. However, the culturing conditions for the wire-shapes samples need to be optimized in future studies. The flat SS supports, which were heat treated with the method HT1, exhibited still the dissolution of iron oxides from the surface.

A better controlled, reducing sintering atmosphere was hence applied to the coatings on flat SS in the so-called method HT2. Cells grew well on the titania coatings in the NRL- and *RL*-modifications. They exhibited a normal morphology with a flat, spread shape. Cells were interconnected and distributed all over the coating. However, the quantitative evaluation of the cell's viability could not be deduced. A test to prove the cytocompatibility of the TiO_2-coated SS supports heat-treated with the method HT2, which was indicated in the preliminary test, are under current investigation.

6.6 References

[1] B.D. Ratner, A.S. Hoffman, F.J. Schoen, J.E. Lemons, "Biomaterials Science: An Introduction to Materials in Medicine", *Elsevier Academic Press*, 2004.

[2] N. Kukreja, Y. Onuma, J. Daemen, P.W. Serruys, "The future of drug-eluting stents", *Pharmacological Research*, Vol. 57, 2008, pp. 171-180.

[3] M. Joner, G. Nakazawa, A.V. Finn, S.C. Quee, L. Coleman, E. Acampado, P.S. Wilson, K. Skorija, Q. Cheng, X. Xu, H.K. Gold, F.D. Kolodgie, R. Virmani, "Endothelial Cell Recovery Between Comparator Polymer-Based Drug-Eluting Stents", *Journal of the American College of Cardiology*, Vol. 52, 2008, pp. 333-342.

[4] T.L.P. Slottow, R. Waksman, "Drug-Eluting Stent Safety", *The American Journal of Cardiology*, Vol. 100, 2007, pp. S10-S17.

[5] "Biological evaluation of medical devices, part 5: Test for *in vitro* cytotoxicity", *International Standard ISO 10993-5*, 1999.

[6] A. Tourvieille de Labrouhe, " Nanostructured ceramic coatings for deformable medical implants such as stents", Thesis, Ecole Polytechnique Fédérale de Lausanne, 2009.

[7] "Cell Adhesion and Growth on Coated or modified Glass or plastic surfaces," *Bulletin No. 13, Thermo Fisher Scientific (Nunc GmbH & Co. KG), http://www.nuncbrand.com/us/frame.aspx?ID=593*, November 2008.

[8] R.I. Freshney, "Culture of Animal Cells: A Manual of Basic Technique", *Wiley & Sons*, 2005.

[9] E. Wintermantel, S.-W. Ha, "Medizintechnik mit biokompatiblen Werkstoffen und Verfahren", *Springer Verlag*, 2002.

[10] T. Mosmann, "Rapid colorimetric assay for cellular growth and survival: application to proliferation and cytotoxicity assays", *Journal of Immunological Methods*, Vol. 65, 1983, pp. 55-63.

[11] J. O'Brien, I. Wilson, T. Orton, F. Pognan, "Investigation of the Alamar Blue (resazurin) fluorescent dye for the assessment of mammalian cell cytotoxicity", *European Journal of Biochemistry*, Vol. 267, 2000, pp. 5421-5426.

[12] R.H. Batchelor, M. Zhou, "Use of cellular glucose-6-phosphate dehydrogenase for cell quantitation: applications in cytotoxicity and apoptosis assays", *Analytical Biochemistry*, Vol. 329, 2004, pp. 35-42.

[13] M.K. McMillian, L. Li, J.B. Parker, L. Patel, Z. Zhong, J.W. Gunnett, W.J. Powers,

M.D. Johnson, "An improved resazurin-based cytotoxicity assay for hepatic cells", *Cell Biology and Toxicology*, Vol. 18, 2002, pp. 157-173.

[14] J. Lemaître, Design of Experiment, available at: http://ltp.epfl.ch/page14769.html, February 2009.

[15] T. Kokubo, T. Matsushita, H. Takadama, "Titania-based bioactive materials", *Journal of the European Ceramic Society*, Vol. 27, 2007, pp. 1553-1558.

[16] H-I. Yeh, S-K. Lu, T-Y. Tian, R-C. Hong, W-H. Lee, C-H. Tsai, "Comparison of endothelial cells grown on different stent materials", *Journal of Biomedical Materials Research Part A*, Vol. 76A, 2005, pp. 835-841.

[17] G. Mendonça, D.B. Mendonça, F.J. Aragao, L.F. Cooper, "Advancing dental implant surface technology - From micron- to nanotopography", *Biomaterials*, Vol. 29, 2008, pp. 3822-3835.

[18] A. Curtis, S. Affrossman, H. Johnstone, M. O. Riehle, M.J. Dalby, "*In vitro* reaction of endothelial cells to polymer demixed nanotopography", *Biomaterials*, Vol. 23, 2002, pp. 2945-2954.

[19] D. Peckner, I.M. Bernstein, "Handbook of Stainless Steels", *McGraw-Hill Inc.*, 1977.

[20] K. Nomura, Y. Ujihira, "Analysis of oxide layers on stainless steel (304 and 316) by conversion electron Mössbauer spectrometry", *Journal of Materials Science*, Vol. 25, 1990, pp. 1745-1750.

[21] S. Vives, C. Meunier, "Mixed SiO_2-TiO_2 (1:1) sol-gel films on mild steel substrates: Sol composition and thermal treatment effects", *Surface and Coatings Technology*, Vol. 202, 2008, pp. 2374-2378.

[22] R.Y. Chen, W.Y.D. Yuen, "Oxidation of Low-Carbon, Low-Silicon Mild Steel at 450–900°C Under Conditions Relevant to Hot-Strip Processing", *Oxidation of Metals*, Vol. 57, 2002, pp. 53-79.

[23] T. Shozui, K. Tsuru, S. Hayakawa, Y. Shirosaki, A. Osaka, "XPS study on potential suppression factors suppressing *in vitro* apatite formation on anatase films prepared on various substrates", *Surface and Coatings Technology*, Vol. 203, 2009, pp. 2181 – 2185.

[24] J. Liu, D. Yang, F. Shi, Y. Cai, "Sol-gel deposited TiO2 film on NiTi surgical alloy for biocompatibility improvement", *Thin Solid Films*, Vol. 429, 2003, pp. 225-230.

[25] K. Sternberg, S. Kramer, C. Nischan, N. Grabow, T. Langer, G. Hennighausen, K. Schmitz, "*In vitro* study of drug-eluting stent coatings based on poly(l-lactide) incorporating cyclosporine A–drug release, polymer degradation and mechanical

integrity", *Journal of Materials Science: Materials in Medicine*, Vol. 18, 2007, pp. 1423-1433.

CHAPTER VII

7 GENERAL CONCLUSION AND PERSPECTIVES

The feasibility to use nanostructured titania (TiO$_2$) films as drug-releasing coatings in drug-eluting stents (DESs) was studied. The characterization of the coatings on silicon wafer and stainless steel (SS) supports was accomplished in regard to their structure and chemical composition. A particular emphasis has been laid on the development of methods to load the titania coatings with the pharmaceutical agent paclitaxel (PTX) in therapeutical doses and to study its release. Preliminary *in vitro* cell tests were carried out to get information about the cytocompatibility of the non-drug-loaded coatings.

The thin nanostructured TiO$_2$-films were produced by dip coating the SS or silicon wafer supports with TiO$_2$-nanopartiles and spherical polymer templates. A subsequent heat-treatment burned the organic components to create a structured porosity in the coatings. It consisted of a titania porous structure enclosing ellipsoidal drug reservoirs, which had a diameter of 1 μm. The reservoirs have the functions to increase the porosity of the coating and to store a sufficient amount of medicament, which will be controlled-released through the surrounding porous structure. The structure of the porous coatings on SS could not be characterized completely. The coating adhered too strongly on the support to be detached from it, which would have been necessary for the analyses of the porosity or density. The TiO$_2$-coatings fabricated on silicon wafer supports represented a good model to measure these parameters. The specifications of the coatings, which were heat-treated at a maximum sintering temperature, T_{max}, of 730 °C and did not contain reservoirs (NRL), were determined. The pore size distribution (PSD) of the NRL, which is equivalent to the structure

surrounding the reservoirs in a reservoir layer (*RL*), exhibited a median pore width below 100 nm and an open porosity of 50 %. The influence of the reservoir size and density on the overall porosity in the coatings could not be measured, but calculated. The *RL*s applied in the present study contained theoretically 3 % more pore volume compared to the NRL of the same thickness. The calculations showed that the total pore volume can be increased by creating thicker coatings with bigger reservoirs, or by increasing the reservoir density.

It was shown that in our days it is still a challenge to measure the PSDs and porosities of thin films, which exhibit high pore volumes and pore widths of a few nanometers up to several micrometers. A large amount of film sample was required to perform one measurement by mercury intrusion porosimetry (MIP), which covers all pore sizes. Hence bulk, cylindrical samples with a NRL-structure were prepared by slip casting. A bimodal PSD and a porosity of 50 % was recorded by MIP. The influence of constrained sintering in the films was shown by comparing the results of the bulk specimens sintered at T_{max} of 800 °C with the ones of a NRL-coating, which was identically heat-treated. The densification was lower in the films. But the differences in densification due to constrained film sintering were not as pronounced in the start of the initial stage of sintering of the TiO_2-nanoparticles, as in the intermediate or the final stage. Hence similar properties in regard to the specific surface area and porosity of the TiO_2-bulks and the NRLs were detected when heat-treated at T_{max} of 730 °C. The TiO_2-films heat-treated at T_{max} of 730 °C were composed of mainly anatase, the residual amount was rutile. Stoichiometric TiO_2 was detected on the top of the coatings by X-ray photoelectron spectroscopy (XPS). The roughnesses of the porous NRLs and *RL*s depended on the roughnesses of the underlying support material: it was lower of the coatings on smooth silicon wafers compared to the coatings on SS. The TiO_2-coatings on wafers featured a high hydrophilicity, whereas the films on SS featured a more hydrophobic character. The presence of the reservoirs did not significantly influence the wettability behavior of these two types of coatings.

PTX was successfully loaded into the well characterized, nanostructured TiO_2-coatings. The load of the pharmacological agent into the NRLs could be varied from as small as 0.06 µg/mm^2 to a maximum load of 1.06 µg/mm^2, depending on the parameters of the drug-loading procedures. The maximum load of 1.21 µg/mm^2 was obtained for the *RL*s, with PTX being accumulated in the drug reservoirs, in the surrounding porous ceramic structure and being present as a burst-layer on top of the coating. The drug quantity was comparable to the PTX-concentration in the commercially available Taxus^{TM} stent.

Different factors, which influence the drug-load in the films, could be identified. They

were related to the *structure of the TiO₂-coating* and the *process parameters applied in the drug-loading procedure*. A higher porosity in the coating increases the PTX-load. The presence of the reservoirs in the *RL*s thus added 14 % more PTX into the porous film compared to the NRLs. Bigger reservoirs as well as a higher density of them will further increase the PTX-load, as was obtained from theoretical calculations. Film structures with a higher reservoir density can be realized in future studies by densely packing the spherical polymer template particles in a monolayer instead of using randomly arranged particles. A higher porosity or directed pores can be formed in the porous structure surrounding the reservoirs by employing a higher binder content or a filler in the TiO₂-suspension. An increase of the thickness of the coating will also increase the space available to store PTX. But one should be cautious in manipulating any of the structural parameters of the coating, because they are linked to the mechanical stability. The critical film thickness in respect to the mechanical stability was evaluated in the studies performed by A. Tourvieille de Labrouhe*, in parallel to the present study.

The amount of PTX in the coating depended furthermore on the *parameters of the drug-loading process*. The solvent evaporation method has proven to be powerful to adapt the PTX-loads for different needs. Various PTX-polymorphs could be created in the films depending on the used solvents. By varying the immersion times of the specimens into the PTX/solvent solution different drug-loads could be obtained in the NRLs and the *RL*s. Besides PTX being present in the porous structure of the coating, it was accumulated on the surface of the film as a burst-layer. The thickness of the PTX-burst-layer can theoretically be decreased by applying a lower withdrawal velocity to remove the samples from the PTX/solvent solution. This needs to be tested in future experiments.

The PTX-loaded *RL*s were subjected to drug-release experiments into water. The obtained release profiles into water fitted well the release profiles reported for the commercially available Taxus^{TM} stent. The factors influencing the PTX-release were evaluated. They can be categorized into belonging to the *structure of the coating*, to the *features of PTX* and to the *release experiment*. The diffusion of PTX out of the coating can theoretically be modulated by altering the structure of the porous ceramic surrounding the reservoirs. For instance a decrease in pore-width, an increase in the pore's tortuosity and of the thickness of the nanoporous layer on top of the reservoirs can reduce the drug flux out of the coating.

*A. Tourvieille de Labrouhe, " Nanostructured ceramic coatings for deformable medical implants such as stents", Thesis, Ecole Polytechnique Fédérale de Lausanne, 2009.

A 10 times smaller median pore size in the porous structure surrounding the reservoirs, compared to the one applied in the present study, will trigger molecule to pore-wall interactions. They slow down the diffusion and hence the drug flow. Smaller pores in the coating can be obtained by decreasing the size of the primary TiO_2-nanoparticles in the TiO_2-suspension from 21 nm to about 5–10 nm.

The features of the drug can manipulate the drug-release. If the drug particle size in the coating increases, which can be realized by completely filling the pores with the drug, a prolonged drug-release can be supported. The drug-morphology can influence the drug-release kinetics, as was shown in the present study. The amorphous form of PTX exhibited a higher release constant than the crystalline ones when immersed into water. A release test of PTX from *RL*s into bovine plasma revealed that almost half of the PTX-load was released after 1 d of testing. This was the amount of PTX in the burst-layer. After 4 d, no more drug was liberated and PTX stayed trapped in the pores of the coating. The release profile of PTX from the commercially available Taxus^{TM} stent into bovine plasma was different. For that DES, a continuous release up to 7 d with a low burst-effect was recorded. The data fitted well the predicted release kinetics.

That more than half of the amount of totally incorporated PTX remained in the thin *RL* in the release test into bovine plasma was caused by the formation of a layer composed of proteins and inorganics on top of the titania coating. It blocked small pores and thus the diffusion of PTX out of the coating into the medium. If the hindrance of the drug diffusion due to the presence of this layer will be as pronounced under *in vivo* conditions needs to be evaluated in future studies. As the case may be, applying higher sintering temperatures to increase the amount of rutile and to provoke the metal-ion diffusion into the top part of the coating can lower the tendency for protein adsorption and calcium phosphate precipitation.

Several preliminary *in vitro* cytotoxicity tests were performed applying isolated, primary, bovine endothelial cells (ECs) to different non-PTX-loaded specimens. A first assay with NRLs and *RL*s on wafer supports resulted in cytocompatibility after 8 d of incubation. The TiO_2-coated SS supports, heat treated in a protecting sintering atmosphere at elevated sintering temperatures, were covered by ECs. Cells exhibited a normal morphology with a flat, spread shape. A test to prove the cytocompatibility of the titania coatings on SS supports, which was indicated in this preliminary test, are under current investigation.

Next tests to prove the feasibility to use the nanostructured titania coatings in DESs might be the following. The efficiency of the drug doses, which are released from the coatings, should be evaluated. The doses need to be high enough to inhibit smooth muscle

cell (SMC)-proliferation and migration when implanted as a DES in the coronary artery. This will contribute to prevent the re-blocking of the artery. If necessary, the coating's structure can further be optimized to create the wanted medication. Following these testing it is conceivable to apply the drug-loaded titania coatings in animals to study its performance under *in vivo* conditions.

In summary, it has been shown that the nanostructured TiO_2-coatings with incorporated drug reservoirs have a high potential to be used as drug-eluting coatings on stent-implants. A technology platform comprising methods and understandings of the characterization, drug-loading, drug-release and the cytotoxicity tests of the TiO_2-coatings was established. It provides a powerful tool to adapt the ceramic coatings for various applications despite in DESs. One can think of applying them in orthopedic or dental medical implants. The nanostructured coatings might then release antibiotics or growth factors besides triggering cell attachment due to the bioactive titania matrix and its nanotopography.

ABBREVIATIONS

Abbreviation	Meaning
ACET	Acetone
AcN	Acetonitrile
AFM	Atomic Force Microscope
ANOVA	ANalysis Of VAriance
AP	Atmospheric Pressure drug-loading procedure
Ar	Argon
BET	Brunauer-Emmett-Teller (method to determine specific surface area)
BJH	Barrett, Joyner, Halenda for determination of pore size distribution
BMS	Bare Metal Stent
BP	Biodegradable Polymer
C	Carbon
CAD	Coronary Artery Disease
CCD	Charge Coupled Device
CHUV	Centre Hospitalier Universitaire Vaudois
CIME	Center for Electron Microscopy, EPF Lausanne
CME	Center of Electron Microscopy, Université de Lausanne
CoCr	Cobalt Chromium alloy
Cr	Chromium
Cu	Copper
CVD	Chemical Vapor Deposition
D_2O	deuterated water; deuterium oxide
DCM	DiChloroMethane
DES	Drug-Eluting Stent
DMEM	Dulbecco's Modified Eagle Medium
DMSO	DiMethyl SulfOxide
DP	Durable Polymer
DSC	Differential Scanning Calorimetry
EA	Ethyl Acetate
EC	Endothelial Cell
EDTA	EthyleneDiamineTetraacetic Acid
EP	Ellipsometric Porosimetry
FBS	Fetal Bovine Serum
FDA	US Food and Drug Administration
FIB	Focused Ion Beam
FT-IR	Fourier Transform InfraRed Spectroscopy
G-6-P	Glucose-6-Phosphate
H_2O	Water

He	Helium
HPLC	High Performance Liquid Chromatography
HRSEM	High Resolution Scanning Electron Microscope
HT1, HT2	special Heat Treatments 1, 2
IR	InfraRed
ISO	International Organization for Standardization
IUPAC	International Union of Pure and Applied Chemistry
LCD	Living Cell Density
LP	Low Pressure drug-loading technique
Mg	Magnesium
MIP	Mercury Intrusion Porosimetry
Mn	Manganese
Mo	Molybdenum
MTT	3-(4,5-Dimethylthiazol-2-yl)-2,5-diphenyltetrazoliumbromid
Ni	Nickel
NIST	National Institute of Standards and Technology
NiTi	Nickel Titanium; Nitinol
NRL	Non-Reservoir Layer
NSP	Nitrogen Sorption Porosimetry
OH	hydroxyl group
P	Phosphorus
PBS	Phosphate Buffered Saline
PLGA	Poly-Lactic-Glycolic Acid
PLLA	Poly-L-Lactic Acid
PS	PolyStyrene
PSA	Penicillin, Streptomycin, Amphotericin
PSD	Pore Size Distribution
PSI	Paul Scherrer Institute, Villigen
PTCA	Percutaneous Transluminal Coronary Angioplasty
PTX_K	Paclitaxel obtained from Knowshine (Shanghai) Pharmaceuticals Inc.
PTX_S	Paclitaxel obtained from Sigma Aldrich
PVA	PolyVinyl Chloride
PVD	Physical Vapor Deposition
RL	Reservoir Layer
S	Sulfur
SANS	Small Angle Neutron Scattering
SEM	Scanning Electron Microscope
Si	Silicon
SIBS	polystyrene-b-IsoButylene-b-Styrene
SiC	Silicon Carbide
SiO_2	Silicon Oxide
SMC	Smooth Muscle Cell

SS	Stainless Steel
TBME	Tert.-Butyl Methyl Ether
TGA	ThermoGravimetric Analysis
Ti	Titanium
TiO_2	Titanium oxide; titania
TP1, TP2	Titania nanoparticle suspension 1, 2
UP-water	UltraPure water
XPS	X-ray Photoelectron Spectroscopy
XRD	X-Ray Diffraction

SYMBOLS

Symbol	Unit	Meaning
Δ	°	phase shift
ΔG	mJ/m^2	difference of free energy of adhesion
ΔH	J/g	heat of fusion
ΔH_v	J/(mol·K)	evaporation enthalpy
Δp	Pa	pressure difference
$(\rho'/\rho)_c$	-	densification rate of the constrained film
$(\rho'/\rho)_u$	-	densification rate of the unconstrained film
$A_{apparent}$	m^2	geometrical surface area
$A_{effective}$	m^2	effective surface area
C	g/ml	concentration
Ci	g/ml	initial drug concentration in the drug-release system
C_s	g/ml	maximum solubility concentration
C_t	g/ml	concentration at time t
D	m^2/s	diffusion coefficient
d_{BET}	m	grain diameter deduced from the specific surface area
D_{eff}	m^2/s	effective diffusion coefficient
d_g	m	grain diameter
d_h	m	thickness of the hydrodynamic layer
d_{mode}	m	most frequent pore diameter
d_p	m	pore diameter
D_{SE}	m^2/s	Stokes Einstein diffusion coefficient
D_{sim}	m^2/s	simulated diffusion coefficient
d_{v50}	m	median pore diameter
E	eV	energy of the emitted wave
E_p	eV	parallel component of the energy of the emitted wave
E_s	eV	perpendicular component of the energy of the emitted wave
f	-	roughness factor
g	m/s^2	9.81, acceleration due to gravity
H	m	thickness of deposited liquid film
h, h1, h2	m	thickness of the diffusion layer
J	mol/(m^2·s)	flux
K″	-	constant
k_0	g/(m^2·s)	zero order release constant
k_1	%/s	first order release constant
k_B	J/K	1.381·10^{23}, Boltzman constant
k_h	g(m^2·s)	Higuchi release constant

k_{KP}	%/s	release constant depending on the release exponent
l	m	distance between capillary inlet and capillary meniscus of fluid
L	m	thickness of the porous coating
M_0	g	initial amount of drug in the drug-eluting system
M_{is}	g	initial amount of drug in solution
M_t	g	amount of drug released at a certain time
n	-	release exponent
n_p	-	pore number density
p^0	Pa	saturation vapor pressure
p_1	Pa	$1.0133 \cdot 10^5$, atmospheric pressure
p_2	Pa	saturation pressure
p_c	Pa	capillary pressure
p_e	Pa	equilibrium vapor pressure
R	J/(mol·K)	8.3145, ideal gas constant
r_1, r_2	m	radii of curvature
R_a	m	average surface roughness
R_g	m	radius of gyration
r_h	m	hydrodynamic radius
r_k	m	Kelvin radius
r_p	m	pore radius
S	m^2	solid area accessible to drug dissolution
S_{BET}	m^2/g	specific surface area
t	s	time
T_1	°C	boiling point at room temperature
T_2	°C	room temperature
tanψ	-	relative wave amplitude
T_{max}	°C	maximum sintering temperature
U	m3/g	specific volume of drug in the porous structure
v	m/s	withdrawal speed
V	ml	volume of liquid dissolution media for drug-release
V_m	m^3/mol	molar volume
vp	m/s	velocity through pore channels
V_p	m^3	pore volume
γ	N/m	surface tension
$γ_{LV}$	N/m	liquid/vapor surface tension
$γ_{SL}$	N/m	solid/liquid surface tension
$γ_{SV}$	N/m	solid/vapor surface tension
ε	-	porosity
η	Pa·s	dynamic viscosity
$θ_{c0}$	°	contact angle
$θ_{c0}$	°	ideal contact angle
λ	m	wavelength

ν	m^2/s	kinematic viscosity
ν$_P$	-	viscous poisson's ratio
ρ	g/cm^3	density
ρ$_{Arch}$	g/cm^3	Archimedes density
ρ$_s$	g/cm^3	skeletal density
σ	Pa	sintering stress
τ	-	pore tortuosity
χ	-	molecule-to-pore ratio
ω	rad/s	angular velocity

APPENDIX

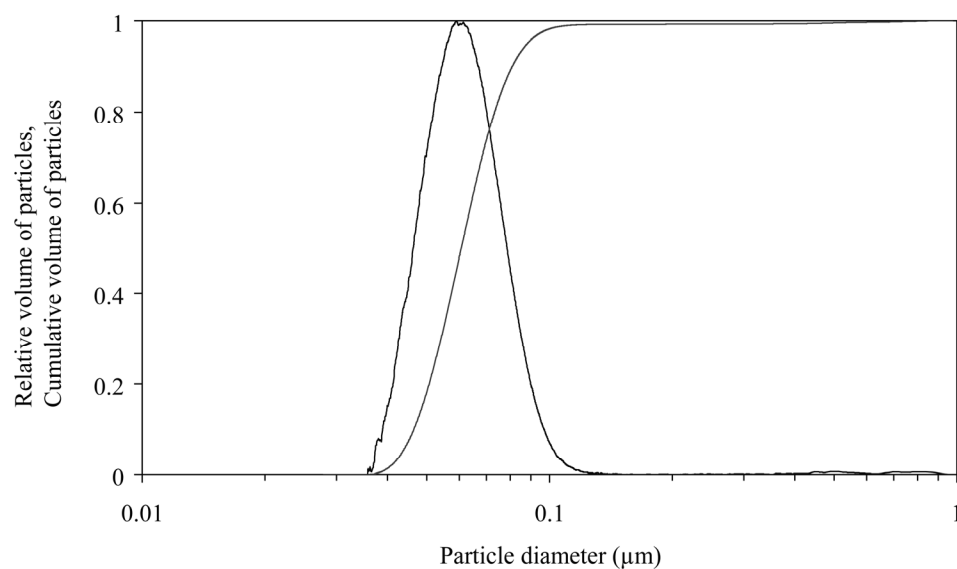## *Particle size distribution*

Figure A-1 Particle size distribution of the titania particle suspension as obtained by differential disc centrifuge particle size analysis.
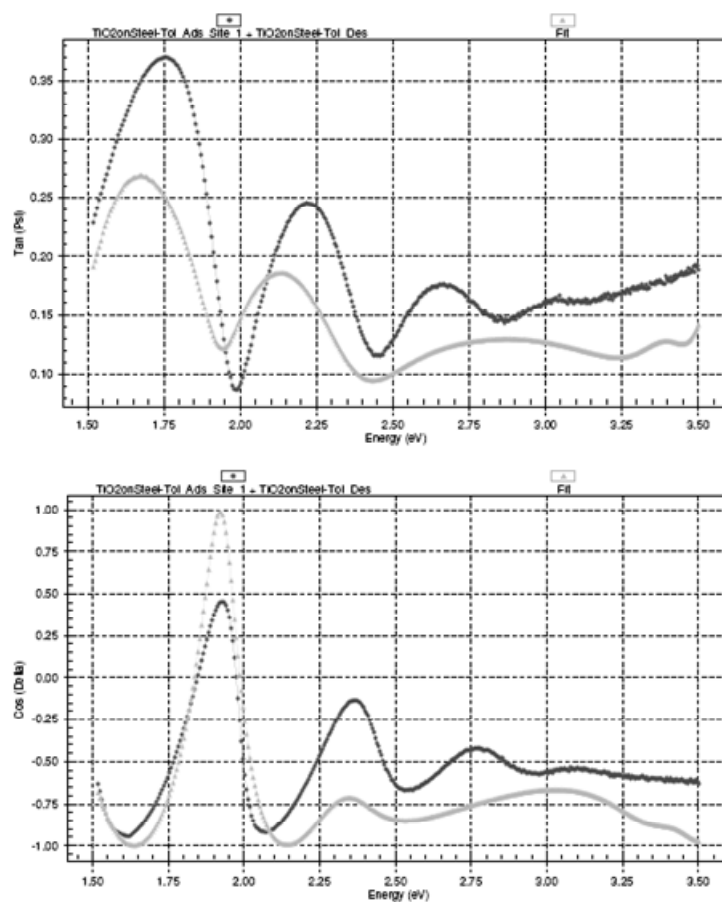
Ellipsometry porosimetry

Figure A-2 Ellipsometric parameters tan(ψ) (upper image) and cos(Δ) (lower image) of the non-reservoir titania coating on stainless steel support. The measured data are represented by black dots, the mathematical fits in grey dots.
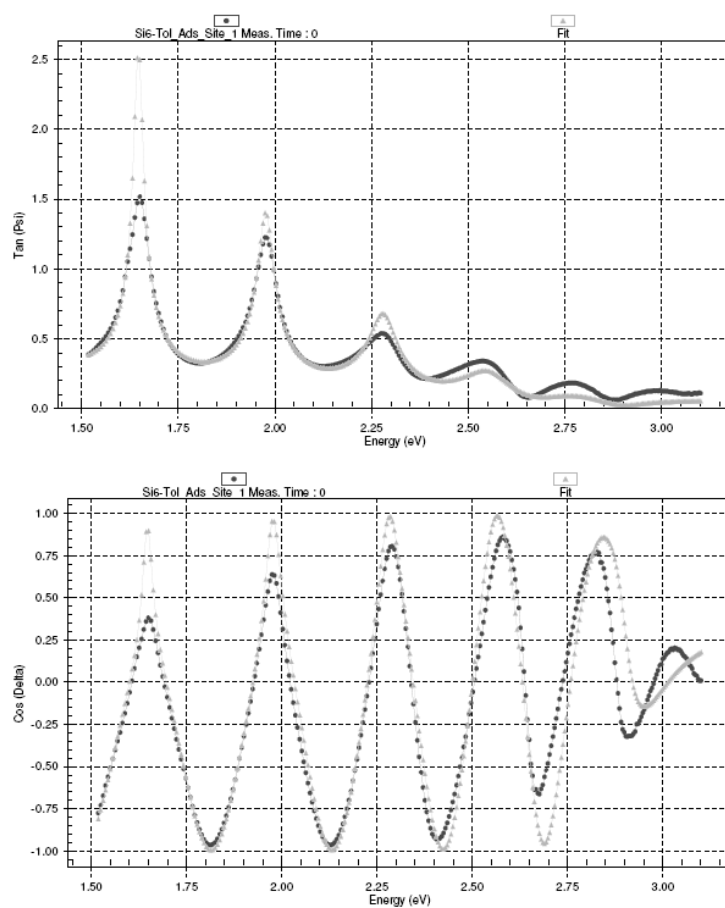
Figure A-3 Ellipsometric parameters tan(ψ) (upper image) and cos(Δ) (lower image) of the non-reservoir titania coating on wafer support. The measured data are represented by black dots, the mathematical fits in grey dots.

CURRICULUM VITAE

Karin Dittmar

Date of birth	9th of February, 1981
Place of birth	Schmalkalden, Germany
Nationality	German
Civil state	Single

Formation

Apr. 2006-present	Ph.D. studies in Materials Science, Swiss Federal Institute of Technology, Lausanne, Switzerland *Nanostructured Titania Coatings For Drug-Eluting Medical Implants*
May-Nov. 2005	Diploma thesis, Friedrich-Baur Research Institute for Biomaterials, Bayreuth, Germany *Development of drug carrier systems for the local-antibiotic releasing*
Oct. 2000-Nov. 2005	Studies in Bioengineering Science (Materials Science and Process Engineering), University of Bayreuth, Bayreuth, Germany *Characterization of polysilazane coatings on CoCrMo-alloys for biomedical applications*
Jun. 2000	University entrance diploma, Werratalgymnasium Schwallungen, Schwallungen, Germany

Working experience

Oct. 2004-Apr. 2005	Trainee, Research and Development of Biomaterials, Aesculap AG, Tuttlingen, Germany *Characterization of a resorbable polymer-ceramic composite for spinal implants*

Publications

K. Dittmar, A. Tourvieille de Labrouhe, L.-D. Piveteau, H. Hofmann, "Nanostructured Ceramic Coatings for Drug Delivery", MRS Proceedings Vol. 1140: Advances in Material

Design for Regenerative Medicine, Drug Delivery and Targeting/Imaging, Editors V. Prasad Shastri, A. Lendlein, L.-S. Liu, 2009.

Hobbies

Travelling, painting, swimming, hiking